Delft University of Technology

MSc Thesis

Environmental Engineering

Characterization of Gas Transport Pathways in an Aerated Landfill Using In-Situ Measurement Techniques

Author:
Sean Paul Scott (6057195)

Supervisors:
Dr. Julia Gebert
Dr. Leonardo Duarte Campos
Dr. Richard Beaven

Assessment Committee:
Dr. Julia Gebert
Dr. Timo Heimovaara

Acknowledgements

I am very proud to submit this thesis, which represents more than half a year of research, fieldwork, and analysis. At various times throughout the last eight months, I have felt excited, inspired, exhausted, and overwhelmed. I could not have gotten through the latter parts without the support of my family, friends, and especially my partner, Gen Shymanski.

Of course, this work would not have been possible without the assistance and feedback I received from my supervisors and assessors. Julia, Richard, Leo, and Timo provided invaluable insight and structure which greatly helped in my understanding of the context and our results. Leo, however, requires special acknowledgement for the countless hours he spent with me in the field, in the lab, in the van, and in the Bastion Hotel. Tristan Rees-White, while not officially a supervisor, also joined for many of my update presentations and provided very useful input. Similarly, Dr. John Barker of the University of Southampton helped me greatly with the mathematical parts of this thesis.

Quite a few other people also contributed to this project. I would like to thank my friend Bas van Dort for driving me to Almere when nobody else could. Hans Lammen from Afvalzorg was always quick to respond when I had questions for the landfill operators. Carmen Cruz and Susan Buisma-Yi were also always helpful and understanding when I had issues on-site. Nathali Meza and Nasim Ghadikolaei helped me to obtain useful data from other parts of the CURE project. Also, several professors took time out of their busy schedules to help me with this project. For this, I would like to thank Dr. Dennis Voskov for helping me with my numerical model, Dr. Juan Aguilar Lopez for helping me try to implement COMSOL, and Dr. Paul Imhoff of the University of Delaware for helping me to understand his dual porosity model.

Abstract

Low-pressure aeration is a sustainable landfill management technique in which atmospheric air is introduced to the waste body with the aim of promoting aerobic respiration and thereby speeding up waste stabilization. This strategy has been implemented at Braambergen, a pilot landfill in the Netherlands, for several years. Landfill operators and regulators are eager to determine the efficacy of this intervention. In this thesis, several novel testing methods were implemented to characterize the gas flow properties of the pilot landfill and evaluate the significance of preferential pathways, which are considered a limiting factor in landfill aeration. The test methods were also evaluated for their utility in landfill monitoring.

Pressure field tests (PFTs) were used in combination with two gas flow models to quantify the gas permeability of the waste body. Partitioning gas tracer tests (PGTTs) were used to evaluate the saturation of the waste body. Additionally, a dual porosity model was applied to estimate the immobile gas fraction, gas velocity, dispersion coefficient, and mass transfer rate. Finally, gas push-pull tests (GPPTs) were used to calculate the oxygen consumption rate.

The results showed that PFTs could be used to estimate gas permeability anisotropy and monitor the high-permeability pathways, but the method did not seem to capture the differences between aerobic and anaerobic regions of the waste body. PGTTs seemed to better represent these differences, but there were major problems with the quality of the data and the applicability of the dual porosity model. If these issues are resolved, the method could be of great use to landfill operators. GPPTs were successfully used to estimate respiration rates, but the methodology needs improvement. Not enough successful GPPTs were performed to determine their relationship to other test methods.

List of Abbreviations

BTC	Breakthrough Curve
CD	Coordinate Descent
CURE	Coupled Multiprocess Research for Reducing Landfill Emissions
DFM	Difluoromethane
ERT	Eletrical Resistance Tomography
GC	Gas Chromatography
GHG	Greenhouse Gas
GPPT	Gas Push-Pull Test
LEL	Lower Explosive Limit
LFD	Landfill Directive
LFG	Landfill Gas
LS	LumaSense
MSW	Municipal Solid Waste
NAA	Normalized Aerobic Activty
NWO	Nederlandse Organisatie voor Wetenschappelijk Onderzoek
PAA	Percentage Anaerobic Activity
PAS	Photoacoustic Infrared Spectroscopy
PFT	Pressure Field Test
PGTT	Partitioning Gas Tracer Test
REV	Representative Elementary Volume
UEL	Upper Explosive Limit

List of Symbols

b	Thickness of Waste Body
b'	Thickness of Cover Layer
c_∞	Concentration in Injection Mixture
c_p	Intercept of Drawdown vs Time
c_g	Concentration in Gas Phase
c_g^m	Concentration in Mobile Fraction Gas Phase
c_g^{im}	Concentration in Immobile Fraction Gas Phase
D	Dispersion Coefficient
d	Unscreened Depth of Well
F_{dil}	Dilution Factor
f	Mixing Factor
k	Gas Permeability
k'	Cover Layer Gas Permeability
k_r	Radial Gas Permeability
k_z	Vertical Gas Permeability
k_{rz}	Gas Permeability Anisotropy Ratio
K_n	n-Order Modified Bessel Function of the Second Kind
K_H	Henry's Constant
Kb	Transmissivity
L	Distance Between Wells
L_{far}	Distance Far Past the Monitoring Well
l	Total Depth of Well
L_k	Leakage Factor
$M_{n,t}$	n-Order Temporal Moment of Area
m	Recovered Tracer Mass
P	Pressure
Q	Flow Rate
R	Universal Gas Constant
R_f	Retardation Factor

r	Radial Distance from Extraction/Injection Well
r_w	Well Radius
S	Storativity
S_w	Saturation
s	Drawdown
s_m	Steady-State Drawdown
s_p	Drawdown at Inflection Point
$\bar{t}$	Mean Arrival Time
t_{inj}	Injection Time
t_{samp}	Sampling Time
t_p	Time at Inflection Point
v_g	Gas Velocity
z	Depth from Bottom of Cover Layer
γ	First-order Rate Constant
Δs_p	Slope of Drawdown vs Time
θ	Total Porosity
θ_g	Gas-Filled Porosity
θ_g^m	Mobile Gas-Filled Porosity
θ_w	Water-Filled Porosity
μ	Dynamic viscosity of LFG
ρ	Density of LFG
ϕ_g^m	Mobile Fraction of Gas-Filled Porosity
ϕ_g^{im}	Immobile Fraction of Gas-Filled Porosity
ψ	Squared Pressure
ψ_{atm}	Squared Atmospheric Pressure
ω	Average Molar Mass of Gas Phase

Contents

1 Introduction

1.1 Landfilling in Europe

Although the European Union intends to reduce its reliance on landfills for waste disposal, there are still a variety of waste streams which cannot be treated otherwise. This includes materials which are too hazardous to be handled for recycling or reuse, as well as materials which cannot be recycled or reused with our current technologies. Both technical and economic hurdles may limit the circularity of certain materials. Additionally, there are thousands of existing landfills across Europe which have been filled over the last few centuries. Some of these still require decades or even centuries of care to prevent hazardous situations from developing. For these reasons, it remains important to consider the environmental and health impacts of future and historical landfills (Scharff et al., 2011).

Since the advent of sanitary landfilling in the late 20th century, landfill management has followed the philosophy of containing potential environmental contaminants within the waste body. This is achieved by the addition of an impermeable layer underneath the landfill which prevents landfill leachate from entering the adjacent soil. Depending on the geohydrological conditions at the landfill location, this may be a solely geological barrier (typically low-permeability clay) or may be reinforced by an artificial layer. Additionally, a system of drains and pumps is used to control the leachate level and direct leachate to water treatment facilities. Finally, a cover layer is placed atop the landfill to limit how much water can enter the landfill and flush away hazardous compounds, as well as to facilitate recovery of landfill gas (LFG). The cover layer generally consists of a plastic liner overlain by cover soil. Underneath the cover layer, there is a layer of high-permeability soil or gravel which aids in LFG distribution (European Commission, 2024; *Stortbesluit bodembescherming*, 2016).

This approach, outlined for example in the EU's Landfill Directive (LFD), implies that the containment measures must continue to work indefinitely to avoid release of contaminants. Since the waste body is sealed against the entry of air, all degradation of reactive compounds must proceed anaerobically. These reactions are much slower than aerobic reactions, and not all compounds which can be broken down aerobically can also be broken down anaerobically. Additionally, since water cannot enter the landfill, regions of the waste are likely to be dry, which inhibits microbial activity (Kattenberg et al., 2013; Read et al., 2001). This means that the hazardous components of the waste are likely to remain intact for a very long time (Brand et al., 2016; Woodman et al., 2017). At the same time, the measures used to contain contaminants cannot last forever. While the geomembranes used to reinforce clay barriers can last hundreds of years in some situations, they can also fail in as little as a few decades depending on their handling during installation and the conditions they are exposed to in the landfill itself (Rowe, 2005). The clay portion of the liner may last thousands of years if installed properly, but can also fail by cracking if improper design or installation allows desiccation to occur (Philip et al., 2002; Rowe, 2005). Even if these installations do last for their full design lifetimes, it is very possible that the contents of the landfill will still be hazardous in hundreds or even thousands of years (Turner et al., 2017).

Additionally, the anaerobic conditions inside the landfill lead to methane production. While landfills in the EU are required to have methane collection systems (European Commission, 2024), the waste sector is still the second-biggest contributor to methane emissions in Europe (European Environment Agency, 2025). While part of this is due to other sources such as unsealed landfill cells, some emissions still happen at closed landfills due to factors like insufficient methane oxidation capacity in the cover soil (Stern et al., 2007), cracks in the sealing layers (Rachor et al., 2013), and leakages in pipes (Kumar et al., 2024). In addition to potential explosion hazards, this is a critical issue and a focus of European environmental policy due to methane's strong greenhouse gas (GHG) potential (European Environment Agency, 2022).

The LFD states that landfill operators are responsible for maintenance and monitoring of a closed landfill until the local authority deems that the landfill does not pose a hazard (European Commission, 2024). The implementation of this directive varies by member state, but in the Netherlands, operators are required to make financial provisions for aftercare, with the amount being determined by the province and the municipality. After this amount is paid, the responsibility for maintenance of the landfill is transferred to the local authorities (*Wet milieubeheer*, 2025). In practice, sufficient funds must be set aside that accumulating interest can pay for eternal aftercare. This prevents excess burden from falling onto the local authorities if the fund were to run out (Lieten, 2018; Scharff, 2010). However, this also represents an eternal financial risk in addition to the environmental risk. If aftercare must continue indefinitely based on this fund, mismanagement or unforeseen costs can cause the resources to be depleted, thereby transferring financial burden onto the local authorities.

In these ways, our current landfilling practices pass the environmental and social impacts of our consumption on to future generations. This violates the principles of sustainability, and thus a better solution is required.

1.2 Sustainable Landfilling

An alternative approach, called sustainable landfill management, entails taking measures to degrade and stabilize landfilled waste as fast as possible. Ideally, the dangerous compounds in the landfill can be degraded or stabilized as quickly as possible, minimizing the hazard they pose to human health and the environment in the long term (Rich et al., 2008). This generally includes ensuring that the moisture level of the waste is sufficient for bacterial life, and/or introducing air to the waste body so that aerobic bacteria can thrive (Kattenberg et al., 2013).

Moisture levels may be increased by adding fresh water, also called irrigation, or by recirculating leachate. Without moisture addition, contact between microbes, substrates, and nutrients may be limited in areas of the landfill, limiting microbial activity (Barlaz et al., 1990). Adding water can alleviate this limiting factor and improve stabilization rates. It can also potentially flush contaminants out of the waste, reducing the emissions potential (Turner et al., 2017; Woodman et al., 2017). Recirculating leachate instead of using fresh water may help redistribute nutrients between different parts of the landfill and reduce heterogeneity (Kattenberg et al., 2013; Ma et al., 2021) and has the added benefit of reducing treatment needs (Šan & Onay, 2001). However, this technique requires careful optimization to avoid issues with over-saturation and nutrient imbalance. It also tends to promote anaerobic conditions in the landfill due to pore spaces being occupied with water (Barlaz et al., 1990; Ma et al., 2021; Šan & Onay, 2001).

Aeration is another sustainable landfilling approach in which oxygen is introduced into the waste body via atmospheric air in order to promote aerobic respiration. Under aerobic conditions, the degradation rate within the landfill can be much higher (Jain et al., 2005; Read et al., 2001) and a larger proportion of organic carbon can be decomposed (Fricke et al., 2005), leading to faster and more complete stabilization. In fact, several aerated landfills in Germany have shown more than 90% reduction of biodegradable organic carbon within 4-6 years (Ritzkowski & Stegmann, 2012). Additionally, aerobic respiration does not produce methane, so the GHG emissions of the landfill are lowered (but not completely eliminated as anaerobic pockets remain) (Jain et al., 2005; Read et al., 2001). Leachate production is also reduced in many cases, and the remaining leachate tends to have lower concentrations of contaminants (Read et al., 2001; Ritzkowski & Stegmann, 2012), leading to a lower leachate treatment burden overall.

Several methods of landfill aeration have been implemented, with the most popular being low-pressure methods. High pressure methods are largely used for landfill mining and other short-term projects (Ritzkowski & Stegmann, 2012). Within low-pressure aeration, there are the subcategories of active aeration and passive aeration. Under active aeration, air is injected directly into the waste via vertical aeration wells which span the full depth of the waste. Depending on the implementation, it may be extracted at parallel wells (in which case it is sometimes called combi-aeration) or be allowed to reach the surface and be filtered by the cover soil (Meza et al., 2022; Ritzkowski & Stegmann, 2012). In a passive aeration scheme, air is not directly injected. Instead, a negative pressure is induced at the bottom of the landfill by an extraction pump, which causes atmospheric air to be pulled through the permeable cover layer and into the waste. This method relies on the extraction rate being much higher than the gas production rate and is thus sometimes called over-extraction (Meza et al., 2022; Ritzkowski & Stegmann, 2012).

While aeration techniques may significantly lower the environmental impacts of landfilling, they are not without their difficulties. For one, the extreme heterogeneity in landfill environments makes it very difficult to aerate all of the waste. In particular, leachate-saturated areas near the bottom of the landfill are difficult to access with aeration (Hrad & Huber-Humer, 2017; Raga & Cossu, 2014). Additionally, the increased aerobic activity can lead to greatly increased temperatures (Meza et al., 2022; Ritzkowski & Stegmann, 2012). Given the presence of oxygen and methane, this can lead to fires (Berge et al., 2007). Temperature must therefore be carefully managed by controlling aeration flow rates and application of moisture. It is doubly important that moisture levels are managed properly because of the potential drying effect caused by the infiltration of atmospheric air (Baehr & Hult, 1991; Han et al., 2006), which is much cooler and less humid than LFG. At the same time, if too much moisture is added, gas transport can be hindered (Read et al., 2001).

Cost estimates for low-pressure aeration are generally in the range of several euros per ton of waste, including installation and operation for up to eight years (Heyer et al., 2005; Read et al., 2001; Ritzkowski & Stegmann, 2012). While this may not seem significant, it is a significant fraction of the amount that landfill companies earn per ton of waste, which can be as low as €20/ton (Aracil et al., 2018; Scharff, 2014). In the Netherlands, landfill companies often already run at a loss, which is largely a consequence of the huge decrease in landfilling rates in the past few decades (Scharff, 2014). This trend may be expected to spread elsewhere in Europe as member states attempt to reduce landfilling as instructed in the LFD. However, this operational cost may result in significant long-term savings. Due to reduced emissions potential in the waste body, costs for installation and maintenance of the cover layer are expected to decrease, as are leachate treatment costs and gas collection costs. The likelihood of significant groundwater contamination is also decreased, which reduces the likely cleanup costs (Read et al., 2001; Rich et al., 2008; Ritzkowski & Stegmann, 2012). Additionally, the landfill is likely to be released from aftercare earlier, which greatly decreases long-term costs (Heyer et al., 2005; Rich et al., 2008). Aftercare costs may be reduced by 10-25% by means of earlier stabilization (Heyer et al., 2005). This is especially important given that aftercare represents a large uncertainty in traditional landfilling and funding for aftercare remains difficult in countries like the Netherlands (Scharff, 2014).

1.3 Project Background

Currently, a ten-year pilot program is being carried out in the Netherlands to investigate the feasibility of sustainable landfill management in enhancing waste stabilization. As part of a special Green Deal between the Dutch government, various provincial governments, and industry partners, the project has been given special permission to bypass the requirements for conventional landfill management (*Green Deal Duurzaam Stortbeheer*, 2015). Three landfills are being investigated, which each have different contents and environmental conditions. The project will be considered successful if the concentration of contaminants in the leachate of each landfill can be reduced below site-specific environmental protection criteria, which were developed based on local transport and exposure conditions (Brand et al., 2016). If this is achieved, it can be said that the landfill would not pose a hazard to nearby environments and populations even if its containment measures were to fail. In this case, the landfill could responsibly be released from ongoing aftercare requirements (Kattenberg et al., 2013).

This thesis is part of the Coupled Multiprocess Research for Reducing Landfill Emissions (CURE) project, which has been funded by the Nederlandse Organisatie voor Wetenschappelijk Onderzoek (NWO) and studies all three pilot landfills enabled by the Green Deal. This work will focus on only one of these landfills, namely the Braambergen landfill near Almere. This landfill has an active aeration system, but not irrigation or leachate recirculation systems. As part of the Green Deal, the landfill was constructed without an impermeable top liner, which means that air and water can enter the waste. A layer of cover soil is present, however, to contain the waste and prevent odour release. An impermeable bottom liner is also present to prevent contamination of groundwater (*Green Deal Duurzaam Stortbeheer*, 2015).

This project aims to help characterize gas transport within the waste body, since this is critical to its accelerated degradation. Previous research has shown that organic matter degradation is largely controlled by channelling of flow through preferential pathways (Gebert et al., 2023). In the extreme case, almost all of the introduced oxygen could be transported through these larger flow paths, with the bulk of the waste being isolated in pockets which are only oxygenated by diffusion. This could limit the effectiveness of the aeration scheme in accelerating waste degradation. It is hoped that characterization of gas transport in the waste body can contribute to a better understanding of aeration as a sustainable landfill management practice and improve the efficacy of future projects.

1.4 Test Methods

Characterization of the gas transport characteristics will include pressure field tests (PFTs), partitioning gas tracer tests (PGTTs), and gas push-pull tests (GPPTs). All three methods were originally developed for soil research, and their application to landfill monitoring is relatively new.

Pressure field testing is a method of measuring the gas permeability of a landfill waste body, as well as demonstrating connectivity between pairs of wells. During such a test, air is injected into or extracted from one of the landfill's aeration wells while the resulting pressure is measured at other nearby wells. This provides a measure of the gas permeability of the portion of the waste body between the two wells. Application of this novel method was applied to the Braambergen landfill in a preliminary study by Duarte Campos et al. (2023), and similar methods have been applied to other landfills by Jain et al. (2005) and Wu et al. (2012).

Other studies which have applied PFTs to landfills have used a single-well approach, in which air is injected into or extracted from one well and the resultant pressure is measured at the same well (Jain et al., 2005; Wu et al., 2012). This method has the advantage of being easier to set up and less disruptive to landfill aeration but has the disadvantage of providing only one value of gas permeability for each well. This neglects the fact that gas can travel in all directions from the injection/extraction well and some directions may be favoured over others. The multi-well approach, on the other hand, can provide data on the heterogeneity of gas permeability. This method was applied during preliminary testing on the Braambergen landfill (Duarte Campos et al., 2023), but has otherwise never been applied to landfill research. In both PFT methods, one must consider well losses, in which some of the applied pressure is lost as the injected/extracted air travels through the well itself rather than the waste body (Duarte Campos et al., 2023). With a multi-well test, however the distance between the injection well and the monitoring wells reduces the relative contribution of well losses. Pressure changes at the monitoring wells can thus be considered more representative of the waste body properties, and the test as a whole is less dependent on the characteristics of the aeration wells. As with single-well tests, there is still a risk of annulus leakage. This is a phenomenon in which an imperfect seal allows gas to flow directly to the surface along the side of the well, rather than through the waste body. The prevalence of this can potentially be evaluated by performing stepped tests, in which the driving pressure is gradually increased.

PGTTs are a method of determining the moisture content of porous media and can also provide information about gas flow paths. In these tests, two tracer gases are injected into the waste body, one of which is conservative and one of which is partitioning. The partitioning tracer has a strong tendency to partition into liquid water, thereby slowing its transport through the waste body. The conservative tracer, on the other hand, does not have such a tendency. After the tracers are injected, the gas composition is monitored at nearby aeration wells. By comparing the breakthrough curves of the two tracers, the water content of the medium can be calculated. It should be noted that the calculated water content is something of a volumetric average over the various flow paths followed by the gases. By recording the breakthrough curves at several nearby wells instead of only one, information can be gathered about the heterogeneity in gas flow paths. These tests have been performed on other aerated landfills in research contexts (Han et al., 2007, 2006; Jung et al., 2012; Yazdani et al., 2010) but are not often performed by operators due to high cost and complexity.

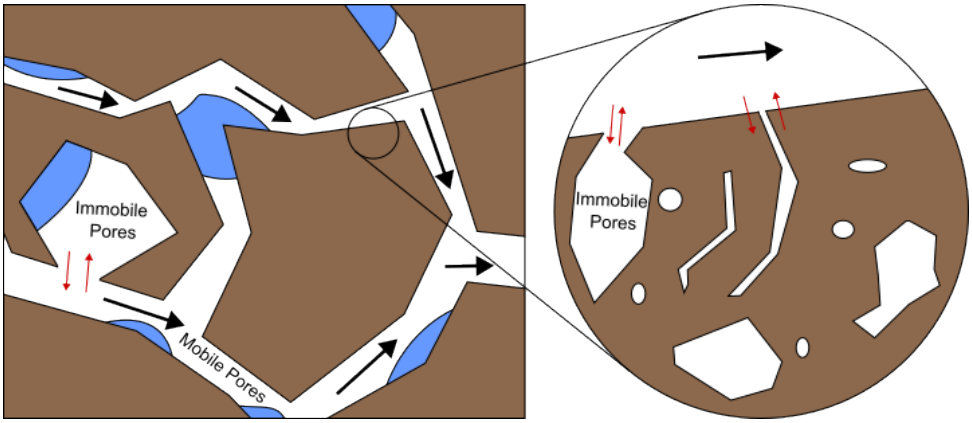

Figure 1: Mobile and immobile pores

The breakthrough curves resulting from PGTTs have previously been fitted to dual-porosity mass transport models (Yazdani et al., 2010). In these models, the pore space of a porous medium is considered to be made up of two overlapping regions. One region, called the mobile zone, participates in advective and dispersive mass transport. The other region, called the immobile zone, participates only in first-order mass exchange with the mobile zone. As long as it is in the immobile zone, tracer gas cannot be transported further along within the porous medium, but rather only to the mobile pores in the same location. Thereby, the immobile zone acts as a kind of storage for gases and delays their transport through the waste body. This is illustrated in Figure 1. In fitting the model, one finds the percentage of the gas-filled pores which are part of the immobile zone, which could be used to characterize the prevalence of preferential pathways.

The application of PGTTs to landfill monitoring is somewhat less novel, with previous studies taking place at various landfills in Europe and the United States (e.g. Han et al., 2007, 2006; Jung et al., 2012; Yazdani et al., 2010). A variety of gases have been used as partitioning and conservative tracers, including difluoromethane

(DFM, also called R-32) and propane, which were used in this work. Most studies have included only one injection well and one monitoring well, but tests have been performed using several monitoring wells to obtain spatial data (Han et al., 2007). During this study, a much higher number of wells were monitored, which provides a better picture of spatial heterogeneity in the waste body.

Single-well push-pull tests have been used for some time to quantify microbial activity. Although originally developed for liquid solutions, a technique for gas push-pull tests (GPPTs) has also been developed. The principle of a push-pull test is that a reactive compound is injected into an environment such as an aquifer or topsoil where microbial activity is taking place, along with a nonreactive tracer with similar mass transport properties. During injection, both compounds travel some distance from the well, with the reactive compound being consumed by microbial processes along the way. After a short transition period, the flow is then reversed. By comparing the recovery of the reactive compound to that of the tracer, the reaction rate can be estimated while accounting for some percentage of the tracer and reactant not being recovered (Istok et al., 1997; Urmann et al., 2005).

GPPTs have been performed in the cover soil of several landfills with the aim of quantifying methane oxidation (Gómez et al., 2009; Ma et al., 2021; Streese-Kleeberg et al., 2011). Additionally, liquid push-pull tests have quantified the oxygen consumption rate in substrates such as sandy sediment and peat bogs (Obradović et al., 2023; Vandenbohede et al., 2008). However, to the author's knowledge, no research has yet been performed on oxygen consumption using GPPTs and no push-pull tests of any kind have been performed in the waste body of a landfill. Tests have been performed on the oxidation of chlorinated organic solvents at an informal military dumping site in the USA (Azizian et al., 2007), but these were liquid push-pull tests and the site was not a formal landfill.

While these tests have been performed individually on other landfills, their combination represents a valuable opportunity to combine the utility of the three methods in evaluating landfill aeration performance. Comparison of the results of the various test methods may provide valuable insights into the effectiveness of landfill aeration. Additionally, long-term data sets are available for such factors as temperature and gas composition, which may provide additional context for the collected data.

1.5 Research Questions

This culminates in the following research question, which can be deconstructed into several sub-questions.

Can partitioning gas tracer testing, in combination with pressure field testing, be used to characterize the gas transport pathways of a sustainably managed landfill?

1. *How well can breakthrough curves from partitioning gas tracer testing be reliably measured and fitted to a dual domain model?*
2. *How well can pressure field testing be used to characterize the gas permeability of the landfill?*
3. *How spatially heterogeneous are the gas transport characteristics of the landfill?*
4. *Do the results of partitioning gas tracer testing and pressure field testing show similar spatial trends?*
5. *Do the results of partitioning gas tracer testing and pressure field testing correlate with the measurements of landfill gas composition?*
6. *Can gas push-pull tests be used as an alternative to partitioning gas tracer tests to characterize water saturation in addition to respiration rate?*

A combination of fieldwork and modelling was implemented in order to answer these questions. As will be discussed further in Section 2, a set of PFTs and PGTTs were performed, along with measurements of gas composition and respiration rates via GPPTs. The resulting data was then analyzed using two gas permeability models and a dual porosity model. Analysis was also performed on retardation factors and respiration rates. Hypotheses for each of the sub-questions are presented below.

1. *Previous research has shown that organic matter degradation in aerated landfills is strongly influenced by preferential pathways, implying that the waste body contains large pores which direct most of the advective transport. This agrees with the flow regime described by a multi-domain model, with a dual domain model being chosen here for simplicity.*

2. *Flow and pressure travel through the waste body by means of connected pore spaces, which also control gas permeability. By applying a flow and measuring a pressure, a good estimate of the gas permeability should be achievable, although it must be seen as a large-scale spatial average.*

3. *The waste body contains many different types of waste which have undergone various levels of degradation and compaction during the construction and operation of the landfill. Due to the heterogeneity of content, a high degree of heterogeneity of properties should be expected. Based on previous research at Braambergen, it is expected that this heterogeneity is relevant at well scale.*

4. *Since advective gas transport occurs only through the air-filled portion of the porosity, gas permeability is largely controlled by water content. This also determines the retardation of partitioning gas tracer testing and thereby the measured saturation. Areas of higher water content should therefore show low gas permeability. Conversely, mobile pores should be larger on average than immobile pores and thus present less resistance to flow. Areas with higher mobile porosity should therefore show higher gas permeability.*

5. *Waste which is more effectively aerated should be expected to have a higher concentration of nitrogen in its pore space. It should also be expected to have a higher temperature due to increased microbial activity, unless it is already fully oxidized. At the same time, waste is likely to be better aerated if it has a higher proportion of mobile porosity. Thus, a correlation should be expected between gas permeability, mobile porosity, temperature, and nitrogen content.*

6. *If both a conservative and partitioning tracer are used for a gas push-pull test, the partitioning gas should be expected to be recovered with a delay relative to the conservative tracer. Thus, it is expected that the water saturation can be calculated from the resulting recovery curves. Also, the aeration of the site means that there are aerobic microorganisms present in the waste body. Injected oxygen should be quickly consumed by these bacteria, allowing the respiration rate to be calculated.*

2 Materials and Methods

2.1 Site Description

Braambergen is a landfill located approximately 6 km from the center of Almere, the largest city in the Dutch province of Flevoland. The location of the landfill is shown in Figure 2, along with a satellite view of the site. The landfill terrain is highlighted in red, while the portion of the landfill used for the aeration project is highlighted in blue. The other cells of the landfill are managed in a traditional manner and used for solar power generation. The landfill is operated by Afvalzorg, a private waste management company, and has been part of the iDS program since its inception (*Green Deal Duurzaam Stortbeheer*, 2015). As part of this program, four of the landfill compartments have been aerated since 2017. Two possible aeration methods are possible: combi-aeration and over-extraction. Under combi-aeration, atmospheric air is injected into one set of wells, while gas is simultaneously extracted from other wells. This causes gas to be transported within the waste body between wells. Under over-extraction, all wells extract gas, with more gas being extracted than is produced within the landfill. This causes air to be pulled through the cover soil and introduce oxygen to the waste body (Meza et al., 2022). The landfill is usually operated using over-extraction (Duarte Campos et al., 2023), including during the time that this research was conducted.

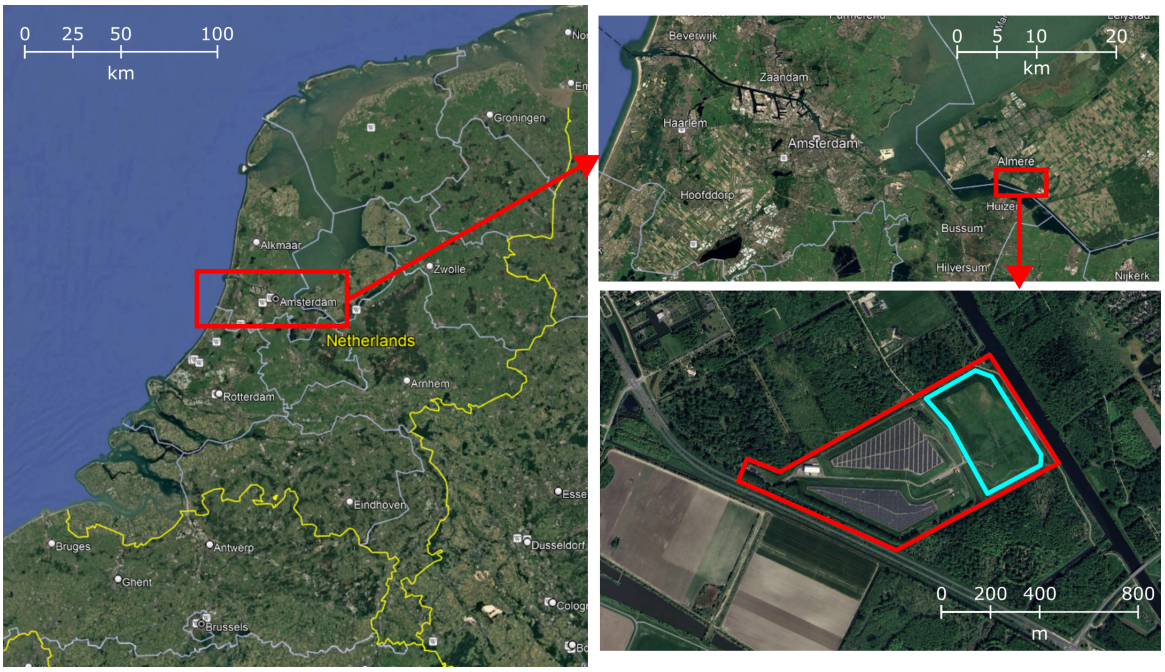

Figure 2: Location of Braambergen landfill, adapted from Google Earth (2025)

In order to realize these aeration schemes, a system of wells has been constructed, as shown in Figure 3a. Figure 3b shows the naming convention of the wells which will be used throughout this work. Rows which include the letter "n" were installed in 2022, while the other rows have been in operation since the aeration project began in 2017.

The aeration wells are spaced 15 to 20 m apart from each other and are drilled to a depth of 10 to 12 m. The bottom 1.8 m of each well is screened, which allows gas transport but prevents ingress of solid particles (Duarte Campos et al., 2023). The wells are constructed of HDPE pipes with outer and inner diameter of 32 and 24 mm, respectively. Gas is extracted from the wells using a network of pipes connected to a central pumping system. Once extracted, the LFG can either be sent to a flare to burn the methane or to a biofilter to remove the methane microbially.

To allow atmospheric air to enter the landfill, it was constructed without a cover layer, as agreed upon in the Green Deal (*Green Deal Duurzaam Stortbeheer*, 2015). As such, it was expected that the waste would be overlain directly with cover soil. However, when trenches were dug to conduct a leachate tracer test in 2023, it was discovered that a layer of incineration bottom ash was present between the cover soil and the waste body. Due to the presence of oxygen, the ash had carbonated to form a low-permeability cementitious layer. Among

the three trenches and five gas injection pits that were dug in 2023, three locations were underlain by ash layers with thicknesses between 20 and 70 cm, while the others did not have underlying ash layers. Additionally, the entire waste body is covered with approximately one meter of cover soil.

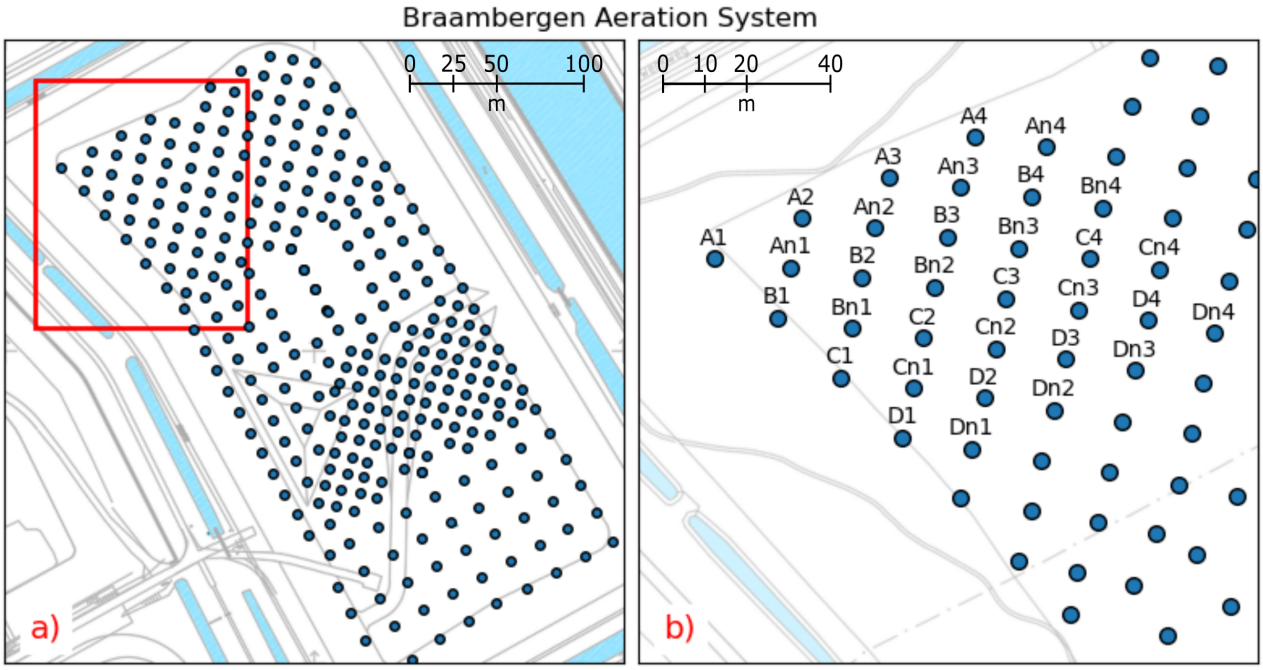

Figure 3: Aeration well locations
a) Whole site b) Research area

Braambergen is divided into several cells, or compartments, which were filled during different periods of the landfill's lifecycle and have slightly different composition. The landfill cell which was studied for this work is 11N, which was chosen because it has higher gas extraction rates than other cells (Meza et al., 2022). It was hoped that this would be correlated with higher connectivity between wells, thus making tracer tests easier to conduct. This cell was filled between 1999 and 2008, and has the composition provided in Table 1. The total volume of waste is 300,637 m^3 (Meza et al., 2022). In particular, testing was focused on the northeastern portion of cell 11N, since the wells in this area had already been modified with an extra valve which allows isolation from the extraction system as required by the testing procedures.

Table 1: Contents of landfill cell 11N (Meza et al., 2022)

Type of Waste	Volume Percentage
Soil and soil decontamination residues	73.4%
Commercial waste	12.1%
Construction and demolition waste	8.4%
Other	6.1%

It is important to note that the pumping system was turned off intermittently during the weeks preceding the first tracer test due to operational issues with the blower. This means that the landfill was not consistently aerated during this period. Additionally, the pumping system was turned off from 29 April to 7 May for another round of maintenance. After these periods without aeration, it was noticed that it took several weeks for the CO_2 and CH_4 concentrations to return to steady-state values. Some tests were performed during these periods of anaerobic activity and recovery, and it is unknown how the results might be affected.

2.2 Overview of Field Tests

In light of the aeration interruptions and changing weather conditions, it is worth keeping track of when tests were carried out. Tables 2 through 4 provide an overview of which tests were performed, on which dates, and on which wells. Details about the test methodologies are given in the following sections. In addition to these

tests, some preliminary investigations into dipole PGTTs were performed in April and May. These could not be successfully performed with the equipment at hand, so further details are not included in this report.

Table 2: Overview of Pressure Field Tests

Date	Test ID	Injection or Extraction Well	Type	Monitoring Wells
2025-03-03	PFT1	D2	Extraction	Bn1, Bn2, C1, C2, C3, Cn1, D1, D3
2025-03-03	PFT2	Cn2	Extraction	Bn1, Bn2, C1, C2, C3, Cn1, D1, D2, D3
2025-03-03	PFT3	D3	Injection	Bn1, Bn2, C1, C2, C3, Cn1, D1, D2
2025-03-03	PFT4	C2	Extraction	Bn1, Bn2, C1, C3, Cn1, D1, D2
2025-03-03	PFT5	Bn1	Extraction	Bn2, C1, C2, C3, Cn1, D1, D2
2025-03-07	PFT1	Cn2	Stepped Extraction	Bn1, Bn2, C2, C3, Cn1, Cn3, D2
2025-03-07	PFT2	Cn2	Injection	Bn1, Bn2, C2, C3, Cn1, Cn3, D2
2025-03-07	PFT3	C3	Extraction	Bn1, Bn2, C2, Cn1, Cn2, Cn3, D2
2025-03-07	PFT4	C3	Injection	Bn1, Bn2, C2, Cn1, Cn2, Cn3, D2
2025-03-07	PFT5	Cn3	Extraction	Bn1, Bn2, C2, C3, Cn1, Cn2, D2
2025-03-07	PFT6	Cn3	Injection	Bn1, Bn2, C2, C3, Cn1, Cn2, D2
2025-03-18	PFT1	Bn1	Extraction	An1, B2, B3, Bn2, Bn3, C1, C2, Cn1, Cn2
2025-03-18	PFT2	Bn1	Injection	An1, B2, B3, Bn2, Bn3, C1, C2, Cn1, Cn2
2025-03-18	PFT3	Cn2	Extraction	An1, An2, B2, B3, Bn1, Bn2, Bn3, C1, C2, Cn1
2025-03-18	PFT4	Cn2	Injection	An1, An2, B2, B3, Bn1, Bn2, Bn3, C1, C2, Cn1
2025-03-18	PFT5	Bn2	Extraction	An1, An2, B2, B3, Bn1, Bn3, C1, C2, Cn1, Cn2
2025-03-18	PFT6	Bn2	Injection	An1, An2, B2, B3, Bn1, Bn3, C1, C2, Cn1, Cn2
2025-03-18	PFT7	B2	Extraction	An1, An2, B3, Bn1, Bn2, Bn3, C1, C2, Cn1, Cn2
2025-03-18	PFT8	C1	Extraction	An1, An2, B2, B3, Bn1, Bn2, Bn3, C2, Cn1, Cn2
2025-03-18	PFT9	B3	Extraction	An1, An2, B2, Bn1, Bn2, Bn3, C1, C2, Cn1, Cn2
2025-03-18	PFT10	B3	Injection	An1, An2, B2, Bn1, Bn2, Bn3, C1, C2, Cn1, Cn2
2025-04-25	PFT1	Cn2	Injection	An2, B2, B3, Bn1, Bn2, C1, C2, C3, Cn1, D3
2025-04-25	PFT2	Cn2	Extraction	An2, B2, B3, Bn1, Bn2, C1, C2, C3, Cn1, D3
2025-04-25	PFT3	Bn1	Stepped Extraction	An2, B2, B3, Bn2, C1, C2, C3, Cn1, Cn2, D3
2025-04-30	PFT1	C2	Extraction	B2, Bn1, C3, Cn1
2025-06-11	PFT1	C3	Stepped Extraction	Bn2, C2, Cn2, Cn3
2025-06-11	PFT2	Bn2	Injection	C2,C3,Cn2,Cn3
2025-06-11	PFT3	Bn2	Extraction	C2,C3,Cn2,Cn3
2025-06-11	PFT4	Bn2	Stepped Extraction	B2, Bn1, C3, Cn1

Table 3: Overview of Partitioning Gas Tracer Tests

Start Date	Test ID	Injection Well	Monitoring Wells
PGTT-1	2025-02-12	C3	Bn2, Bn3, Bn4, C2, C4, Cn2, Cn3, D3
PGTT-2	2025-04-02	Cn2	An2, Bn2, C1, C2, C3, Cn1, Cn3, D3

Table 4: Overview of Gas Push Pull Tests

Date	Test ID	Injection Well	Injection Time (min)
2025-06-10	GPPT-10	Bn2	10
2025-06-10	GPPT-20	Bn2	20
2025-06-11	GPPT-15	Bn2	15

2.3 Gas Composition, Temperature, and Flow Rate

Once per quarter, Afvalzorg employees perform a "gas round," in which they measure various properties of the gas extracted from each well. First, the pressure at the well head is measured using a BlueLine S4601 ST pressure meter. The device is simply connected to the well using a length of tubing and allowed to equalize before being read. Second, the flow rate and temperature in the pipe is measured using a Höntzsch TA10 ATEX thermal flow meter. The probe is inserted into the well head such that the sensor is in the center of the pipe, then slightly rotated to find the maximum flow rate. This ensures that the probe is aligned correctly. Finally,

the gas composition is measured using a GeoTech Biogas 5000 (hereafter referred to as the GeoTech), which measures the methane, carbon dioxide, and oxygen content in volume percent, as well as the hydrogen sulfide concentration in ppm. This device is connected to the well head using a piece of tubing, at which point an internal pump samples gas from the well. Methane and carbon dioxide are measured via a dual-wavelength infrared sensor, while oxygen and hydrogen sulfide are measured using an electrochemical cell (*Geotech Biogas 5000 Datasheet*, n.d.). The gas round used in this work was performed during the week of 2025-02-10 and thus overlaps with the first PGTT. The results were shared by Afvalzorg, along with previous data. The data was analysed for correlations with the results of the PFTs and PGTTs.

The gas round data is also used to calculate several related parameters. First, it is assumed that once the carbon dioxide, methane, and oxygen have been measured, the remainder of the LFG is composed of nitrogen. Next, the percentage of anaerobic activity (PAA) is calculated from Equation 1, which is based on the fact that anaerobic respiration produces equal parts methane and carbon dioxide, while aerobic respiration produces only carbon dioxide (Meza et al., 2022; Yazdani et al., 2010). This was then used to calculate the normalized aerobic activity (NAA) using Equation 2, which compares the PAA at each well to the maximum value observed anywhere in compartment 11N. Finally, conductance is considered as a kind of inverse resistance to flow. It is calculated by dividing the flow rate by the aeration pressure.

$$PAA = \frac{2c_{CH_4}}{2c_{CH_4} + [c_{CO_2} - c_{CH_4}]} \cdot 100\% \tag{1}$$

$$NAA = 1 - \frac{PAA}{PAA_{max}} \tag{2}$$

2.4 Pressure Field Testing

2.4.1 Test Procedure

For the PFTs, one well was selected as the extraction/injection well, with up to eleven surrounding wells being selected as monitoring wells. All wells were isolated from the central aeration system by means of the blue valve shown in Figure 4. It should be noted that only the wells named in Figure 3 are fitted with this valve, with the exception of A1. Thus, PFTs are only possible on these wells unless more valves are installed. The monitoring wells were then fitted with custom-built pressure transducers, which were constructed around Honeywell TruStability pressure sensors with a range of ± 70 mbar. These were connected to HOBO UX120-014M data loggers, which recorded the voltages output by the pressure sensors. One data point was recorded every ten seconds. The voltages were later converted to pressure using previously determined linear calibrations, which were unique to each sensor. The HOBO data loggers also provided real-time readouts of the measurements, which was used to indicate when a steady state was reached.

Figure 4: PFT monitoring well

At the extraction/injection well, a Dutair DB204G air blower was used to generate a flow of gas through the well. The blower was controlled using an Invertek Optidrive E3 Variable Frequency Drive. This controller does not support flow or pressure control, so the blower could only be controlled by frequency, with higher frequency corresponding to a higher flow rate. The blower could be set up to extract gas from the well or inject air into

it, depending on the test. Between the blower and the well, a custom-built flow meter box was installed to measure the gas flow. The flow meter box included a J-TEC VF563C flow meter with instant read-out from an Intercontrol F-126EG Flow Computer. Additionally, two Lascar EL-USB-4 data loggers were used to record pressure and flow rate throughout each test, and a Lascar EL-USB-TC-LCD data logger was used to record the temperature. All of these devices had a measurement frequency of 1 Hz. The setup at the extraction/injection well is shown in Figure 5.

Two types of PFT were performed: steady extraction/injection tests and stepped extraction tests. Prior to any test, the sensors were allowed to record the background pressure at each well for ten to fifteen minutes. Before beginning a test, the pressure sensors were checked to confirm that the pressures were steady. Additionally, the leachate levels and well depths were measured using a Waterline EnviroTech depth probe.

Figure 5: PFT extraction well

For a steady extraction/injection test, the blower was then activated and set to full power. The HOBO data loggers were monitored to determine when steady state was reached. After five to ten minutes of steady state extraction/injection, the blower would be turned off. Before starting another test, the HOBO data loggers were monitored to ensure that all monitoring wells had returned to background pressure for at least ten minutes.

For a stepped test, the blower would first be set to approximately one fourth of its maximum frequency. After steady state was reached, the blower frequency was increased to one half of its maximum. This was continued until the pressure had reached steady state at the blower's maximum frequency, at which point the blower was turned off and the pressure was allowed to return to background.

In one stepped PFT, a CTD-Diver from van Essen Instruments was included at the bottom of the extraction well. This device was connected to the top of the well via a length of paracord such that it hung within the leachate but did not touch the bottom of the well. Throughout the test, the CTD-Diver recorded changes in the leachate depth via a pressure sensor with a sampling frequency of 1 Hz.

2.4.2 Gas Permeability Models

The data from the PFTs were used to map the gas permeability of the waste body using two different models. The first is the Hantush inflection point method (Hantush, 1956), which was chosen for comparison with Duarte Campos et al. (2023). The second model is referred to as the Baehr and Joss model, originally developed by Baehr and Hult (1991) and by Baehr and Joss (1995). The model has been applied to a landfill context previously. In previous studies, however, a single-well approach was used, in which pressure was measured at the same well where flow was applied (Jain et al., 2005; Wu et al., 2012).

Both models were originally developed for soil science and are based upon a leaky aquifer model. This indicates that the soil of interest (in this case, the waste body) is overlain by another material which has much lower gas permeability. This cover material restricts, but does not entirely prevent, ingress of air and water from the surface. At the bottom of the waste is assumed to be a confining layer which does not allow downward flow (Kruseman et al., 2000). For groundwater applications, this confining layer may be clay or stone. For gas transport in the unsaturated zone, it is considered to be the leachate table, as gas cannot flow through pores which are occupied by water.

Hantush Inflection Point Method

The inflection point method was one of several methods proposed by Hantush (1956), which is based around graphical analysis of the pressure response before it reaches steady state. It should be noted that this method is based around the pressure response of a saturated aquifer and has not been explicitly adapted to the flow of air. This means that it does not account for compressibility effects, which are considered in the Baehr and Joss model. Additionally, since the method is based on the unsteady portion of the pressure response, it assumes that the pressure prior to the test is the baseline background pressure. This method therefore cannot be applied to the stepped extraction tests.

The method is based around analytical solutions to Equation 3, which was derived by (Hantush & Jacob, 1955). In this equation, S is the storativity of the waste, which is the volume of water released from the medium per unit decline in hydraulic head under saturated conditions (Kruseman et al., 2000). Kb is the transmissivity, which is the hydraulic conductivity multiplied by the depth of the waste body. Finally, s is the drawdown, i.e. the change in hydraulic head induced by the pumping test.

$$s = \frac{Q}{4\pi Kb} \int_u^\infty \frac{1}{y} \exp\left(-y - \frac{r^2}{4L_k^2 y}\right) dy \tag{3}$$

$$u = \frac{r^2 S}{4Kbt} \tag{4}$$

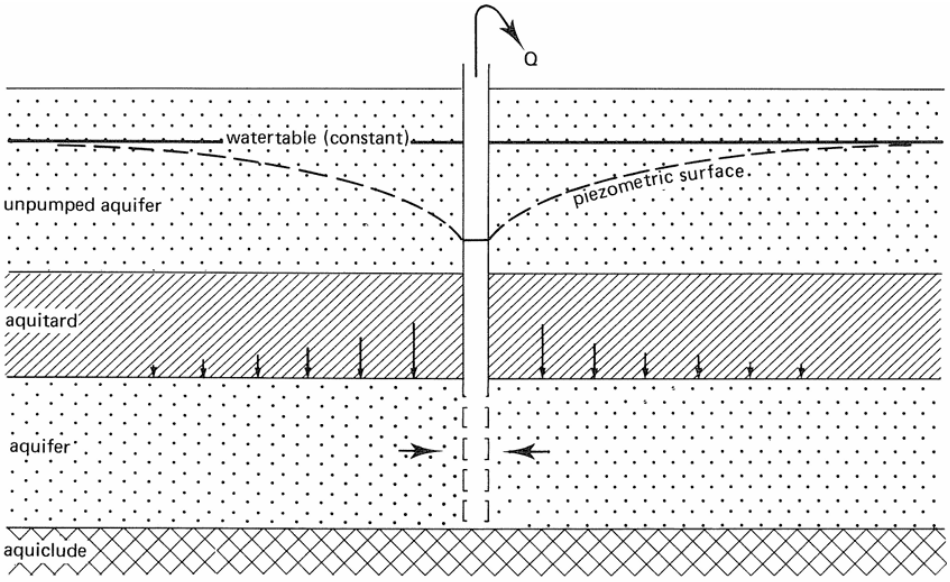

Figure 6: Geometry used in Hantush model (Kruseman et al., 2000)

The geometry used by this model is shown in Figure 6. Since this model is being used for air flow in this case, the region labelled as the aquifer in the diagram is effectively the unsaturated zone of the waste, while the aquiclude is the leachate table. The aquitard is then the cover layer of the landfill, and the unpumped aquifer is the atmosphere. It is assumed that the composition and thickness of each layer is uniform extends far enough radially to be effectively infinite. Additionally, it is assumed that the well is screened along its entire length within the waste body and that the waste body is isotropic. It is also assumed that each layer has uniform gas transport properties (Hantush, 1956; Kruseman et al., 2000). Finally, this model assumes that the porous medium is fully saturated with the fluid of interest, which is carried forward from the original application to

aquifers. This is not fully characteristic of gas flow in the unsaturated zone, since there is both gas and leachate present. Some literature shows that varying levels of saturation can significantly affect gas permeability in porous media (J.-F. Liu et al., 2014; Ni et al., 2023; D. Zhang et al., 2020), while others show that gas permeability is relatively constant until saturation nears 100% (Jucá & Maciel, 2012; Kallel et al., 2004; Stoltz et al., 2010). Research which specifically investigates waste rather than soil tends to support the latter trend, but this research was performed on municipal solid waste (MSW), which is not entirely comparable to the contents of Braambergen (Kallel et al., 2004; Stoltz et al., 2010).

The procedure followed was taken from Kruseman et al. (2000), which presents the work of Hantush (1956) in a more step-by-step manner. First, the transient portion of the pressure response is isolated. The background pressure is subtracted to obtain the relative pressure over time, which is then converted to drawdown. In this case, the Hantush method is adapted by using meters of air head instead of water head. The drawdown is then plotted against the logarithm of time and a linear fit is calculated, with the slope being called Δs_p and the intercept being called c_p. The steady-state drawdown is called s_m, with the value of the drawdown at the inflection point taken to be $s_p = 0.5 s_m$. The time at which the inflection point occurs is then calculated using Equation 5. These values are then used to solve Equation 6 for r/L_k. This is done numerically using the `optimize` function of Python's `scipy` library. In Equation 6, K_0 is the zero-order modified Bessel function of the second kind, r is the distance between the monitoring well and the extraction/injection well, and L_k is a leakage factor which describes the gas permeability of the cover layer. This is then used to calculate the transmissivity using Equation 7.

$$t_p = \frac{s_p - c_p}{\Delta s_p} \tag{5}$$

$$2.3 \frac{s_p}{\Delta s_p} = e^{r/L_k} K_0(r/L_k) \tag{6}$$

$$Kb = \frac{2.3Q}{4\pi \Delta s_p} e^{r/L_k} \tag{7}$$

The gas permeability is then calculated using Equation 8 (Duarte Campos et al., 2023). Here, ρ and μ are the density and the dynamic viscosity of the landfill gas, and b is the thickness of the waste body. However, since the composition of the LFG is both unknown and heterogeneous, the values for atmospheric air were used. Additionally, these values depend on temperature, which is also unknown and heterogeneous. To represent an average temperature within the landfill, the values for 35°C were taken, using the temperature data discussed in Section 2.3 as a reference. The kinematic viscosity was taken to be $1.895(10)^{-5}$ kg/ms and the density was taken to be 1.127 kg/m^3 (Evans, 2015). It should be noted that these values also depend on pressure. Since the waste body is not separated from the atmosphere, however, the ambient pressure is very close to atmospheric pressure.

$$k = \frac{Kb\mu}{\rho g b} \tag{8}$$

In all cases, the thickness of the waste body was taken to be the distance between the bottom of the cover layer and the leachate table, since the presence of water prevents the gas transport from permeating deeper into the waste body. Although the depth of the leachate table is known to vary significantly across the site (Gebert et al., 2022), the model does not consider changes in the geometry of the domain. Thus, the average leachate depth for the measured region of the landfill was used for all calculations, excluding the thickness of the cover layer. The resulting thickness was approximately 7.23 meters.

Baehr and Joss Method

The Baehr and Joss method is a modification of Hantush's leaky aquifer model which is explicitly designed to model air flow and therefore includes compressibility effects. Additionally, the model accounts for the well being screened only at the bottom, as opposed to the Hantush model, and considers the porous medium to be anisotropic as represented by separate radial and vertical gas permeabilities k_r and k_z. The Baehr and Joss model works on the steady-state pressure change and can thus be applied to the stepped tests as well. The majority of the model is put forth by Baehr and Hult (1991), with some corrections to the leakage term being implemented by Baehr and Joss (1995). Similarly to the Hantush method, the Baehr and Joss method assumes that the porous medium and cover layer are homogeneous, of uniform thickness, and extend far enough radially as to be approximately infinite. The assumed geometry is shown in Figure 7.

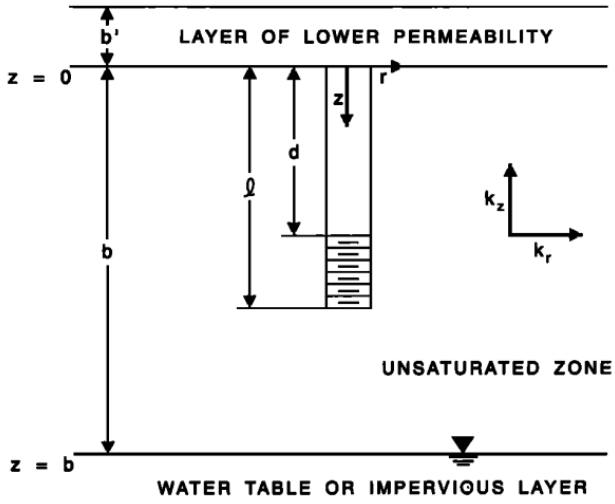

Figure 7: Geometry used in Baehr model (Baehr & Hult, 1991)

The model is derived using Darcy's law for compressible fluids along with conservation of mass. To make the equations more manageable, a variable ψ is defined as the square of the pressure P. Both of these are continuous variables which exist at all points within the waste body. This transformation, given in Equation 9, results in Equation 10 as the governing equation.

$$\psi = P^2 \tag{9}$$

$$k_r \frac{\partial^2 \psi}{\partial r^2} + k_r \frac{\partial \psi}{\partial r} + \tag{10}$$

Leakage from the atmosphere is assumed to be proportional to the known gas permeability of the cover layer, while leakage from the bottom is assumed to be impossible. Additionally, the pressure is assumed to return to atmospheric pressure far from the well, and pressure at the well is determined by the imposed flow rate. By neglecting nonlinear flow effects and assuming uniform temperature and gas composition, the analytical solution in Equation 11 is obtained. This equation determines the pressure at any point in the waste body. The constants in this equation are given by Equations 12 through 16. Additionally, k' and b' are the gas permeability and thickness of the cover layer, ω is the average molecular weight of the air phase, and r_w is the radius of the well. Finally, q_n is the nth solution to Equation 17, which has infinite roots. In the evaluation of these equations, the same assumptions were made for temperature, gas composition, and waste body thickness as in the Hantush method.

$$\psi(r,z) = \psi_{atm} + \zeta \left[\sum_{n=1}^{\infty} \alpha_n \cos\left(\frac{q_n(b-z)}{b}\right) K_0\left(\frac{q_n r}{ab}\right) \right] \tag{11}$$

$$\zeta = \frac{2hQ^* ab}{\pi k_r (l-d) r_w} \tag{12}$$

$$a = \sqrt{\frac{k_r}{k_z}} \tag{13}$$

$$h = \frac{k'b}{k_z b} \tag{14}$$

$$Q^* = \frac{Q\mu RT}{\omega} \tag{15}$$

$$\alpha_n = \frac{\sin\left(\frac{q_n(b-d)}{b}\right) - \sin\left(\frac{q_n(b-l)}{b}\right)}{q_n^2 K_1\left(\frac{q_n r_w}{ab}\right)\left(h + \sin^2(q_n)\right)} \tag{16}$$

$$\tan(q_n) = \frac{h}{q_n} \tag{17}$$

Equation 11 includes an infinite sum for the calculation of pressure. Since this must be truncated to a finite sum ending at the integer N, the sum was evaluated for a trial set of data for each N. It was found that after 100 terms, very little change was observed in the truncated sum. To be sure that the sum had converged, 500 terms were used in all function evaluations. To obtain q_n at each n, Equation 17 must be solved numerically. This was achieved using Newton's method.

Unlike in the Hantush model, this model uses the depth of the extraction/injection well and the monitoring point. In these tests, however, the pressure sensor was above the ground and connected to a point within the waste body via the well itself, which can be treated as a long tube. Since the tube is closed on the end, no flow can take place within the well. Additionally, the diameter is large enough that there should be little resistance and the pressure at the top should very quickly equal the pressure at the bottom. Therefore, the depth of the measuring point was taken to be the highest point at which the well was open to the waste body. Three depth scenarios were identified, for which the depth of the well was assumed differently:

1. The well is intact, and the screen is not entirely below the leachate level. In this case, the monitoring depth is taken to be the top of the screen.
2. The well is intact, but the screen is entirely submerged in leachate. In this case, the monitoring depth is taken to be the top of the leachate.
3. The well is collapsed. In this case, the monitoring depth is taken to be the depth at which the well is collapsed.

Most of the studied wells fell into the first category. No wells fell into the second category. Several wells had collapsed, namely C1, C2, C3, Cn1, and D2. This represents about 30% of the studied wells. This distinction was based on the measured bottom of the well being closer to the surface than previous measurements. In four of these cases, the difference was about two meters. For D2, the difference was about five meters. These wells were not eliminated from consideration, but were modelled under the assumption that the well interacts with the waste at the depth where it has collapsed. Individual tests were treated the same as other wells for the purpose of eliminating outliers, as discussed in Section 3.1.1. With the exception of D2, these wells did not stand out as different from their neighbours, indicating that this treatment was well-founded.

Additionally, the Baehr and Joss method requires certain characteristics of the cover layer, namely its thickness b' and gas permeability k'. As mentioned in Section 2.1, however, there is some uncertainty in this due to the unexpected and uneven application of a carbonated ash layer. However, the Baehr and Joss method assumes that the cover layer is uniform throughout the study area. Based on measurements taken when the leachate trenches were dug, the ash layer was assumed to have a constant thickness of 35 cm across the waste body. Previous testing performed within this research group (unpublished), showed that the gas permeability of this ash layer was approximately $6 \cdot (10)^{-12}$ m^2. The ash was assumed to be overlain by a layer of cover soil with a thickness of one meter. Since no data was available on the particular cover soil, a gas permeability of 10^{-8} m^2 was assumed (Moon et al., 2008; Ni et al., 2023; Wen et al., 2023). These two materials were combined into a single layer with a thickness of 1.35 m and a gas permeability of $2.4 \cdot (10)^{-11}$ m^2 using the inverse average formula in Equation 18. Since the gas permeability of the ash layer is so much lower than that of the cover soil, it dominated the calculation. Therefore, the assumption made for the cover soil gas permeability did not make a large difference to the results.

$$\frac{1}{k'} = \left(\frac{b_{soil}}{k_{soil}} + \frac{b_{ash}}{k_{ash}}\right)\left(\frac{1}{b_{soil} + b_{ash}}\right) \tag{18}$$

For each well pair in each PFT, the flow rate and resulting pressure change were known and could be used to solve for the gas permeability. For an assumed anisotropy ratio k_{rz}, this was done by rearranging Equation 11 into Equation 20 and then using the bisection method to numerically solve for the value of k_r that satisfied the equation.

$$k_{rz} = \frac{k_r}{k_z} \tag{19}$$

$$\psi(r,z) - \left(\psi_{atm} + K\left[\sum_{n=1}^{\infty} \alpha_n \cos\left(\frac{q_n(b-z)}{b}\right) K_0\left(\frac{q_n r}{ab}\right)\right]\right) = 0 \tag{20}$$

2.5 Partitioning Gas Tracer Testing

2.5.1 Test Procedure

For the PGTTs, one well was designated as the injection well and eight nearby wells were selected as monitoring wells. The decision for which wells would be monitored was based largely upon the composition of the LFG at each well, as methane content above 15% could cause invalid measurements of tracer concentration during the PGTT. The wells selected for each PGTT are shown in Table 3, along with the start date of each test. The locations of the wells can be found in Figure 3b. Throughout the duration of each test, the site-wide extraction of gas was disabled at the injection well but left on at the monitoring wells. This caused the tracer gases to be pulled towards the monitoring wells.

There were unfortunately some environmental differences between the two tests. Prior to PGTT-1, the extraction system was out of operation for several weeks for maintenance. A buffer period of several more weeks was allowed before the test began, but decreasing background methane concentrations were observed during the test, indicating that a steady state had not quite been re-established. Between this test and PGTT-2, the site-wide extraction was operational the entire time and a steady state was reached during the intervening weeks. Additionally, PGTT-1 was performed at the end of a very rainy winter, so a high degree of saturation was expected in the cover soil. Between the two tests, there was very little precipitation and the site was much drier.

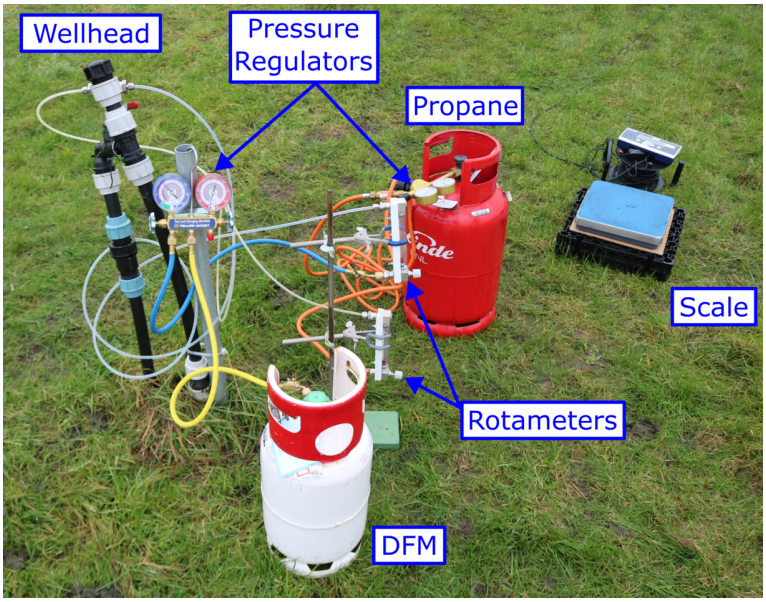

Figure 8: Injection apparatus for PGTT

The apparatus for gas injection is shown in Figure 8. The well head at the injection well was fitted with a T-piece fitting, which allowed for simultaneous injection of conservative and partitioning tracers. For all tests, propane was used as the conservative tracer and difluoromethane (DFM), also known as R-32, was used as the partitioning tracer. A rotameter was fitted to each gas line and was monitored continuously throughout injection to ensure a consistent flow rate of each gas. Additionally, the gas canisters were measured before and after the injection to quantify the total amount of injected gas. In both tests, the injection rate of propane was 14 L/min, while the injection rate of DFM was 2 L/min. The injection took place over two hours, after which approximately 4 kg of propane and 0.5 kg of DFM should have been injected. This was verified based on weighing of the gas cylinders before and after the test.

The monitoring wellheads were fitted with a different T-piece, as shown in Figure 9. The sampling tube allowed gas from the well to be sampled by the LumaSense Innova 1512 Photoacoustic Gas Monitor (hereafter referred to as the LumaSense), which will be discussed in further detail in the following paragraphs. The sampling valve was closed during the normal operation of the experiment but could be opened and attached to the GeoTech to allow measurement of gas composition and collection of gas samples in gas bags. If propane was present at the well, the GeoTech would report a greatly increased methane concentration compared to background, which allowed for verification of propane breakthrough when indicated by the LumaSense. The

non-return valve ensured that gas samples were taken directly from the well rather than from stagnant gas in the sampling tube. Gas bags were reused for several samples, but only from one well to prevent contamination with tracer gases. Additionally, they were cleaned between uses by repeated flushing with compressed air.

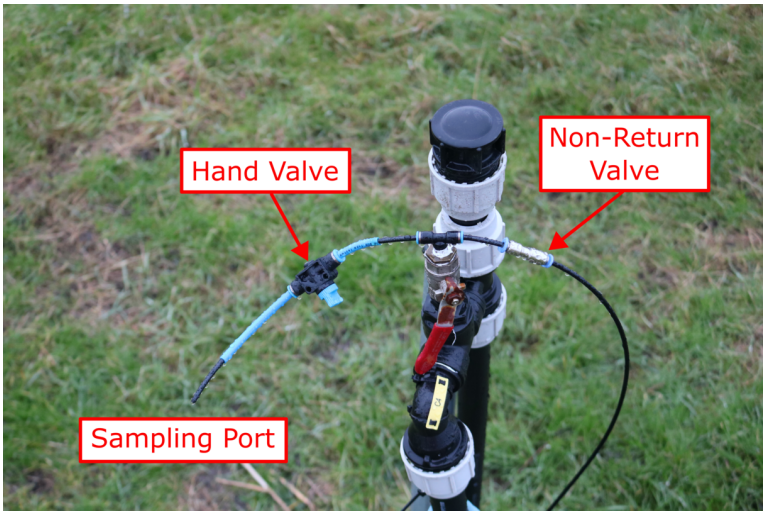

Figure 9: Monitoring well for PGTT

The LumaSense, shown in Figure 10, consists of two modules which work in concert to measure gas concentrations at up to 24 wells, although only eight were used for these tests. The first module is the multiplexer, which samples gas periodically from each wellhead. Prior to the measured quantity of gas, the device pulls through enough gas to flush the tubes and the measurement chamber. The combined flushing and sampling process takes about one minute. In addition to the eight wells, a ninth channel was set up which could be used to measure the contents of gas bags and other miscellaneous samples during the course of the test. Thus, each channel was sampled every nine minutes, approximately.

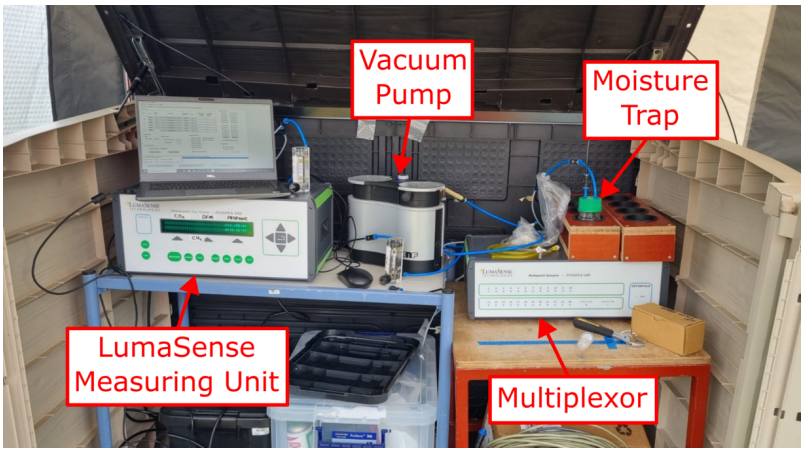

Figure 10: LumaSense installation

The samples from the multiplexer are then sent to the measuring unit, which operates based on photoacoustic infrared spectroscopy (PAS). A representation of the system is shown in Figure 11. PAS is based on the principle that gases increase in temperature when they absorb electromagnetic radiation. In an enclosed space, this corresponds to an increase in pressure. By modulating the light source at a frequency in the acoustic range, a pressure response with a frequency in the acoustic range is produced by the measured gases and measured by embedded microphones. The modulation is performed using a rotating propeller-like wheel which intermittently blocks the light source (Harren & Cristescu, 2019). Each gas absorbs different frequencies more readily, so a wheel of optical filters can be used to selectively pass different frequencies of light to the measuring chamber and measure the concentration of each gas in turn (Harren & Cristescu, 2019). However, the absorption spectra of the different gases may overlap somewhat, resulting in interference between the measured gases. This is addressed by an internal cross-compensation system, in which a system of linear equations is constructed and

solved based on the photoacoustic response and absorption coefficient of each gas (Jung et al., 2012). Still, it was found that high methane concentrations could affect the measured propane and DFM concentrations without being corrected by the internal cross-compensation. This was addressed with an additional compensation curve, which is discussed further in Section 2.7.

Between the two components of the LumaSense, a Laboport N 840 G vacuum pump was installed to ensure that sufficient suction pressure was available to extract samples from far-away wells. Additionally, a set of moisture traps was installed just before the multiplexer. While the LumaSense does contain a filter to compensate for the effects of water vapour (*Innova 1512 Datasheet*, 2020), the LFG cools significantly after leaving the landfill and thus condensation can be expected. The moisture traps prevent liquid water from entering the measurement chamber of the LumaSense.

Prior to injecting the tracer gases, each wellhead was checked for leaks by closing the valve which connects it to the well and attaching a gas bag filled with calibration gas. After the well was sampled by the LumaSense, it was checked whether the LumaSense reading agreed with the composition of the landfill gas as measured by the GeoTech. Different calibration gas mixtures were used throughout the tests due to limited availability, but all were within the calibration range of the LumaSense for all constituent gases. Additionally, the background composition of gas at each well was measured with the GeoTech and samples were taken in gas bags for further analysis. Finally, the depth and leachate level of each well was measured using a Waterline Envirotech depth meter. If the leachate level was higher than the screened length of the well or the well had collapsed (as indicated by lower depth than anticipated) other wells were considered instead. Wells were also rejected if the background composition measurements from the LumaSense and GeoTech could not be made to agree, or if the composition indicated that the well was filled with atmospheric air.

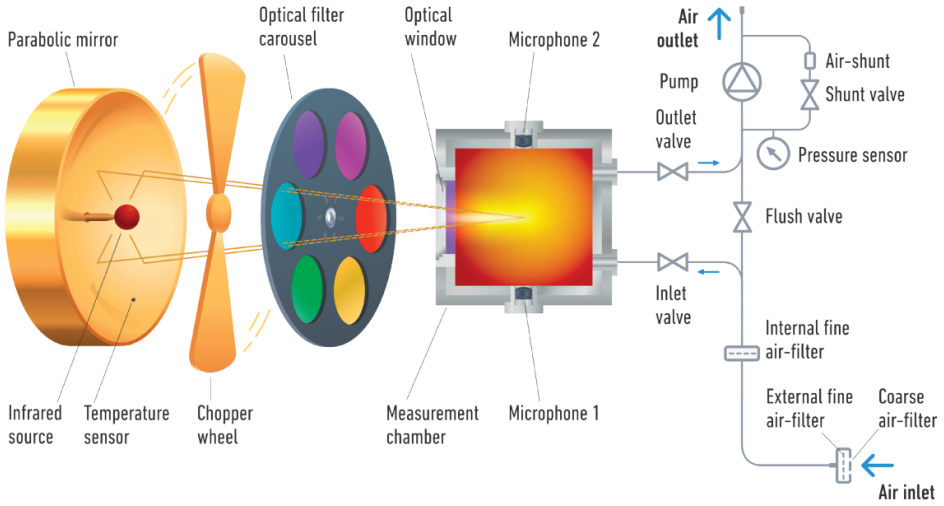

Figure 11: Operation of LumaSense (*Innova 1512 Datasheet*, 2020)

Before and after the injection of tracer gases, the gas composition at each monitoring well was measured periodically using the GeoTech. It was known that the presence of trace amounts of propane could cause a significant increase in the measured methane concentration. This was used to find wells which exhibited breakthrough and thus needed particular attention. At wells with breakthrough, gas bag samples were taken at regular intervals. At wells without any indication of breakthrough, gas bag samples were taken less frequently. Gas bag samples were also occasionally taken from surrounding wells which were not connected to the LumaSense. After being collected, the gas bags were tested on the extra channel of the LumaSense to check whether the measured concentrations agreed with the normal measurements. Any discrepancies could indicate leaks or insufficient flushing of the sampling tubes.

All gas bags were taken to the Geosciences lab at TU Delft and tested with gas chromatography (GC) within 48 hours of being sampled. Two GC devices were used – the Agilent 490 Micro-GC and the Agilent 8860 GC System. The Agilent 490 operates using a thermal conductivity detector (Agilent Technologies, 2017) and was used to measure methane, carbon dioxide, oxygen, and nitrogen. The Agilent 8860 was used to measure propane and contains both a thermal conductivity detector and a flame ionization detector (Agilent Technologies, 2021). By comparing these results with those from the GeoTech and the LumaSense, it was confirmed that the devices

were measuring properly. Unfortunately, no GC in the Geosciences lab was capable of measuring DFM, so these results could not be verified from the gas bags.

After the concentration of both tracers had decreased to near-background levels, the LumaSense sampling was stopped. Gas bag sampling was continued until propane was no longer measured, which could take up to two weeks.

2.5.2 Retardation Factor, Water Saturation, and Recovery

For each well monitored during the PGTT, the retardation factor and water saturation were calculated according to the approach of Han et al. (2006). Additionally, the tracer recovery rate was calculated for each test. To calculate the retardation factor, the mean arrival time of each tracer was calculated using Equation 21. In this equation, $M_{0,t}$ and $M_{1,t}$ are the zeroth and first temporal moments of area and are calculated according to Equation 22, where $c_g(t)$ is the concentration of the tracer in the gas phase. Additionally, t_{inj} is the total time over which the tracers were injected, and t_{samp} is the time taken for each sample to be taken by the LumaSense. The retardation factor and water saturation were then calculated using Equations 23 and 24, where K_H is Henry's constant. Here, saturation is defined according to Equation 25 as the volume of water divided by the pore volume. Therefore S_w ranges from 0 for totally dry waste to 1 for fully saturated waste.

$$\bar{t} = \frac{M_{1,t}}{M_{0,t}} - \frac{t_{inj}}{2} - t_{samp} \tag{21}$$

$$M_{k,t} = \int_0^\infty t^k c_g(t) dt \tag{22}$$

$$R_f = \frac{\bar{t}_{DFM}}{\bar{t}_{propane}} \tag{23}$$

$$S_w = \frac{(R_f - 1)K_H}{1 + (R_f - 1)K_H} \tag{24}$$

$$S_w = \frac{\theta_w}{\theta} \tag{25}$$

Since the integral in Equation 22 goes to infinity, the declining portions of the breakthrough curves (BTCs) were first fitted to an exponential function of the form provided in Equation 26 and then extrapolated until the normalized concentration (i.e. measured concentration divided by input concentration) was below 10^{-9} and was thus effectively zero. This fit was based on the combined LumaSense and GC data.

$$f(t) = Ae^{-Bt} \tag{26}$$

However, the BTCs did not entirely follow this equation, consisting instead of an initial bump followed by an exponential decay. The fitting was performed on only the exponential decay part of the curve. To avoid subjectivity in deciding where this began, an approach was followed similar to that of Han et al. (2006). A fit was performed using the last ten points in the tail in the curve and the r^2 was calculated to indicate the quality of the fit. This was then repeated using the last eleven points of the tail and so forth until the entire curve was used. The fit with the best r^2 was then used for the subsequent calculations.

The Henry's constant for DFM has been shown to vary fairly significantly depending on temperature (Han et al., 2007; Kutsuna, 2017). Salinity has also been shown to influence the Henry's constant (Kutsuna, 2017), but is unlikely to be as significant in the salinity range of landfill leachate. While tests at room temperature report a Henry's constant of around 1.56 (Sander, 2023), the constant has been shown to decrease with temperature (Kutsuna, 2017), meaning that a smaller portion of the gas partitions into the aqueous phase when temperature is increased. Based on these relations, a Henry's constant of 1.27 was used to reflect the assumption of a constant 35°C temperature within the waste body (Kutsuna, 2017). It should be noted that this is the dimensionless solubility version of the Henry coefficient, which is essentially the ratio of the equilibrium concentration in the aqueous phase to that in the gaseous phase. Various other forms of this constant exist, which can be easily converted into one another (Sander, 2023).

The recovery rate was calculated based on the amount of tracer recovered at each well. At each time step t, the mass recovery rate of each tracer can be calculated according to Equation 27. Here, ω is the molar mass

of the tracer gas. Q, P, and T are the flow rate, pressure, and temperature of the gas in the extraction system of the well in question. Since these were not measured in real time, the measurement taken at the previous gas round was taken as an approximation. The mass recovery rate was then numerically integrated over the duration of the experiment to find the total mass of tracer extracted from that well. Since only the concentration was taken to be a function of time, the integral can be simplified as shown in Equation 28. Once the mass recovery was calculated for each well, the values were summed to find the tracer recovery of the overall experiment.

$$\dot{m}(t) = \frac{\omega Q P c_g(t)}{RT} \tag{27}$$

$$m(t) = \int_0^t \frac{\omega Q P c_g(t)}{RT} dt = \frac{\omega Q P}{RT} \int_0^t c_g(t) dt \tag{28}$$

Finally, the time of breakthrough and the time of peak concentration were recorded for each tracer at each well. The time of breakthrough was considered as the moment when the concentration reached 5% of its peak value. The peak time was simply the time at which the maximum concentration was reached.

2.5.3 Dual Porosity Model

To find the fraction of mobile porosity, a dual porosity model was set up according to the formulation of Yazdani et al. (2010). The mathematical formulation of the model is modified somewhat due to differences in assumptions made when deriving the equations. A derivation of the new formulation can be found in Appendix A, as well as some comments about the differences in derivation. This formulation consists of a one-dimensional "stream tube" between the injection well and each extraction well. Throughout the experiment, both tracers move through the tube via advective and dispersive transport in the mobile zones as represented by Equation 29. At the same time, the tracers move between the mobile and immobile zones according to Equation 30. In these equations, the superscript m denotes parameters relating to the mobile zone of gas-filled porosity, while the subscript im refers to the immobile zone. Also, γ is a kinetic rate constant which characterizes mass exchange between the mobile and immobile zones, L is the distance between the two wells, θ_g is the gas-filled porosity, v_g is the velocity of the gas phase, and D is the dispersion coefficient.

$$\phi_g^m \frac{\partial c_g^m}{\partial t} + (1 - \phi_g^m) R_f \frac{\partial c_g^{im}}{\partial t} = \phi_g^m D \frac{\partial^2 c_g^m}{\partial x^2} - v_g \frac{\partial c_g^m}{\partial x} \tag{29}$$

$$(1 - \phi_g^m) R_f \frac{\partial c_g^{im}}{\partial t} = \frac{\gamma}{\theta_g} \left(c_g^m - c_g^{im} \right) \tag{30}$$

$$\phi_g^m = \frac{\theta_g^m}{\theta_g} \tag{31}$$

In addition, the following boundary conditions apply. Equation 32 denotes that the concentration at the injection well is controlled by the concentration of the tracer gas in the injection mixture (indicated by c_∞), as well as gas being transported further down the stream tube. Equation 33 denotes that tracer concentration very far from the extraction well should be approximately constant due to the influence of dispersion. It should be noted that L_{far} is taken to be much further than the inter-well distance L.

$$c_g^m(0, t) = c_\infty(t) + \frac{D}{v_g} \frac{\partial c_g^m}{\partial x}(0, t) \tag{32}$$

$$\frac{\partial c_g^m}{\partial x}(L_{far}, t) = 0 \tag{33}$$

This dual domain model was then implemented in Python. The forward model is based on a finite volume discretization in order to ensure mass is conserved and uses implicit time stepping to preserve numerical stability. An inverse model was also created, which uses the coordinate descent (CD) method to estimate ϕ_g^m, v_g, D, and γ. The data from Yazdani et al. (2010) was used to validate the model, by checking whether the results match those reported in that work. During validation, it was noted that the BTC could not be made to match the reference data for any set of parameters. This was attributed to the fact that the model does not account for the fact that the monitoring well extracts gas from all directions, not only from the stream tube which contains the tracer gasses. Additionally, the injected gasses do not follow one single stream tube but are instead split

between many. The model therefore does not account for tracer gas dilution. This was accounted for using a "dilution factor," called F_{dil}, as shown in Equation 34. This factor was also estimated using the inverse model. More details on the construction of both models are provided in Appendix B.

$$c^m_{meas} = \frac{c^m_g}{F_{dil}} \tag{34}$$

While ϕ^m_g, v_g, D, and γ were estimated using the inverse model, the total porosity and the retardation factor were considered fixed. The retardation factor was taken from the analysis described in Section 2.5.2. In accordance with Yazdani et al. (2010), the total porosity was taken to be a constant at 0.5. The gas-filled porosity was then calculated according to Equation 35. Models have been developed to estimate the total porosity and/or gas-filled porosity based on the gas permeability of a waste sample (Stoltz et al., 2010; Xu et al., 2020; Zeng et al., 2017), but these require calibration with waste samples. These were not available during this project, so the porosity was instead taken to be constant.

$$\theta_g = (1 - S_w)\theta \tag{35}$$

2.6 Gas Push-Pull Tests

2.6.1 Test Procedure

The setup for GPPTs is shown schematically in Figure 12. Quick-connects on the hose allow for easy switching between injection and extraction. During both injection and extraction, the same flow meter box was used as for the PFTs. Temperature, flow, and pressure were again measured with a frequency of 1 Hz. The attachment of the gas cylinders is very similar as for the PGTTs, except that they are attached to the hose instead of the well head. The gases are injected after the flow meter, so that the measured flow rate during injection is only that of air. The LumaSense is also attached very similarly as in the PGTTs, but it has only one sampling point which is on the hose instead of the wellhead. Since the LumaSense does not have to cycle between multiple measuring points, the sampling rate is higher than in the PGTTs at around one sample every 90 seconds. The GeoTech was installed at the same sampling point as the LumaSense and set to continuously monitor. The device was set to take a reading of CH_4, CO_2, O_2, and H_2S every minute for the duration of the test. Each reading was preceded by 40 seconds of flushing. Before the start of the test, the maximum extraction rate of the well was determined by activating the pump at full power. Additionally, the mass of the gas cylinders was measured. All nearby wells were disconnected from the extraction system, in addition to the well being tested.

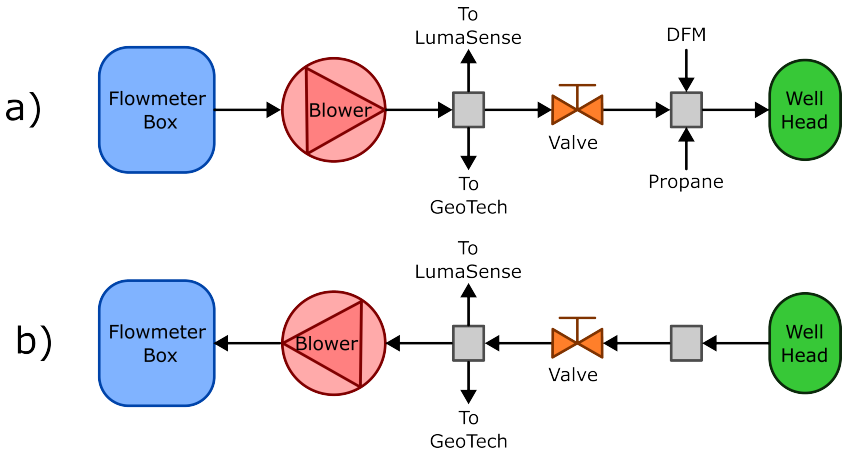

Figure 12: GPPT Setup - a) Injection b) Extraction

The GPPTs differed from the PGTTs because the propane was mixed with atmospheric air during injection, creating the potential for an explosive mixture. To avoid this possibility, the concentration of propane in the injection mixture must be kept under the lower explosive limit (LEL) or above the upper explosive limit (UEL), which are 2.1% and 9.5% by volume respectively (NOAA, n.d.). The maximum flow rates on the aeration wells varied between 5 and 50 m^3/h. Additionally, the flow rate of propane cannot be less than 0.8 L/min or more than 40 L/min due to the scales of the available rotameters. The flow of DFM should be kept proportional to that of propane, but similarly cannot be less than 0.4 L/min or more than 3 L/min. The resulting safety region is shown in Figure 13. For high-flow wells, a mixture below the LEL can safely be injected. For wells

which cannot supply flow of more than approximately 25 m^3/h, however, the injection mixture must be above the UEL to create a non-explosive mixture with a sufficient safety factor. In this work, high-flow wells were selected so that lower propane concentrations could be used, thereby shortening test times.

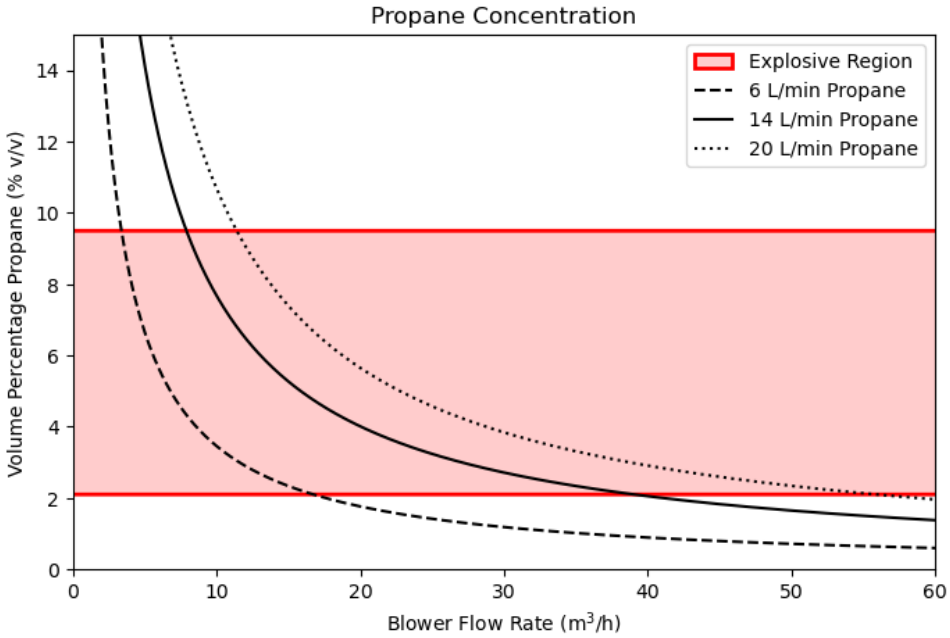

Figure 13: Explosive limits of propane

At the start of the test, the blower was set up in an injection configuration and set to 85% of the maximum extraction flow rate. Simultaneously, DFM and propane were set to the desired flow rates. In this work, only high-flow wells were tested, so the flow rates of propane and DFM were set to 6 L/min and 1 L/min respectively. The injection was continued for a predetermined period of time between 10 and 20 minutes, with longer injection times causing a higher waste volume to be tested. After this period, the valve in Figure 12 was closed to isolate the well from the blower, and the blower was switched into an extraction configuration. After a five-minute rest period, the valve was reopened, and the blower was reactivated and set to the same flow rate as was used during injection. Extraction continued until the propane and DFM concentrations measured by the LumaSense returned to background levels. The gas cylinders were weighed again at the end of the test to confirm how much gas was injected.

A total of three GPPTs were performed, as listed in Table 4. It was intended to test multiple wells in order to obtain some spatial data, but issues with well flow and LumaSense measurements meant that the only successful tests were performed on Bn2. Different injection times were tested, which should change the volume of waste which comes into contact with the injected mixture. GPPT-10 and GPPT-20 were performed on June 10th, but it was discovered that the site extraction had been accidentally disabled early that morning. The next day, the extraction system was turned back on and GPPT-15 was performed approximately one hour later, after the ambient pressure had stabilized. Although the extraction system was disabled at all nearby wells, a change of 1 - 1.5 mbar was seen at the monitoring wells. Therefore, the environmental conditions during each test were not identical.

2.6.2 Data Analysis

The resulting tracer curves were subjected to the same analysis of R_f and S_w as was described in Section 2.5.2 to obtain a value of saturation local to the aeration well. It should be noted that this procedure was developed based on chromatography principles (Han et al., 2006), which involves a linear travel of the tracer gases. It was not adapted to the radial flow regime which is expected for the GPPTs.

Additionally, the procedure described by Streese-Kleeberg et al. (2011), in turn based on Yang et al. (2007), was used to calculate the oxygen consumption rate. First, a mixing factor f is calculated according to Equation 36, which is a measure of how much tracer is recovered at each time step. The net mass transfer is then calculated

according to Equation 37, which essentially compares the amount of oxygen recovered to the amount of tracer recovered. The difference is assumed to have been consumed by reactions in the waste body. In these equations, the subscript tr refers to the tracer, while the subscript r refers to the reactive gas. Additionally, the superscript 0 refers to the injection mixture and the superscript b refers to background. This is then plotted against time and a linear fit is calculated. The slope of the linear fit is the zero order rate constant. The same process was also applied to the concentration of methane.

$$f(t) = \frac{c_{tr}(t) - c_{tr}^{b}}{c_{tr}^{0} - c_{tr}^{b}} \tag{36}$$

$$\hat{c_r}(t) = c_r(t) - \left(f \cdot c_r^0 + (1 - f) \cdot c_r^b\right) \tag{37}$$

2.7 LumaSense Compensation Curves

In previous testing, it was found that a high methane concentration could induce false propane readings in the LumaSense, despite its built-in cross-compensation. To account for this, a lab test was conducted in which the LumaSense was set up to sample a closed loop of a gas mixture as shown in Figure 14. This setup meant that the gas sampled by the LumaSense was exhausted back into the mixing chamber, so the volume and composition of the gas stayed constant unless deliberately modified.

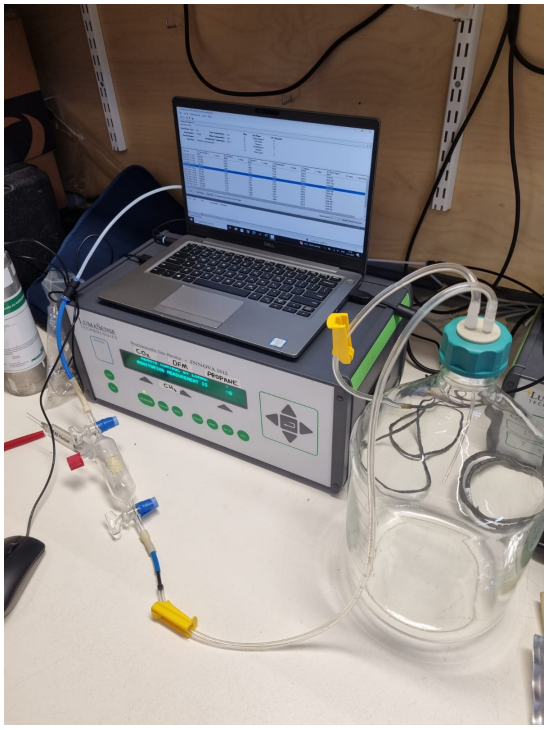

Figure 14: Looped setup for compensation test

At first, the volume was filled entirely with nitrogen, to prevent the possibility of an explosive atmosphere being created. Over time, samples of the gas mixture were removed using a syringe and their composition was measured using the Agilent 490 Micro GC to compare with the LumaSense readings. The sample was then replaced with an equivalent volume of pure methane, such that the methane concentration in the loop increased throughout the course of the test. This was continued until a concentration of approximately 20% was reached, which represents the maximum concentration likely to be observed in the field. At this point, a small amount of propane was added in the same manner. By checking the concentration of the gas mixture using the Agilent 8860 GC System, it could be checked whether or not the compensation adequately removes the effect of methane.

The propane, DFM, and CO_2 concentrations indicated by the LumaSense during the compensation testing are shown in Figure 15. Since only methane and nitrogen were in the system, these concentrations are fully an artifact of the LumaSense's cross-compensation. A cubic equation was found to fit well to each test, with the coefficients given in Table 5. Equation 38 was used to remove the cross-compensation artifacts from all of the LumaSense data collected during the PGTTs and GPPTs.

$$c_{gas} = c_{gas}^{measured} - \left(A \cdot c_{CH_4}^3 + B \cdot c_{CH_4}^2 + C \cdot c_{CH_4} + D\right) \tag{38}$$

The compensation curves were applied to all subsequent LumaSense data analysis without further correction. In addition to the discrepancy at high concentrations, it should be kept in mind that the effects of background CO_2 and elevated temperature were not investigated. It is unknown how these factors would affect the fit of the compensation curves. These limitations should be kept in mind during the processing and interpretation of the BTCs.

Table 5: Compensation curves

Gas	A	B	C	D
Propane	$3.6333(10)^{-13}$	$-2.3463(10)^{-7}$	$1.4880(10)^{-2}$	$-2.5308(10)^{1}$
DFM	$-4.4344(10)^{-16}$	$2.9293(10)^{-10}$	$-1.8186(10)^{-5}$	$7.2793(10)^{-2}$
CO_2	$-5.9650(10)^{-13}$	$3.9987(10)^{-7}$	$-2.6368(10)^{-2}$	$1.4516(10)^{1}$

Figure 16 shows the results of adding propane to the recirculating system and applying the compensation curve. At lower concentrations, the compensated LumaSense data matches the actual concentration well. At higher concentrations, however, there is a difference of as much as 40% between the compensated concentration and the actual concentration. This difference does not seem to be constant and is not well understood. At all concentrations, the compensated LumaSense data matches the actual concentration much better than the raw data exported by the LumaSense.

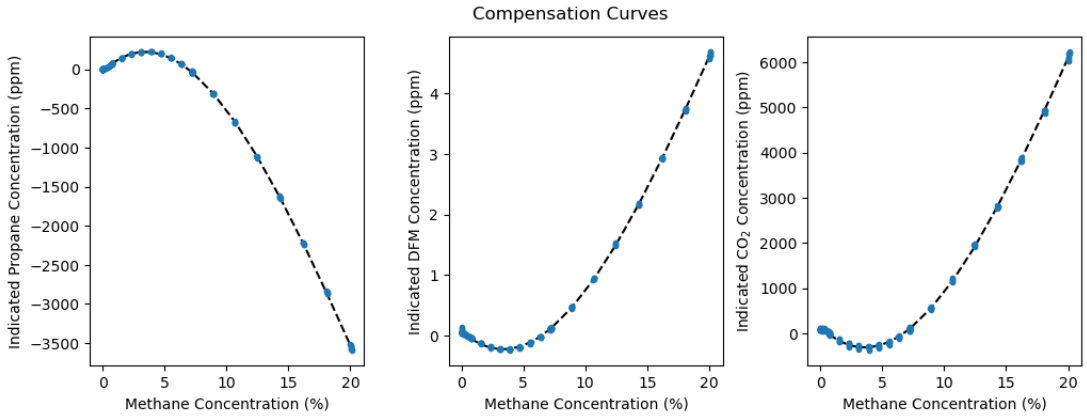

Figure 15: Compensation curves

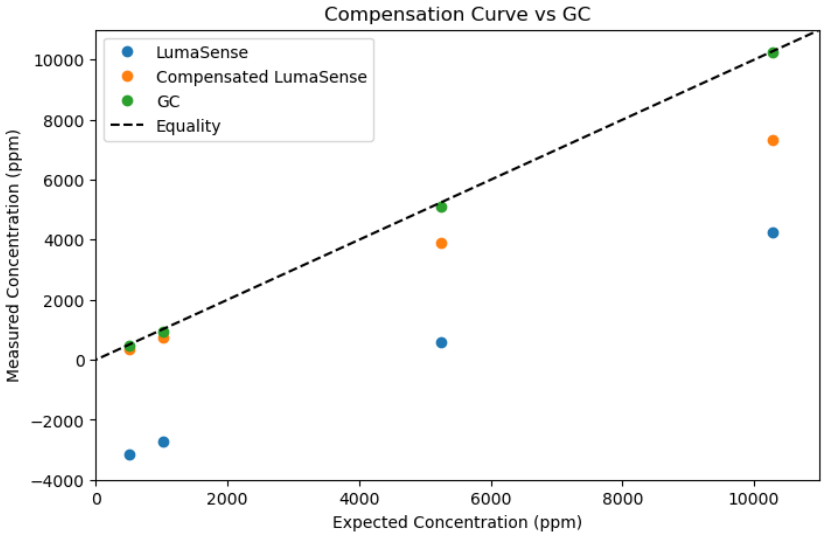

Figure 16: Compensated LumaSense compared to GC

2.8 Uncertainty Quantification

Due to the nonlinear nature of all the calculations, uncertainty was evaluated numerically. For values which were measured at steady state, such as pressure and flow rate during PFTs, the standard deviations of the steady-state values were used to construct error distributions. Calculations were then repeated using the high and low end of these distributions in order to estimate the maximum and minimum possible values for the calculated parameters.

For calculations based on LumaSense data, an error distribution was constructed using data from lab testing, which showed a constant standard deviation of around 11 ppm for the propane concentration, regardless of the concentration. The same deviation was assumed for the DFM concentration. Each value of the BTC was then modified using the error distribution and calculations were repeated a number of times to determine their sensitivity to error in the data.

Further details are provided in Appendix C. All uncertainty ranges provided in this work are 95% confidence intervals.

3 Results

3.1 Pressure Field Testing

3.1.1 Outliers

Before drawing conclusions from the PFT results, it was deemed necessary to eliminate well pairs with significant uncertainty. Well pairs were considered as outliers if the ratio between the nominal gas permeability and the bounds of the confidence interval was at least an order of magnitude. These tests were then removed from further analysis. Out of 274 tested well pairs, 190 displayed a pressure connection and 25 were designated as outliers. This corresponds to approximately 13%.

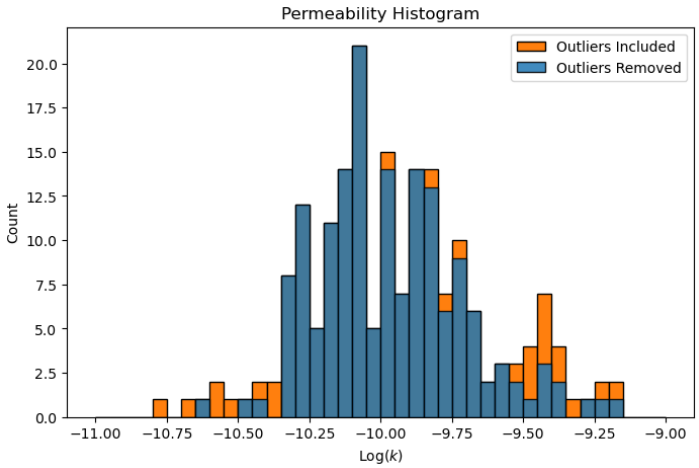

Figure 17: Gas permeability histogram with outliers

Figure 17 shows a histogram comparing the distribution of gas permeability before and after removing the outliers. Here it can be seen that the excluded well pairs primarily had higher than average gas permeability. These wells tended to have a lower-magnitude pressure response, such as the one shown in Figure 18, which caused the variation in the pressure measurement to become significant. It is worth noting that the variation in the pressure signal is very regular. This could indicate that it is caused by an actual fluctuation at the test location, such as the vibration caused by the blower or the fluctuation in landfill pressure caused by the extraction system. However, these are both much higher frequency than the wellhead pressure measurement, which only records one data point every ten seconds. Instead, the variation is likely electrical noise. The TruStability pressure sensors have a rated accuracy of 0.25% of full scale (Honeywell, 2024), which corresponds to about 0.2 mbar for the particular model used in this study. Many of the low-magnitude pressure responses are below this value. Other well pairs were eliminated due to extreme irregularity in the flow rate, which is indicative of issues with the extraction/injection well.

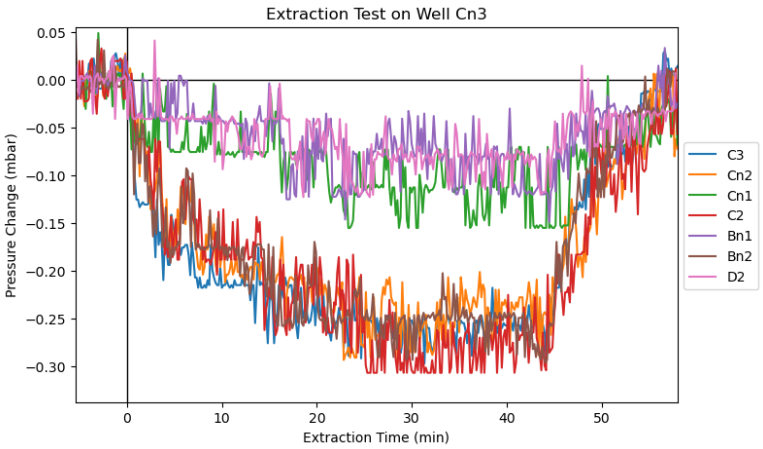

Figure 18: Low-magnitude pressure response during extraction test (2025-03-07)

It is possible that eliminating these well pairs has the result of biasing the results towards lower gas permeability wells, but given the very significant uncertainty around these points, it was considered prudent to remove them from consideration. If sensors with lower pressure ranges are used in future testing, the noise would likely be reduced and these well pairs would potentially no longer be outliers.

3.1.2 Anisotropy

Initially, it was assumed that the waste body was isotropic. Although it is known that landfills are generally much more permeable in the horizontal direction than the vertical direction due to the compaction of lower waste layers as successive layers are constructed on top of them (Fei et al., 2024; Hu et al., 2021; Jain et al., 2005; Ke et al., 2022; Singh et al., 2014), the anisotropy of the Braambergen landfill had never been quantified. However, when isotropy was assumed, the calculated values of gas permeability showed a strong negative correlation with distance. No physical phenomenon could be found to explain this trend, so it was assumed to indicate an issue with the implementation of the Baehr and Joss model. In fact, it was found that varying the anisotropy ratio had a significant effect on this trend, as shown in Figure 19. When a higher value of anisotropy was used in the calculations, the magnitude of the negative correlation decreased. If a high enough anisotropy ratio was used, the correlation became positive.

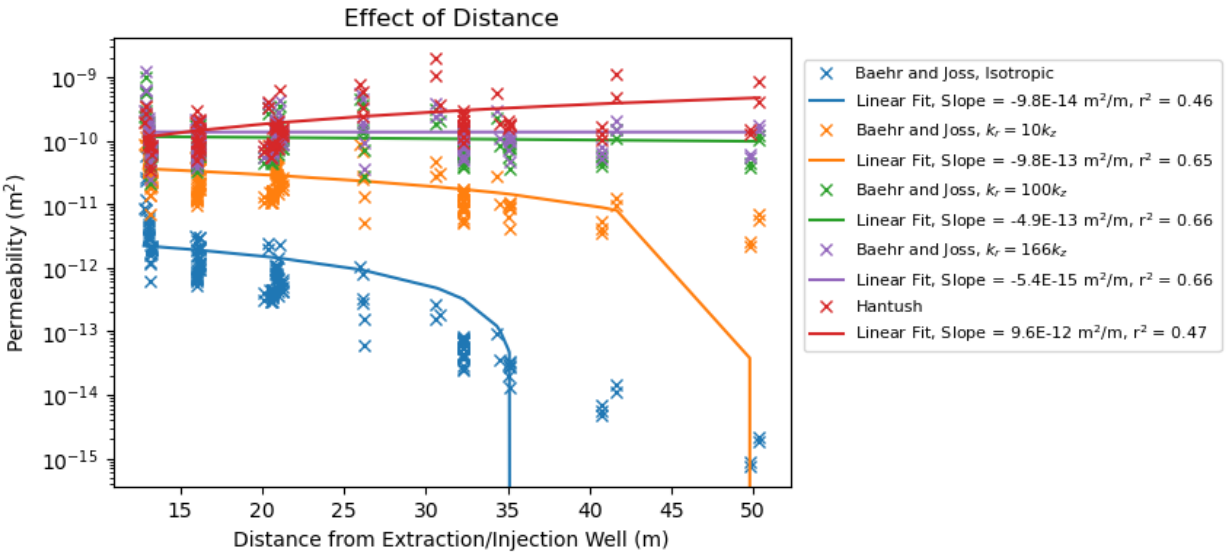

Figure 19: Anisotropy and effect of distance

The assumption was then made that there should be no trend in gas permeability with distance. This assumption may not hold for a single test, as there may be actual differences between well pairs which coincidentally correlate with distance. When the whole data set is considered, however, many different combinations of wells are included, such that any local differences should average out. The assumption is therefore considered to be well founded. Based on this idea, the slope was evaluated for various values of the anisotropy ratio, as shown in Figure 20. From this plot, it can be seen that the slope of gas permeability against distance goes to zero at an anisotropy ratio of 166 $\pm$ 5. As expected, the horizontal gas permeability is higher than the vertical gas permeability.

In a landfill context, there are no values of anisotropy in gas permeability in the literature to compare with, but anisotropy in hydraulic conductivity has been reported. Most studies report values between 5 and 10 (Fei et al., 2024; Hu et al., 2021; Ke et al., 2022), but values of up to 100 (Singh et al., 2014) and even 1000 (Beaven et al., 2024) have been reported previously. Hydraulic conductivity and gas permeability are related to similar physical parameters, but are not directly comparable. It should therefore not necessarily be expected that the anisotropy ratio would be the same. In their paper which analyses single-well PFT results, Jain et al. (2005) consider anisotropy ratios of 1, 10, and 100 when calculating gas permeability, but do not attempt to determine which value best represents their data.

It should be kept in mind that this fitting procedure gives a single value of anisotropy for this entire region of the waste body, which can be seen as a kind of rough spatial average. In reality, anisotropy is likely to vary

widely throughout the waste body as waste composition and structure is highly heterogeneous. In particular, anisotropy in hydraulic conductivity is known to vary with waste depth due to differences in compressive stress (Ke et al., 2022; Singh et al., 2014). In deeper waste, pores tend to be compressed due to the weight of overlying waste, causing them to be horizontally skewed. This results in the vertical conductivity being reduced more than the horizontal conductivity, increasing the anisotropy ratio as depth increases (Ke et al., 2022).

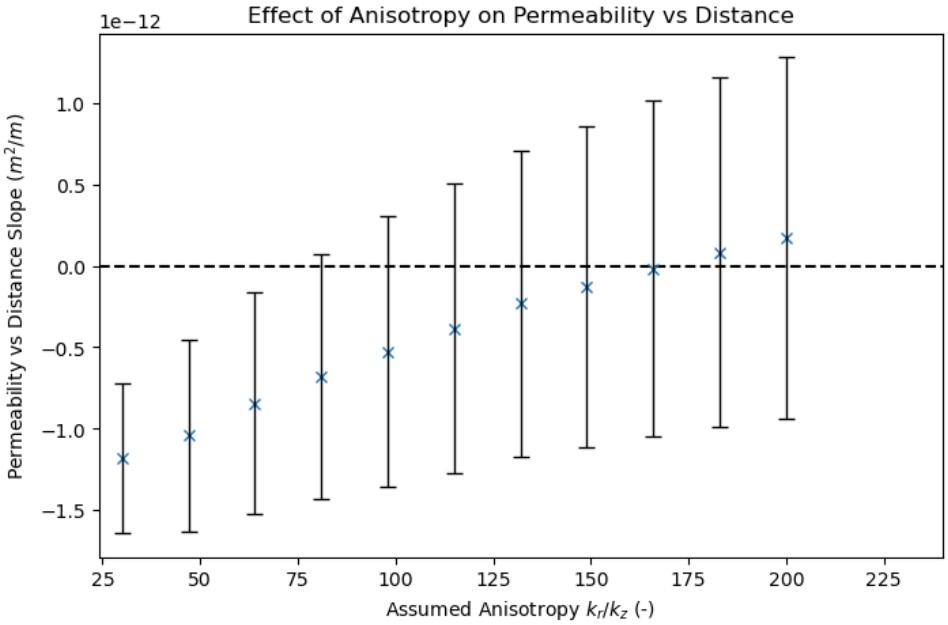

Figure 20: Distance trend vs anisotropy
(Error bars represent uncertainty in slope, carried forward from gas permeability)

For the rest of the PFT analysis in this report, the Baehr and Joss gas permeability was calculated using an anisotropy ratio of 166. Additionally, the term gas permeability is used to mean radial gas permeability. The Hantush method assumes the waste to be isotropic, so this consideration is not included. As shown in Figure 19, there is a small positive correlation between gas permeability and distance for the Hantush method which may be explained by this discrepancy.

3.1.3 Model Comparison

A comparison of the results from the two gas permeability models is shown in Figure 21. There is apparently a fairly good agreement between the two models, although the Baehr and Joss method tends to output a slightly lower gas permeability for high-permeability wells. A comparison of the uncertainty is shown in Figure 22, where well pairs are grouped into bins based on their Hantush gas permeability to improve readability. In general, the Hantush model results in a slightly wider confidence interval than the Baehr and Joss model, which is more pronounced at higher gas permeabilities. Additionally, the confidence interval tends to be slightly asymmetric due to some tests where very low pressure changes were observed. This results from the log-linear fit in the transient part of the pressure response. The quality of this fit may vary between well pairs, with higher quality fits leading to lower uncertainty.

The calculated values of gas permeability range between $2.5(10)^{-11}$ and $1.2(10)^{-9}$ m^2, with the majority of values around $1.0(10)^{-10}$ m^2. The values reported by Duarte Campos et al. (2023) are in a similar range, with an average of around $4.1(10)^{-11}$ m^2. While this is slightly lower than the values reported here, the measurements were taken in a different region of the landfill cell and during a different period of time and were calculated using the Hantush method. Most of the measurements performed in this work were taken during a particularly dry period, which may affect the saturation and gas permeability of the cover layer and thereby influence the calculations. The gas permeabilities measured by Wu et al. (2012) were in the range of $1.2(10)^{-13}$ to $1.9(10)^{-12}$ m^2. The values of gas permeability measured by Jain et al. (2005) were between $1.6(10)^{-13}$ and $3.2(10)^{-11}$ m^2 when the medium was assumed to be isotropic. When anisotropy was assumed, the gas permeability increased but stayed within the same order of magnitude. Additionally, gas permeabilities between $1.0(10)^{-10}$ and $1.0(10)^{-9}$ m^2 have been measured during lab testing (Kallel et al., 2004; Stoltz et al., 2010).

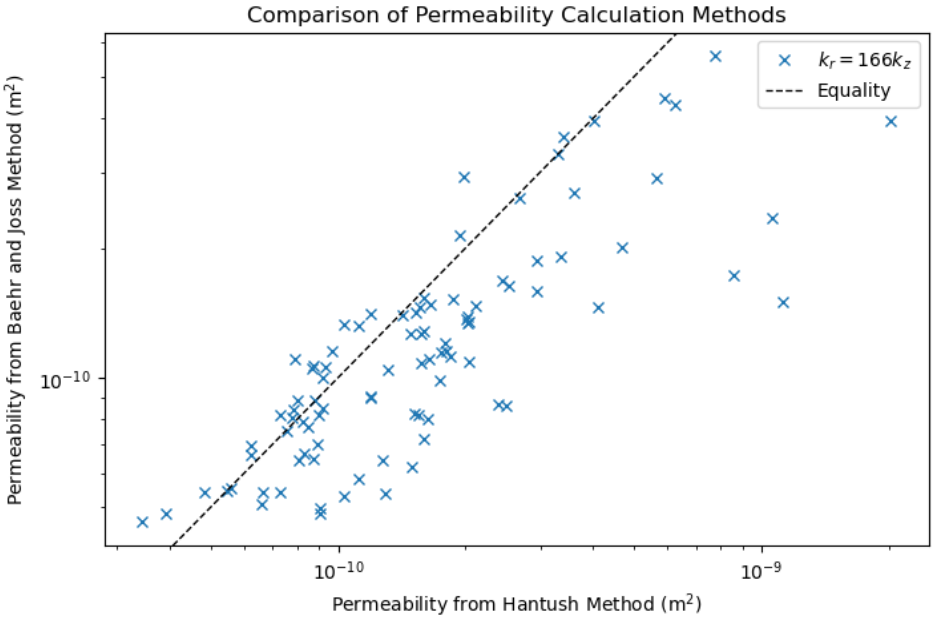

Figure 21: Comparison of gas permeability models

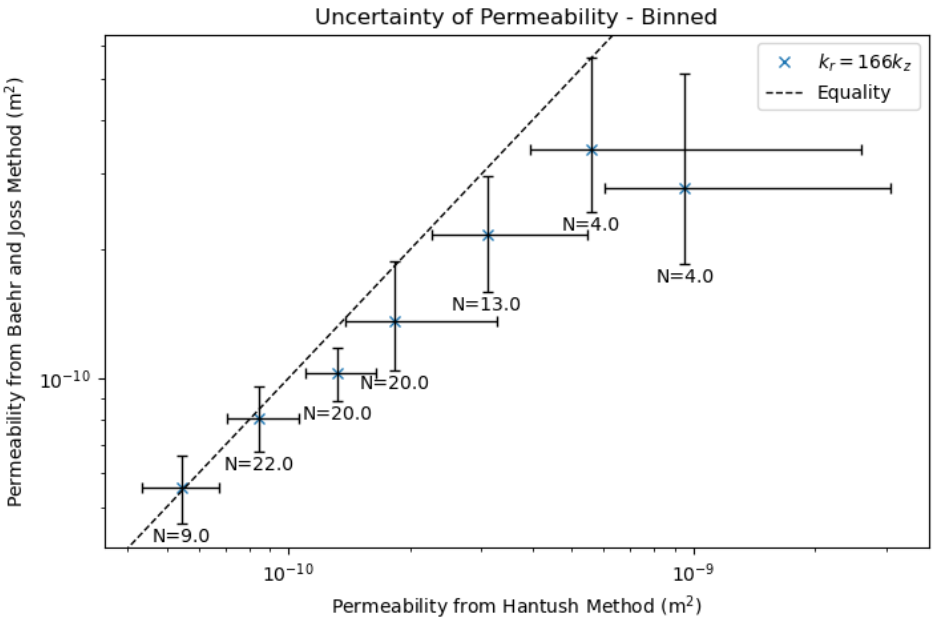

Figure 22: Comparison of gas permeability models uncertainty
(Crosses represent mean gas permeability of binned data points.
Error bars represent mean confidence intervals of binned data points.)

3.1.4 Injection-Extraction Comparison

For well-pairs which were tested in both extraction and injection, the resulting gas permeabilities are compared in Figure 23. For the Baehr gas permeability, the average ratio of extraction gas permeability to injection gas permeability was 1.03 $\pm$ 0.34, while for the Hantush method it was 1.20 $\pm$ 0.71. Thus, there was not a significant difference between the gas permeability as determined by either test method. However, it was noted that the flow rate was often much less stable during extraction tests. Curves like the one presented in in Figure 24 were much more common, whereas the flow rate during injection tests was generally quite stable throughout the test. This fluctuation led to higher uncertainty in the gas permeability from extraction tests than injection tests. Potential reasons for this will be discussed in Section 4.2.

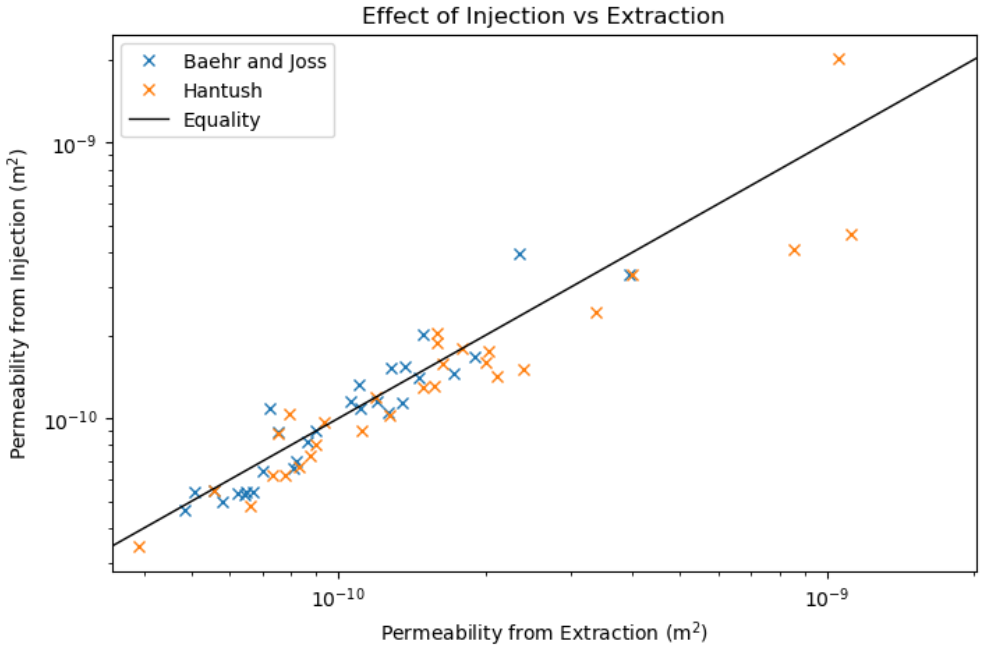

Figure 23: Comparison of injection and extraction

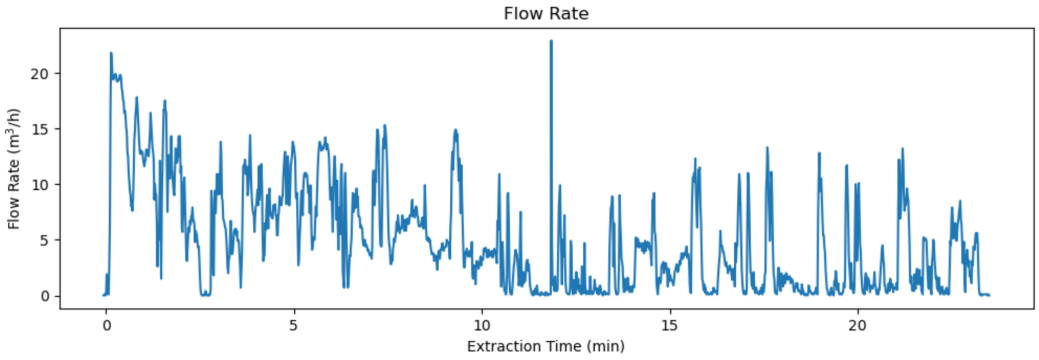

Figure 24: Flow instability during extraction test (2025-03-03)

3.1.5 Repeatability and Spatial Trends

Figure 25 shows the mean gas permeability for well pairs which were tested multiple times in the same flow regime (extraction/injection) and at a similar flow rate (within 20%). The variability is relatively low, with an average factor of around 1.2 between the maximum and gas minimum permeability for each well pair, although some well pairs exhibit higher variability. Some wells in particular seem to be problematic, particularly D2 and Cn2. This could potentially be attributed to differences between the model and the actual system, such as an annulus leakage or a break in the well. In general, the low variability between duplicate tests, even with a long time period in between, indicates that the test method is relatively repeatable.

Figure 26a shows the mean gas permeability for each extraction/injection well as calculated from different monitoring wells, while Figure 26b shows the mean gas permeability of each monitoring well as calculated from different extraction/injection wells. Significant variability can be seen in the extraction/injection wells, with a factor of more than 10 between the maximum and minimum gas permeability at each well. For the monitoring wells, the difference between the maximum and minimum gas permeability is a factor of 3-5 for most wells. Since the duplicate tests showed that repeatability is relatively good for duplicate tests, this variability can be attributed to differences in the flow paths between each well and its various neighbours. It is widely accepted that landfills are highly heterogeneous, so it should be expected that there would be large variability at each well when multiple directions of flow are considered.

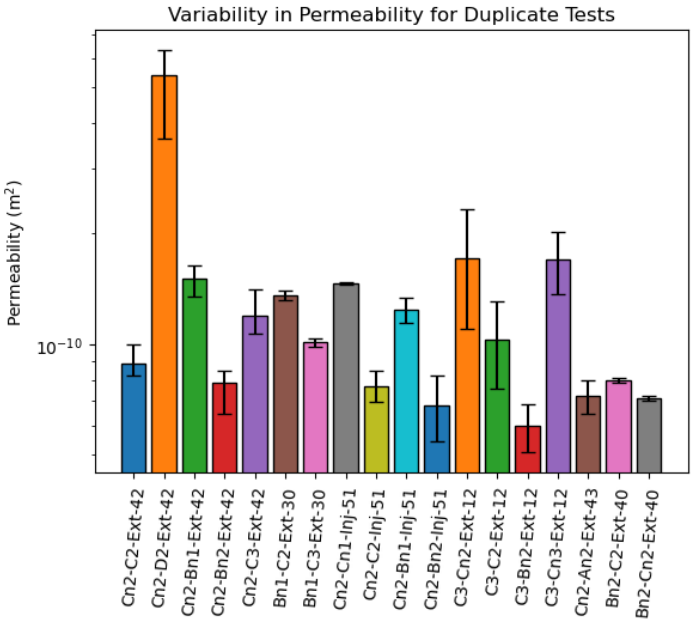

Figure 25: Gas permeability variation for duplicate tests
(Columns represent mean gas permeability for duplicate tests. Error bars represent standard deviation of these gas permeabilities. Number of tests varies per well.)

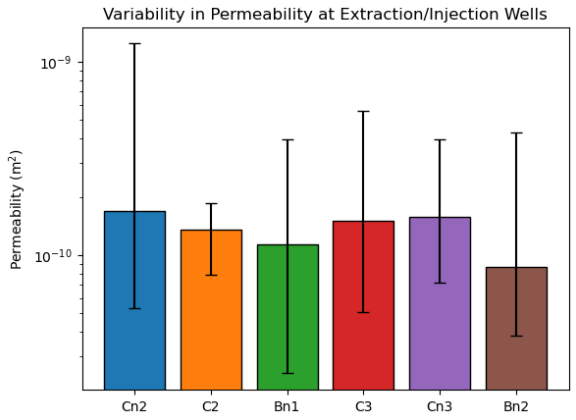

(a) Extraction/injection wells
(Columns represent mean gas permeability as measured from different monitoring wells)

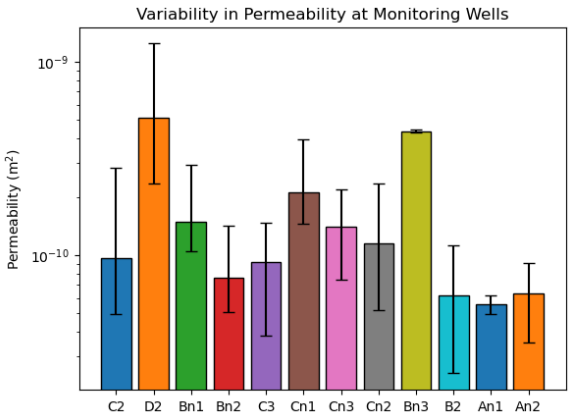

(b) Monitoring wells
(Columns represent mean gas permeability as measured from different extraction/injection wells)

Figure 26: Mean gas permeability by well type
(Error bars represent standard deviation of these gas permeabilities. Number of tests varies per well.)

It should also be noted that PFTs were performed over a period of several months. During this period, there were varying weather conditions and precipitation levels, which could affect the moisture content of the landfill and thereby the gas permeability. Although the leachate levels stayed very consistent throughout the study period, the cover soil and the unsaturated region of the waste body may have had varying levels of moisture. Additionally, tests were performed during periods when the landfill aeration system was active and during times when it was disabled for maintenance. Therefore, some of the variability in Figures 26 and 25 may have been related to actual variability in the gas permeability due to changing site conditions, rather than details of the test method itself.

For each PFT, a map was generated using the Baehr and Joss gas permeability. The gas permeability map for every test is provided in Appendix D. These were then combined into a map of the mean gas permeability by well across the site, which is displayed in Figure 27a. The relative standard deviation of this data (i.e. standard deviation divided by mean) is provided in Figure 27b. The data shows a slight trend towards higher

gas permeability in the southeastern part of the test area. The same trend is seen in extraction tests and injection tests. While previous testing on leachate levels and composition at Braambergen showed almost no relationship between neighbouring wells (Gebert et al., 2022), research on gas composition showed a stronger spatial relationship (Meza et al., 2022). Still, the spatial trend in gas permeability appears to be stronger than that of gas composition.

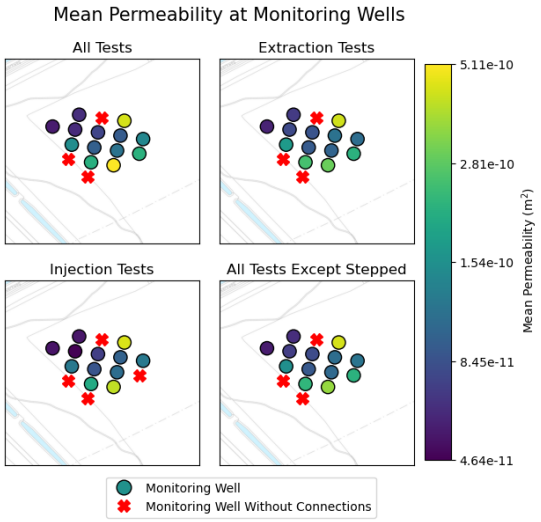

(a) Mean gas permeability as measured from different extraction/injection wells between 2025-03-03 and 2025-06-11. Number of tests varies per well.

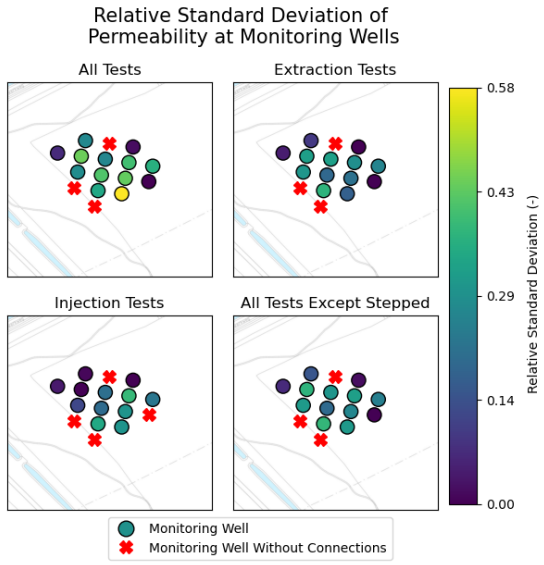

(b) Relative standard deviation in gas permeability as measured from different extraction/injection wells between 2025-03-03 and 2025-06-11. Number of tests varies per well.

Figure 27: Gas permeability map

3.1.6 Stepped Tests

Three successful stepped tests were performed. The results of the successful tests are shown in Figures 28 through 30. It can be seen that there is in general a slight positive correlation between flow rate and gas permeability. On average, the gas permeability measured at full pump power was 6.2% higher than that measured at 25% pump power, though it should be noted that the corresponding flow rates were different per well. When a linear fit was applied to each plot, the average slope was $2.93(10)^{-12}$ $\frac{m^2}{m^3/h}$. For many wells, the confidence intervals for the highest and lowest gas permeabilities overlap, indicating that the slope may be an artifact of uncertainty in the measurements. However, this is not the case for all wells, as shown in Figure 31 in which some wells have been removed to improve readability with the error bars.

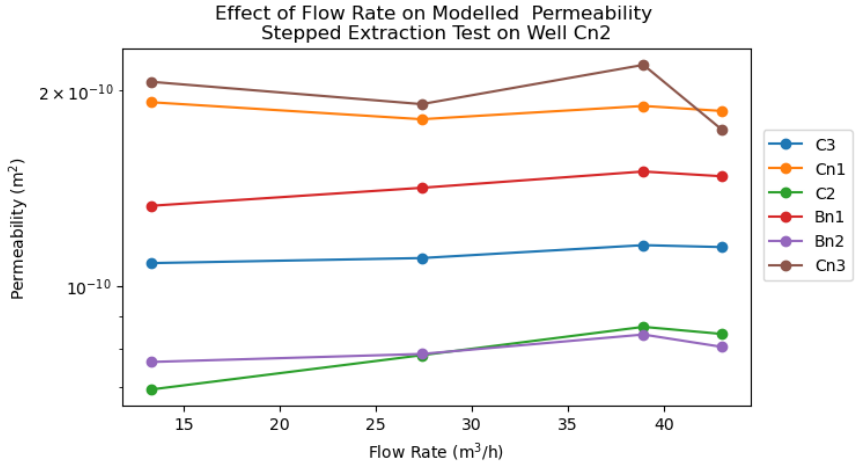

Figure 28: Stepped test on Cn2 (2025-03-07)

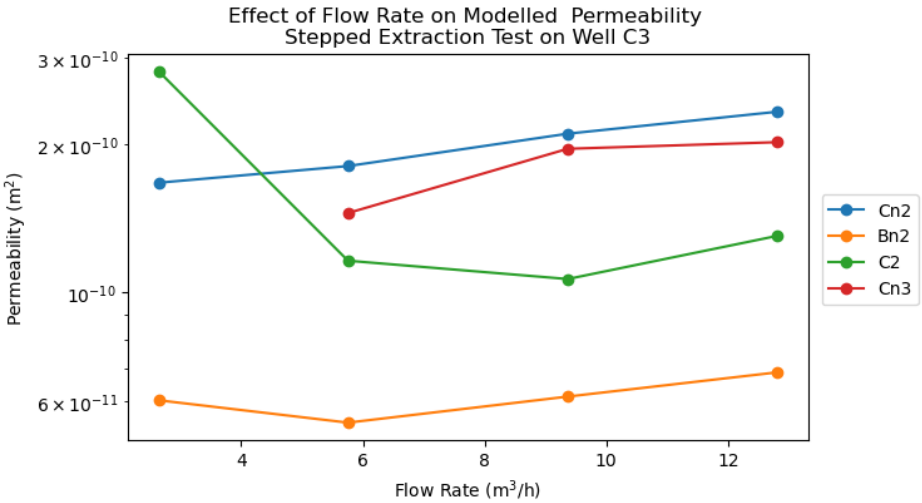

Figure 29: Stepped test on C3 (2025-06-11)

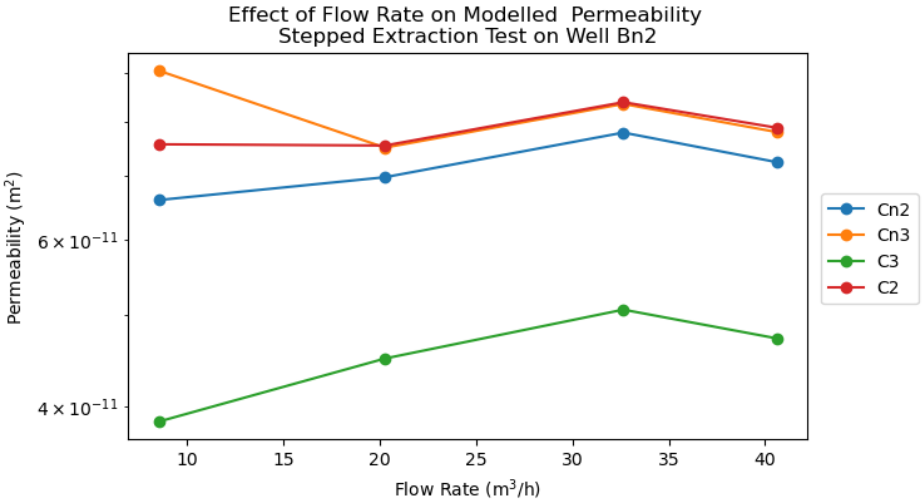

Figure 30: Stepped test on Bn2 (2025-06-11)

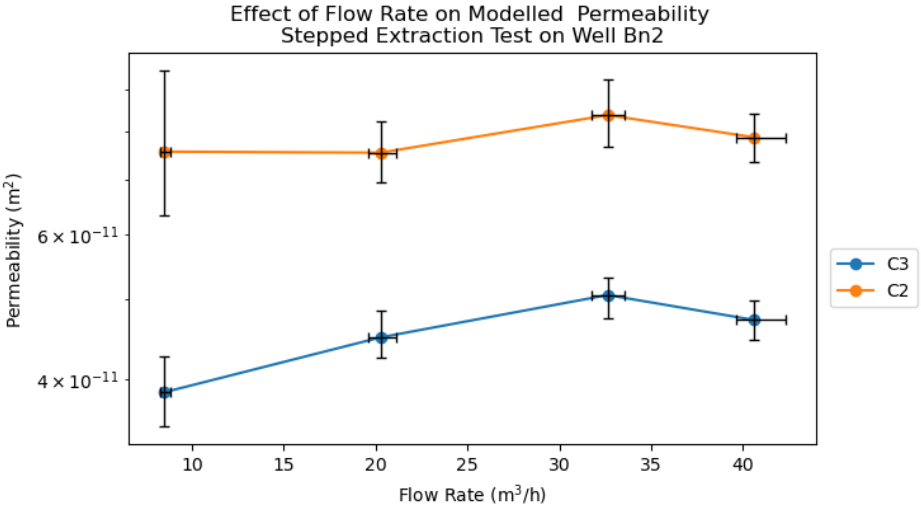

Figure 31: Stepped test on Bn2 (2025-06-11) - Uncertainty

During the stepped PFT which included the CTD-Diver, a high degree of flow instability was observed, especially at the low flow rates. This caused many of the data points to be excluded as outliers, so the test was excluded from the above analysis. However, the data recorded by the CTD-Diver, which are presented in Figure 32, are still useful. As can be seen in the figure, decreasing flow rate is often accompanied by fluctuating leachate levels. However, this is not universal. There are some periods with decreasing flow or even zero flow in which the leachate level remains steady at its background level.

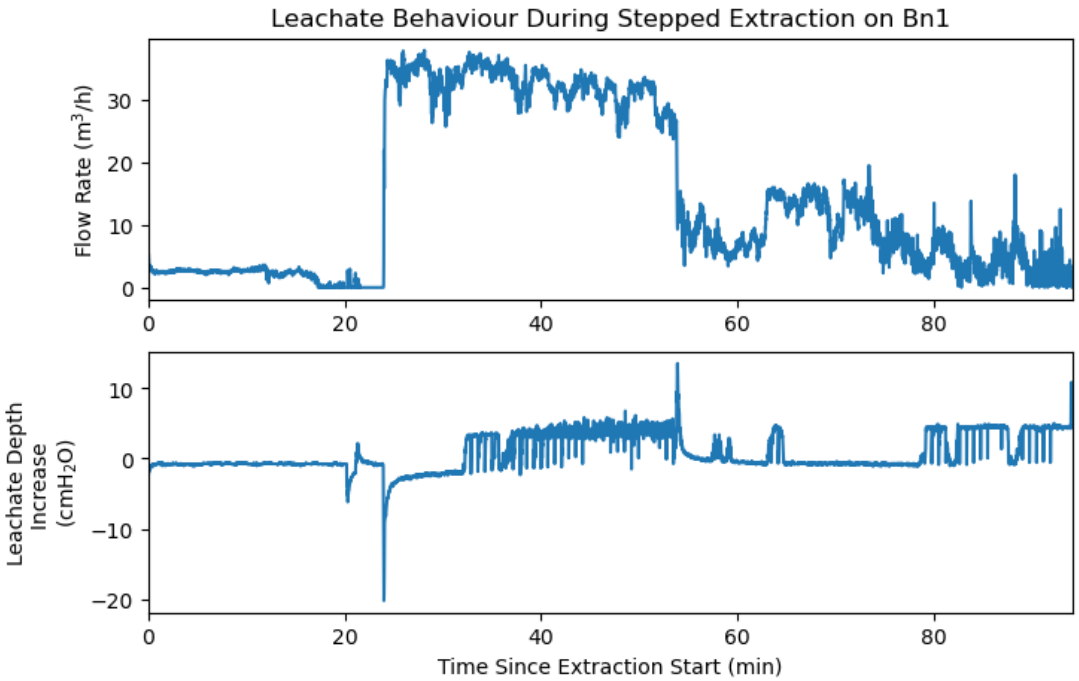

Figure 32: Change in leachate depth from steady state during stepped test on Bn1 (2025-04-25)

3.1.7 Correlations

The average gas permeability for each monitoring well and each extraction/injection well is plotted against the temperature, gas composition, and flow characteristics in Figure 33. Additionally, it is plotted against nitrogen content, NAA, and conductance, which are calculated from the data recorded in the gas round. The figure also shows the maximum flow rate achievable with the blower in either injection or extraction configuration. The mean gas permeability does not seem to correlate with any of these parameters. This was highly unexpected, as it was thought that the aeration pressure and speed at a given well would be mostly determined by the waste surrounding the well. Similarly, it was thought that high PAA and low oxygen content would be related to high water content and large anaerobic areas which would impede flow. It was expected that high gas permeability would be correlated with high temperature, given that aerobic respiration proceeds more rapidly than anaerobic. On the other hand, however, areas with high gas permeability may already be fully stabilized, allowing the temperature to return to background.

Figure 34 shows the gas permeability of each test plotted against the depth of the extraction/injection well, the depth of the monitoring well, and the depth difference between the two. In this case, there may be some negative correlation between monitoring well depth and gas permeability. This is to be expected, as previous studies have shown that gas permeability in landfills decreases with depth due to compaction of the waste (Jain et al., 2005; Singh et al., 2014; Wu et al., 2012). Additionally, there may be some positive correlation between the depth difference and the gas permeability. Here, a positive depth difference means that the extraction well is deeper than the monitoring well.

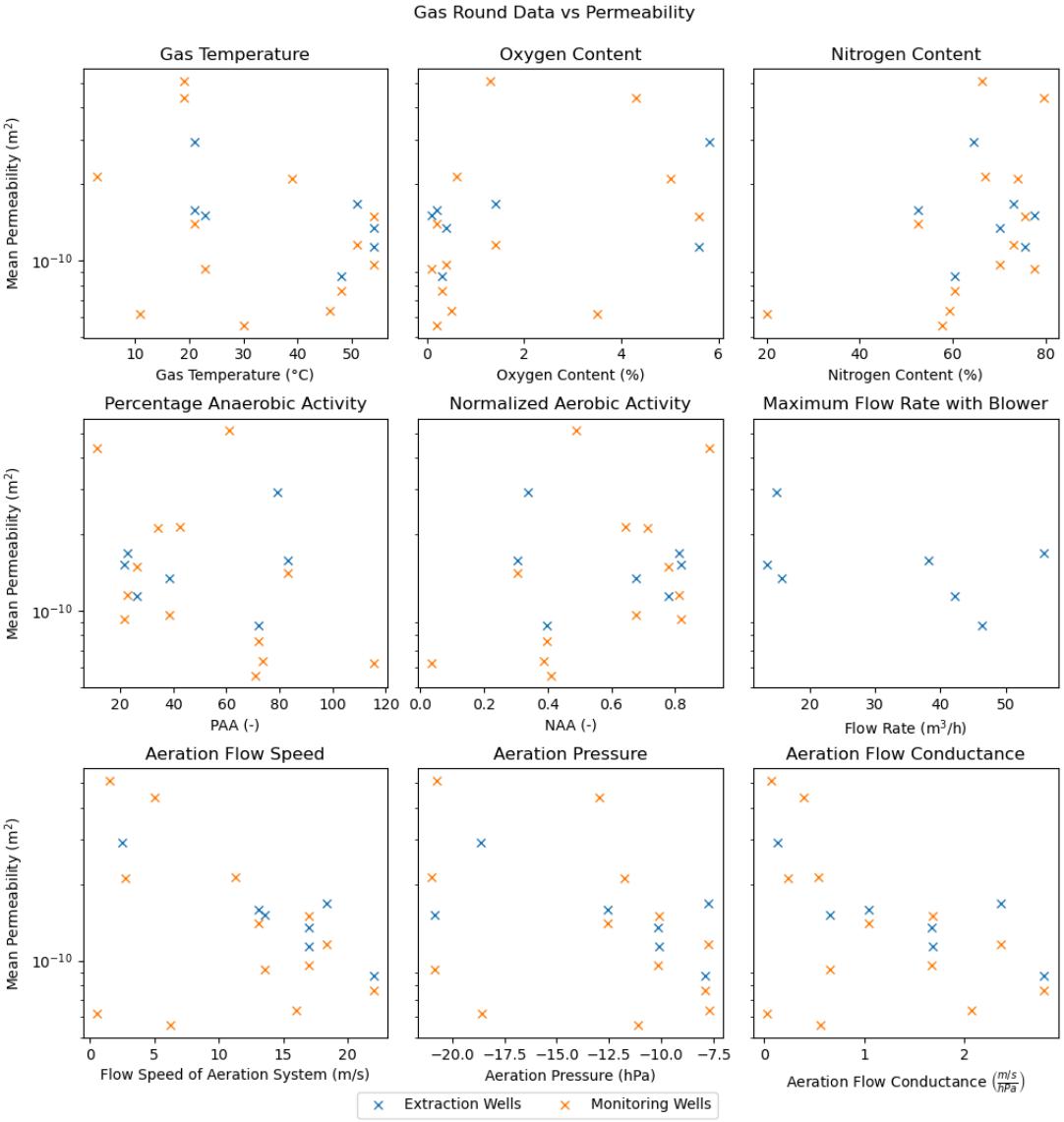

Figure 33: Correlation of gas permeability with gas round measurements from 2025-02-14

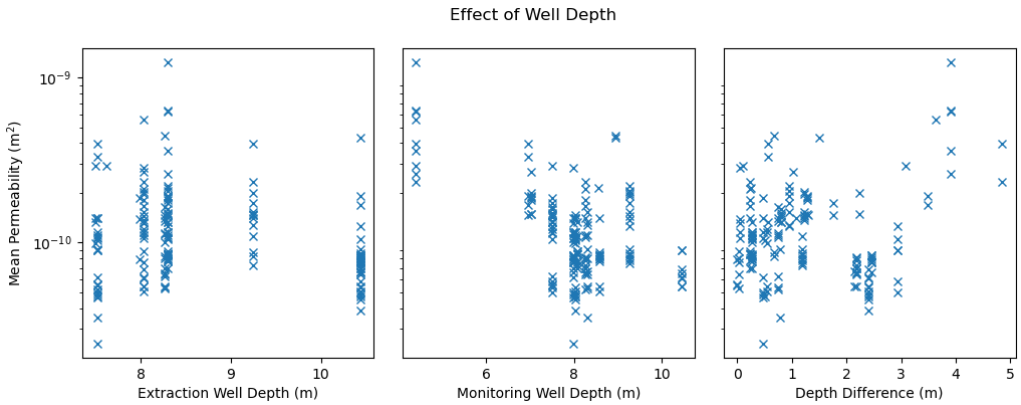

Figure 34: Correlation with well depth

3.2 Partitioning Gas Tracer Testing

3.2.1 Data Post-Processing

During analysis of the PGTT results, it was quickly noticed that the LumaSense data exhibited a strong diurnal fluctuation as shown in Figure 35. The same fluctuations were not seen in the GC or GeoTech data, so it was assumed that the effect was not caused by gas transport phenomena in the waste body. Instead, temperature changes in the tent where the LumaSense was housed were identified as a likely cause. Additionally, the effect was seen to be more significant during PGTT-2, when the weather was warmer, and was seen in all four measured gasses. Therefore, these portions of the LumaSense curves were not included in further calculations, except when supported by GC measurements. It can be seen in the figure that the effect is present throughout the test for CO_2 and, to a lesser extent, CH_4. It presumably also affects the measurements of propane and DFM throughout the test, but seems to become significant only when their concentrations decrease. Additionally, it was found that there was often an offset such that the background concentration was not equal to zero. Given the absence of propane and DFM from the waste body prior to injection, which was confirmed by GC measurements, the curves were scaled such that the background concentration was zero. This was performed after the compensation curve was applied. Finally, it was found that the uncertainty of the GC measurement of propane was around 5 ppm. Thus, measurements of below 25 ppm were excluded from consideration. The same cutoff was applied to all curves, which means that the BTCs end at different points for different wells, despite the same number of samples being taken.

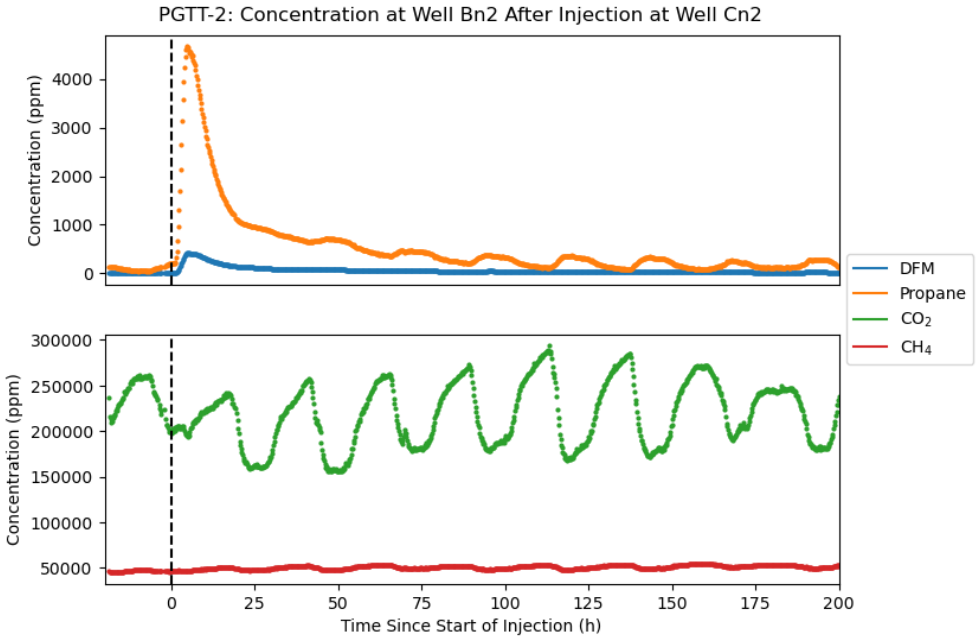

Figure 35: Temperature-induced fluctuations (PGTT-2)

3.2.2 Breakthrough Curves

Two tracer tests were performed, with eight wells being monitored in each case. In the first test, tracers were injected into well C3 and breakthrough was recorded at wells Bn2 and Cn3. No tracer was recorded at the other monitored wells, nor at neighbouring wells which had samples taken for GC analysis. Unfortunately, the methane concentration at Cn3 was very high, which interfered with the LumaSense measurement of the propane concentration. DFM seems to have been measured successfully. For this well, the calculations were performed using the LumaSense measurements for DFM and the GC measurements for propane. The post-processed BTCs are shown in Figures 36 and 37. The concentrations are normalized to the concentrations of propane and DFM in the injection mixture.

During the second test, tracers were injected into well Cn2. Clear BTCs were recorded at wells Bn2, C2, and C3. Additionally, propane was measured at well Cn3, but the concentration was very low, and the BTC was masked by the temperature-induced fluctuations discussed previously. DFM was also measured, but the BTC was atypical compared to the other wells. For this well, calculations for propane were carried out using

the GC measurements. Calculations for DFM were not carried out due to the unclear and inconsistent BTC, which made most of the further analysis impossible. The post-processed BTCs are shown in Figures 38 through 41.

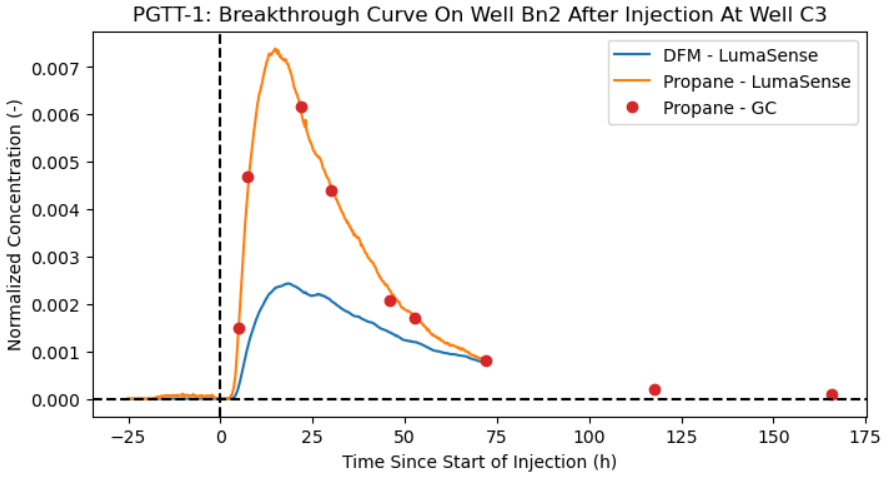

Figure 36: BTC at Bn2 (PGTT-1)

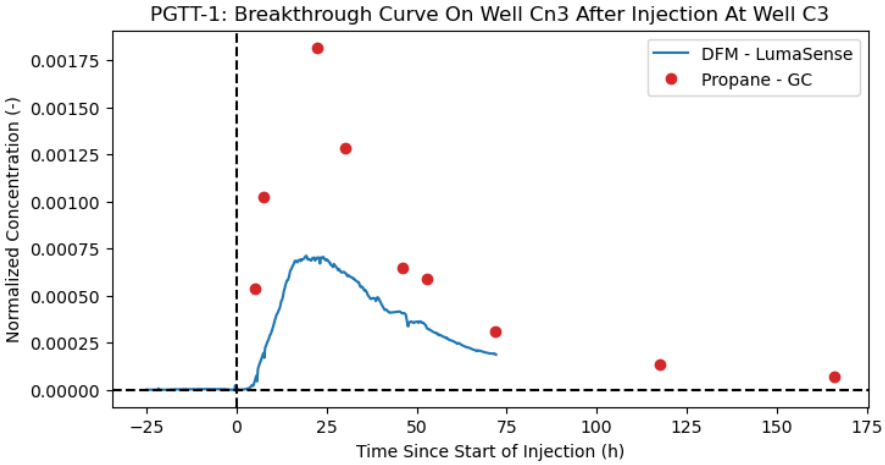

Figure 37: BTC at Cn3 (PGTT-1)

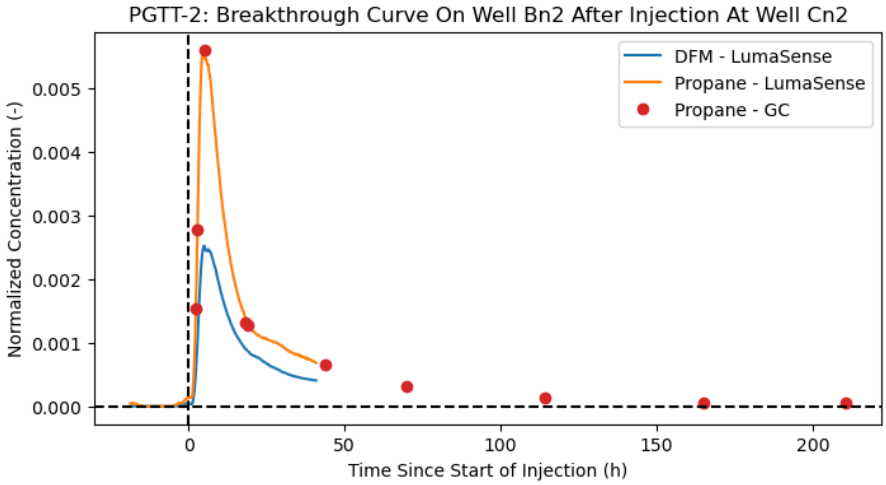

Figure 38: BTC at Bn2 (PGTT-2)

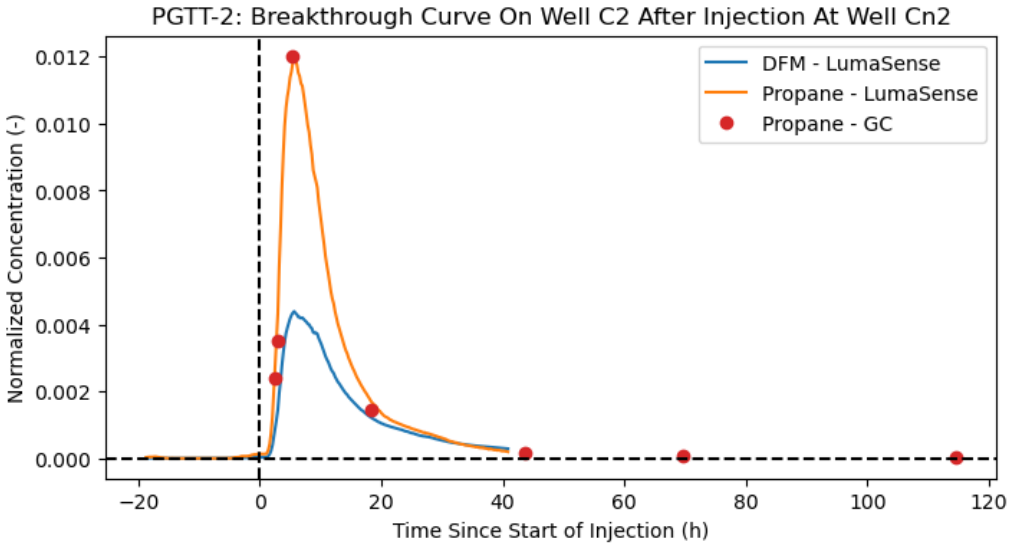

Figure 39: BTC at C2 (PGTT-2)

The peak time and breakthrough time for each well are shown in Table 6, along with the peak normalized concentrations. It should be noted that, for well Cn3 in PGTT-1, the peak occurs later for propane than for DFM, contrary to expectations. However, the peak in this case is based only on the GC measurements. By comparison with well Bn2, it seems that the peak likely occurred earlier but no sample was taken, because it happened during the nighttime. In all other cases, the peak for DFM occurred later than or at the same time as the peak for propane. The same is true for the breakthrough time. Breakthrough and peak concentration were reached very quickly for Bn2 and C2 during PGTT-2, while the other successful wells had similar breakthrough and peak times. This is not correlated with the distance between wells. The well pairs with faster travel times do have smaller differences in their depths, but there is also one well pair with a small depth difference and a slow travel time.

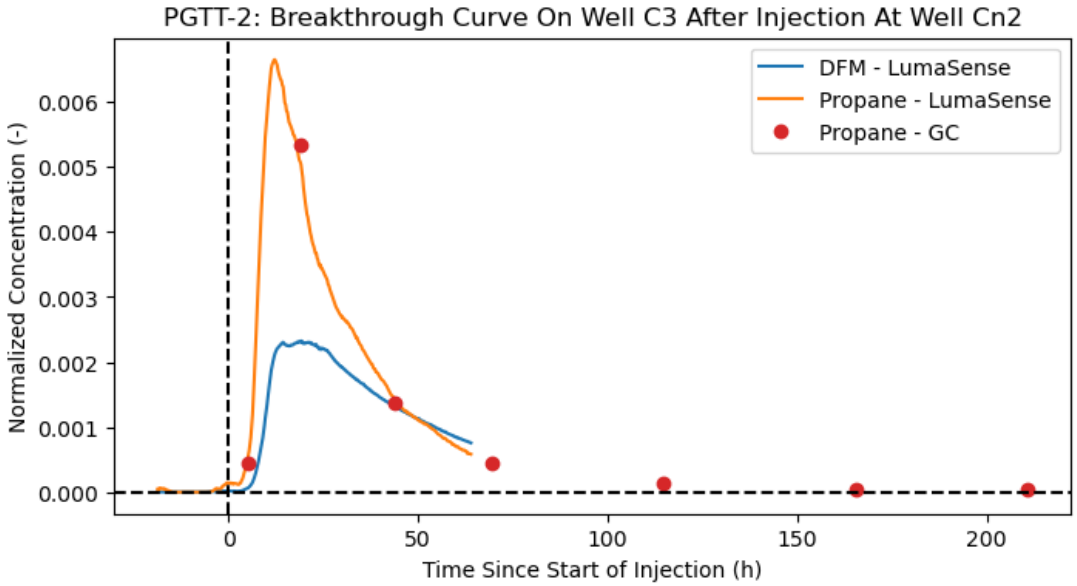

Figure 40: BTC at C3 (PGTT-2)

In all wells, the peak normalized concentration of DFM was always lower than that of propane, but the slope at the end of the curve was lower, indicating that gas would continue to arrive at the monitoring wells for a longer period of time if it could be reliably measured. This is a logical consequence of the partitioning nature of DFM. Additionally, the measurements of propane from the GC agreed with those from the LumaSense.

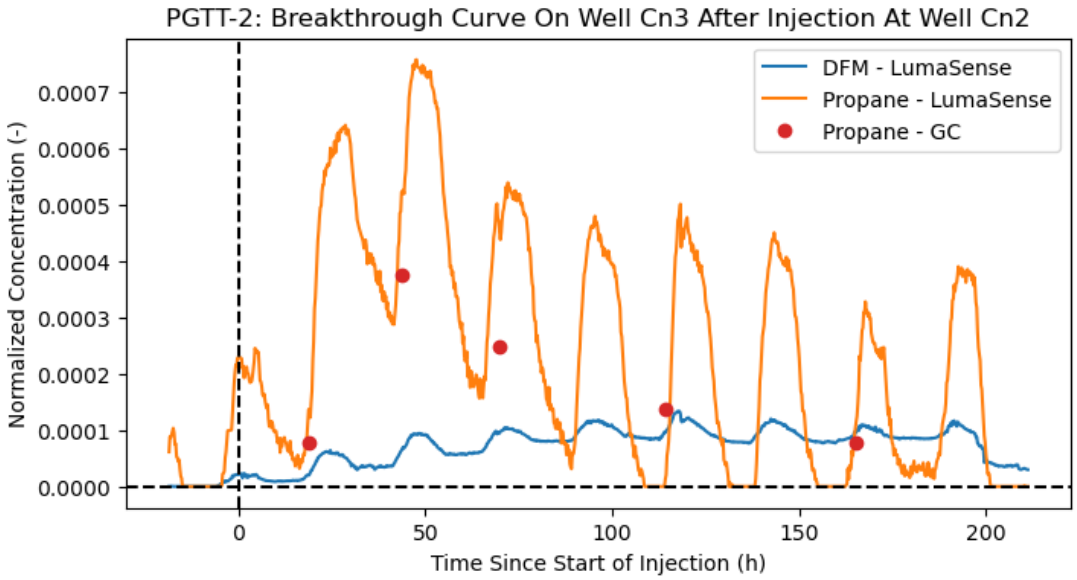

Figure 41: BTC at Cn3 (PGTT-2)

Table 6: Breakthrough curve parameters

Test	Well	Breakthrough Time (h)		Peak Time (h)		Peak Normalized Concentration (-)		Distance (m)	Depth Difference (cm)
		Propane	DFM	Propane	DFM	Propane	DFM		
PGTT-1	Bn2	4.0	4.3	14.8	18.6	$6.22(10)^{-3}$	$4.56(10)^{-3}$	16.1	-54
	Cn3[i]	3.8	4.5	22.2	19.4	$1.64(10)^{-3}$	$1.39(10)^{-3}$	16.2	-122
PGTT-2	Bn2	1.6	1.7	4.8	5.0	$5.84(10)^{-3}$	$2.53(10)^{-3}$	20.6	-27
	C2	1.8	1.9	5.7	5.7	$1.11(10)^{-2}$	$4.39(10)^{-3}$	16.2	24
	C3	5.0	6.2	12.2	19.2	$6.87(10)^{-3}$	$2.33(10)^{-3}$	13.1	27
	Cn3[ii]	6.6	N/A	43.6	N/A	$3.73(10)^{-4}$	N/A	20.8	-95

3.2.3 Retardation, Water Saturation, and Recovery

When the BTCs were extrapolated to zero concentration, it was found that the extrapolated curve did not match the GC data taken after the LumaSense was removed, as shown in Figure 42. This discrepancy is unlikely to be attributable to the measuring limit of the GC, as the uncertainty is known to be approximately 5 ppm, which corresponds to a normalized concentration of approximately $6(10)^{-6}$, whereas the data stops matching at a normalized concentration of around $1(10)^{-4}$. A similar trend was not seen by Han et al. (2006), where the decay curve remained linear as long as it was measured. However, the BTCs in that study were only measured until 12 hours after injection, when the normalized concentration was around 10^{-3}. It is possible that the log-linear nature of those BTCs would have also changed, given enough time. Alternatively, it is also possible that the character of the flow is somehow different, as indicated by the much slower tracer attenuation in this work.

To compensate for this, it would have been preferable to adjust the extrapolation based on the GC data. However, this would have been possible only for the propane BTC, since DFM concentration was not measured with GC. Since the subsequent calculations are based on comparison of the two BTCs, they cannot be treated differently. Also, the curves were very different between well pairs. Thus, a simple correction factor could not be applied universally. As such, the log-linear curves were used for the calculation of the retardation factor and saturation despite the discrepancy.

[i] Propane measurement was invalidated by high background methane concentration. Values taken from GC measurements.

[ii] Propane and DFM were measured but the LumaSense concentration was very low and masked by temperature fluctuations. Values for propane taken from GC measurements.

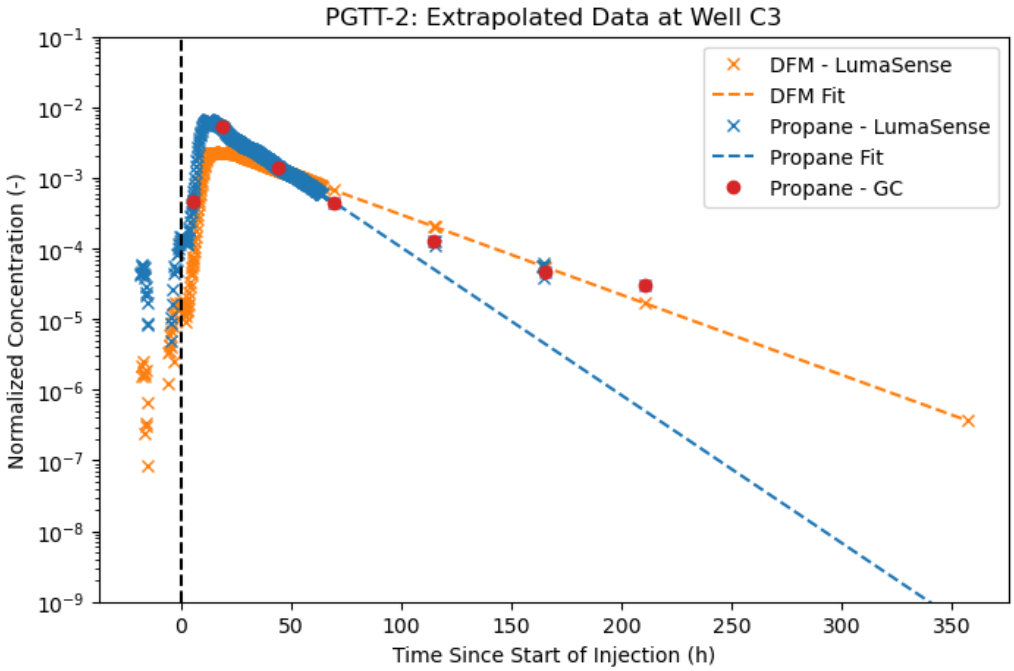

Figure 42: GC vs LumaSense in Extrapolated BTC (PGTT-2)

The retardation factor and water saturation are shown for each well pair with a complete BTC in Table 7. The results before extrapolation are also reported, but the results including extrapolation should be considered more accurate. In PGTT-2, well Cn3 is not included due to the lack of a clear BTC for DFM. In PGTT-1, the extrapolation of the propane BTC at Cn3 introduced a high degree of uncertainty due to the lack of LumaSense data and the sparse GC data. In this case, the values calculated without extrapolation are potentially more useful due to the very high uncertainty. However, the values of R_f and S_w are almost certain to be underestimated due to the fact that the slower decay of the DFM curve is not captured without extrapolation, leading to a shorter mean arrival time. Indeed, R_f and S_w are lower before extrapolation for all other well pairs. The same trend was seen by Han et al. (2006), who also reported lower saturation overall, with an average of around 0.25 for the tests which did not have recovery rate issues. However, the landfill studied in that paper included an impermeable cover layer, which prevents water from entering and can result in a relatively dry waste body (Brand et al., 2016; Kattenberg et al., 2013; Woodman et al., 2017). It should also be kept in mind that the calculation of saturation is dependent on the Henry constant, which depends significantly on temperature (Han et al., 2007; Kutsuna, 2017). The temperature was assumed to be constant spatially and temporally at 35°C, despite the large variability. For comparison, the temperature at each well from the last gas round is shown in Table 8, along with other parameters from the gas round.

Table 7: Retardation factor and saturation

Test	Well	With Extrapolation		Without Extrapolation	
		Retardation Factor	Saturation	Retardation Factor	Saturation
PGTT-1	Bn2	1.53 ± 0.02	0.41 ± 0.01	1.24 ± 0.01	0.24 ± 0.01
	Cn3^i	1.1 ± 0.4	0.2 ± 0.4	1.41 ± 0.01	0.34 ± 0.01
PGTT-2	Bn2	1.89 ± 0.03	0.53 ± 0.02	1.09 ± 0.01	0.11 ± 0.01
	C2	1.60 ± 0.08	0.43 ± 0.03	1.28 ± 0.01	0.26 ± 0.01
	C3	1.70 ± 0.07	0.47 ± 0.02	1.28 ± 0.01	0.26 ± 0.01

Research on Braambergen using Electrical Resistance Tomography (ERT) has shown that the landfill has an average water content of approximately 5 m^3/m^2 throughout its entire thickness (Wang & Heimovaara, 2025b). Given that the thickness is approximately 12 meters when the cover layer and saturated zone are included, this corresponds to a bulk volumetric water content of around 0.42. However, this is the fraction of the total volume made up of water, while the saturation value obtained from the BTC is the fraction of pore volume occupied by water. To compare the two, an assumption must be made for the waste porosity. If the porosity is assumed to be 0.5 as in the dual domain model and the (on average) 3.4 m thick saturated zone is accounted for, the

average saturation of the remaining waste is 0.37. This is slightly lower than the values reported in this work, but it is an average of the whole thickness of the landfill. In contrast, the PGTTs primarily measure the deepest part of the unsaturated zone, where the screened part of the wells are located. It is likely that this part of the waste body has a higher saturation than the part nearer to the surface. Additionally, if a porosity of 0.4 is assumed, then the average saturation is 0.46 for the unsaturated zone of the landfill, which is more similar to the values in Table 7. As such, the measured values of S_w may or may not agree with the literature values, but it is difficult to say with certainty due to heterogeneity and lack of porosity data.

Table 8: Well characteristics

Well	Temperature (°C)	Aeration Flow Speed (m/s)	Aeration Pressure (hPa)	PAA (-)
Bn2	48	22.03	-7.88	0.721
C2	54	16.95	-10.16	0.386
C3	23	13.59	-20.93	0.215
Cn2	51	18.33	-7.77	0.227
Cn3	21	13.08	-12.58	0.831

The tracer recovery rate is detailed in Table 9. It should be noted that the injected mass is calculated based on the flow rate measured by the rotameters rather than directly measured with the scale. This is because the scale indicated that 3.45 kg of propane and 0.46 kg of DFM were injected in the first test, compared to expected masses of 3.21 kg and 0.54 kg respectively. In the second test, the scale indicated that 4.23 kg and 1.00 kg were injected respectively, despite the same flow rates being used. The difference was attributed to leaks in the injection system which were detected during subsequent GPPTs and the calculated mass was seen as more reliable.

Table 9: Tracer recovery

Test	Well	Distance (m)	Propane Recovered (g)	DFM Recovered (g)	Time for 50% Propane Recovery (h)	Time for 50% DFM Recovery (h)	Total Propane Recovered (g)	Total DFM Recovered (g)	Propane Injected (g)	DFM Injected (g)	Propane Recovery (%)	DFM Recovery (%)
PGTT-1	Bn2	16.1	11380 ± 40	1670 ± 10	26.7 ± 0.1	41.0 ± 0.3	12600 ± 200	1840 ± 20	3210	540	393 ± 6	341 ± 6
	Cn3^i	16.2	1200 ± 200	170 ± 20	10.3 ± 0.2	31.0 ± 0.3						
PGTT-2	Bn2	20.6	4760 ± 30	780 ± 10	17.6 ± 0.2	34.0 ± 0.3	13870 ± 70	2150 ± 30	3210	540	432 ± 2	398 ± 6
	C2	16.2	3700 ± 20	470 ± 10	8.3 ± 0.3	11.3 ± 0.1						
	C3	13.1	5410 ± 60	900 ± 20	22.3 ± 0.3	38 ± 1						

In both tests, the total tracer recovery was much higher than 100% for both gases. This is likely a result of the fact that the calculations were based on the flow rate from the most recent gas round and may have changed significantly leading up to the test or even during the test. The historical flow rates at well Bn2 are shown in Figure 43 as an example, where it can be seen that there is significant variation over time. It could also be the case that there was an issue with the flow speed measurement. If the flow rate is assumed to be constant during the test, the recovery of propane and DFM can still be compared, as they are calculated based on the same assumed flow. In this case, the recovery rate of propane was 15% higher in the first test and 8% higher in the second test than that of DFM. This may indicate that the flow characteristics of propane and DFM were not entirely comparable, with less DFM reaching the extraction well. It could also be caused by inconsistent flow rates in the extraction system, since the BTC of DFM is slightly offset from that of propane. These variations are not measured and thus cannot be accounted for in the calculations.

Additionally, the time for 50% propane and DFM recovery indicates that, in most cases, the majority of tracer recovery occurs during the portion of the test when the LumaSense was still running, as can by seen by comparison with Figures 38 through 41. This is the period in which the calculation is the most reliable. For some wells, such as C3 in PGTT-2, a large portion of DFM is recovered after the LumaSense data became unreliable, meaning that is based on the extrapolated curve which has some discrepancies with the GC measurements. This could be potentially also contribute to the recovery being higher than 100%.

It is also worth noting that the amount of tracer recovered at each well does not seem to be correlated with its distance from the injection well, nor with its saturation. There is, however, a proportionality between the amount of propane recovered and the amount of DFM recovered.

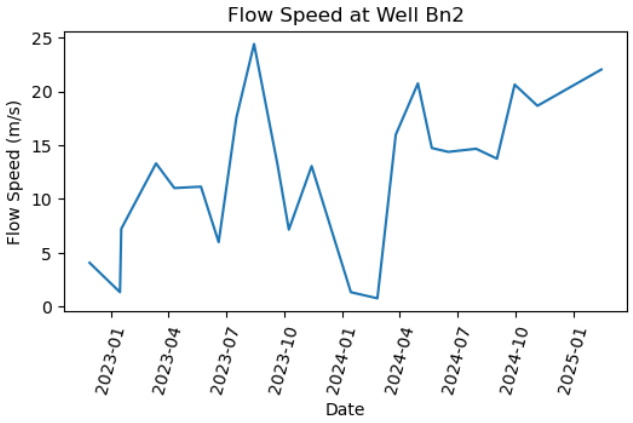

Figure 43: Flow speed variability at Bn2 (2022-11-28 to 2025-02-14)

3.2.4 Dual Domain Model

Before applying the dual domain model to the PGTT data, it was validated by application to the data collected by Yazdani et al. (2010). The resulting parameters are listed in Table 10 alongside those fitted in the referenced work. The r^2 value is also listed for comparison, as well as the squared error which was used for the fitting algorithm It should be noted that the original work did not report the dispersion coefficient or gas velocity obtained by the fitting procedure.

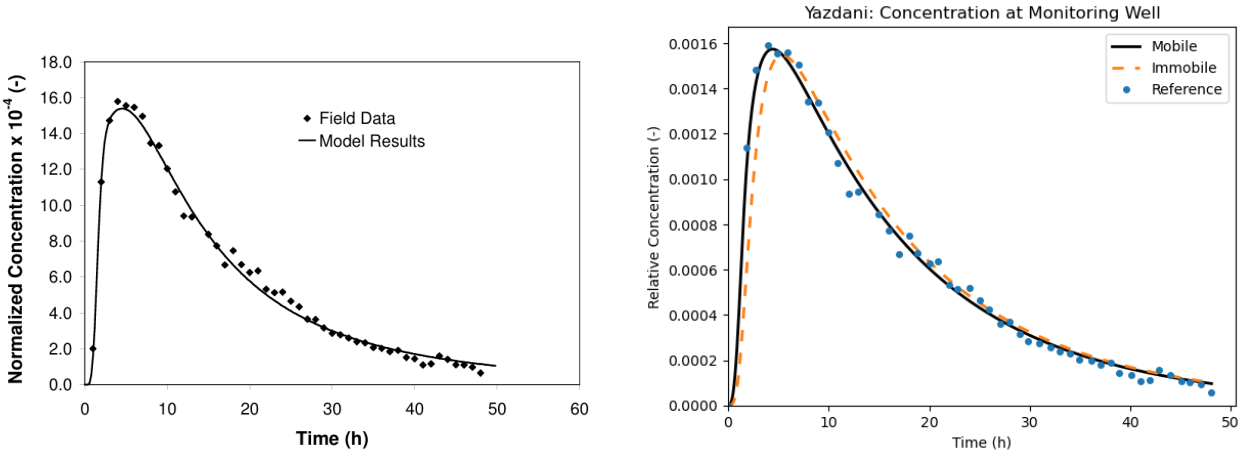

(a) Fit by Yazdani et al. (2010)

(b) Fit using modified model

Figure 44: Dual domain validation fit

There is a significant difference between the value of ϕ_g^{im} obtained in this work and in the reference. However, this is likely caused by a difference in the governing equation. In the referenced work, the term ϕ_g^m is divided by R_f in the terms of Equations 29 and 30 which relate to the immobile zones, but not the first term of Equation 29. This is discussed in more detail in Appendix A. A difference in the resulting value of ϕ_g^{im} may be expected due to these differences in the governing equations, but the exact effect is difficult to predict. Since the change does not apply to every term involving ϕ_g^m, the change also cannot be corrected without modifying and re-running the numerical model. Differences may also be caused by modelling differences between the two works. In this work, a numerical implementation of the governing equations was used, with the time and space steps selected to be small enough that the forward model was stable for any value of D and v_g. Even with careful selection of these values, it is well known that differences in meshing can cause different amounts of numerical dispersion, which ultimately affects the estimated parameters (Versteeg & Malalasekera, 2007). In contrast, Yazdani et al. (2010) used CXTFIT to perform the parameter estimation, which is based on analytical solutions to the governing equations using Laplace transforms (Tang et al., 2010; Toride et al., 1999). The same value of γ was estimated by both models. Both fits had an value of r^2 greater than 0.99, but the shapes of the fit are slightly different, as shown in Figure 44. The curves are very similar in the tail, but the fit developed in this work

captures the peak slightly better, while the fit developed by Yazdani et al. (2010) does a slightly better job of describing the initial concentration decline. Figure 44b also shows the concentration in the immobile pores, which slightly lags that in the mobile pores because of the first-order exchange term. Overall, the agreement between this model and the results of Yazdani et al. (2010) was considered good enough to continue with the PGTT data. Other data was available in the referenced work but was not fitted due to time constraints. The chosen BTC was the one which most closely resembled the BTCs in this work.

Table 10: Dual domain model validation

	ϕ_g^{im} (-)	v_g (m/h)	D (m^2/h)	γ (h^{-1})	F_{dil} (-)	r^2 (-)	Squared Error (-)
Yazdani et al. (2010)	0.32 ± 0.03	N/A	N/A	0.18 ± 0.03	N/A	0.99	N/A
This Work	0.24 ± 0.03	0.71 ± 0.02	2.3 ± 0.1	0.18 ± 0.04	32.9 ± 0.4	0.997	$1.19(10)^{-9}$

The results of the parameter estimation are summarized in Table 11. An example convergence plot is shown in 45, with the fitted BTC for each well pair shown in Figures 46 through 50. In all cases, there is a very good visual fit, as corroborated by a very low value of the error function. Additionally, r^2 was above 0.999 for all cases. It should be noted that several tests have a value of 10^6 for γ, which is marked with an asterisk in the table. In these cases, it was found that the fitting algorithm would continually increase γ regardless of the initial guess. To prevent this from interfering with the fitting of the other parameters, an artificial upper bound of 10^6 was set. Several different upper boundaries were tested and it was found that the choice did not significantly impact the values to which the other parameters converged. A very high value of γ means that the tracer moves very quickly between the mobile and immobile pores. It was considered that temperature may influence this, since the mass transfer rate is related to partitioning and the Henry's constant is dependent on temperature (Han et al., 2007; Kutsuna, 2017). However, while both wells which had unconstrained γ were high-temperature wells, there was one more high-temperature well (C2 in PGTT-2) which did not have an unconstrained value of γ. This can be seen by comparison with Table 8. It should also be kept in mind, however, that these temperatures are taken from the gas round and are only representative of the gas in the wells, not necessarily the whole part of the waste body which is traversed during the PGTT. From Equation 30, it can be seen that the rate constant is divided by the total gas porosity θ_g, which is derived from the total porosity θ and the saturation S_w. While S_w was calculated from the BTCs, θ was assumed constant at 0.5. If this assumption is not representative of certain well pairs, it could potentially contribute to the unconstrained nature of γ.

Table 11: Estimated dual domain parameters

Test	Injection Well	Monitoring Well	R_f (-)	T (°C)	Distance (m)	ϕ_g^{im} (-)	v_g (m/h)	D (m^2/h)	γ (h^{-1})	F_{dil} (-)	Squared Error (-)	Pe (-)
PGTT-1	C3	Bn2	1.53	48	16.1	0.72 ± 0.01	1.93 ± 0.02	18.1 ± 0.1	$10^{6,iii}$	14.7 ± 0.1	$8.15(10)^{-10}$	1.71 ± 0.02
	C3	Cn3	1.41[i]	21	16.2	0.74 ± 0.01	1.28 ± 0.01	7.6 ± 0.2	1.1 ± 0.5	56.8 ± 0.4	$1.97(10)^{-10}$	2.74 ± 0.08
PGTT-2	Cn2	Bn2	1.89	23	20.6	0.4 ± 0.1	2.29 ± 0.03	18 ± 1	0.0132 ± 0.0005	38.4 ± 0.7	$1.06(10)^{-9}$	2.6 ± 0.2
	Cn2	C2	1.60	54	16.2	0.29 ± 0.01	1.97 ± 0.01	9.5 ± 0.2	0.0010 ± 0.0004	30.8 ± 0.2	$4.42(10)^{-9}$	3.34 ± 0.06
	Cn2	C3	1.70	48	13.1	0.85 ± 0.01	1.96 ± 0.02	8.68 ± 0.04	$10^{6,iii}$	16.6 ± 0.2	$3.43(10)^{-9}$	2.9 ± 0.1

While it may seem contradictory to have a distinction between mobile and immobile zones in these cases, the value of ϕ_g^{im} does still make a difference to the fitted curve. The construction of the governing equations makes the assumption that retardation takes place only in the immobile regime. While the tracer can move freely between the two domains for these well pairs, only the fraction which resides in the immobile zone experiences partitioning and thereby retardation. Other well pairs had values of γ which were lower than the values reported by Yazdani et al. (2010), which were between 0.13 and 0.92 h^{-1}. The mass transfer rate is not fundamental to the gas, but is dependent on factors like temperature, surface area, and pressure. Thus, the values should not necessarily match between the two studies or even between wells. However, the significantly lower values in some tests, along with the extremely high values in other tests, may indicate that the model as formulated is not the ideal fit for this situation. The values of ϕ_g^{im} from Yazdani et al. (2010) are between 0.32 and 0.92, which is almost the whole possible range of values. The values found in this work span a similar range. No other literature could be found with which to compare the results.

The Peclet number Pe is also provided in Table 11. This parameter is calculated using Equation 39 (Yazdani et al., 2010) and is essentially a ratio of the contribution of the dispersive transport to the convective transport. In all cases, the convective transport and the dispersive transport are similar in significance. Since

[iii] γ increased indefinitely. Artificial upper bound was set to allow other parameters to converge.

bulk gas transport is deliberately induced by the aeration wells, it is logical for advective transport to be significant. Previous research has shown that when flow rates in porous media are high, dispersion is dependent on flow rate such that a Peclet number between 1 and 10 is maintained regardless of flow rate (Delgado, 2006). The exact numbers vary depending on the test method and the properties of the porous media and fluid, but the same trend is seen in these results. The fitted data from Yazdani et al. (2010) also showed a Peclet number of 1.20 ± 0.03, which is in the same range. A high concentration gradient is induced by the injection of the tracer, and high concentration gradients of background gases exist naturally in the waste body (Meza et al., 2022). These concentration gradients result in significant gas diffusion, which may also increase the dispersion coefficient. Additionally, the values of v_g and D are very similar across all well pairs. This could be taken as an indication that the aeration is performing relatively uniformly across the tested area, but this is complicated by the fact that the majority of nearby wells did not see breakthrough. Instead, it is possible that these values of v_g and D represent the flow conditions only in the preferential pathways which carry most of the tracers. Velocity in the bulk waste may be much lower, with the dispersion coefficient being somewhat proportional. In this case, the similarity in v_g and D would indicate that that the preferential pathways are relatively uniform across the tested area.

$$Pe = \frac{v_g L}{D} \tag{39}$$

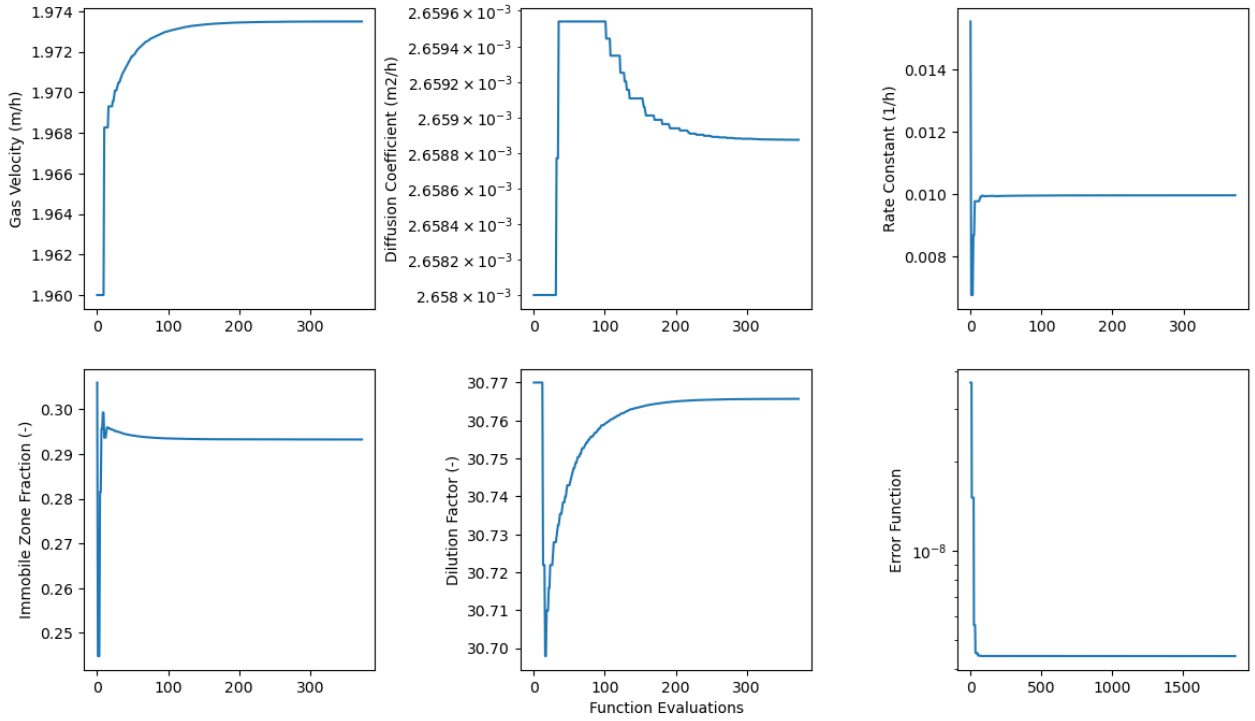

Figure 45: Convergence plot of C2 (PGTT-2)

Figures 46 through 50 show that the fitted BTC generally fits the collected data quite well, although there is sometimes some difference at the peak. This is likely due to the LumaSense issues discussed in Section 3.2.1, as the peaks seem to be quite irregular in most cases. This resembles the temperature fluctuations and happens over a similar time scale. It is also possible that this peak is a genuine result of flow conditions in the waste body which the model does not capture. This is considered less likely, however, as the model is capable of simulating double peaks and other unusual behaviour, but this did not seem to be the best fit for the other parts of the BTCs. Indeed, the fitted model matches the data quite well in the rising and falling parts of the curve.

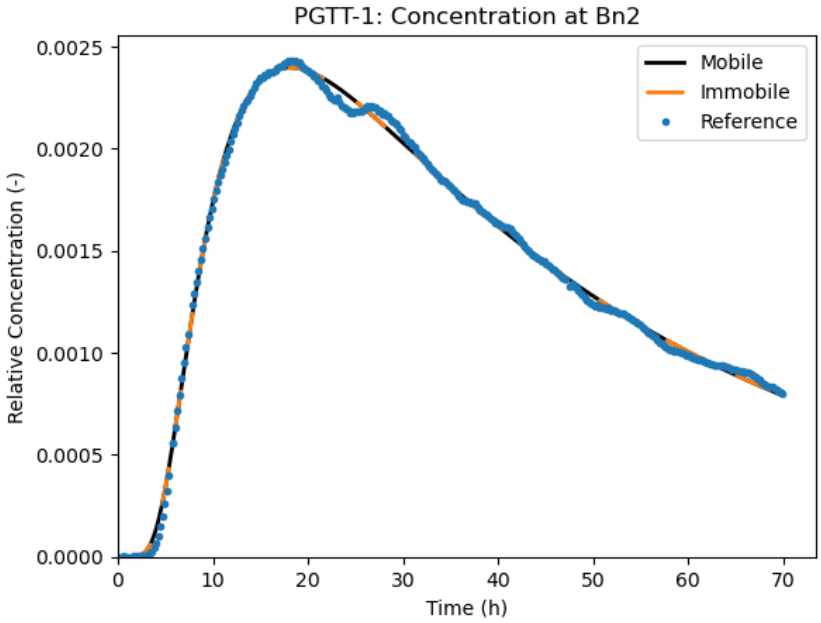

Figure 46: Fitted BTC at Bn2 (PGTT-1)

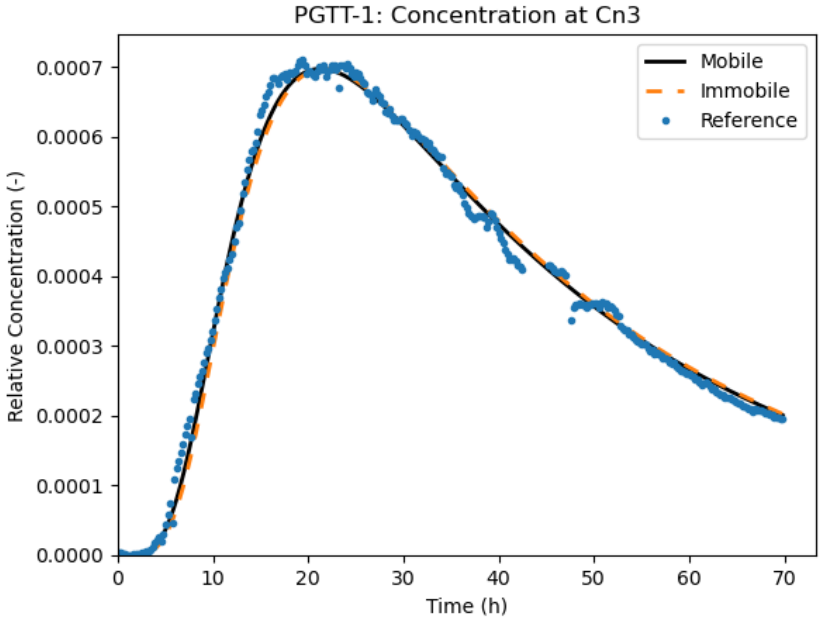

Figure 47: Fitted BTC at Cn3 (PGTT-1)

As discussed in detail in Appendix B, the model was not set up with a Total Variation Diminishing (TVD) scheme. A TVD scheme guarantees that instability in the model does not grow and lead to oscillations, which is particularly important when there is a large gradient between adjacent points (Versteeg & Malalasekera, 2007), as is the case at the beginning of the PGTT. Still, the total variation was tracked throughout each simulation, as calculated by Equation 40 (Versteeg & Malalasekera, 2007). In each case, there was an increase in the total variation during the portion of the test when tracer was injected, but the total variation decreased monotonically as soon as the injection stopped. An example is shown in Figure 51. This indicates that the model was stable and non-oscillatory under the discretization scheme used, at least once the injection was finished.

$$TV = \sum_{i=0}^{N-1} |c_{i+1}^m - c_i^m| \tag{40}$$

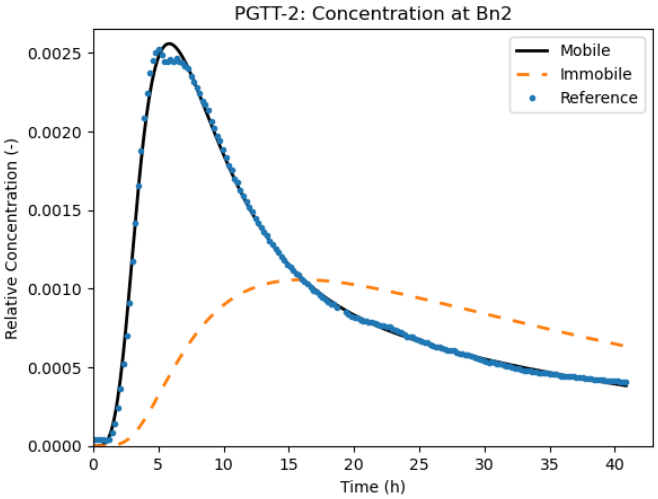

Figure 48: Fitted BTC at Bn2 (PGTT-2)

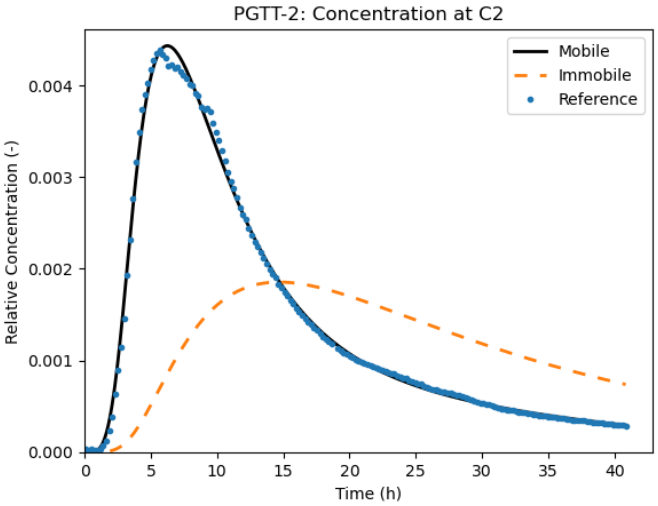

Figure 49: Fitted BTC at C2 (PGTT-2)

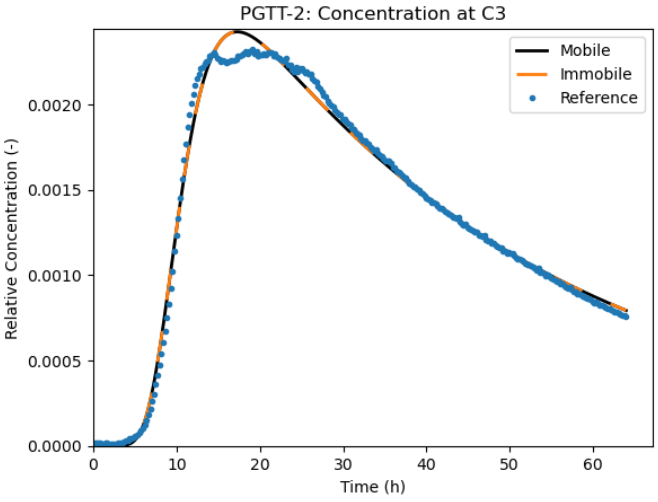

Figure 50: Fitted BTC at C3 (PGTT-2)

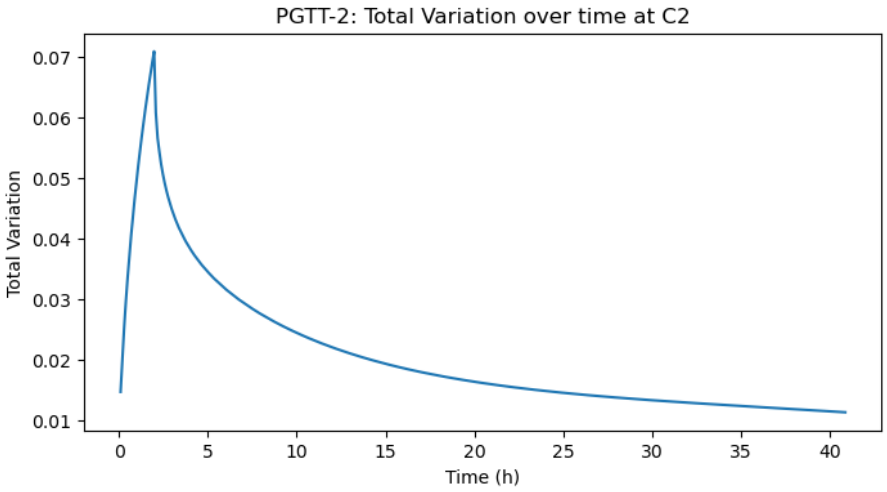

Figure 51: Decrease in total variation (PGTT-2)

Although the model did eventually converge to an optimal set of parameters, the inverse model sometimes found "troughs" in the solution space. In these troughs, model parameters can change significantly with minimal effect on the quality of fit. An excerpt of one of the convergence plots is shown in Figure 52. In this plot, the model parameters change by up to 50% while the quality of the fit changes by only 0.5% as indicated by the squared error. This indicates that, while there is an optimal solution to the parameter estimation problem, there is a wide variety of parameters that result in an almost equally good fit.

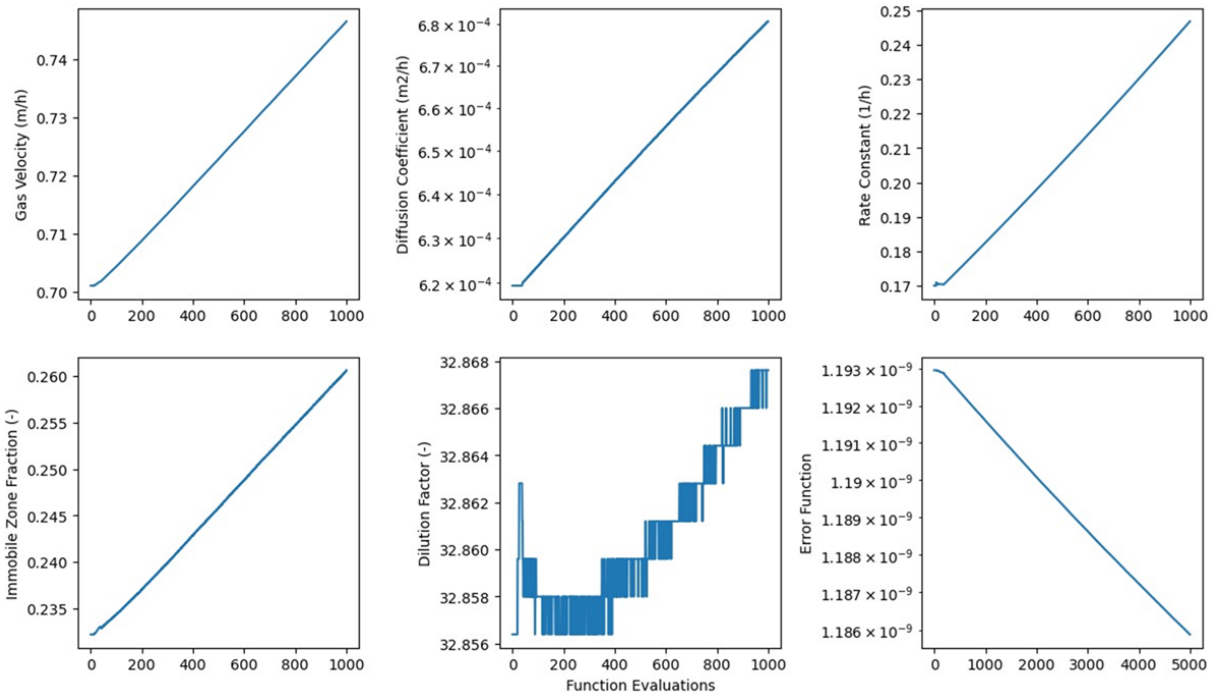

Figure 52: Trough in convergence plot (Validation data)

3.2.5 Spatial Trends

Unfortunately, only two PGTTs could be completed due to maintenance on the landfill's central extraction system, which is central to the test procedure. It was intended to supplement the PGTTs with dipole tests, which can be performed on a pair of wells without the central extraction system. However, issues with equipment availability made this impossible. With the limited amount of data, it is difficult to draw conclusions about spatial trends. Nevertheless, some connections can be made.

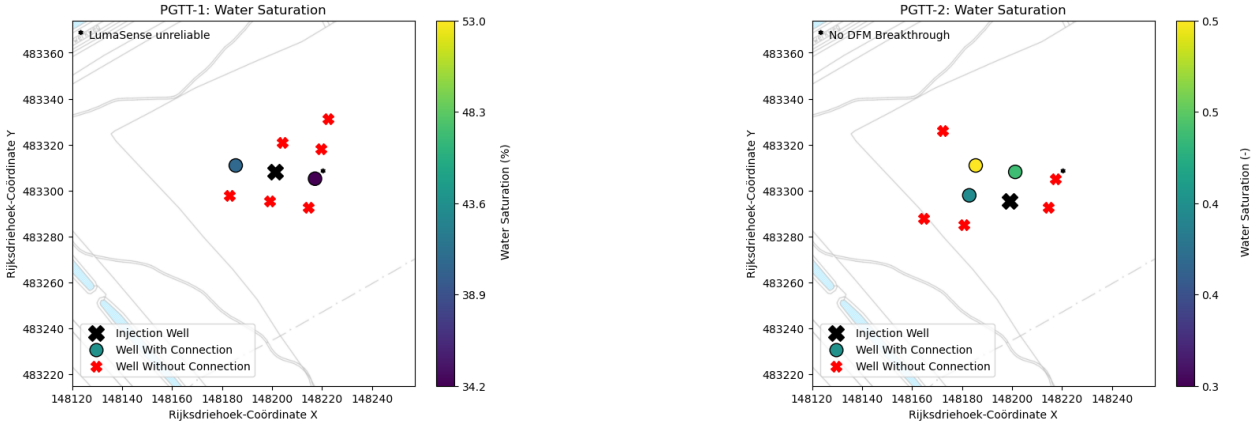

(a) PGTT-1

(b) PGTT-2

Figure 53: Saturation maps

The water saturation for each test is plotted in Figure 53. It is clear that only the nearest wells experienced breakthrough in both tests. It can also be seen that well Bn2 has different values of saturation in the first and second tests. This is not a contradiction, as the tracer gases were injected at different wells and thus travelled different paths in the two tests. The values derived from PGTTs are a sort of volumetric average of the waste traversed by the tests, so this discrepancy indicates a high level of heterogeneity in this part of the waste body. The water saturation is universally higher in the second test. Approximately 2 months passed in between the two tests, so it is possible that conditions inside the waste body changed in the intervening time. However, it was quite a dry period with only 13.4 mm of rain, compared to 77.0 mm in the previous two-month period (as measured at the nearest weather station, which is at Lelystad Airport) (KNMI, 2025). It would therefore be unexpected for the actual moisture content of the landfill to have increased, implying that the change is due to differences in flow paths rather than changing environmental conditions.

Figures 54 through 57 show the saturation, immobile zone fraction, gas velocity, and dispersion coefficient for both tests on a single map. Each parameter is plotted per well pair, since it is the waste between the wells that influences their values rather than the wells themselves. There does not appear to be any spatial trend in any of the values, with the possible exception of the dispersion coefficient. There is a higher value of D for the two well pairs which involve Bn2. However, the difference is relatively small. It should be kept in mind that not much spatial data is available, so trends may start to appear as more data is collected.

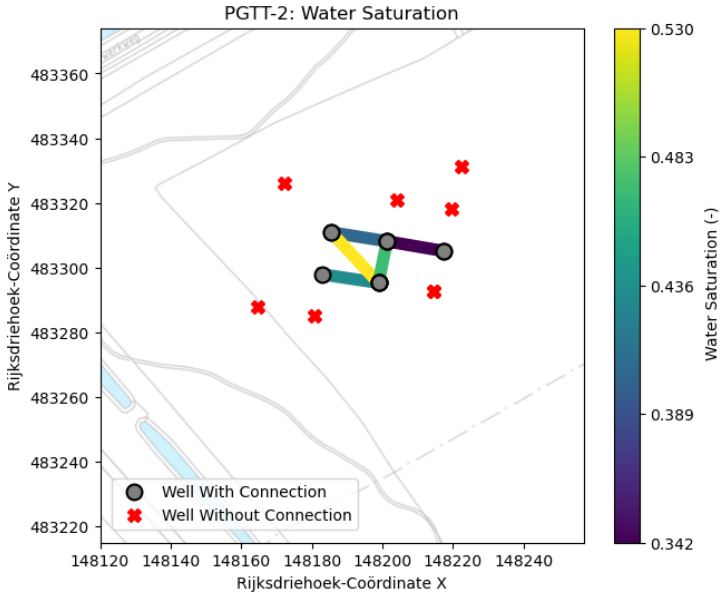

Figure 54: Saturation Map

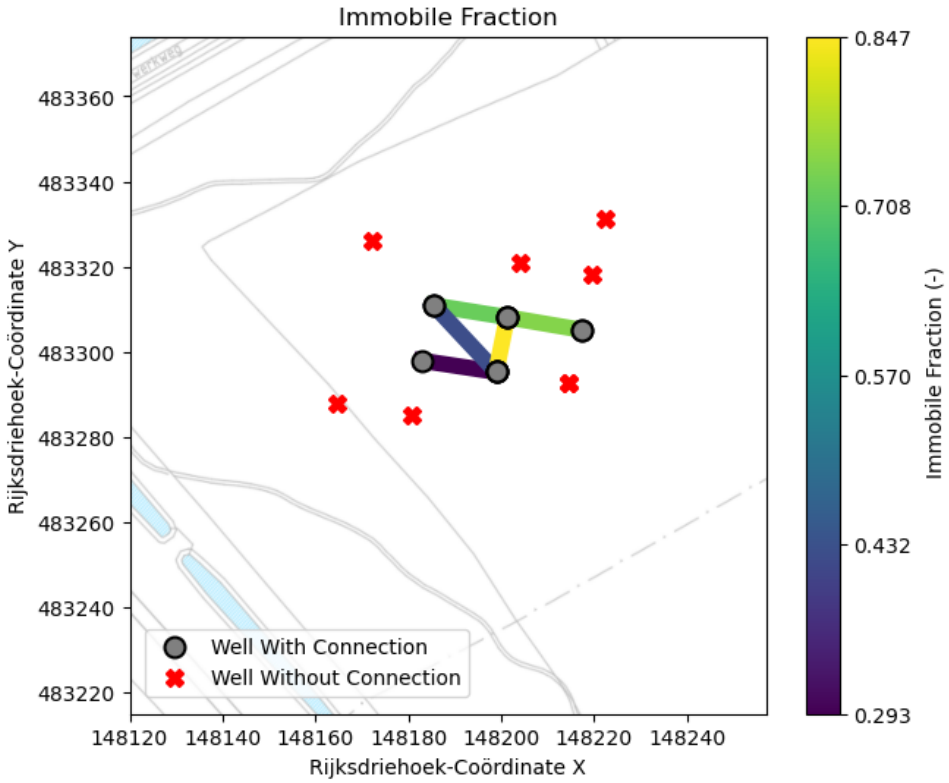

Figure 55: Immobile fraction map

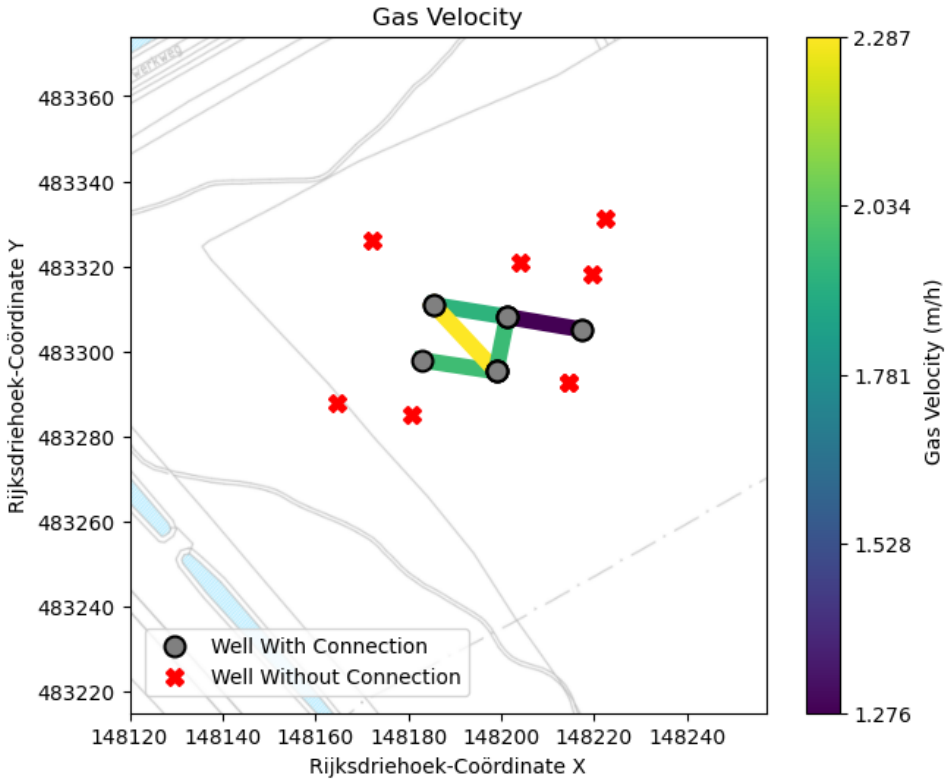

Figure 56: Velocity map

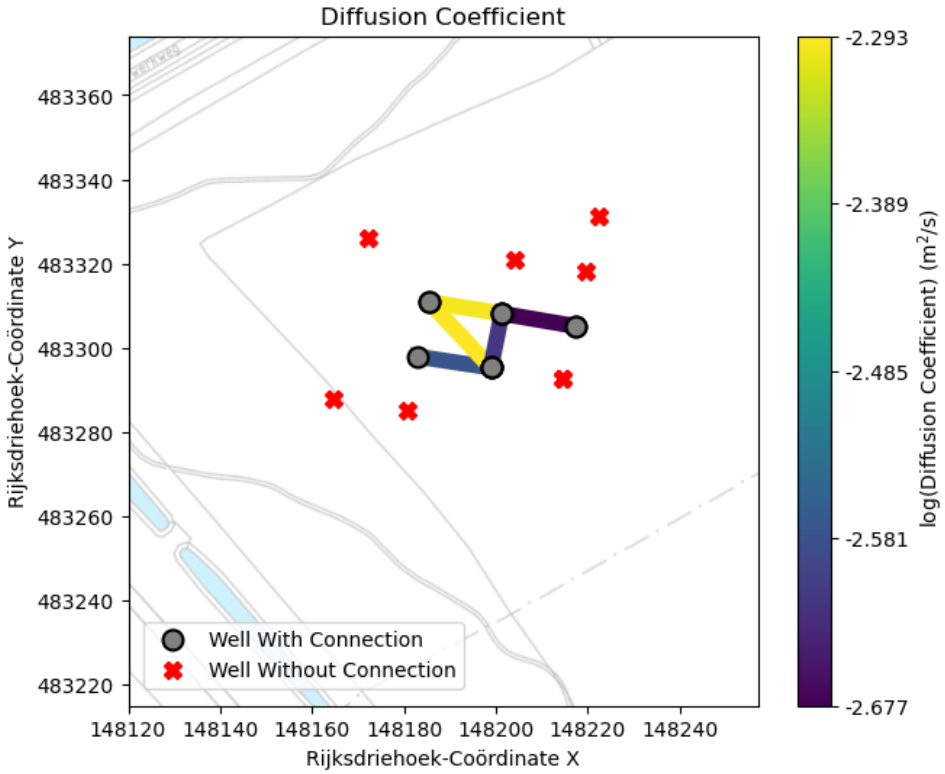

Figure 57: Dispersion coefficient map

3.2.6 Correlations

Figure 58 shows the immobile fraction and gas velocity plotted against saturation. There appears to be a minor correlation between saturation and the immobile fraction, although it is not totally clear. There is a clearer correlation between the saturation and the gas velocity, which appears to be almost linear.

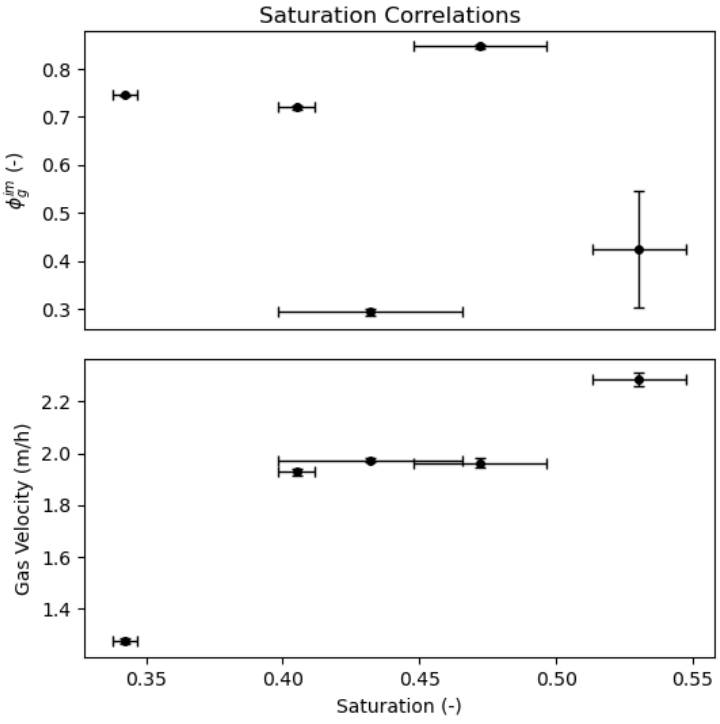

Figure 58: Dual domain correlations with saturation

Figure 59 shows a comparison of the gas permeability of the well pairs with breakthrough to the average of all wells. The well pairs with breakthrough have values of gas permeability which are well within the expected range. In fact, by comparison with Figure 17, it can be seen that the breakthrough well pairs have values of gas permeability very close to the peak of the gas permeability histogram. This was unexpected, as it was theorized that both tests would be highly influenced by preferential pathways and thus show similar trends. Figure 60 shows the saturation, immobile fraction, gas velocity, and dispersion coefficient plotted against the well pair gas permeability. There may be some weak negative correlation between permeability, velocity, and diffusion coefficient. However, these correlations are unclear due to the relatively high uncertainty in the gas permeability and the small number of data points. There does not seem to be any correlation with immobile fraction or saturation. A much more clear correlation was expected due to the association between gas permeability and advective transport. It was thought that a high value of gas permeability would be associated with a high fraction of pores which participate in advective transport as well as a high gas velocity. Conversely, saturation and immobile zones are thought to hinder advective transport, and thus a negative correlation was expected. The lack of correlation with saturation could indicate that the gas permeability does not vary significantly with saturation until saturation nears 100%. This trend has been reported for some porous media (Jucá & Maciel, 2012), including landfilled waste (Kallel et al., 2004; Stoltz et al., 2010), but is not universal (J.-F. Liu et al., 2014; Ni et al., 2023; D. Zhang et al., 2020).

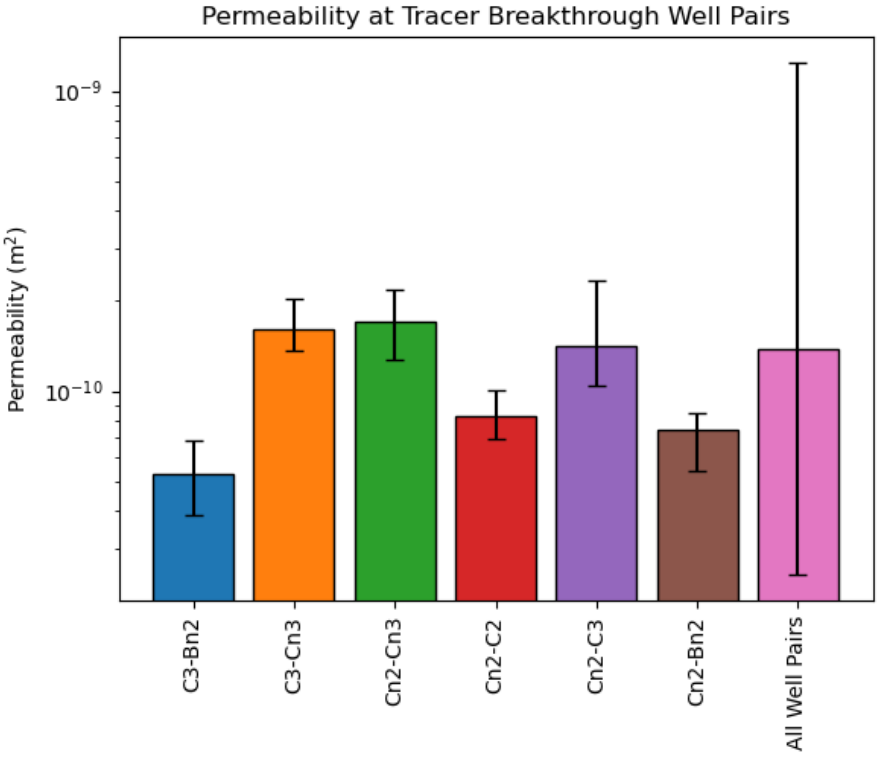

Figure 59: Gas permeability of well pairs with breakthrough
(Columns represent mean gas permeability of all tests using a given well pair. Error bars represent standard deviation of these gas permeabilities. Number of tests varies per well pair.)

Figure 61 shows the immobile fraction, gas velocity, and saturation plotted against the PAA, oxygen content, and nitrogen content at the monitoring well, as measured by the GC before the start of the test. There seems to be a correlation such that wells with higher oxygen content and lower PAA have a lower fraction of immobile zones. This was expected, as immobile zones are associated with anaerobic respiration due to lack of oxygen infiltration. These wells also tend to have higher gas velocity. Similar trends are seen with nitrogen as with oxygen. Nitrogen is an inert gas, so the amount of nitrogen in the LFG is strongly indicative of the quality of aeration. Thus, the trend in nitrogen can be interpreted similarly to those in oxygen. Counterintuitively, wells with lower PAA and higher oxygen content tend to have a higher value of saturation.

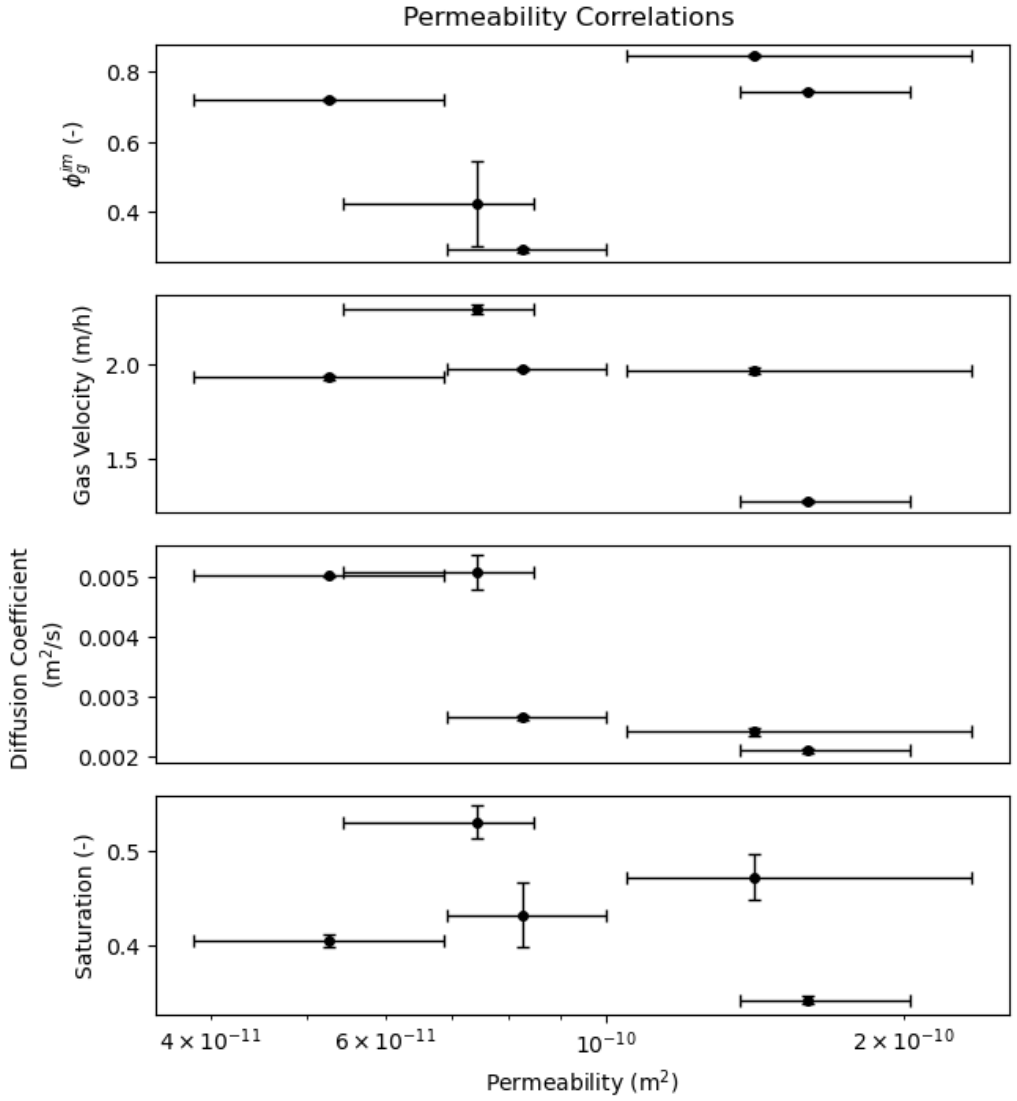

Figure 60: Dual domain correlations with gas permeability
(Gas permeability points represent mean gas permeability of all tests using a given well pair. Error bars represent standard deviation of these gas permeabilities. Number of tests varies per well pair.)

Figure 62 shows the same parameters plotted against the aeration flow speed, aeration pressure, and gas temperature measured in the most recent gas round. Wells with higher immobile fractions tend to have lower aeration flow speed, higher pressure differentials, and lower temperature. This matches expectations, as the immobile fraction is understood to impede the aeration system, resulting in higher pressure in the pipe system as flow cannot penetrate the waste. Since microbial activity is decreased under anaerobic conditions, this also results in a lower LFG temperature. Higher gas velocity is also associated with higher flow in the aeration system and higher temperatures, which agrees with expectations for similar reasons. Increased dispersion coefficient is correlated with increased flow speed, lower pressure difference, and higher temperature. Figure 63 shows the dual domain parameters plotted against some features of the breakthrough curves, namely the time at which the DFM peak occurred and its normalized concentration. The same parameters for propane are not plotted, but they correlate very closely with those of DFM. There is once again some correlation with ϕ_g^{im} and gas velocity. Wells with a higher immobile fraction tend to have a higher peak time and a lower peak concentration. The opposite trend is seen with gas velocity.

Some additional parameters were checked for correlation with the dual domain results, but no correlation was found. Plots of some of these factors can be found in Appendix E.

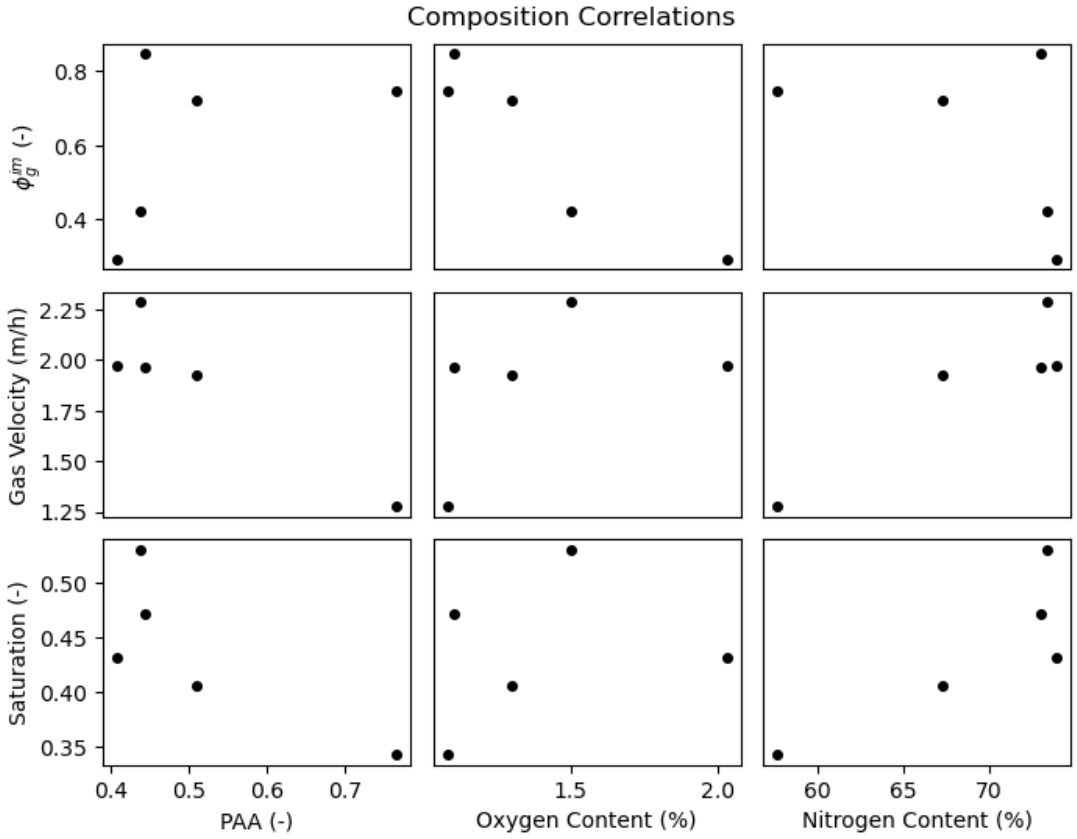

Figure 61: Dual domain correlations with LFG composition

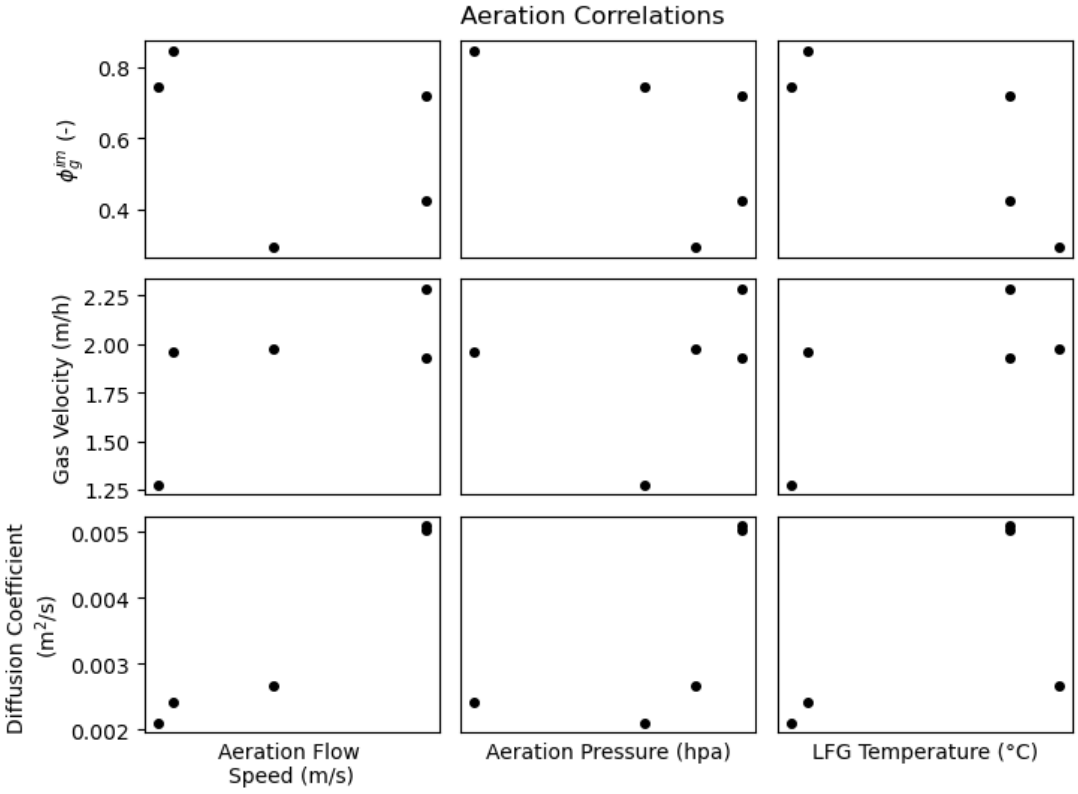

Figure 62: Dual domain correlations with aeration parameters

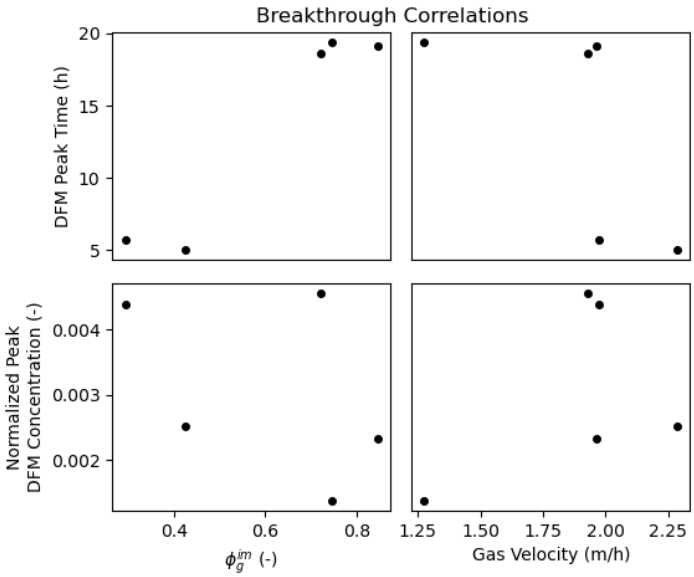

Figure 63: Dual domain correlations with BTC parameters

3.3 Gas Push-Pull Tests

3.3.1 Retardation Factor, Water Saturation, and Recovery

The recovery curves from the LumaSense and GeoTech are shown in Figures 64 through 65 below, with the propane and DFM having been corrected using the compensation curves. In this test, the compensation is especially important because the methane concentration changes throughout extraction. The black lines demarcate the beginning of injection, the end of injection, and the beginning of extraction. It should be noted that the GeoTech measurement of methane is heavily affected by the presence of propane. The values in these figures should therefore be considered as more representative of propane concentration than methane concentration.

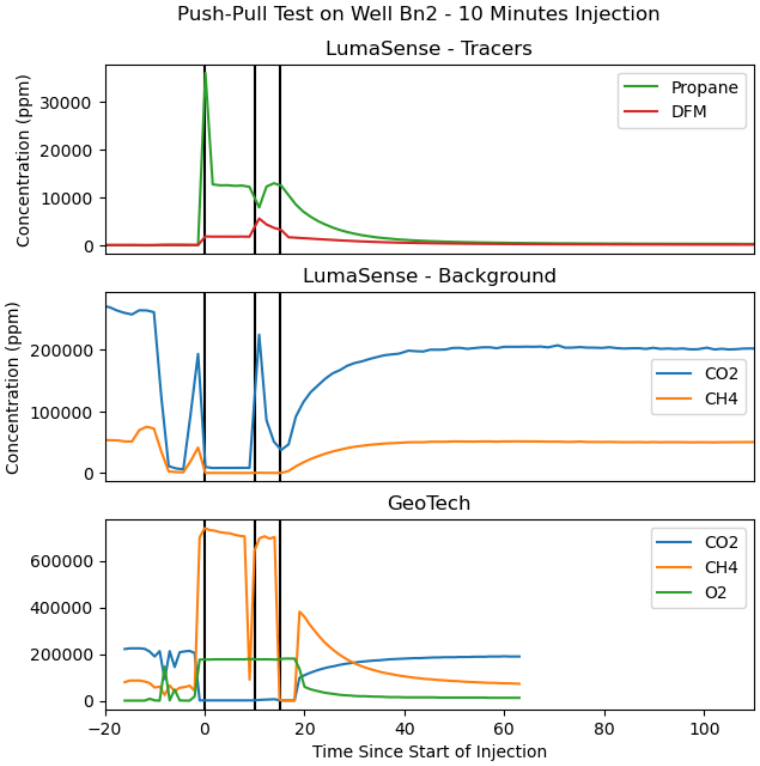

Figure 64: Gas concentrations during GPPT-10 (2025-06-10)

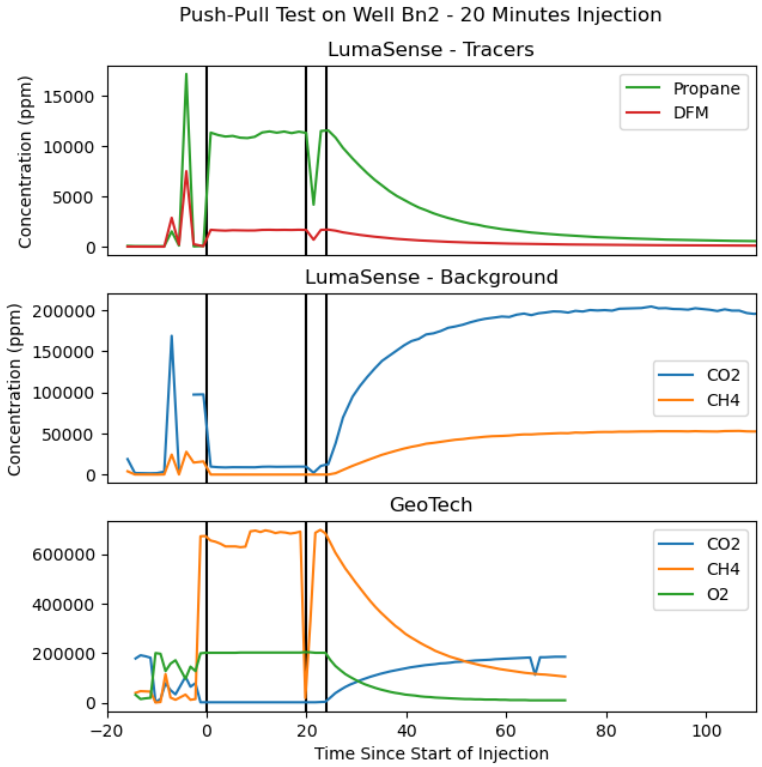

Figure 65: Gas concentrations during GPPT-20 (2025-06-10)

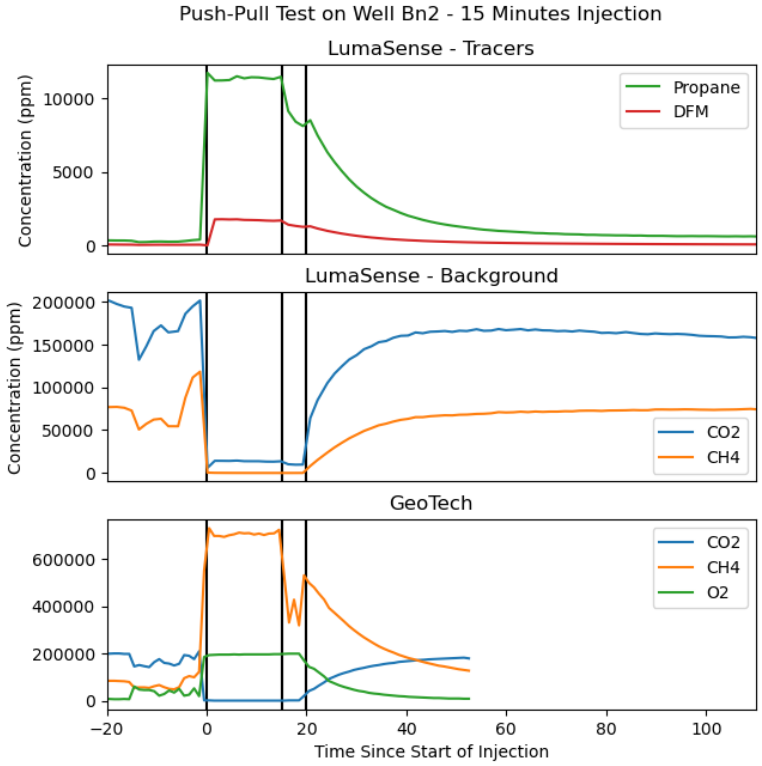

Figure 66: Gas concentrations during GPPT-15 (2025-06-11)

When normalized to the input concentration, the recovery curves of DFM and propane are extremely similar, as shown in Figure 67. When the calculation for R_f and S_w was carried out, all three tests showed a retardation factor of slightly less than one and a value of saturation which was negative and very close to zero. Of course,

a negative value of saturation is not possible and a very low value does not match the analysis of the PGTTs, previous research on the Braambergen landfill (Wang & Heimovaara, 2025a), or the fact that a meter of leachate was present in the screened part of the aeration well.

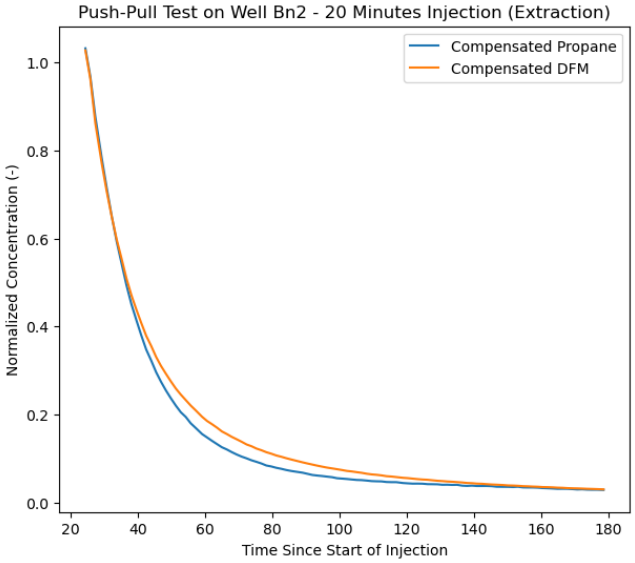

Figure 67: GPPT-20: Normalized BTC (2025-06-10)

The amount of tracer injected and recovered in each test is listed in Table 12. It is noted that in the ten-minute test, more DFM was recovered than injected. This was the first tracer test performed at Braambergen in several weeks, so it is unlikely that any residual tracer was extracted from the waste body. Rather, it seems that something went wrong with one of the measurements. In the other tests, on the other hand, the amount of DFM and propane recovered is similar. This is in agreement with the very similar recovery curves and the idea that the two gases have similar transport properties. It also adds confidence that the test proceeded as intended, without major losses of tracer to other flow paths (Han et al., 2006). It is also noteworthy that less tracer was recovered with a 15-minute injection time than with a 20-minute injection time. This is contrary to expectations, as the tracer should travel further from the injection well in the 20-minute injection and thus be harder to recover. This difference may indicate that the environmental conditions were significantly changed by the reactivation of the site-wide extraction system.

Finally, it should be kept in mind that all tests were performed on the same well shortly after one another. It is therefore possible that residual tracer from each test could remain in the well and influence the following tests, especially since the aeration system was not operational for the first two tests. During each test, extraction was continued until the tracer concentration was close to background, but this can be difficult to determine in the moment due to the issues with the LumaSense compensation. This could affect the calculation of recovery rate, but should not affect the reaction rate since the background concentration is accounted for in Equation 36. GPPT-20 is likely to be more affected than GPPT-15, since a full night passed in between GPPT-20 and GPPT-15 as opposed to a few hours. Although the aeration system was not operational, gas diffusion would reduce the concentration of tracers near the well. This could potentially account for the higher mass recovery in GPPT-20.

Table 12: Tracer recovery rates from GPPTs

Test	Injection Time (min)	DFM Mass Injected (g)	DFM Mass Recovered (g)	DFM Recovery (%)	Propane Mass Injected (g)	Propane Mass Recovered (g)	Propane Recovery (%)
GPPT-10	10	23	34	149	114	95	83
GPPT-15	15	34	22	66	172	117	68
GPPT-20	20	45	38	85	229	198	87

3.3.2 Reaction Rates

While performing the linear fit to find the reaction rates, it was found that the first few minutes of the extraction are critical. Within around five minutes, the net mass transfer begins to increase again. The same trend was observed by Streese-Kleeberg et al. (2011) in some tests and was attributed to the concentration of the reactive gas returning to its background level, which is very low. However, during the first test, the GeoTech failed right as extraction began. This failure was caused by clogging of the filter which protects the device from condensation when sampling very humid LFG and was corrected for in subsequent tests by frequent replacement of the filter. This made it impossible to determine the reaction rates for GPPT-10.

The net mass transfer of oxygen is plotted in Figure 68 for GPPT-15 and GPPT-20, with the net mass transfer of methane shown in Figure 69. The zero-order reaction rate was calculated relative to both propane and DFM, with the results shown in Table 13. As suggested by the saturation results, there is no significant difference between the calculated reaction rates relative to DFM or propane. This means that future tests do not necessarily need to include both tracers. A much higher oxygen consumption rate was measured during the GPPT-20.

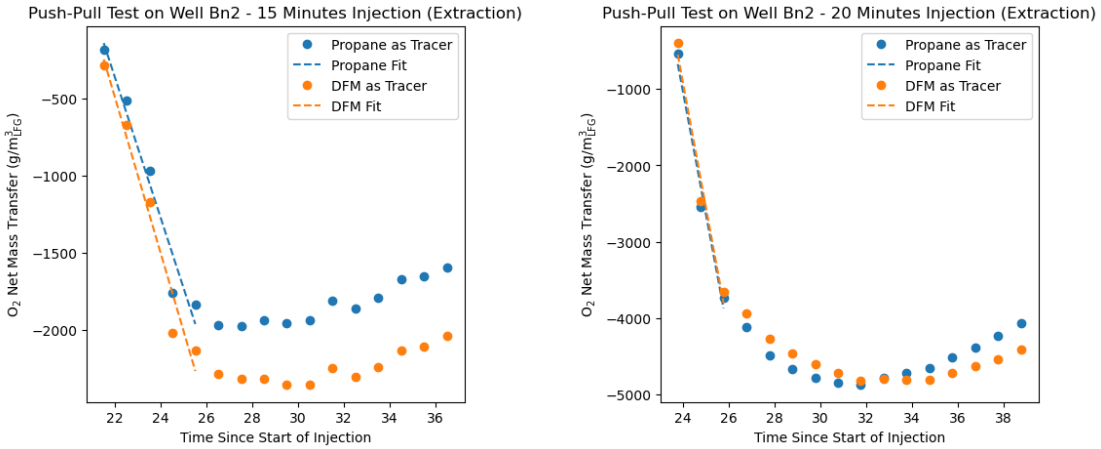

(a) GPPT-15 (2025-06-11) (b) GPPT-20 (2025-06-10)

Figure 68: Oxygen mass transfer

(a) GPPT-15 (2025-06-11) (b) GPPT-20 (2025-06-10)

Figure 69: Methane mass transfer

In contrast, the net mass transfer rate of methane was not significant for either test. The shapes of the curves resemble those of the oxygen respiration plots, but with fewer points in the declining portion. Additionally, the net mass transfer in the 20-minute test was positive, indicating that proportionally more methane was recovered than DFM or propane. Still, the initial mass transfer rate rate was negative. It is unclear what this means in terms of microbial reactions.

Table 13: Net mass transfer rates from GPPTs

Test	Oxygen Mass Transfer Rate $(g/m^3_{LFG}h)$		Methane Mass Transfer Rate $(g/m^3_{LFG}h)$		PAA Before Test (%)
	Propane as Tracer	DFM as Tracer	Propane as Tracer	DFM as Tracer	
GPPT-15	-520 ± 80	-570 ± 80	-20 ± 20	-10 ± 20	62
GPPT-20	-1600 ± 300	-1600 ± 300	-10 ± 20	-10 ± 20	44

As mentioned in Section 1.4, GPPTs have not previously been used for in-situ measurement of reaction rates in landfill waste bodies. However, some reaction rates have been measured by other means. For example, Yazdani et al. (2010) performed an in-situ measurement of oxygen consumption rate at an aerated landfill by disabling the aeration system and recording the rate at which oxygen concentrations decreased. They estimated a mean first-order reaction coefficient of 0.70 h^{-1}. This can be converted to the same units as Table 13 by multiplying with the molar density of landfill gas at the measured mean temperature and pressure, as well as by the mean initial concentration of oxygen and molar mass of oxygen. This is calculated to be 100 $g/m^3_{LFG}h$, as shown in Equation 41.

$$\left(0.70\,h^{-1}\right)\left(\frac{101325\,N/m^2}{(8.3145\frac{Nm}{molK})(328\,K)}\right)\left(0.12\frac{mol\,O_2}{mol}\right)\left(31.99\,\frac{g}{mol\,O_2}\right)=100\,\frac{g}{m^3_{LFG}h} \tag{41}$$

Using the same method, the first-order reaction rate measured by Ma et al. (2025) for methane oxidation can be converted to the same units. This results in a reaction rate of 0.02 - 0.1 $g/m^3_{LFG}h$. This reaction rate was measured in lab-scale aerobic bio-reactors using fresh waste. This was meant to mimic the top layers of an aerated landfill.

Additionally, Gebert et al. (2023) reported that at another aerated landfill in the Netherlands, 1500 tons of carbon were degraded aerobically over a six-year period. On a landfill in Northern Italy, it has been recorded that 0.5 moles of CO_2 are produced for each mole of O_2 consumed, taking into account aerobic respiration only (Raga & Cossu, 2014). Assuming that a similar ratio holds for the landfill studied by Gebert et al. (2023), the landfill-scale oxygen consumption rate can be calculated according to Equation 42. This is converted to the same units by dividing by the average flow rate, which is 550 m^3/h. By this method, a value of 276 $g/m^3_{LFG}h$ is obtained.

$$\left(\frac{1500\,tCO_2}{6\,y}\right)\left(\frac{1\,mol\,CO_2}{44.01\,g\,CO_2}\right)\left(\frac{1\,mol\,O_2}{0.5\,mol\,CO_2}\right)\left(\frac{31.99\,g\,O_2}{mol\,O_2}\right)\left(\frac{1\,y}{8760\,h}\right)\left(10^6\frac{g}{t}\right)=1.52(10)^5\,\frac{g\,O_2}{h} \tag{42}$$

It should be kept in mind that some significant simplifications and assumptions were made in these calculations. Thus, the orders of magnitude of the results should be considered rather than the exact values. The oxygen reaction rates calculated from Yazdani et al. (2010) and Gebert et al. (2023) are both in the same order of magnitude as the one recorded in GPPT-15, although they are lower. GPPT-20 had a much higher reaction rate than these literature values, but the discrepancy could potentially be explained by the scale of the tests. Both of the literature values were recorded at landfill-scale, while the GPPTs in this report are at well-scale. It is possible that regions of the referenced landfills had similar reaction rates to the one measured here, but the overall reaction rates were lower due to other, less reactive areas. This could be evaluated by repeating the test procedure on other aeration wells.

The methane oxidation rate measured by Ma et al. (2025) was almost zero, which matches the results of the GPPTs. This was attributed to the fact that aerobic biodegradation is a much more energy-efficient use of oxygen than methane oxidation, and thus waste-degrading bacteria can out-compete the aerobic methanotrophs. In regions with less degradable organic matter, this may not be the case. In landfill cover soil, for example, methane oxidation rates have been measured which are similar in magnitude to the oxygen consumption rates measured in this work (Streese-Kleeberg et al., 2011).

Lab-scale tests have also been performed to measure oxygen consumption rates in waste samples, which are likely to give much more reliable results than the ones used here. However, these studies all report respiration rates relative to the dry matter, volatile solids, or total carbon in the waste sample (e.g. Adani et al., 2004; Lee et al., 2016; Sohoo et al., 2021). While useful for comparing lab tests, this convention makes it difficult to compare with field tests where these quantities are not known.

4 Discussion

4.1 Comparability with Literature

When analyzing the gas permeability data, it was found that the gas permeability in this region of the Braambergen landfill was higher than the values reported in previous research (Jain et al., 2005; Wu et al., 2012). However, these studies were performed on landfills which primarily MSW. Compared to the soil residues which are primarily contained at Braambergen, MSW contains a much higher proportion of organic material and has a higher water content. This may lead to decreased gas permeability, as the high saturation may cause a significant portion of the pores to be blocked against gas flow.

No literature could be found which reported anisotropy in gas permeability in a landfill context. Previous research which reported anisotropy in hydraulic conductivity reported lower ratios than were observed in this work (Fei et al., 2024; Hu et al., 2021; Ke et al., 2022; Singh et al., 2014). While hydraulic conductivity and gas permeability have some underlying factors in common, such as pore size distribution, they are not directly comparable. For example, a higher saturation would tend to increase hydraulic conductivity but decrease gas permeability. Additionally, these landfills were also filled primarily with MSW. For theses reasons, it is difficult to compare the results of this work with existing literature.

For the results of the PGTTs, there was very little data with which to compare. Previous research which calculated saturation from tracer tests was also performed on landfills containing primarily MSW (Han et al., 2007, 2006; Jung et al., 2012). The same is true of the research on dual porosity modelling (Yazdani et al., 2010). In these cases, however, the results from the Braambergen landfill are largely comparable to those from the MSW landfills despite the differences in composition.

For the GPPTs, there was no literature available in which the same tests were performed. While this technique has been previously applied in landfill contexts, it has been exclusively used for cover soil processes rather than in the waste body itself. Additionally, research has focused on methane oxidation rather than oxygen consumption (Gómez et al., 2009; Ma et al., 2021; Streese-Kleeberg et al., 2011). However, oxygen consumption rates were compared with results from Yazdani et al. (2010) and (Gebert et al., 2023). As discussed, the landfill studied by (Yazdani et al., 2010) is largely composed of MSW. Conversely, the landfill studied by Gebert et al. (2023) has a relatively similar composition to Braambergen. Although it has more commercial waste and less soil decontamination residue and is considerably older, it also has a relatively low organic matter content (van Meeteren et al., 2009). While these two landfills are very different from each other, they had similar oxygen consumption rates to each other. The values obtained at well Bn2 were in a similar order of magnitude.

In addition to waste composition, factors such as landfill construction and degree of waste degradation can cause significant differences in transport characteristics (Ke et al., 2022; Stoltz et al., 2010; Zeng et al., 2017). In particular, a major contributor to anisotropy is the way in which landfills are constructed. Waste is applied in successive layers and compacted to provide stability (Powrie & Beaven, 1999; Stoltz et al., 2010), often with intermittent soil layers (Nanda & Berruti, 2021). Variations in the construction of the landfill could cause major differences in the research results. In this sense, the uniqueness of each landfill must be kept in mind when comparing results from different research locations.

4.2 Instability of Extraction Flow During Pressure Field Testing

When comparing PFTs with extraction against those with injection, it was noted that there was no significant difference in the calculated gas permeability, but the flow rates in the extraction tests were much less stable. It was theorized that the instability in the flow rate was caused by fluctuating leachate levels at the bottom of the well. If the interface between the inside of the well and the gas phase of the waste body is small, it could be intermittently blocked by leachate, causing the flow rate to be reduced. The fluctuation was not seen at every extraction well, nor was it correlated with the measured leachate depth. This hypothesis was tested by adding a CTD-Diver to the bottom of the well during a stepped test, with the data presented in Figure 32. The results show fluctuation in the leachate level during periods when the flow rate was decreasing. This was especially true towards the end of the test when the flow rate approached zero. However, there was a period in the middle of the test in which the flow also reached zero, but the same fluctuation was not seen. This indicates that fluctuations in the leachate level may explain part of the phenomenon, but there may be other effects involved as well. It is also possible, for example, that water vapour in the extracted gas condenses inside the blower and interrupts the flow. It is known that there is significant variation in leachate depth throughout this landfill cell

(Gebert et al., 2022) and that zones of perched leachate exist in the cell which are separated from the lower leachate table (Wang & Heimovaara, 2025a). It is therefore possible that these irregularities in leachate content contribute to the fluctuation, for example via cracks in the well casing that might allow water ingress at various depths when a negative pressure is present.

It should be remembered that this is only a single preliminary test of this hypothesis, and further testing must be performed before any conclusions can be drawn. Also, this stepped test was eliminated as an outlier due to the high flow instability, so the presence of the CTD-Diver does not influence the interpretation of the stepped test results.

4.3 Changing Connectivity In Pressure Field Testing

Results were also monitored to determine whether connection between well pairs were consistent. Analysis of the maps in Appendix D shows that, in most cases, well pairs which initially showed a connection continued to display a connection through subsequent tests. There did not seem to be a difference between extraction and injection in this regard, except in instances where a much higher flow rate could be generated in injection. On well Bn1, for example, the flow rate increased from 24.0 to 42.2 m^3/h when the flow was switched from extraction to injection during testing on 18 March. This caused a weak pressure response to be measured at Bn3 which was not measured during injection. Due to the change in flow rate, this is likely not related to a fundamental difference. Instead, flow is likely limited by a mechanism such as the fluctuation of the water table discussed in Section 4.2, which in turn limits pressure propagation in the waste body.

However, there were some well pairs which displayed an initial pressure connection that was not present in subsequent tests. For example, well Cn2 showed connections with wells Bn2 and Cn1 during an extraction test on 7 March, but these connections were not measured during an extraction test on 25 April. The initial pressure responses were not weak, so the difference is not due to poor signal. It is possible instead that flow paths within the waste body changed during the seven weeks which separate the tests. This cannot be attributed to plant maintenance, as only limited interruptions to the blower operation took place during these weeks.

The connections may have changed due to varying environmental conditions such as weather or shifting transport pathways caused by factors like settlement. Previous research at Braambergen has shown that the water content of the landfill does not have a significant seasonal variation, but water content in the cover soil does (Wang & Heimovaara, 2025b, 2025c). Research on a similar aerated landfill has shown that this cover soil variation may significantly affect the aerobic fraction of respiration (Gebert et al., 2023). Thus, it is possible that changes in the cover soil saturation affect the connectivity of flow paths within the waste body. Changing leachate levels may also contribute, although the leachate levels measured before each test were very consistent throughout the test period. It is still possible that the distribution of leachate changed during the test period. Whatever the cause, the change in connectivity does call into question whether all of the tests performed during this work can be compared. The two PGTTs are separated by three months for example, during which significant changes may have occurred. Monitoring a few wells over time could help answer this concern.

4.4 Stepped Pressure Field Tests

From the stepped PFTs, it was noted that there is a slight positive slope of gas permeability against flow rate. A higher gas permeability at a higher flow rate indicates that the pressure induced at the monitoring well does not change proportionally with the flow rate. This could be caused by several factors. For one, a higher flow rate means a higher pressure differential at the extraction/injection well. This could cause flow paths to open which were not significant at lower pressure. In particular, it is possible that gas may flow along with the side of the well directly to the surface. During installation of the wells, a hole was drilled which was slightly larger than the diameter of the pipe, with the understanding that the waste would expand to fill the remaining annulus. It is possible, however, that this seal would not be complete, allow flow to "short-circuit" to the surface (Wu et al., 2012). No tests have been performed to quantify this effect at Braambergen or, to the author's knowledge, at other landfills.

Alternatively, the observed increase in gas permeability could be caused by the fact that the Baehr and Joss model neglects the Klinkenberg effect in order to obtain a closed-form analytical solution (Baehr & Hult, 1991; Baehr & Joss, 1995). The Klinkenberg effect is a nonlinear phenomenon by which the gas permeability of porous media seems to increase when the driving pressure is greater. This effect is attributed to slippage between the gas and the pore walls, and is not seen with liquid flow in porous media (Klinkenberg, 1941). The Klinkenberg

effect is more significant when the driving pressure is higher and when gas permeability is lower. For the tests in this work, the driving pressure was never less than 90% or more than 110% of the ambient pressure. Given this range, along with the gas permeability range given in Section 3.1.3, the maximum possible error induced by the Klinkenberg is between 8 and 12% for extraction and between -1 and -5 % for injection, as estimated by Baehr and Hult (1991). Given that the error increases with the flow rate, this effect may explain the slight positive trend seen in the stepped tests.

It should be noted that stepped tests were only performed in extraction. It is unknown whether the same trends would apply to similar tests in an injection configuration.

4.5 Gas Push-Pull Tests

4.5.1 Saturation

When method for calculating saturation (S_w) was taken from the PGTT analysis and applied to the GPPTs, all three tests showed a value of S_w which was negative and very close to zero. A negative saturation is not physical, but similar results in previous research have been attributed to very dry waste in which surface sorption becomes significant (Han et al., 2006). A very low value, however, would not match the analysis of the PGTTs, previous research on the Braambergen landfill (Wang & Heimovaara, 2025b), or the fact at a meter of leachate was present at the bottom of the well.

Instead, the lack of difference between the partitioning tracer and the conservative tracer may simply be due to insufficient time being allotted for partitioning to take place. Only a few minutes took place between injection and extraction, compared to hours of travel in the PGTTs. Lab-scale column tests have shown that it may take several hours for DFM partitioning to reach equilibrium when flow rates are relatively high (Imhoff et al., 2003). While differences in the PGTT breakthrough curves of DFM and propane were apparent even from the initial moment of breakthrough, this took at least 1.6 hours and included the traversal of at least sixteen meters of waste.

This could potentially be addressed by increasing the length of the injection or the rest period to allow more time for partitioning. However, a longer injection would result in a larger radius of waste being probed and likely a lower tracer recovery, which could complicate the analysis. Increasing the rest period would result in more oxygen being consumed before extraction begins, making it more complicated to measure reaction rates. While many researchers have measured Henry's constants for DFM (Sander, 2023), none have reported on the kinetics of partitioning except for Yazdani et al. (2010). This paper reported partitioning coefficients between 0.13 and 0.34 h^{-1}, which indicates that several hours may be required for partitioning to reach equilibrium. While less practical than the existing methodology, this is still much faster than a traditional PGTT. However, this is a long enough time period that the oxygen is likely to be fully consumed before extraction begins. Thus, separate push-pull tests may be required for saturation and reaction rates.

Additionally, it is possible that saturation cannot be calculated from this test using this model. The model is based on gas chromatography and adapted to PGTTs (Han et al., 2006), which both involve linear travel through a retarding medium. The flow regime in this test is very different and can be conceptualized as spherical or cylindrical, depending on the properties of the medium. Thus, the model may need modification before it can be applied. Performing lab-scale GPPTs with real or simulated waste could be a good way of fine-tuning the methodology and model so that saturation can be calculated in future tests.

4.5.2 Reaction Rates

A much higher oxygen consumption rate was measured with a 20-minute injection than with a 15-minute injection. The physical meaning of this is obscured, however, by the fact that the central extraction system was turned on between tests, changing the ambient pressure and flow paths within the waste body. Since GPPT-15 was performed the day after GPPT-20, the waste body had more time without aeration, potentially changing the oxygen demand. This is also supported by the higher PAA. In addition to the change in background conditions, a higher volume of waste was intersected by the 20-minute injection, which may have had different reaction rates. These two effects cannot be disentangled without further testing. It is also noteworthy that less tracer was recovered in GPPT-15 than in GPPT-20. This is contrary to expectations, as the tracer should travel further from the injection well in the 20-minute injection and thus be harder to recover. This difference may indicate that the environmental conditions were significantly changed by the reactivation of the site-wide

extraction system. Since the two tests were performed at the same well, it would be expected that a similar reaction rate would be measured between the two tests in the absence of these confounding factors. Repeat testing on the same well would be helpful in determining the natural variability of the reaction rates. Factors such as weather, time of day, and the performance of the aeration infrastructure might introduce variability into the results.

While a net mass transfer of oxygen can be clearly interpreted as oxygen being consumed by aerobic respiration, the mass transfer of methane is less clear. Since no methane is injected, the method essentially analyzes how quickly the concentration returns to its background level relative to the tracer gas. This could be influenced by oxidation of methane into CO_2 and/or slowed methane production due to competition by aerobic bacteria. Methane oxidation does not seem to have a major impact on the mass transfer rate, as the ratio of CO_2 to methane was slightly lower after the tests than before. The opposite would be expected if methane was being oxidized into CO_2 at a significant scale. In fact, the production of methane in the tested volume of the waste body could be the reason for the positive methane mass transfer rate in GPPT-20. Methane is produced in the waste body, but propane is not, leading methane to return to its background values faster than propane.

In any case, the net mass transfer rate of methane was not significant for either test. This corroborates the idea that anaerobic respiration continues despite the presence of oxygen due to isolated pockets of immobile gas. The same concept has been proposed to explain limitations in waste stabilization rates (Yazdani et al., 2010), variation in landfill gas composition (Meza et al., 2022), and enhanced nitrogen transformation (Yi et al., 2023).

For the methane analysis, there are fewer points in the declining portion of the net mass transfer curve. This could be an indication that the sampling time of the LumaSense (approximately 90 seconds) was too long for the test, and crucial data was missed. The same should be kept in mind for the oxygen mass transfer rate, as the GeoTech has a response time of 20 seconds for a constant concentration of oxygen (*Geotech Biogas 5000 Datasheet*, n.d.). This may be too long for this test, as the oxygen concentration changes rather quickly.

4.6 Model Evaluation

4.6.1 Gas Permeability

The two gas permeability models gave similar results for most wells, with the values being in the same overall range as those reported on other landfills. This provides some reassurance that the calculated values can be relied upon. The Hantush method has the advantage of being easier to set up mathematically, as the Baehr and Joss method requires multiple steps of numerical solutions. However, the Hantush method also requires a log-linear fit of the transient part of the pressure response, which adds uncertainty and requires manual inspection of the transient portion of each pressure curve, which adds subjectivity. The Baehr and Joss method only requires the steady-state pressure response, which is also used in the Hantush method.

Both gas permeability models have the drawback of assuming a homogeneous porous media and geometry. This is not at all representative of the actual situation within the waste body, but is common for landfill modelling due to lack of better data (e.g. Jain et al., 2005; Singh et al., 2014; Woodman et al., 2017). However, the Baehr and Joss model does include the anisotropy of the waste body, which allows the spatially distributed gas permeability measurements to be used to estimate the anisotropy ratio. This is an important finding, as anisotropy in gas permeability has never been quantified before in a landfill context, although it has been assumed to be present. This is a distinct advantage of the Baehr and Joss model, along with the fact that it better represents the actual well geometry in an aerated landfill and is explicitly designed for gas transport.

4.6.2 Saturation

As mentioned previously, the partitioning kinetics of DFM are relatively slow (Yazdani et al., 2010). This means that if a large saturated zone lies along the path travelled by a PGTT, only the surface layer of water will be measured. This has the effect of underestimating saturation when there are large regions with high saturation (Han et al., 2007). However, the partitioning kinetics of oxygen are expected to similar to those of DFM due to their similar diffusion coefficients (Yazdani et al., 2010). Thus, the saturation measured by the PGTT is representative of the water which can be reached by the aeration system.

Similarly, the DFM can only partition into water which it can directly interact with. Therefore, the sur-

face area between the water phase and the gas phase plays a significant role in the measurement of saturation. This surface area is in turn determined by the pore size distribution and the wettability of the waste materials (Tansel, 2023). These factors are not taken into account by the saturation model (Han et al., 2006) and thus the resulting value of saturation should be viewed with this limitation in mind. Nevertheless, research has shown that the saturation calculated from PGTTs matches that measured by gravimetric methods (Han et al., 2007). This is likely dependent on the scale of the saturated zones which are encountered by the tracers and is thus potentially site-dependent.

While these uncertainties do add some complication to the evaluation of the saturation results, they are likely unavoidable due to the heterogeneity of the waste body and the lack of information on location-specific factors like pore size distribution. This saturation model is still suitable for this use case and should not be complicated further by the addition of more parameters, but its results should be interpreted with these limitations in mind.

4.6.3 Dual Domain

The issues with multiple solutions and unconstrained rate constants indicate that the dual porosity model may not be entirely suitable for this application. When developed by Yazdani et al. (2010), it was based on equations for mass transport of dissolved substances in aqueous systems (Cirpka & Kitanidis, 2000; Luo et al., 2005). In a gaseous context, trace substances are much more mobile, so diffusion and dispersion are comparatively higher than in aqueous systems. As such, the tracer can almost freely move between mobile and immobile zones, potentially resulting in the unconstrained behaviour seen in the rate constant in some well pairs. Additionally, the model as proposed assumes that there is no dispersion in the immobile zone. While not explicitly stated, this is likely justified by the assumption that immobile pores are fully isolated from each other, making mass transport impossible. In actuality, the immobile pores are likely separated from each other by water in many cases. The tracer can partition through this water phase, making dispersion possible in the immobile zone, though the dispersion coefficient is likely much lower than that in the mobile zone. If the mobile pores are conceptualized as a fracture system, they likely do contain most of the convective transport. However, lab-scale research on aqueous solute transport in waste material has shown that the less mobile zone, or matrix, still carries up to 30-45% of the leachate flow (W. Zhang & Yuan, 2019). Thus, it is possible that convective gas flow also occurs in the "immobile" zone. Both of these assumptions can be tested by simple modifications of the governing equations (Bear & Cheng, 2010), but fell outside the available time for this project. Similarly, it would be possible to test a model which includes a fully mobile zone (including advection and dispersion), a less mobile zone (including dispersion) and a fully immobile zone (only mass exchange) (Luo et al., 2005) or a stochastic model in which mass transport parameters exist on a continuum instead of in discrete categories (e.g. Brantson et al., 2018). Additionally, it was assumed in the derivation of the model that the interface between the water phase and the gas phase was located entirely in the immobile zone (Appendix A) to match the assumptions of Yazdani et al. (2010). This is another parameter which could be adjusted without switching to an entirely different model. However, one must also be careful not to over-parametrize the model. Already in the dual domain model used in this work, there was some indication that the model was over-fitted, as seen by the tendency for the model parameters to change significantly during optimization while the fit quality does not (Figure 52). This tendency may become more significant if additional phases or probabilistic behaviour are introduced.

Another aspect of the model which must be reconsidered is the assumption of one-dimensional flow. This assumption was based on the work of Yazdani et al. (2010), but it neglects the fact that the injection and extraction flow are both radial, so a constant velocity with respect to distance cannot necessarily be expected. This is also the case in the referenced paper. The works of Cirpka and Kitanidis (2000) and Luo et al. (2005) also treated the flow from the injection and extraction wells as one-dimensional instead of radial. Both of these works, however, were based on aqueous tracer transport, and the Peclet numbers found by Cirpka and Kitanidis (2000) are an order of magnitude higher than the ones found in this work. The basis for this approximation is not explained in any of these works, so it is unclear how it might apply to this use case.

It is also important to note that, while the dual domain model used in this study was not perfectly representative of the actual flow system within the waste body, neither is it entirely useless. Given the issues with the model, the values presented in Table 11 should not be taken to describe the exact situation inside the waste body, but they still seem to be indicative of trends that may be better described with alternative governing equations. This can be seen in the correlation that the dual domain parameters have with the gas round data. It should also be kept in mind that even if the model is not ideally suited to the Braambergen landfill, this does not necessarily invalidate its use at the Yolo County landfill where Yazdani et al. (2010) performed their tests.

Landfills can be extremely varied, especially when they contain different types of waste as in these cases.

In addition to the improvements in the conceptual model, significant improvements can be made to the numerical implementation of the forward model, as well as the inverse model. Numerical dispersion is caused by the numerical evaluation of the spatial derivatives in the governing equation. The central differencing scheme used in this discretization evaluates these derivatives using points from upstream and downstream of each node in order to provide a second-order accurate result. This has the unfortunate side effect of "dulling" the concentration front by means of an artificial dispersion effect which is not representative of the actual measured system and is dependent on the discretization (Versteeg & Malalasekera, 2007). Efforts were made to select a small enough time and space discretization that these effects were not significant, but it is possible that they still play a role and could be partially responsible for the differences between this model and that of Yazdani et al. (2010) in the validation step. A TVD implementation of the forward model would provide better control over numerical dispersion by the introduction of a flux limiter (Versteeg & Malalasekera, 2007).

For the inverse model, a coordinate descent method was used. This is a relatively simplistic and inefficient method, which was chosen due to difficulties encountered when setting up other methods. A more efficient algorithm such as gradient descent or a genetic algorithm would likely converge much faster, allowing more flexibility in adjusting the formulation of the forward model.

As an alternative to the numerical methods used in this work, analytical solutions exist to the governing equations as put forth by Yazdani et al. (2010). These solutions are developed using Laplace transforms and were implemented in a software called CXTFIT which is available on request from the United States Department of Agriculture (Toride et al., 1999; USDA, 2019). It has also been adapted to Excel (Tang et al., 2010), although the publicly available version is outdated and no longer runs. However, the Excel file could likely be updated by someone with knowledge of Visual Basic, or the analytical solutions could be freshly implemented in a language such as Python.

Analytical solutions have the advantage of being much faster to run, as well as eliminating the need for numerical discretization and the associated dispersion. However, they have the disadvantage of being less adaptable than numerical methods. CXTFIT, for example, provides solutions for a single porosity model, a dual porosity model of the type used in this work, and a model of parallel, non-interacting stream tubes with different velocities (Toride et al., 1999). Any further changes to the conceptual model, such as extra pore zones or stochastic mass exchange, may require the development of new Laplace transforms or even reverting to numerical methods. Nevertheless, the analytical solutions used by Yazdani et al. (2010) would have likely performed better for the purposes of this work. Efforts should be made to refit the CXTFIT methods to a modern interface so they can be used in future research.

4.6.4 Mixing Factors

For the GPPTs, there is unfortunately not enough data available to make broad conclusions about the mixing/decay model. It seems that net mass transfer rates for oxygen and methane were successfully estimated, but only a few data points were available for fitting in each test, which may significantly affect results. Additionally, interpretation of the data is difficult due to the changing background conditions and lack of spatial coverage.

4.7 Correlations Between Test Methods

In analyzing the results of the PFTs, it was found that there was essentially no correlation with any indicators of landfill aeration efficiency (LFG composition and aeration system flow characteristics). There was also very little correlation the results of the PGTTs, especially with the immobile fraction. This was an unexpected development, as it was thought that all these parameters would largely be controlled by the ability of atmospheric air to enter the waste body, which would in turn be determined by gas permeability. On the other hand, the fact that the immobile fraction and gas velocity determined by the PGTTs was correlated with LFG composition shows that there is some relationship between gas transport characteristics and landfill aeration efficiency.

To explain this, it is theorized that bulk gas flow occurs mostly or entirely in the macropores, which is in agreement with this formulation of the dual domain model (Yazdani et al., 2010), along with other related models (Bear & Cheng, 2010). This means that preferential flow pathways are exceedingly important in determining which wells see tracer breakthrough. These preferential pathways are also likely to be highly influential

in determining the flow paths of atmospheric air as it enters the waste. At the same time, tracer gases are dispersed and attenuated as they travel through the waste body, as well as being extracted from the landfill by the aeration wells which see breakthrough. This means that when a far-away well which does not see breakthrough, there are three possibilities as to the reason:

1. There is no connection to the injection well via the mobile zone.
2. Tracer gases did reach the well, but the concentration decreased too much for the LumaSense to measure before reaching the monitoring well.
3. Some tracer would have reached the well, but was intercepted by a nearer well.

The second possibility is complicated by the significant temperature fluctuations in the LumaSense data which necessitated part of the BTC being discarded. The third possibility is difficult to evaluate without further testing. One possibility would be to repeat the PGTTs, but disconnect the extraction system at the wells which have already exhibited breakthrough. In this manner, the tracer may be pulled to further-away wells without interception, allowing BTCs to be recorded at additional wells. However, there may be a risk in this case that the further-away wells do not have as much influence at the injection well, causing the injected tracer to simply remain stagnant.

In contrast, air pressure in a porous medium can propagate through both macropores and micropores (Olny & Boutin, 2003). This means that nearby wells which are blocked by low-permeability zones can still demonstrate a pressure response to a PFT. This behaviour is not explicitly accounted for in either permeability model, as they both assume a homogeneous porous medium and do not differentiate pore zones (Baehr & Hult, 1991; Kruseman et al., 2000). Furthermore, a low-permeability zone may not even be detected on a PFT, as the gas transport may be controlled by higher-permeability pathways. This can be conceptualized by analogizing the pneumatic system with an electrical system, a common method in control theory (Ogata, 2010). In this simplified analogy, shown in Figure 70, the blower is essentially a current generator and the waste acts as a resistor. A low-permeability region may be thought of as a resistor added in parallel. The pressure sensor is analogous to a voltmeter which measures the voltage between the ground (atmospheric pressure) and the resistor (waste body near the monitoring well). Under this conception, it is clear that the current will flow almost entirely through the resistor with the lower resistance if the difference is sufficiently large. Additionally, if the resistance of the two parallel resistors is added using the parallel resistors rule, the large resistance will hardly contribute. The same logic applies in the landfill context, except that gas can flow in all directions. This means that there is very likely to be a route that the gas can travel which bypasses the low-permeability zone, even if it is more circuitous.

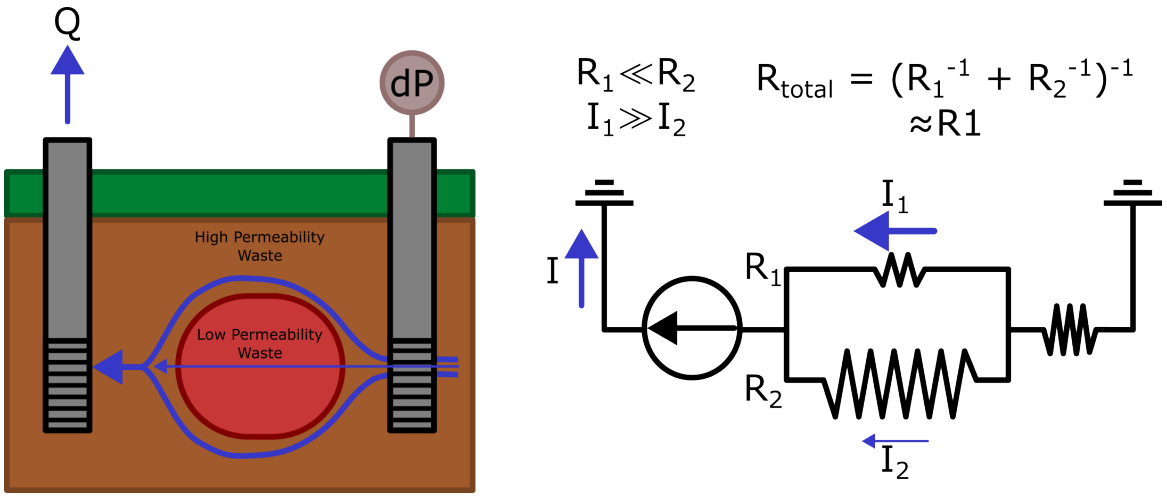

Figure 70: Circuit Analogy for PFTs

Additionally, the measurement of a pressure response at one well does not preclude its propagation. This means that pressure changes can be detected far away from the extraction/injection well without interference from closer wells. For the PGTT, tracer which is measured at one well is removed from the system and thus cannot be measured at another well. These mechanisms may explain why there seems to be little relationship between the results of the PFTs and those of the PGTTs.

The same reasons could explain why the results of the PFT do not seem to correlate with the measurements of landfill composition, while the PGTT results do. The highest-permeability sections of the waste body are measured preferentially by the PFTs, which neglects the regions which are most likely to be anaerobic. During the PGTTs, the majority of the tracer likely also bypasses these regions by flowing through preferential pathways, but it still interacts with them due to the partitioning nature of DFM. Since low gas permeability is associated with high saturation, these regions may have a large effect on the flow characteristics of the tracer gas.

Additionally, gas permeability did not seem to correlate with aeration pressure or gas velocity, nor with well depth difference. A correlation with aeration pressure and aeration speed was expected due to the understanding that these parameters would be mostly determined by the properties of the waste surrounding the well. However, it seems that factors such as the construction of the pipe network may play a significant role. The pressure is measured at the wellhead, which is connected directly to the extraction pump via a long series of pipes. Leakages in these pipes would then affect the pressure at the wellhead. This is an especially likely explanation due to the fact that significant leakages were reported at the site, requiring major maintenance in the month of May. The values of aeration pressure and flow were taken from the gas round in February, before the maintenance.

It was expected that a large difference in well depth between the extraction/injection well and the monitoring well would result in a lower measured gas permeability, since the waste is less permeable in the vertical direction. However, the opposite correlation was seen. This may be explained by the heterogeneity of the waste. As the depth difference increases, there may be a higher likelihood that the flow travels through a preferential channel, so proportionally less gas flows past the monitoring well and a smaller pressure change is detected. Since heterogeneity is not accounted for in the Baehr and Joss model, this is falsely interpreted as a higher gas permeability. An alternative explanation is that as the depth difference increases, the gas must flow along a longer vertical distance and the effect of anisotropy becomes more significant. However, the anisotropy ratio calculated in Section 3.1.2 is an average across this section of the waste body and may not be accurate for an individual well. If the anisotropy between two wells is higher than average, a lower pressure will be measured than expected, resulting in a lower value of gas permeability.

Some unexpected correlations were also seen with the PGTT results. First, it was expected that higher saturation would lead to a higher calculated immobile fraction, due to water closing off more pores and rendering them immobile. However, the opposite trend was seen. This may be because the water instead fills the pores entirely, with smaller pores being filled preferentially. This would result in a lower gas-filled porosity θ_g, but a higher mobile fraction as the smaller pores are more likely be part of the immobile zone. Additionally, it was seen that a higher saturation was correlated with a higher gas velocity. This was contrary to expectations, as it was thought that the increased moisture would hinder transport of the partitioning tracer. This may be explained by similar mechanisms, however. As more water is present, the porosity decreases and flow is forced through a smaller fraction of the pores (effectively a smaller cross-section), resulting in a higher velocity. It should be kept in mind that a higher velocity does not necessarily mean a higher mass flow rate, as the cross-section which participates in flow may also be smaller. If saturation increased further, it may be expected that the velocity would decrease as the gas-filled porosity becomes too low. Finally, wells with higher saturation had higher oxygen content and lower PAA, indicating higher aerobic activity. This was unexpected because water-saturated areas should have limited oxygen ingress and thus remain primarily anaerobic. Indeed, previous research has indicated that the limiting factor in aeration is rate at which oxygen diffuses from preferential pathways into less-mobile regions, rather than bulk oxygen supply (Gebert et al., 2023; Yazdani et al., 2010). The unexpected correlation seen here could potentially be related to short-circuiting or leaks at the wells.

4.8 Representative Elementary Volumes

Another important factor in differentiating the PFT results from the PGTT results is the volume of waste probed by each test. This also determines the scale of heterogeneity which is relevant to the results. It is worthwhile to consider the representative elementary volume (REV) for each type of test. This is a necessary simplification in the modelling of porous media due to their multiphase nature. Rather than consider all of the microscopic heterogeneities in the porous medium, we instead construct a fictitious "average" material with properties such as porosity and saturation to define its composition. For a given model, the REV is the minimum volume for which all the relevant properties (such as porosity, radial gas permeability, or mobile zone fraction) can be averaged without dependence on the size of the volume. At each point in the porous medium, a volume

of similar size can be constructed which gives a representative average of the properties near that point. Thus, these properties may still vary by location, depending on the heterogeneity of the medium. There may also be a maximum size of the REV, above which larger-scale heterogeneities become dominant (Bear & Cheng, 2010). The REV is thus dependent on the characteristics of the porous medium itself, as well as the relevant properties in the model of interest. Heterogeneities in the composition of the porous medium are smoothed out if they are smaller than the REV. This is shown for the example property of porosity in Figure 71. The REV also has a characteristic length (for example, diameter in a radial coordinate system) which represents the maximum distance at which the properties at one point are expected to be correlated with those at another (Bear & Cheng, 2010).

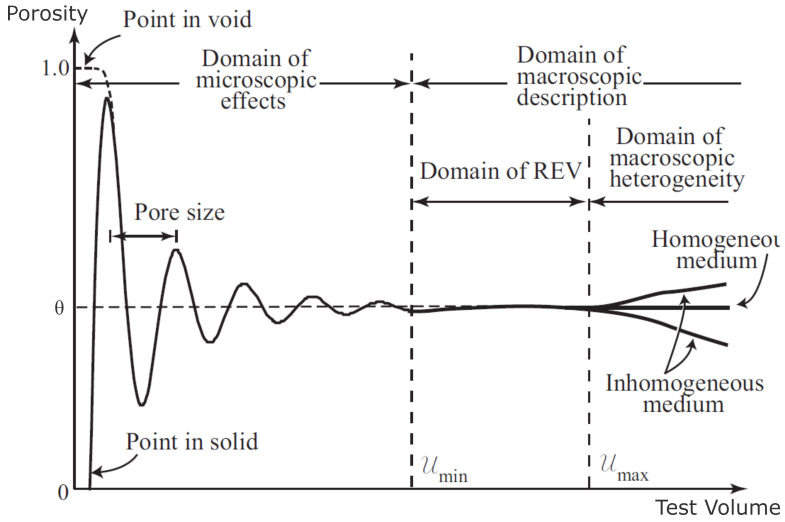

Figure 71: Porosity of a test volume, adapted from Bear and Cheng (2010)

In a PFT, a very large volume of waste is affected by the injection or extraction of air. This is evidenced by the measured pressure response up to fifty meters away, as shown in Figure 19. It is also corroborated by various numerical studies, which have shown that the radius of influence of a landfill aeration well is between 7 and 33 meters, depending on factors such as cover layer permeability and suction pressure (Ke et al., 2023; L. Liu et al., 2018; Vigneault et al., 2004). At the same time, high-density zones within another aerated Dutch landfill have been measured using seismic methods and found to be approximately 1-2 meters in length (Konstantaki et al., 2015). These high-density zones are thought to impede fluid flow (Konstantaki, 2016) and are thus analogous to the immobile zones described in this report. If it is assumed that the immobile zones at Braambergen are of similar size, it is then possible that many such zones are contained within the volume of waste measured by a PFT. While gas likely still flows around these zones as described in Section 4.7, the concentration of immobile zones in a particular part of the landfill may affect the bulk gas permeability. Smaller-scale heterogeneity, such as variations in pore size and moisture content are less relevant. If the tested volume is very large, the volumetric averages of properties like saturation are likely to change rather gradually, even if local changes may be sharp. This would then contribute to the gradual trend in gas permeability shown in Figure 27, as compared to the very local trends in gas composition (Meza et al., 2022), leachate table Gebert et al. (2022), saturation, and dual domain parameters. This could also explain the lack of correlation between gas permeability and saturation. Since the trend in permeability seems to be quite gradual, it can be said that the characteristic length of the REV is on the scale of tens of meters. This would be classified as megascopic by Bear and Cheng (2010). Macroscopic heterogeneities like the immobile zones measured by Konstantaki et al. (2015) are then averaged into the equivalent field-scale material which is represented by the permeability models.

For PGTTs, on the other hand, the aim is to characterize a particular flow path. While the dual porosity model is conceptualized as a single stream tube, there are likely a variety of stream tubes which travel from the injection well to the extraction well along slightly varying paths. The modelled stream tube is then an approximation of all of these different paths. Since the characteristics of the individual flow paths are relevant to the resulting breakthrough curves, smaller-scale heterogeneities become significant. Heterogeneity in the pore size distribution is likely to be particularly important in determining these pathways, since larger pores have lower resistance to fluid flow (W. Zhang & Yuan, 2019). Previous research on leachate flow at field scale showed that 90% of flow took place in only 47% of pores (Rosqvist & Destouni, 2000). While it has not been researched,

this trend may be even more pronounced for gas flow, since small pores are likely to be fully saturated with leachate and thus inaccessible to gas flow. Small, saturated pores can still contribute to retardation, however, as it has been shown that DFM is able to partition into water contained in pores on the micrometer scale (Han et al., 2006). While the large pores likely contribute significantly to convective flow and gas velocity, they also contain proportionally less water than smaller pores. This is significant, as the amount of water surface area which is exposed to the gas phase determines the retardation of DFM and thereby the calculation of saturation. This is incorporated into the dual domain model via the formulation of the retardation factor (Bear & Cheng, 2010). Thus, the heterogeneity in pore size distribution is likely a key factor in predicting the results of PGTTs. While uncompacted waste and settlement-induced cracking can result in pores on the centimeter scale or even larger (Tansel, 2023), inter-particle pores in landfilled waste are typically on the millimeter scale (X. Liu et al., 2020; Tansel, 2023; W. Zhang & Yuan, 2019). Additionally, the meter-scale immobile zones which are relevant for the PFTs likely cannot be measured in a PGTT, since the relatively slow kinetics of DFM partitioning mean that the DFM will likely only interact with the outermost layer of water. These factors mean that the REV for a PGTT is likely much smaller than that of the PFT. This is also supported by the sharp differences in dual domain parameters between adjacent well pairs. Since there is no correlation between these points, the characteristic dimension of the REV must be smaller than the inter-well spacing. Without being able to measure at higher spatial resolution, it is impossible to say exactly what the size of the REV is, but is likely on the macroscopic scale.

The difference in REV and relevant heterogeneities is likely a significant reason behind the lack of correlation. While PGTTs measure local properties along a single discrete flow path (or small number of flow paths), PFTs measure the bulk properties of a much larger volume of waste. The flow is then "averaged" out across the measured volume and individual pore heterogeneities are not differentiated.

Not enough GPPTs were performed to make conclusive statements about the relevant heterogeneities or REV. However, the flow rate and duration is much more similar to a PFT than a PGTT. Thus, the REV is likely relatively large.

4.9 Influence of Outlier Rejection

When eliminating well pairs with very high uncertainty in the gas permeability, it was noticed that the majority of the outliers had relatively high gas permeability. This was due to low-magnitude pressure responses which were difficult to measure with the available pressure sensors. It is possible that if these well pairs were re-tested with more suitable sensors, a valid result would be obtained. To evaluate the significance of this, the conclusions of the PFT tests were revisited without outlier rejection.

When the anisotropy calculation was revisited, a value of 85 ± 4 was obtained, which is approximately half of the value obtained previously. The gas permeability at each well was recalculated using this value of anisotropy and the analysis was repeated. With the new value of anisotropy, the average value of gas permeability decreased to $1.16(10)^{-10}$ m^2, compared to $1.37(10)^{-10}$ m^2 for an anisotropy of 166 with outliers excluded. This decrease is logical, as pressure decrease between wells is driven by both horizontal and vertical gas permeability. For a lower value of anisotropy, the vertical gas permeability is higher. The pressure drop at the monitoring well is the same and must therefore be accounted for with a lower horizontal gas permeability. The reason for the significant change in anisotropy with outlier exclusion is somewhat unclear, as outlier well pairs occurred at all depths and distances. Since the outlying well pairs primarily had high gas permeability and low-magnitude pressure response, it is possible that the pressure losses due to depth differences are more significant in these cases. A lower anisotropy ratio may be better suited when outlier well pairs are included so that the modelled pressure response is not dominated by vertical pressure losses. This could imply that vertical pressure losses are responsible for the low-magnitude pressure response in the outlying well pairs, although it may also be caused by other factors. This could be evaluated by repeating the tests with more suitable pressure sensors so that the uncertainty is reduced and these well pairs may be included. The resulting effect on anisotropy could indicate whether this trend is physical or analytical.

Other than the anisotropy, the results discussed in Section 3.1 did not change significantly when outliers were included. There was still a good correlation between the Hantush method and the Baehr and Joss method, and there was still negligible difference between the results obtained from injection and extraction. There was also no correlation with the gas round data. Finally, none of the outlier well pairs saw breakthrough during the PGTTs, so these conclusions were also unaffected.

4.10 Evaluation of Landfill Aeration

The primary goal of sustainable landfill management practices such as aeration is to accelerate the timeline of aftercare completion. As such, it is hoped that test methods such as the ones in this study can help evaluate the performance of landfill aeration. To this end, PGTTs and GPPTs have obvious applications.

The correlation with LFG composition indicates that the immobile fraction calculated by the dual porosity model is related to waste properties at small enough scale to detect features such as anaerobic pockets. This means PGTTs could be used to locate parts of the landfills where aerobic respiration is limited by immobile regions and allow operators to adjust their aftercare strategies accordingly. This could include changes reduction of leachate recirculation strategies if saturation is also found to be high, since the saturation indicated by PGTTs has been shown to match gravimetric methods (Han et al., 2007). If the saturation is not high or leachate recirculation is not in place, a short-term high-pressure aeration strategy could be used locally, as these are able to penetrate highly compacted waste (Ritzkowski & Stegmann, 2012) and could potentially break up immobile zones. Otherwise, aeration could be extended in areas with immobile zones after it is stopped in other areas of the landfill, thereby reducing operational costs. Monitoring changes in PGTT results over time could also prove useful. As the waste degrades and the landfill settles, it is possible that pores collapse (Hossain et al., 2009; Zeng et al., 2017) and the immobile fraction increases. If this is the case, aeration efficiency would decrease along with the mobile fraction. PGTTs could be used to help determine the point when aeration no longer significantly accelerates degradation.

GPPTs can be used to measure oxygen consumption in the waste body, which is critical to evaluating the progress of landfill aeration. As aeration continues, the amount of degradable organic matter in the waste body should be expected to decrease, resulting in lower oxygen demand. This is unlikely to progress uniformly across the site, however. Measuring the spatial distribution of oxygen demand could allow landfill operators to determine where to target accelerated degradation measures.

The use of PFTs in the evaluation of landfill monitoring is more complicated due to its lack of correlation with other test methods. By extension of the analogy discussed in connection with Figure 70, the method seems to primarily measure the gas permeability of the path of least resistance between two wells. This makes it difficult to use for local aeration efficiency, but overall trends in the gas permeability could be indicative of degradation progress. As waste degrades, its porosity and gas permeability tend to decrease (Hossain et al., 2009; Zeng et al., 2017). By monitoring the trend in the overall gas permeability of the site, it might be possible to evaluate trends in the degradation of the waste, especially if it is found that the rate of change in gas permeability is decreasing, for example. Other measurements, such as surface settlement and bulk gas composition, can likely provide similar information with less expense and interruption to the aeration system. Permeability is still a potentially useful metric, since it relates directly to the performance of the aeration system, but the comparative complexity and large scale of PFTs are a significant drawback.

Additionally, it has been shown that gas permeability can be correlated with porosity using well-known empirical equations (Stoltz et al., 2010; Xu et al., 2020; Zeng et al., 2017). However, these equations require calibration with samples of the specific waste being studied. Such a calibration would allow monitoring of the porosity over time in addition to the gas permeability. In combination with the data collected from PGTTs, the estimated porosity could allow estimation of the aerated fraction of the waste. This would be an extremely valuable quantity for both researchers and landfill operators. From the PGTTs, the percentage of pore space filled with gas was estimated (via S_w), and the percentage of that gas-filled porosity which can contribute to aeration was estimated (via ϕ_g^m). In order to use this to estimate the aerated volume fraction, the total amount of porosity is required, which can be obtained from physical samples. Collecting undisturbed samples from deep in the waste body may be difficult, however, as is obtaining a representative set of samples.

It is also important to note that all of the test methods used in this study rely on the aeration wells to access the gas phase of the waste body. Since the aeration wells are screened only at the bottom and there is a strong preference for horizontal gas transport, all the values measured are representative only of the bottom few meters of the waste body. This is the last part of the waste body which will be stabilized with the over-extraction method of aeration, since air enters from the top of the landfill through the cover soil (Ritzkowski & Stegmann, 2012). It is thus very likely that these test methods will under-represent the stabilization rate of the waste. On the other hand, since the bottom layers will be the last to become stable, their stabilization indicates completion of the aeration process. Thus, monitoring these layers is critical. In order to measure the same parameters in other depths of the landfill, different depths of aeration wells would be required, as used by

Jain et al. (2005) and Wu et al. (2012). This would have the added benefit of ensuring that higher layers are well aerated in case the anisotropy is so extreme that air enters the waste body primarily through the sides of the landfill instead of the top. However, it has the obvious disadvantage of increased cost and complexity.

4.11 Improvement of Test Methods

While the PFTs were mostly performed without serious issue, there was still room for improvement in future research. Given that there seemed to be some influence of flow rate during the stepped tests, it would be useful to perform future tests at lower flow rates. This may be particularly relevant at wells which exhibit lower maximum flow rates, as these wells tend to have higher pressures when the blower is set to full power, which increases the relevance of the Klinkenberg effect (Baehr & Hult, 1991; Klinkenberg, 1941). This change would have the effect of reducing the pressure change at all of the monitoring wells. In this case, pressure sensors with a smaller range should be used. This would be a useful change to make regardless, as the current sensors have a range of approximately 70 mbar, while the pressure changes at the monitoring wells were in the range of 5 mbar. Using pressure transducers with a smaller range would reduce the uncertainty in the gas permeability and potentially result in the inclusion of some of the wells that are excluded as outliers in the current analysis. Additionally, it was found that injection resulted in more stable flow rates, which also reduces the uncertainty in the gas permeability, without affecting the results. For this reason (as well as the fact that each extraction test releases several cubic meters of landfill gas to the atmosphere), injection tests would be preferred for future research.

There were also several points of improvement for future PGTTs. Most critical is the need for better climate control of the LumaSense. The system was housed in a garden box within a tent for weather protection, which resulted in significant diurnal temperature fluctuation during warm weather. This was too much for the LumaSense's temperature compensation and resulted in large amounts of data being excluded from the analysis. For future testing, a small air conditioning unit would likely make a big difference. Reducing the temperature fluctuations in this manner would likely allow monitoring of the tail to be continued for much longer. Additionally, neither of the available GC devices were able to measure DFM. However, it is possible to set up a GC to measure this gas (e.g. Shen et al., 2020). Having a confirmation of the LumaSense measurements would improve confidence in the retardation factor, saturation, and results of the dual domain model. Finally, lack of connection between the injection well and far-away monitoring wells was hard to evaluate due to the possibility that closer wells could extract tracer gases that would otherwise reach further away wells. To evaluate this, it would be useful to repeat the tests from the same wells, but with the closest wells isolated from the extraction system.

The GPPT test procedure was not as developed at the beginning of this project and, while adjustments were made during the course of this research, significant changes are still required. Most critically, a higher-frequency measurement of oxygen and methane is required in order to better capture the first few minutes of the recovery curve. The frequency of the LumaSense can be increased by reducing the flushing time and reducing the number of gases which are measured. Reducing the flushing time should not be a problem for wells that are near the LumaSense tent but may require further consideration for far-away wells. The number of gases can be reduced by using one tracer instead of two, since the measurement of saturation proved impossible with the current test design. The measurement frequency of the GeoTech can also be increased slightly by reducing the flushing time, but its response time of 20 seconds (*Geotech Biogas 5000 Datasheet*, n.d.) may become a limiting factor. It is also unclear how this response time, which is based on measurement of constant concentration, would apply to the rapidly changing concentration found during a GPPT. Therefore, an alternative to the GeoTech (such as adding an additional filter to the LumaSense) should be sought. It would also be possible to take frequent gas samples for GC analysis instead of relying upon an in-situ measurement of gas composition.

As an alternative to increasing the measurement frequency, the injection and extraction flow rate could be reduced. This would hopefully have the effect of reducing the rate of change of the gas concentrations. However, in order to maintain a safe concentration of propane, it may be necessary to use a concentration above the UEL instead of below the LEL. This would greatly extend the test duration, especially in combination with a lower bulk flow rate, as well as causing complications for the LumaSense calibration.

Additionally, a moisture trap of some sort should be integrated to prevent clogging of the GeoTech or its replacement, as the humidity of the LFG resulted in one of three tests being unusable. Finally, the long tail of the propane recovery curve indicates that a dual porosity model or something similar may represent the

flow system well. However, the model used in this work was designed for one-dimensional flow in a Cartesian reference frame, not radial flow. An alternative version of this model should be constructed to describe the flow regime in this test.

5 Conclusions and Recommendations

5.1 Research Questions

Each of the sub-components of the research question is revisited below, along with a comparison to the initial hypothesis.

1. *How well can breakthrough curves from partitioning gas tracer testing be fitted to a dual domain model?*

   In every case, the one-dimensional dual domain model was able to produce a very close match with the recorded breakthrough curve. However, there remains some uncertainty about whether this model is ideally suited to the flow regime in the landfill. This uncertainty stems from the tendency for the rate constant to increase indefinitely, meaning that the mass transfer between the mobile and immobile is not limited by first-order exchange as put forth in the model. Indeed, there may not be a distinction between mobile and immobile porosity at all. Additionally, the troughs found by the inverse model indicate that there are multiple possible combinations of parameters which provide essentially the same quality of fit. This indicates that the model may be over-fitted and a simpler model may be better suited.

   Due to this uncertainty, it is difficult to accept or reject the hypothesis that the dual domain model would be a good fit for this system. Further study is likely required in order to compare multiple potential models.

2. *How well can pressure field testing be used to characterize the gas permeability of the landfill?*

   The novel multi-well approach to pressure field testing proved to be quite reliable, as it provided relatively consistent measures of gas permeability for well pairs which were tested repeatedly. This was true in both the extraction configuration and the injection configuration. In contrast to single-well pressure field testing, this method allows for the collection of more data in one test, as well as an indication of spatial heterogeneity. The Baehr and Joss method also allowed estimation of the gas permeability anisotropy for this region of the waste body, which has not been reported before using other methods. There does seem to be some dependence on flow rate, which has been attributed to the Klinkenberg effect and well losses. This issue, along with flow instability in the extraction configuration, can be easily addressed in a future iteration of these tests by adopting an injection configuration and limiting flow rates. However, the method seems to measure a very large volume of waste, so the resulting gas permeability is largely determined by the paths of least resistance. This drawback likely cannot be resolved by adjustment of the test method.

   This result agrees with the hypothesis that the method would be well suited to determining gas permeability, with the added benefit of anisotropy estimation, which was not foreseen. However, the permeability is measured at a larger scale than was expected, which makes it difficult to compare with other data.

3. *How spatially heterogeneous are the gas transport characteristics of the landfill?*

   The results of the PGTTs are extremely heterogeneous, with very large differences between adjacent well pairs and no apparent spatial trends. For the PFTs, the heterogeneity is less pronounced, although there are some wells which exhibit much higher gas permeability than others. The PFTs do show an overall spatial trend, with higher average gas permeability in the southern section of the tested region. This is likely related to the larger scale of waste which is measured in a PFT compared to other methods.

   Based on previous testing of gas and leachate composition at Braambergen, a high degree of heterogeneity was expected throughout the landfill without much of a coherent spatial trend. In this sense, the PGTT results match the proposed hypothesis, while the PFT results do not.

4. *Do the results of partitioning gas tracer testing and pressure field testing show similar spatial trends?*

   The gas permeability as calculated by PFTs showed no clear correlations with any of the results obtained from the PGTTs. In particular, there was no correlation with the immobile fraction, which is perhaps the most important parameter measured by the PGTTs. This was attributed to the inability of the PFTs to measure low-permeability zones as long as preferential pathways are available with lower resistance. In contrast, PGTTs are influenced by low-permeability zones via the mechanism of partitioning.

This is contrary to the hypothesis, as it was expected that the PFTs would be much more significantly influenced by the low-permeability regions.

5. *Do the results of partitioning gas tracer testing and pressure field testing correlate with the measurements of landfill gas composition?*

   There was no identifiable correlation between gas permeability and landfill gas composition or other aeration characteristics measured during the gas round. This was attributed to the same tendency of PFTs to measure high-permeability zones over low-permeability zones. For the PGTTs, there was a tendency for highly anaerobic areas to have higher immobile gas fractions and lower gas velocities. This agrees with the expectation that some regions of the waste body are inaccessible to the aeration flow and thus remain anaerobic. Saturation was not correlated with these factors, which was contrary to expectations.

   Correlation with the gas composition and aeration characteristics was strongly anticipated for both sets of tests. Thus, the PGTT results agree with the hypothesis, while those from the PFTs do not.

6. *Can gas push-pull tests be used as an alternative to partitioning gas tracer tests to characterize water saturation in addition to respiration rate?*

   It was found that the difference between the DFM and propane breakthrough curves was insufficient to calculate the saturation. The timescale of a GPPT is much shorter than that of a PGTT, so it is likely that insufficient time was allotted for partitioning to become significant. However, it was possible to calculate the oxygen consumption rate and determine that the presence of oxygen had negligible effect on the methane production rate. This agrees with the notion that the waste body contains anaerobic and aerobic zones which are separate and independent. Some changes to the test method are recommended before the method is scaled up to cover a larger area, mainly regarding the measurement frequency.

   This does not agree with the hypothesis, as it was thought that the kinetics of partitioning would be fast enough to allow calculation of saturation. This difference could likely be resolved by adjustment of the test procedure.

With all of the sub-questions answered, the main research question can be addressed:

> *Can partitioning gas tracer testing, in combination with pressure field testing, be used to characterize the gas transport pathways of a sustainably managed landfill?*

While there is still work to be done on the modelling side, it seems that partitioning gas tracer testing is much more effective than pressure field testing at characterizing gas transport pathways. Based on the relationship with more fundamental landfill monitoring techniques such as gas composition, the PGTT results seem to better represent the regions of the landfill which are less accessible to the aeration system, conceptualized as low-permeability or immobile zones. PFTs are much faster and less complex than PGTTs, however, and still have a potential role in monitoring changes in the waste body over time. However, PFTs are more complicated than traditional landfill monitoring methods such as surface settlement monitoring, which can provide similar insights into stabilization rates. The ability to estimate anisotropy in gas permeability is also very useful, as this has not been reported by other means and is relevant to ensuring proper aeration of all waste layers. GPPTs can be thought of as a form of PGTT, as they also aim to characterize landfill processes by means of tracer gases. These tests may serve as a useful addition to landfill characterization, as they directly quantify respiration rates inside the waste body. This is of particular use to landfill operators as they try to plan for the end of aftercare, while also being difficult to measure by other means. Altogether, these test methods show positive indications of being useful for the characterization of gas pathways and evaluation of aeration performance, but significant further work is still needed to fine-tune models and procedures.

5.2 Limitations

One of the major limitations of this study is uncertainty around whether the chosen dual domain model was ideally suited to the PGTT analysis. With this uncertainty, it is difficult to draw conclusions about these tests or the efficiency of the landfill aeration as a whole. Additionally, there is insufficient PGTT and GPPT data available to make determinations about spatial trends and heterogeneity. Repeat tests were also not performed for the PGTTs or GPPTs due to time constraints, which limits confidence in the results.

In addition to uncertainty about the model, there were issues with the field instrument (LumaSense) that could not be fully resolved. Field testing showed that the internal compensation did not prevent high background methane concentrations from affecting the tracer measurements. A supplemental compensation curve was constructed to fix this, but lab testing showed this to be insufficient. In addition, there seemed to be significant environmental effects related to the instrument's temperature. Finally, although it seemed that the GC measurements agreed with the LumaSense measurements while the LumaSense was installed, the GC measurements which were taken after the LumaSense was removed did not agree with the extrapolated curve. The GC measurements seemed to stop following the log-linear curve that was present in the beginning, and the reason why is not clear. These factors cast doubt upon all of the calculations which stem from the LumaSense data.

In addition, there are differences between the assumptions made in the model formulation and the actual flow regime in the waste body. Perhaps the most critical difference is the assumption of homogeneous properties in the waste body. It is known that factors such as porosity and saturation vary widely throughout the waste body, which affects the gas transport equations significantly. However, actual data on the spatial variation of these parameters are unavailable or insufficient to allow inclusion in the modelling. Even if it this data were available, their inclusion would necessitate a hugely complicated numerical model which would be impractical. One of the significant parameters which was assumed to be constant is temperature. In addition to affecting pressure distribution (Baehr & Hult, 1991; Hantush, 1956) and thereby flow distribution, it also has a strong effect on the Henry constant (Han et al., 2007; Kutsuna, 2017). Variations in the temperature could thereby significantly affect the results of the PGTTs and GPPTs. It is known that the temperature in the tested landfill cell varies from around 20°C to over 60°C, with very little spatial correlation. This is enough to make a significant difference in the Henry constant, which is not accounted for in the dual porosity or saturation models. Also, the characteristics of the cover layer were assumed to be constant as specified in the Baehr and Joss model (Baehr & Hult, 1991). However, it is known from the previous installation of leachate infiltration ditches that the distribution of carbonated incinerator ash is not uniform. Initial testing showed that the assumed cover layer is very important in the gas permeability calculations, meaning that this assumption could have a major impact on the conclusions of this research. Similarly, both gas permeability models assume the geometry of the landfill to be both uniform and infinite. In actuality, the thickness of the unsaturated zone is not uniform due to uneven settlement and a leachate table which is highly variable (Gebert et al., 2022) The landfill is also far from infinite, and many of the tests were performed relatively close to the edges due to the location of the power supply and the installation of the necessary valves.

Another important limitation is the fact that tests were performed over a four-month period. Over this time frame, significant seasonal changes occurred which could greatly affect gas transport within the waste body. Additionally, there were periods of maintenance in which the extraction system was disabled, which could allow transport pathways to shift. Some natural changes in transport pathways could also be expected due to the continued degradation of the landfill contents and settlement of the waste body. As discussed in Section 4.3, changes in PFT connectivity were already noticed over a six-week time frame. For these reasons, some changes in the measured parameters could be expected between the start and end of the test period, which is not quantitatively accounted for in the analysis.

Additionally, there was very little data available with which to compare the results of these tests, as all three types of tests are quite novel in a landfill context. This makes it more difficult to evaluate the reliability of the results. Hopefully, future research will be conducted on similar landfills which will allow the results of this study to be better contextualized.

5.3 Recommendations for Future Work

For future research, it would be worthwhile to investigate how repeatable the PGTTs are and how much the measured gas transport pathways change over time. Duplicate tests were not performed at either injection well during this test due to time constraints and maintenance periods. Dipole PGTTs, in which gas is injected into one well at a high flow rate and simultaneously extracted from another at the same rate, could also be a useful method for measuring the same parameters. Preliminary tests showed that these tests are somewhat faster than traditional PGTTs (although still require several days to a week), which could speed up the testing of large areas of the landfill. Further tests were not performed during the course of this thesis due to equipment availability, which made it impossible to leave the dipole tests running overnight. More thorough testing should be performed to determine whether the results obtained from dipole tests match those from regular PGTTs.

Additionally, some investigation should be undertaken to determine the best model to describe the BTCs obtained from the PGTTs. This should include attempts to apply the analytical solutions used by Yazdani et al. (2010), as well as an evaluation of different conceptual models. It would be especially valuable to consider adapting transport models for gas transport, as the one used in this work were developed for a groundwater context (Toride et al., 1999).

It would also be beneficial to take some physical samples from the waste body. This would allow for measurement of the porosity to replace the assumed value used in the dual domain model. It would also allow the saturation to be measured gravimetrically for comparison with the values obtained from the breakthrough curves. Of course, taking representative samples of landfills is challenging (Han et al., 2007), especially for tests such as these which involve large volumes of waste. Still, a sufficiently large number of physical samples could provide some insight into the degree of variability of these properties. Additionally, lab-scale PGTTs and GPPTs could be performed to help fine-tune and interpret the field-scale tests. Even relatively large-scale lab tests tend to significantly under-represent the influence of preferential flow (Wu et al., 2012), which means that the results of lab-scale tests should not be expected to directly correspond with those from field tests. However, the methodological improvements would likely still prove valuable.

Next, several assumptions were made during the modelling of the PFTs which should be tested. The first is that measuring the pressure at the wellhead provides a good measure at the pressure at the bottom of the well. This was justified by the fact that the extraction system was disabled and there was no flow in the pipe. This could be tested by installing a second pressure sensor at the bottom of the well (above the leachate), perhaps on a long string as was done with the CTD-Diver. Repeat tests with the CTD-Diver as discussed in Section 4.2 could also provide insight into the behaviour of the well-waste interface. Similarly, the depth at which the well interacts with the waste was assumed based on the depth of the leachate and the bottom of the well, as well as whether or not the well was collapsed. However, it is also possible that the wells were open to the waste at lesser depths due to damage to the HDPE pipes. This could be tested by inserting a borescope to record images of the inside of the pipes.

Finally, better area coverage should be a major goal for future research. PGTTs were performed on only two wells. Successful PFTs were performed on seven wells, but all extraction/injection wells and all monitoring wells were in the same region of the landfill due to the location of the power supply and the presence of the necessary valves at the wellhead. This area was picked as it had a higher aerobic fraction and a higher gas extraction rate (Meza et al., 2022), but it would be interesting to see how these methods perform in less favourable areas of the waste body. In particular, the GPPTs were performed on only one well. It would be very valuable to extend this method to other wells and see whether the results correlate with the results of these tests and/or background gas composition.

References

Adani, F., Confalonieri, R., & Tambone, F. (2004). Dynamic Respiration Index as a Descriptor of the Biological Stability of Organic Wastes. *Journal of Environmental Quality*, *33*(5), 1866–1876. doi: 10.2134/jeq2004.1866

Agilent Technologies. (2017). *Agilent 490 Micro GC Solution Data Sheet.* Agilent Technologies, Inc. Retrieved 2025-08-13, from https://www.agilent.com/cs/library/datasheets/public/5991-6034EN.pdf

Agilent Technologies. (2021). *Agilent 8860 Gas Chromatograph System.* Agilent Technologies, Inc. Retrieved 2025-08-13, from https://www.agilent.com/cs/library/datasheets/public/datasheet-8860-gas-chromatograph-5994-0453en-agilent.pdf

Aracil, C., Haro, P., Fuentes-Cano, D., & Gómez-Barea, A. (2018). Implementation of waste-to-energy options in landfill-dominated countries: Economic evaluation and GHG impact. *Waste Management*, *76*, 443–456. doi: 10.1016/j.wasman.2018.03.039

Azizian, M. F., Istok, J. D., & Semprini, L. (2007). Evaluation of the *in-situ* aerobic cometabolism of chlorinated ethenes by toluene-utilizing microorganisms using push–pull tests. *Journal of Contaminant Hydrology*, *90*(1), 105–124. doi: 10.1016/j.jconhyd.2006.09.015

Baehr, A. L., & Hult, M. F. (1991). Evaluation of Unsaturated Zone Air Permeability Through Pneumatic Tests. *Water Resources Research*, *27*(10), 2605–2617. doi: 10.1029/91WR01655

Baehr, A. L., & Joss, C. J. (1995). An Updated Model of Induced Airflow in the Unsaturated Zone. *Water Resources Research*, *31*(2), 417–421. doi: 10.1029/94WR02423

Barlaz, M. A., Ham, R. K., Schaefer, D. M., & Isaacson, R. (1990). Methane production from municipal refuse: A review of enhancement techniques and microbial dynamics. *Critical Reviews in Environmental Control*, *19*(6), 557–584. doi: 10.1080/10643389009388384

Bear, J., & Cheng, A. H.-D. (2010). Modeling Contaminant Transport. In *Modeling Groundwater Flow and Contaminant Transport* (1st ed.). Dordrecht, Germany: Springer Science and Media B.V.

Beaven, R., White, J., Woodman, N., Rees-White, T., Smethurst, J., Stringfellow, A., ... Kanen, T. (2024). Causes of High Internal Pore Pressure in a Downward-Draining MSW Landfill. *Journal of Geotechnical and Geoenvironmental Engineering*, *150*(3), 04023143. doi: 10.1061/JGGEFK.GTENG-11520

Berge, N., Reinhart, D., & Hudgins, M. (2007). The Status of Aerobic Landfills in the United States. In *Landfill Aeration.* CISA. Retrieved 2025-06-24, from https://net0air.org/PDFs/AM0083%20Validation/The%20Status%20of%20Aerobic%20Landfills%20UCF-%20Hudgins[1].pdf

Brand, E., de Nijs, T. C. M., Dijkstra, J. J., & Comans, R. N. J. (2016). A novel approach in calculating site-specific aftercare completion criteria for landfills in The Netherlands: Policy developments. *Waste Management*, *56*, 255–261. doi: 10.1016/j.wasman.2016.07.038

Brantson, E. T., Ju, B., Wu, D., & Gyan, P. S. (2018). Stochastic porous media modeling and high-resolution schemes for numerical simulation of subsurface immiscible fluid flow transport. *Acta Geophysica*, *66*(3), 243–266. doi: 10.1007/s11600-018-0132-3

Cirpka, O. A., & Kitanidis, P. K. (2000). An advective-dispersive stream tube approach for the transfer of conservative-tracer data to reactive transport. *Water Resources Research*, *36*(5), 1209–1220. doi: 10.1029/1999WR900355

Delgado, J. M. P. Q. (2006). A critical review of dispersion in packed beds. *Heat and Mass Transfer*, *42*(4), 279–310. doi: 10.1007/s00231-005-0019-0

Duarte Campos, L., Rees-White, T., Beaven, R., Cruz, C., Lammen, H., & Gebert, J. (2023). Pressure field tests to infer permeability of waste bodies under in situ aeration. In *Sardinia 2023.* Cagliari, Italy: CISA Publisher. Retrieved 2024-12-10, from https://pure.tudelft.nl/ws/portalfiles/portal/163389512/2372_Duarte_Campos.pdf

Eberly College of Science - Department of Statistics. (2024). Simple Linear Regression. In *STAT 415: Introduction to Mathematical Statistics.* Pennsylvania State University. Retrieved 2025-05-23, from https://online.stat.psu.edu/stat415/lesson/7

European Commission. (2024). *Council Directive 1999/31/EC of 26 April 1999 on the Landfill of Waste.* Retrieved 2025-01-19, from http://data.europa.eu/eli/dir/1999/31/2024-08-04/eng

European Environment Agency. (2022). *Methane emissions in the EU: The key to immediate action on climate change* (Briefing No. 21/2022). European Environment Agency. Retrieved 2025-06-23, from https://www.eea.europa.eu/publications/methane-emissions-in-the-eu/methane-emissions-in-the-eu

European Environment Agency. (2025). *Greenhouse gas emissions inventory.* Retrieved 2025-06-23, from https://climate-energy.eea.europa.eu/topics/climate-change-mitigation/greenhouse-gas-emissions-inventory/data

Evans, P. (2015). *Properties of air at atmospheric pressure.* The Engineering Mindset. Retrieved 2025-04-10, from https://theengineeringmindset.com/properties-of-air-at-atmospheric-pressure/

Fei, S., Xie, H., Cai, P., Xu, W., & Li, H. (2024). Investigation of preferential flow and leakage location in landfill: A field tracer test and numerical analysis. *Waste Management*, *190*, 600–612. doi: 10.1016/j.wasman.2024.10.021

Fricke, K., Santen, H., & Wallmann, R. (2005). Comparison of selected aerobic and anaerobic procedures for MSW treatment. *Waste Management*, *25*(8), 799–810. doi: 10.1016/j.wasman.2004.12.018

Gebert, J., de Jong, T., Ramos, P. N. M., Tristan, R.-W., Beaven, R. P., & Lammen, H. (2022). Spatial variability of leachate tables, leachate composition and hydraulic conductivity in a landfill stabilized by in situ aeration. *Detritus*(19), 114. doi: 10.31025/2611-4135/2022.15189

Gebert, J., Meza, N., Cruz Osorio, C., & Lammen, H. (2023). Assessing the efficiency of landfill aeration with a carbon mass balance approach: 19th International Symposium on Waste Management, Resource Recovery and Sustainable Landfilling. In *Sardinia 2023*. Cagliari, Italy: CISA Publisher.

Geotech Biogas 5000 Datasheet. (n.d.). Hatech Gasdetectietechniek, Geotech. Retrieved 2025-02-18, from `https://www.hatechgas.com/wp-content/uploads/2016/05/Geotech-Biogas5000-Datasheet.pdf`

Gómez, K. E., Gonzalez-Gil, G., Lazzaro, A., & Schroth, M. H. (2009). Quantifying methane oxidation in a landfill-cover soil by gas push–pull tests. *Waste Management*, *29*(9), 2518–2526. doi: 10.1016/j.wasman.2009.05.011

Google Earth. (2025). *Satellite Map of the Netherlands.* Retrieved 2025-05-30, from `https://www.google.com/earth/about/versions/`

Green Deal Duurzaam Stortbeheer. (2015). Rijksdienst voor Ondernemend Nederland. Retrieved 2025-02-19, from `https://www.duurzaamstortbeheer.nl/wp-content/uploads/2023/09/Green-Deal-Duurzaam-Stortbeheer-C186-ondertekend-door-deelnemers.pdf` (Green Deal C-186)

Han, B., Imhoff, P. T., & Yazdani, R. (2007). Field Application of Partitioning Gas Tracer Test for Measuring Water in a Bioreactor Landfill. *Environmental Science & Technology*, *41*(1), 277–283. doi: 10.1021/es061233e

Han, B., Jafarpour, B., Gallagher, V. N., Imhoff, P. T., Chiu, P. C., & Fluman, D. A. (2006). Measuring seasonal variations of moisture in a landfill with the partitioning gas tracer test. *Waste Management*, *26*(4), 344–355. doi: 10.1016/j.wasman.2005.11.004

Hantush, M. S. (1956). Analysis of data from pumping tests in leaky aquifers. *Eos, Transactions American Geophysical Union*, *37*(6), 702–714. doi: 10.1029/TR037i006p00702

Hantush, M. S., & Jacob, C. E. (1955). Non-steady radial flow in an infinite leaky aquifer. *Eos, Transactions American Geophysical Union*, *36*(1), 95–100. doi: 10.1029/TR036i001p00095

Harren, F. J., & Cristescu, S. M. (2019). Photoacoustic Spectroscopy in Trace Gas Monitoring. In *Encyclopedia of Analytical Chemistry* (pp. 1–29). John Wiley & Sons, Ltd. doi: 10.1002/9780470027318.a0718.pub3

Heyer, K. U., Hupe, K., Ritzkowski, M., & Stegmann, R. (2005). Pollutant release and pollutant reduction – Impact of the aeration of landfills. *Waste Management*, *25*(4), 353–359. doi: 10.1016/j.wasman.2005.02.007

Honeywell. (2024). *TruStability Board Mount PRessure Sensors: HSC Series Data Sheet.* Honeywell International Inc. Retrieved 2025-08-13, from `https://prod-edam.honeywell.com/content/dam/honeywell-edam/sps/siot/en-gb/products/sensors/pressure-sensors/board-mount-pressure-sensors/trustability-hsc-series/documents/sps-siot-trustability-hsc-series-high-accuracy-board-mount-pressure-sensors-50099148-a-en-ciid-151133.pdf?download=false`

Hossain, M. S., Penmethsa, K. K., & Hoyos, L. (2009). Permeability of Municipal Solid Waste in Bioreactor Landfill with Degradation. *Geotechnical and Geological Engineering*, *27*(1), 43–51. doi: 10.1007/s10706-008-9210-7

Hrad, M., & Huber-Humer, M. (2017). Performance and completion assessment of an in-situ aerated municipal solid waste landfill – Final scientific documentation of an Austrian case study. *Waste Management*, *63*, 397–409. doi: 10.1016/j.wasman.2016.07.043

Hu, J., Ke, H., Chen, Y. M., Xu, X. B., & Xu, H. (2021). Analytical analysis of the leachate flow to a horizontal well in dual-porosity media. *Computers and Geotechnics*, *134*, 104105. doi: 10.1016/j.compgeo.2021.104105

Imhoff, P. T., Jakubowitch, A., Briening, M. L., & Chiu, P. C. (2003). Partitioning Gas Tracer Tests for Measurement of Water in Municipal Solid Waste. *Journal of the Air & Waste Management Association*, *53*(11), 1391–1400. doi: 10.1080/10473289.2003.10466306

Innova 1512 Datasheet. (2020). Lauper Instruments, Advanced Energy. Retrieved 2025-02-24, from `https://www.lauper-instruments.ch/fileadmin/pdf/Lumasense/1512_EN_Rev01.9.20.pdf`

Istok, J. D., Humphrey, M. D., Schroth, M. H., Hyman, M. R., & O'Reilly, K. T. (1997). Single-Well, "Push-Pull" Test for In Situ Determination of Microbial Activities. *Groundwater*, *35*(4), 619–631. doi: 10.1111/j.1745-6584.1997.tb00127.x

Jain, P., Powell, J., Townsend, T. G., & Reinhart, D. R. (2005). Air Permeability of Waste in a Municipal Solid Waste Landfill. *Journal of Environmental Engineering*, *131*(11), 1565–1573. doi: 10.1061/(ASCE)0733-9372(2005)131:11(1565)

Jucá, J. F. T., & Maciel, F. J. (2012). Gas Permeability of a Compacted Soil Used in a Landfill Cover Layer. In *Proceedings of the Fourth International Conference on Unsaturated Soils* (pp. 1535–1546). Carefree, AZ, USA: American Society of Civil Engineers. doi: 10.1061/40802(189)128

Jung, Y., Han, B., Mostafid, M. E., Chiu, P., Yazdani, R., & Imhoff, P. T. (2012). Photoacoustic infrared spectroscopy for conducting gas tracer tests and measuring water saturations in landfills. *Waste Management*, *32*(2), 297–304. doi: 10.1016/j.wasman.2011.09.016

Kallel, A., Tanaka, N., & Matsuto, T. (2004). Gas Permeability and Tortuosity for Packed Layers of Processed Municipal Solid Wastes and Incinerator Residue. *Waste Management & Research*, *22*(3), 186–194. doi: 10.1177/0734242X04044880

Kattenberg, W. J., van der Sloot, H. A., & Heimovaara, T. J. (2013). New Dutch legislation to allow research of natural biodegradation at landfills. In *Proceedings Sardinia 2013.* Cagliari, Italy: CISA Publisher.

Ke, H., Liu, Y., Hu, J., Qin, R., Xu, X. B., & Chen, Y. M. (2022). Experimental study on anisotropy of hydraulic conductivity for municipal solid waste. *Waste Management*, *137*, 39–49. doi: 10.1016/j.wasman.2021.10.030

Ke, H., Zhang, C. S., Zhang, M. L., Xu, X., Liang, X., Xiao, D. K., ... Hu, J. (2023). Air Injection Tests via Single Wells and Multiple Wells in a Municipal Solid Waste Landfill. *Journal of Geotechnical and Geoenvironmental Engineering*, *149*(11), 04023099. doi: 10.1061/JGGEFK.GTENG-11555

Klinkenberg, L. J. (1941). The permeabiulity of porous media to liquids and gases. In *Drilling and Productions Practices* (pp. 200–213). American Petroleum Institute.

KNMI. (2025). *Daggegevens van het Weer - Nederland - Lelystad Airport* [Weather Data]. Retrieved 2025-06-26, from `https://www.knmi.nl/nederland-nu/klimatologie/daggegevens`

Konstantaki, L. A. (2016). *Imaging and characterization of heterogeneous landfills using geophysical methods* (Doctoral dissertation, TU Delft, Delft, NL). Retrieved 2025-08-25, from `https://repository.tudelft.nl/record/uuid:f1034020-f996-458e-a614-85735dd03bf9`

Konstantaki, L. A., Ghose, R., Draganov, D., Diaferia, G., & Heimovaara, T. (2015). Characterization of a heterogeneous landfill using seismic and electrical resistivity data. *GEOPHYSICS*, *80*(1), EN13-EN25. doi: 10.1190/geo2014-0263.1

Kruseman, G., de Ridder, N., & Verweij, J. (2000). Leaky aquifers. In *Analysis and Evaluation of Pumping Test Data* (2nd ed.). Wageningen, The Netherlands: International Insititute for Land Reclamation and Improvement (ILRI).

Kumar, P., Caldow, C., Broquet, G., Shah, A., Laurent, O., Yver-Kwok, C., ... Ciais, P. (2024). Detection and long-term quantification of methane emissions from an active landfill. *Atmospheric Measurement Techniques*, *17*(4), 1229–1250. doi: 10.5194/amt-17-1229-2024

Kutsuna, S. (2017). Experimental determination of Henry's law contants of difluoromethane (HFC-32) and the salting-out effects in aqueous salt solutions relevant to seawater. *Atmospheric Chemistry and Physics*, *17*, 7495–7507. doi: 10.5194/acp-17-7495-2017,2017

Lee, N.-H., Park, J.-K., Kang, J.-Y., & Kang, J.-H. (2016). Method to estimate the required oxygen amount and aeration period for the completion of landfill aeration. *Journal of Material Cycles and Waste Management*, *18*(4), 695–702. doi: 10.1007/s10163-015-0370-2

Lieten, S. H. (2018). *Landfill Management in the Netherlands.* Witteveen and Bos, Interreg Europe, and European Regional Development Fund. Retrieved 2025-06-22, from `https://projects2014-2020.interregeurope.eu/fileadmin/user_upload/tx_tevprojects/library/file_1531246928.pdf`

Liu, J.-F., Skoczylas, F., & Liu, J. (2014). Experimental research on water retention and gas permeability of compacted bentonite/sand mixtures. *Soils and Foundations*, *54*(5), 1027–1038. doi: 10.1016/j.sandf.2014.09.011

Liu, L., Ma, J., Xue, Q., Wan, Y., & Yu, X. (2018). Modeling the oxygen transport process under preferential flow effect in landfill. *Environmental Science and Pollution Research*, *25*(19), 18559–18569. doi: 10.1007/s11356-018-2053-8

Liu, X., Zhang, L., Wu, S., Shao, Y., Wu, X., & Li, Z. (2020). Changes in municipal solid waste pore structure during degradation: Analysis of synthetic waste using X-ray computed microtomography. *Science of The Total Environment*, *708*, 135089. doi: 10.1016/j.scitotenv.2019.135089

Luo, J., Cirpka, O. A., Wu, W., Fienen, M. N., Jardine, P. M., Mehlhorn, T. L., ... Kitanidis, P. K. (2005). Mass-Transfer Limitations for Nitrate Removal in a Uranium-Contaminated Aquifer. *Environmental Science & Technology*, *39*(21), 8453–8459. doi: 10.1021/es050195g

Ma, J., Chen, Z., Li, J., Liu, L., Yang, Q., Wan, Y., ... Fei, X. (2025). Concurrent aerobic methane oxidation and

biodegradation of waste in shallow layer of landfill during aeration. *Journal of Environmental Management*, *381*, 125282. doi: 10.1016/j.jenvman.2025.125282

Ma, J., Li, Y., & Li, Y. (2021). Effects of leachate recirculation quantity and aeration on leachate quality and municipal solid waste stabilization in semi-aerobic landfills. *Environmental Technology & Innovation*, *21*, 101353. doi: 10.1016/j.eti.2021.101353

Meza, N., Lammen, H., Cruz, C., Heimovaara, T., & Gebert, J. (2022). Spatial Variability of Gas Composition and Flow in a Landfill Under In-Situ Aeration. *Detritus*(19), 104. doi: 10.31025/2611-4135/2022.15191

Moon, S., Nam, K., Kim, J. Y., Hwan, S. K., & Chung, M. (2008). Effectiveness of compacted soil liner as a gas barrier layer in the landfill final cover system. *Waste Management*, *28*(10), 1909–1914. doi: 10.1016/j.wasman.2007.08.021

Nanda, S., & Berruti, F. (2021). Municipal solid waste management and landfilling technologies: A review. *Environmental Chemistry Letters*, *19*(2), 1433–1456. doi: 10.1007/s10311-020-01100-y

Ni, J., Zhou, J., Wang, Y., & Guo, H. (2023). Gas permeability and emission in unsaturated vegetated landfill cover with biochar addition. *Biochar*, *5*(47). doi: 10.1007/s42773-023-00246-6

NOAA. (n.d.). *Propane.* National Oceanic and Atmospheric Administration - Cameo Chemicals. Retrieved 2025-04-28, from `https://cameochemicals.noaa.gov/report?key=CH9018`

Obradović, N., Joshi, P., Arn, S., Aeppli, M., Schroth, M. H., & Sander, M. (2023). Reoxidation of Reduced Peat Organic Matter by Dissolved Oxygen: Combined Laboratory Column-Breakthrough Experiments and In-Field Push-Pull Tests. *Journal of Geophysical Research: Biogeosciences*, *128*(11), e2023JG007640. doi: 10.1029/2023JG007640

Ogata, K. (2010). Mathematical Modeling of Fluid Systems and Thermal Systems. In *Modern Control Engineering* (5th ed., pp. 100–158). Upper Saddle Hill, NJ, USA: Pearson Education.

Olny, X., & Boutin, C. (2003). Acoustic wave propagation in double porosity media. *The Journal of the Acoustical Society of America*, *114*(1), 73–89. doi: 10.1121/1.1534607

Philip, L., Shimell, H., Hewitt, P., & Ellard, H. (2002). A field-based test cell examining clay desiccation in landfill liners. *Quarterly Journal of Engineering Geology and Hydrogeology*, *35*(4), 345–354. doi: 10.1144/1470-9236/2001-37

Powrie, W., & Beaven, R. P. (1999). Hydraulic properties of household waste and implications for landfills. *Proceedings of the Institution of Civil Engineers - Geotechnical Engineering*, *137*(4), 235–237. doi: 10.1680/gt.1999.370409

Rachor, I. M., Gebert, J., Gröngröft, A., & Pfeiffer, E.-M. (2013). Variability of methane emissions from an old landfill over different time-scales. *European Journal of Soil Science*, *64*(1), 16–26. doi: 10.1111/ejss.12004

Raga, R., & Cossu, R. (2014). Landfill aeration in the framework of a reclamation project in Northern Italy. *Waste Management*, *34*(3), 683–691. doi: 10.1016/j.wasman.2013.12.011

Read, A. D., Hudgins, M., Harper, S., Phillips, P., & Morris, J. (2001). The successful demonstration of aerobic landfilling: The potential for a more sustainable solid waste management approach? *Resources, Conservation and Recycling*, *32*(2), 115–146. doi: 10.1016/S0921-3449(01)00053-2

Rich, C., Gronow, J., & Voulvoulis, N. (2008). The potential for aeration of MSW landfills to accelerate completion. *Waste Management*, *28*(6), 1039–1048. doi: 10.1016/j.wasman.2007.03.022

Ritzkowski, M., & Stegmann, R. (2012). Landfill aeration worldwide: Concepts, indications and findings. *Waste Management*, *32*(7), 1411–1419. doi: 10.1016/j.wasman.2012.02.020

Rosqvist, H., & Destouni, G. (2000). Solute transport through preferential pathways in municipal solid waste. *Journal of Contaminant Hydrology*, *46*(1), 39–60. doi: 10.1016/S0169-7722(00)00127-3

Rowe, R. K. (2005). Long-term performance of contaminant barrier systems. *Géotechnique*, *55*(9), 631–678. doi: 10.1680/geot.2005.55.9.631

Šan, I., & Onay, T. T. (2001). Impact of various leachate recirculation regimes on municipal solid waste degradation. *Journal of Hazardous Materials*, *87*(1), 259–271. doi: 10.1016/S0304-3894(01)00290-4

Sander, R. (2023). Compilation of Henry's law constants (version 5.0.0) for water as solvent. *Atmospheric Chemistry and Physics*, *23*, 10901–12440. doi: 10.5194/acp-23-10901-2023

Scharff, H. (2010). Landfill Closure, Aftercare and Final Use. In *Solid Waste Technology & Management* (pp. 932–947). John Wiley & Sons, Ltd. doi: 10.1002/9780470666883.ch57

Scharff, H. (2014). Landfill reduction experience in The Netherlands. *Waste Management*, *34*(11), 2218–2224. doi: 10.1016/j.wasman.2014.05.019

Scharff, H., van Zomeren, A., & van der Sloot, H. A. (2011). Landfill sustainability and aftercare completion criteria. *Waste Management & Research*, *29*(1), 30–40. doi: 10.1177/0734242X10384310

Shen, T., Ge, X., Zhao, H., Xu, Z., Tong, S., Zhou, S., ... Chen, X. (2020). A safe and efficient process for the preparation of difluoromethane in continuous flow. *Chinese Journal of Chemical Engineering*, *28*(7), 1860–1865. doi: 10.1016/j.cjche.2020.02.024

Singh, K., Kadambala, R., Jain, P., Xu, Q., & Townsend, T. G. (2014). Anisotropy estimation of compacted municipal solid waste using pressurized vertical well liquids injection. *Waste Management & Research*, *32*(6), 482–491. doi: 10.1177/0734242X14532003

Sohoo, I., Ritzkowski, M., & Kuchta, K. (2021). Influence of moisture content and leachate recirculation on oxygen consumption and waste stabilization in post aeration phase of landfill operation. *Science of The Total Environment*, *773*, 145584. doi: 10.1016/j.scitotenv.2021.145584

Stern, J. C., Chanton, J., Abichou, T., Powelson, D., Yuan, L., Escoriza, S., & Bogner, J. (2007). Use of a biologically active cover to reduce landfill methane emissions and enhance methane oxidation. *Waste Management*, *27*(9), 1248–1258. doi: 10.1016/j.wasman.2006.07.018

Stoltz, G., Gourc, J.-P., & Oxarango, L. (2010). Liquid and gas permeabilities of unsaturated municipal solid waste under compression. *Journal of Contaminant Hydrology*, *118*(1), 27–42. doi: 10.1016/j.jconhyd.2010.07.008

Stortbesluit bodembescherming. (2016). Retrieved 2025-01-19, from `https://wetten.overheid.nl/BWBR0005858/2016-07-01` (BWBR0005858)

Streese-Kleeberg, J., Rachor, I., Gebert, J., & Stegmann, R. (2011). Use of gas push–pull tests for the measurement of methane oxidation in different landfill cover soils. *Waste Management*, *31*(5), 995–1001. doi: 10.1016/j.wasman.2010.08.026

Tang, G., Mayes, M. A., Parker, J. C., & Jardine, P. M. (2010). CXTFIT/Excel–A modular adaptable code for parameter estimation, sensitivity analysis and uncertainty analysis for laboratory or field tracer experiments. *Computers & Geosciences*, *36*(9), 1200–1209. doi: 10.1016/j.cageo.2010.01.013

Tansel, B. (2023). Classification of pores, water diffusivity and penetration characteristics of waste materials, and role of water as electron carrier in landfills: A review. *Journal of Environmental Management*, *340*, 118028. doi: 10.1016/j.jenvman.2023.118028

Toride, N., Leij, F. J., & van Genuchten, M. Th. (1999). *The CXTFIT Code for Estimating Transport Parameters from Laboratory or Field Tracer Experiments* (Research Report No. 137). Riverside, California, USA: U.S. Department of Agriculture.

Turner, D. A., Beaven, R. P., & Woodman, N. D. (2017). Evaluating landfill aftercare strategies: A life cycle assessment approach. *Waste Management*, *63*, 417–431. doi: 10.1016/j.wasman.2016.12.005

Urmann, K., Gonzalez-Gil, G., Schroth, M. H., Hofer, M., & Zeyer, J. (2005). New Field Method: Gas Push-Pull Test for the In-Situ Quantification of Microbial Activities in the Vadose Zone. *Environmental Science & Technology*, *39*(1), 304–310. doi: 10.1021/es0495720

USDA. (2019). *CXTFIT Model : USDA ARS.* https://www.ars.usda.gov/pacific-west-area/riverside-ca/agricultural-water-efficiency-and-salinity-research-unit/docs/model/cxtfit-model/.

van Meeteren, M., Timens, D., Heyer, K. U., & van Vossen, W. (2009). *Feasibility study sustainable emission reduction at the existing landfills Kragge and Wieringermeer in the Netherlands. Specific report: Current status of landfill Wieringermeer.* Royal Haskoning Nederland B.V.

Vandenbohede, A., Louwyck, A., & Lebbe, L. (2008). Identification and reliability of microbial aerobic respiration and denitrification kinetics using a single-well push–pull field test. *Journal of Contaminant Hydrology*, *95*(1), 42–56. doi: 10.1016/j.jconhyd.2007.07.003

Versteeg, H. K., & Malalasekera, W. (2007). *An Introduction to Computational Fluid Dynamics: The Finite Volume Method* (2nd ed.). Harlow, England: Pearson Education Limited.

Vigneault, H., Lefebvre, R., & Nastev, M. (2004). Numerical Simulation of the Radius of Influence for Landfill Gas Wells. *Vadose Zone Journal*, *3*(3), 909–916. doi: 10.2113/3.3.909

Wang, L., & Heimovaara, T. (2025a). *Data and scripts underlying the manuscript: Quantifying water content of a landfill with ERT data by Bayesian evidential learning.* 4TU.ResearchData. doi: 10.4121/3D08EE40-04F3-4B8F-94C1-018090AD2A09.V1

Wang, L., & Heimovaara, T. J. (2025b). *Quantifying water content of a landfill with ERT data by Bayesian evidential learning.* ESS Open Archive. doi: 10.22541/essoar.174982586.67677790/v1

Wang, L., & Heimovaara, T. J. (2025c). *Revealing Hidden Leachate Dynamics in a Coupled Travel-Time Landfill Model Using a Particle Filter-Markov Chain Monte Carlo Approach.* ESS Open Archive. Retrieved 2025-08-26, from `https://essopenarchive.org/users/678329/articles/1303502-revealing-hidden-leachate-dynamics-in-a-coupled-travel-time-landfill-model-using-a-particle-filter-markov-chain-monte-carlo-approach` doi: 10.22541/essoar.175087417.79911372/v1

Wen, S., Cheng, W.-C., Li, D., & Hu, W. (2023). Evaluating gas breakthrough pressure and gas permeability in a landfill cover layer for mitigation of hazardous gas emissions. *Journal of Environmental Management*, *336*, 117617. doi: 10.1016/j.jenvman.2023.117617

Wet milieubeheer. (2025). Retrieved 2025-01-19, from `https://wetten.overheid.nl/BWBR0003245/2025-01-01` (BWBR0003245)

Woodman, N. D., Rees-White, T. C., Beaven, R. P., Stringfellow, A. M., & Barker, J. A. (2017). Doublet tracer tests to determine the contaminant flushing properties of a municipal solid waste landfill. *Journal of Contaminant Hydrology*, *203*, 38–50. doi: 10.1016/j.jconhyd.2017.05.008

Wu, H., Chen, T., Wang, H., & Lu, W. (2012). Field air permeability and hydraulic conductivity of landfilled municipal solid waste in China. *Journal of Environmental Management*, *98*, 15–22. doi: 10.1016/j.jenvman.2011.12.008

Xu, X. B., Powrie, W., Zhang, W. J., Holmes, D. S., Xu, H., & Beaven, R. (2020). Experimental study of the intrinsic permeability of municipal solid waste. *Waste Management*, *102*, 304–311. doi: 10.1016/j.wasman.2019.10.039

Yang, C., Park, M., & Zhu, C. (2007). A Method for Estimating In Situ Reaction Rates from Push-Pull Experiments for Arbitrary Solute Background Concentrations. *Environmental & Engineering Geoscience*, *13*(4), 345–354. doi: 10.2113/gseegeosci.13.4.345

Yazdani, R., Mostafid, M. E., Han, B., Imhoff, P. T., Chiu, P., Augenstein, D., ... Tchobanoglous, G. (2010). Quantifying Factors Limiting Aerobic Degradation During Aerobic Bioreactor Landfilling. *Environmental Science & Technology*, *44*(16), 6215–6220. doi: 10.1021/es1022398

Yi, S., Meza, N., Oonk, H., & Gebert, J. (2023). Understanding nitrogen transformation using the ratio of nitrogen to argon in landfills under in-situ stabilisation. In *Proceedings Sardinia 2023*. CISA Publisher.

Zeng, G., Liu, L., Xue, Q., Wan, Y., Ma, J., & Zhao, Y. (2017). Experimental study of the porosity and permeability of municipal solid waste. *Environmental Progress & Sustainable Energy*, *36*(6), 1694–1699. doi: 10.1002/ep.12632

Zhang, D., Wang, J., & Chen, C. (2020). Gas and liquid permeability in the variably saturated compacted loess used as an earthen final cover material in landfills. *Waste Management*, *105*, 49–60. doi: 10.1016/j.wasman.2020.01.030

Zhang, W., & Yuan, S.-s. (2019). Characterizing preferential flow in landfilled municipal solid waste. *Waste Management*, *84*, 20–28. doi: 10.1016/j.wasman.2018.11.023

Appendix A: Dual Porosity Derivation

The derivation starts from the general convection-dispersion equations for dual-porosity media, taken from Bear and Cheng (2010) and shown in Equations A.1 and A.2. It also follows the same general structure as this derivation. However, the original derivation was based on tracer transport in groundwater flow. It has thus been slightly modified to apply to gas transport. However, compressibility is still not included.

$$\frac{\partial \theta_g^m c_g^m}{\partial t} = -\nabla \left[c_g^m \hat{\boldsymbol{q}} - \theta_g^m \hat{\boldsymbol{D_m}}(\theta_g^m) \cdot \nabla c_g^m \right] - f_{m\to s}^{\gamma} - f_{g,m\to im}^{*} c_g^m + f_{g,im\to m}^{*} c_g^{im} + \gamma \left(c_g^{im} - c_g^m \right) - \theta_g^m \lambda_m \quad \text{(A.1)}$$

$$\frac{\partial \theta_g^{im} c_g^{im}}{\partial t} = \nabla \left[\theta_g^{im} \hat{\boldsymbol{D_{im}}}(\theta_g^m) \cdot \nabla c_g^{im} \right] - f_{im\to s}^{\gamma} - f_{g,m\to im}^{*} c_g^{im} + f_{g,im\to m}^{*} c_g^m + \gamma \left(c_g^m - c_g^{im} \right) - \theta_g^{im} \lambda_{im} \quad \text{(A.2)}$$

The terms in these equations are defined as follows:

- The subscript g refers to the gas phase.
- The superscripts m and im refer to the mobile and immobile zones respectively.
- θ_g is the gas-filled porosity.
- $\hat{\boldsymbol{q}}$ is the discharge vector, where discharge is equivalent to velocity v_g divided by gas-filled porosity.
- $\hat{\boldsymbol{D}}$ is the dispersion coefficient vector, which is taken to be dependent on the mobile percentage of porosity.
- In a groundwater context, $f_{m\to s}^{\gamma}$ and $f_{im\to s}^{\gamma}$ are the rates of sorption onto the solid phase. Here, they represent the partitioning of tracer gas into the water phase.
- $f_{g,m\to im}^{*}$ and $f_{g,im\to m}^{*}$ represent the transport rate of bulk gas (i.e. not only tracer) between the mobile and immobile phases.
- γ is the rate constant for tracer transport between the mobile and immobile zones.
- λ is the decay rate.

In an analogy to groundwater transport, the gas-filled porosity can be considered to be fully "saturated" with gas. Thus, there can be no bulk transport between the mobile and immobile zones. Additionally, the decay rate is considered to be negligible in this context. The governing equations therefore simplify to the ones shown below.

$$\frac{\partial \theta_g^m c_g^m}{\partial t} = -\nabla \left[c_g^m \hat{\boldsymbol{q}} - \theta_g^m \hat{\boldsymbol{D_m}}(\theta_g^m) \cdot \nabla c_g^m \right] - f_{m\to s}^{\gamma} + \gamma \left(c_g^{im} - c_g^m \right)$$

$$\frac{\partial \theta_g^{im} c_g^{im}}{\partial t} = \nabla \left[\theta_g^{im} \hat{\boldsymbol{D_{im}}}(\theta_g^m) \cdot \nabla c_g^{im} \right] - f_{im\to s}^{\gamma} + \gamma \left(c_g^m - c_g^{im} \right)$$

The mass balance for tracer on the sorbing surfaces is given by the two equations below, where F_m and F_{im} are the tracer concentrations on the sorbing (partitioning) surface in contact with each phase and ρ_b is the bulk density of the porous medium. Decay is again neglected in the sorbing surfaces, so the equations can be simplified as shown.

$$\frac{\partial \rho_b F_m}{\partial t} = f_{m\to s}^{\gamma} - \rho_b \lambda_{s,m} F_m = f_{m\to s}^{\gamma}$$

$$\frac{\partial \rho_b F_{im}}{\partial t} = f_{im\to s}^{\gamma} - \rho_b \lambda_{s,im} F_{im=} = f_{im\to s}^{\gamma}$$

These equations are then substituted into the governing equations.

$$\frac{\partial \theta_g^m c_g^m}{\partial t} = -\nabla \left[c_g^m \hat{\boldsymbol{q}} - \theta_g^m \hat{\boldsymbol{D_m}}(\theta_g^m) \cdot \nabla c_g^m \right] - \frac{\partial \rho_b F_m}{\partial t} + \gamma \left(c_g^{im} - c_g^m \right)$$

$$\frac{\partial \theta_g^{im} c_g^{im}}{\partial t} = \nabla \left[\theta_g^{im} \hat{\boldsymbol{D_{im}}}(\theta_g^m) \cdot \nabla c_g^{im} \right] - \frac{\partial \rho_b F_{im}}{\partial t} + \gamma \left(c_g^m - c_g^{im} \right)$$

The sorption isotherms for the mobile and immobile phases are given by the two equations below, where p^* is the fraction of water which is in contact with the mobile phase. Here, K_d is a partitioning coefficient which describes the affinity of the tracer for the sorbing surface. This is therefore related to, but not equal to, the Henry constant K_H.

$$F_m = p^* K_d c_g^m$$

$$F_{im} = (1 - p^*) K_d c_g^{im}$$

Additionally, the retardation factors for the mobile and immobile phases are given by the equations below.

$$R_m = 1 + \frac{\rho_b p^* K_d}{\theta_g^m}$$

$$R_{im} = 1 + \frac{\rho_b \left(1 - p^*\right) K_d}{\theta_g^{im}}$$

The retardation factor can then be related to the sorption isotherm by showing that the equality below is true.

$$\frac{\partial \theta_g^m c_g^m}{\partial t} + \frac{\partial \rho_b F_m}{\partial t} = \frac{\partial \theta_g^m R_m c_g^m}{\partial t}$$

This is shown by the chain rule and substitution of the sorption isotherm and retardation factor.

$$\frac{\partial \theta_g^m R_m c_g^m}{\partial t} = \frac{\partial}{\partial t}\left[\theta_g^m R_m c_g^m\right] = \frac{\partial}{\partial t}\left[\theta_g^m \left(1 + \frac{\rho_b p^* K_d}{\theta_g^m}\right) c_g^m\right]$$

$$= \frac{\partial}{\partial t}\left[\theta_g^m c_g^m + \rho_b p^* K_d c_g^m\right] = \frac{\partial}{\partial t}\left[\theta_g^m c_g^m + \rho_b F_m\right]$$

$$= \frac{\partial \theta_g^m c_g^m}{\partial t} + \frac{\partial \rho_b F_m}{\partial t}$$

A similar relation can be shown for the immobile zone. These can then be used to substitute the retardation factors into the governing equations.

$$\frac{\partial \theta_g^m R_m c_g^m}{\partial t} = -\nabla\left[c_g^m \hat{\boldsymbol{q}} - \theta_g^m \hat{\boldsymbol{D_m}}(\theta_g^m) \cdot \nabla c_g^m\right] + \gamma\left(c_g^{im} - c_g^m\right)$$

$$\frac{\partial \theta_g^{im} R_{im} c_g^{im}}{\partial t} = \nabla\left[\theta_g^{im} \hat{\boldsymbol{D_{im}}}(\theta_g^m) \cdot \nabla c_g^{im}\right] + \gamma\left(c_g^m - c_g^{im}\right)$$

Next, it is assumed that all of the water is located in the immobile zone and thus all retardation occurs in this region. Therefore, $R_m = 1$ and $R_{im} = R_f$, where R_f is the retardation factor calculated from the moment analysis of the PGTTs. Also, p^* is equal to zero. Additionally, it is assumed that θ_g, θ_g^m, D, q, and R_f are constant throughout the domain and duration. It is also assumed that no dispersion takes place in the immobile zone, so D_{im} is equal to zero. This results in the following simplified equations.

$$\frac{\partial \theta_g^m c_g^m}{\partial t} = -\nabla c_g^m \hat{\boldsymbol{q}} + \theta_g^m \hat{\boldsymbol{D_m}} \cdot \nabla^2 c_g^m + \gamma\left(c_g^{im} - c_g^m\right)$$

$$R_f \frac{\partial \theta_g^{im} c_g^{im}}{\partial t} = \gamma\left(c_g^m - c_g^{im}\right)$$

This is a one-dimensional problem, which reduces the vector coefficients into scalars and the gradients into partial derivatives.

$$\theta_g^m \frac{\partial c_g^m}{\partial t} = -q \frac{\partial c_g^m}{\partial x} + \theta_g^m D_m \frac{\partial^2 c_g^m}{\partial x^2} + \gamma\left(c_g^{im} - c_g^m\right)$$

$$\theta_g^{im} R_f \frac{\partial c_g^{im}}{\partial t} = \gamma\left(c_g^m - c_g^{im}\right)$$

To more easily compare with the equations from Yazdani et al. (2010), the mobile porosity is converted to the mobile gas fraction ϕ_g^m.

$$\phi_g^m = \frac{\theta_g^m}{\theta_g} = \frac{\theta_g - \theta_g^{im}}{\theta_g}$$

$$\theta_g^m = \phi_g^m \theta_g$$

$$\theta_g^{im} = \theta_g - \phi_g^m \theta_g = \theta_g(1 - \phi_g^m)$$

After making these substitutions and simplifying, the final governing equations are given in Equations A.3 and A.4.

$$\phi_g^m \frac{\partial c_g^m}{\partial t} = -v_g \frac{\partial c_g^m}{\partial x} + \phi_g^m D_m \frac{\partial^2 c_g^m}{\partial x^2} + \frac{\gamma}{\theta_g}\left(c_g^{im} - c_g^m\right)$$

$$(1 - \phi_g^m)\theta_g R_f \frac{\partial c_g^{im}}{\partial t} = \gamma\left(c_g^m - c_g^{im}\right)$$

$$(1 - \phi_g^m) R_f \frac{\partial c_g^{im}}{\partial t} = \frac{\gamma}{\theta_g}\left(c_g^m - c_g^{im}\right) \tag{A.3}$$

$$\phi_g^m \frac{\partial c_g^m}{\partial t} + (1 - \phi_g^m) R_f \frac{\partial c_g^{im}}{\partial t} = \phi_g^m D_m \frac{\partial^2 c_g^m}{\partial x^2} - v_g \frac{\partial c_g^m}{\partial x} \tag{A.4}$$

The equations from Yazdani et al. (2010) are shown in Equations A.5 and A.6 as presented, in nondimensional form. Here, Pe is the Peclet number and ω is the non-dimensional rate constant for tracer transfer between zones.

$$\phi_g^m \frac{\partial c_g^m}{\partial T} + \left(1 - \frac{\phi_g^m}{R_f}\right) \frac{\partial c_g^{im}}{\partial T} = \frac{1}{Pe} \frac{\partial^2 c_g^m}{\partial X^2} - \frac{\partial c_g^m}{\partial X} \tag{A.5}$$

$$\left(1 - \frac{\phi_g^m}{R_r}\right) \frac{\partial c_g^{im}}{\partial T} = \omega\left(c_g^m - c_g^{im}\right) \tag{A.6}$$

The nondimensional coefficients can be dimensionalized using the relationships below. Here, L is the distance between the injection well and the monitoring well

$$\omega = \frac{\gamma L}{\theta_g v_g}$$

$$Pe = \frac{v_g L}{D}$$

The nondimensional time and space coordinates are described by the below equations.

$$X = \frac{x}{L}$$

$$T = \frac{v_g t}{L}$$

The derivatives of these variables can be dimensionalized using the chain rule.

$$\frac{\partial c}{\partial T} = \frac{\partial c}{\partial t}\frac{\partial t}{\partial T} = \frac{\partial c}{\partial t}\frac{L}{v_g}$$

$$\frac{\partial c}{\partial X} = \frac{\partial c}{\partial x}\frac{\partial x}{\partial X} = \frac{\partial c}{\partial t} L$$

$$\frac{\partial^2 c}{\partial X^2} = \frac{\partial}{\partial X}\left[\frac{\partial c}{\partial X}\right] = \frac{\partial}{\partial X}\left[L\frac{\partial c}{\partial x}\right] = \frac{\partial}{\partial x}\frac{\partial x}{\partial X}\left[L\frac{\partial c}{\partial x}\right] = L^2 \frac{\partial^2 c}{\partial x^2}$$

This dimensionalization results in Equation A.7 and A.8.

$$\phi_g^m \frac{\partial c_g^m}{\partial t} + \left(1 - \frac{\phi_g^m}{R_f}\right) \frac{\partial c_g^{im}}{\partial t} = D \frac{\partial^2 c_g^m}{\partial x^2} - v_g \frac{\partial c_g^m}{\partial x} \tag{A.7}$$

$$\left(1 - \frac{\phi_g^m}{R_r}\right) \frac{\partial c_g^{im}}{\partial t} = \frac{\gamma}{\theta_g} \left(c_g^m - c_g^{im}\right) \tag{A.8}$$

By comparison with Equations A.3 and A.4, there are several notable changes. The first is that the coefficient for the time derivative of the immobile zone no longer includes R_f. Also, the term R_r is no longer present, as this was never defined by Yazdani et al. (2010). Finally, the dispersion term includes ϕ_g^m. The derivation of Equations A.7 and A.8 was not detailed by Yazdani et al. (2010) nor by the papers which were cited for the equations (Cirpka & Kitanidis, 2000; Luo et al., 2005). However, the reasons behind the differences were made clear by direct communication with Dr. Paul Imhoff, one of the authors.

The difference in the second term stems from a difference in the definition of R_f. As derived by Bear and Cheng (2010) and in this work, the global retardation factor stems from the immobile zone retardation factor and is thus divided by the immobile gas-filled porosity. This is shown in Equation A.9 after simplification using the assumption that $p^* = 0$. In contrast, the derivation used by Yazdani et al. (2010) uses the definition of R_f in Equation A.10, which was taken from (Toride et al., 1999). This set of equations was developed for contaminant transport in groundwater, rather than gases. The denominator in this case is the gas-filled porosity, which is assumed to be analogous to the total porosity in a saturated groundwater flow. This difference means that the simplifcation of this coefficient proceeds slightly differently.

$$R_f = R_{im} = 1 + \frac{\rho_b K_d}{\theta_g^{im}} \tag{A.9}$$

$$R_f = 1 + \frac{\rho_b K_d}{\theta_g} \tag{A.10}$$

The difference in the dispersion coefficient comes from the simplification $D = \phi_g^m D_m$. This simplification was not implemented in this work, but it does not make a difference to the analysis since it is just a scalar multiplication. The dispersion coefficient found in the inverse model can be quickly corrected to the form used by Yazdani et al. (2010). However, that work does not report the fitted dispersion coefficient, so comparison is impossible in any case.

Appendix B: Numerical Model

Based on the equations derived in Appendix A, a numerical model was developed. The intention of the model was to estimate the mobile fraction of gas-filled porosity ϕ_g^m, gas velocity v_g, dispsersion coefficient D, and first order rate constant γ. Additionally, the dilution factor F_{dil} is estimated by the model. The numerical model consists of a forward model which predicts the breakthrough curve for a given set of parameters. This is used by the inverse model to fit a set of parameters to a measured breakthrough curve.

Forward Model

For convenience, the equations derived in Appendix A are repeated below. The boundary conditions as discussed in Section 2.5.3 are also repeated below. The initial conidition is zero concentration across the whole domain in both the mobile and immobile zones.

$$\phi_g^m \frac{\partial c_g^m}{\partial t} + (1-\phi_g^m)\frac{\partial c_g^{im}}{\partial t} = \phi_g^m D_m \frac{\partial^2 c_g^m}{\partial x^2} - v_g \frac{\partial c_g^m}{\partial x} \tag{B.1}$$

$$(1-\phi_g^m)\frac{\partial c_g^{im}}{\partial t} = \frac{\gamma}{\theta_g}\left(c_g^m - c_g^{im}\right) \tag{B.2}$$

$$c_g^m(0,t) = c_\infty(t) + \frac{D}{v_g}\frac{\partial c_g^m}{\partial x}(0,t) \tag{B.3}$$

$$\frac{\partial c_g^m}{\partial x}(L_{far},t) = 0 \tag{B.4}$$

These equations were then discretized using the Finite Volume Method (FVM) to create a numerical model of the system. To do so, the one-dimensional study area was divided into N control volumes, each containing a node at its center, as well as an eastern and western face. This is shown diagrammatically in Figure B.1.

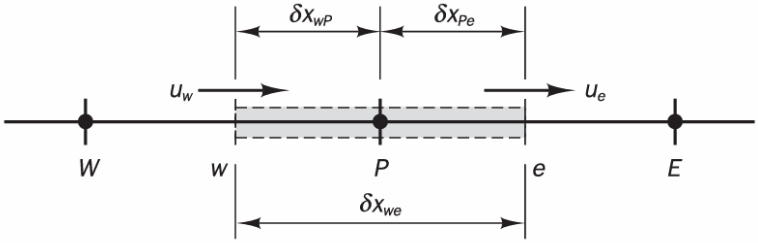

Figure B.1: Control volume definition (Versteeg & Malalasekera, 2007)

Following the FVM procedure, Equation B.2 was integrated over the control volume, resulting in Equation XXXXX, where Gauss's Theorem has been used to transform some of the volume integrals into surface integrals. The surface of the control volume is indicated by Γ, with the east and west surfaces represented by Γ_e and Γ_w. Since Equation B.2 does not involve any mass transport between control volumes, it does not require such transformation.

$$\phi_g^m \frac{\partial c_g^m}{\partial t}\Delta x\Delta y + \left(1-\phi_g^m\right) R_f \frac{\partial c_g^{im}}{\partial t}\Delta x\Delta y = D\phi_g^m \oint_\Gamma \nabla c_g^m \cdot \hat{n} d\Gamma + v_g \oint_\Gamma \mathbf{c_g^m} \cdot \hat{n} d\Gamma$$

$$\phi_g^m \frac{\partial c_g^m}{\partial t}\Delta x\Delta y + \left(1-\phi_g^m\right) R_f \frac{\partial c_g^{im}}{\partial t}\Delta x\Delta y = D\phi_g^m \oint_{\Gamma_e} \nabla c_g^m \cdot \hat{n} d\Gamma + D\phi_g^m \oint_{\Gamma_w} \nabla c_g^m \cdot \hat{n} d\Gamma + v_g \oint_{\Gamma_e} \mathbf{c_g^m} \cdot \hat{n} d\Gamma + v_g \oint_{\Gamma_w} \mathbf{c_g^m} \cdot \hat{n} d\Gamma$$

$$\phi_g^m \frac{\partial c_g^m}{\partial t}\Delta x\Delta y + \left(1-\phi_g^m\right) R_f \frac{\partial c_g^{im}}{\partial t}\Delta x\Delta y = D\phi_g^m \left(\frac{\partial c_g^m}{\partial x}\right)_e \Delta y - D\phi_g^m \left(\frac{\partial c_g^m}{\partial x}\right)_w \Delta y + v_g \left(c_m^g\right)_e \Delta y - v_g \left(c_m^g\right)_w \Delta y$$

$$\phi_g^m \frac{\partial c_g^m}{\partial t}\Delta x + \left(1-\phi_g^m\right) R_f \frac{\partial c_g^{im}}{\partial t}\Delta x = D\phi_g^m \left[\left(\frac{\partial c_g^m}{\partial x}\right)_e - \left(\frac{\partial c_g^m}{\partial x}\right)_w\right] + v_g\left[\left(c_m^g\right)_e - \left(c_m^g\right)_w\right] \tag{B.5}$$

The forward model was then discretized with implicit time stepping. By using an implicit scheme, numerical stability can be ensured regardless of the discretization of t and x. However, reasonably small values of dt and dx must still be used to ensure that simulation results are realistic (Versteeg & Malalasekera, 2007). The terms in Equation B.5 are discretized one-by-one in the equations below and reassembled in Equation B.9 with terms grouped by time step and spatial node. The discretized form of the second governing equation is given in Equation B.10. In these equations, the subscript i refers to the nodes of the spatial discretization, while the superscript n refers to the time step. In order to obtain the implicit time stepping, the spatial derivatives in Equation B.9 and the concentrations in B.10 are evaluated at time step $n+1$ when the equations are constructed for each time step n.

$$\phi_g^m \frac{\partial c_g^m}{\partial t}\Delta x = \phi_g^m \Delta x \left(\frac{c_{g,i}^{m,n+1} - c_{g,i}^{m,n}}{\Delta t}\right)$$

$$\left(1-\phi_g^m\right) R_f \frac{\partial c_g^{im}}{\partial t}\Delta x = \left(1-\phi_g^m\right) R_f \Delta x \left(\frac{c_{g,i}^{im,n+1} - c_{g,i}^{im,n}}{\partial t}\right)$$

$$D\phi_g^m \left[\left(\frac{\partial c_g^m}{\partial x}\right)_e - \left(\frac{\partial c_g^m}{\partial x}\right)_w\right] = D\phi_g^m \left[\left(\frac{c_{g,i+1}^{m,n} - c_{g,i}^{m,n}}{\Delta x}\right) - \left(\frac{c_{g,i}^{m,n} - c_{g,i-1}^{m,n}}{\Delta x}\right)\right] = D\phi_g^m \left[\frac{c_{g,i+1}^{m,n} - 2c_{g,i}^{m,n} + c_{g,i-1}^{m,n}}{\Delta x}\right]$$

$$v_g \left[\left(c_g^m\right)_e - \left(c_g^m\right)_w\right] = v_g \left[\left(c_{g,i}^{m,n} + \Psi(r_{e,i})\left(c_{g,i+1}^{m,n} - c_{g,i}^{m,n}\right)\right) - \left(c_{g,i-1}^{m,n} + \Psi(r_{e,i})\left(c_{g,i}^{m,n} - c_{g,i-1}^{m,n}\right)\right)\right] \tag{B.6}$$

$$r_{e,i} = \frac{c_{g,i}^{m,n} - c_{g,i-1}^{m,n}}{c_{g,i+1}^{m,n} - c_{g,i}^{m,n}} \tag{B.7}$$

$$r_{w,i} = \frac{c_{g,i-1}^{m,n} - c_{g,i-2}^{m,n}}{c_{g,i}^{m,n} - c_{g,i-1}^{m,n}} \tag{B.8}$$

$$\begin{aligned} c_{g,i}^{m,n+1}\left[\frac{\phi_g^m}{\Delta t} + \frac{2D\phi_g^m}{\Delta x^2} + \frac{v_g}{\Delta x} - \frac{v_g}{2\Delta x}\Psi(r_{e,i}) - \frac{v_g}{2\Delta x}\Psi(r_{w,i})\right] + c_{g,i+1}^{m,n+1}\left[-\frac{D\phi_g^m}{\Delta x^2} + \frac{v_g}{2\Delta x}\Psi(r_{e,i})\right] \\ + c_{g,i-1}^{m,n+1}\left[-\frac{D\phi_g^m}{\Delta x^2} + \frac{v_g}{\Delta x} + \frac{v_g}{2\Delta x}\Psi(r_{w,i})\right] + c_{g,i}^{im,n+1}\left[\left(1-\phi_g^m\right)\frac{R_f}{\Delta t}\right] \\ = c_{g,i}^{m,n}\left[\frac{\phi_g^m}{\Delta t}\right] + c_{g,i}^{im,n}\left[\left(1-\phi_g^m\right)\frac{R_f}{\Delta t}\right] \end{aligned} \tag{B.9}$$

$$c_{g,i}^{im,n+1}\left[\left(1-\phi_g^m\right)\frac{R_f}{\Delta t} + \frac{\gamma}{\theta_g}\right] - \frac{\gamma}{\theta_g}c_{g,i}^{m,n+1} = \left(1-\phi_g^m\right)\frac{R_f}{\Delta t}c_{g,i}^{im,n} \tag{B.10}$$

It should be noted that $\Psi(r)$ in Equation B.6 is a flux limiter, which is the heart of the TVD scheme. The flux limiter is derived by setting up a numerical model which uses a linear combination of central differencing and upwind differencing. The goal of this is to retain the reduced numerical dispersion offered by upwind differencing, while gaining the second order spatial accuracy of central differencing. This function is used in situations where there is a large gradient between adjacent nodes, such as at the beginning of the tracer test.

As discussed in depth in Chapter 5 of Versteeg and Malalasekera (2007), a flux limiter function must respect certain bounds in order to ensure the TVD property of the solution, which are shown in Figure B.2. In order to be second-order spatially accurate, the flux limiter function must fit into the even more restrictive bounds shown in Figure B.3. A variety of flux limiter functions have been developed by various researchers, including the Van Leer limiter in Equation B.11, the Van Albada limiter in Equation B.12, and the Minmod limiter in Equation B.13. For most applications, there is negligible functional difference between the three limiters, as all three are second-order accurate and symmetric (positive and negative gradients are treated the same) (Versteeg & Malalasekera, 2007).

It should also be noted that if $\Psi(r)$ is set to one, a central difference scheme is recovered. This scheme is not TVD, but is second-order accurate. Additionally, if $\Psi(r)$ is set to zero, an upwind differencing scheme is created. This scheme is TVD, but is only first-order accurate and thus introduces some numerical dispersion.

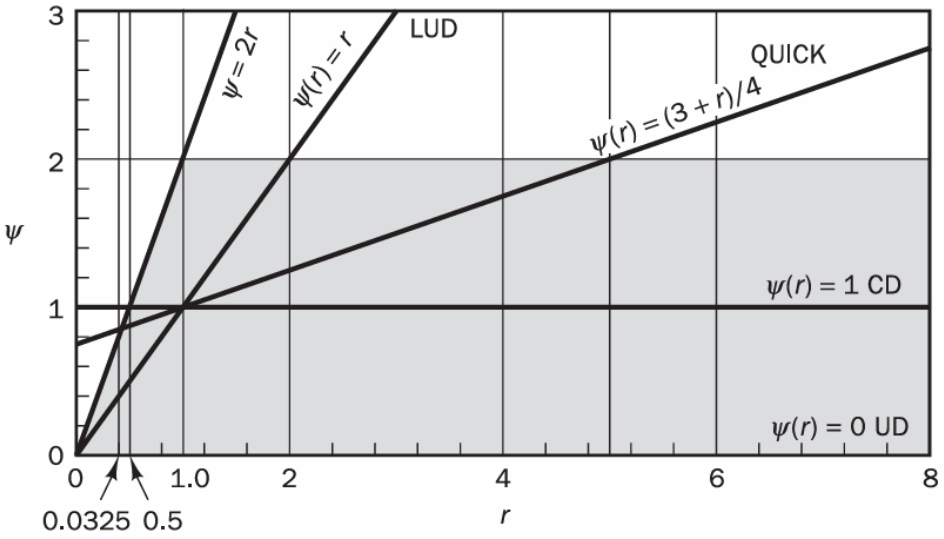

Figure B.2: Bounds for flux limiter function (Versteeg & Malalasekera, 2007)

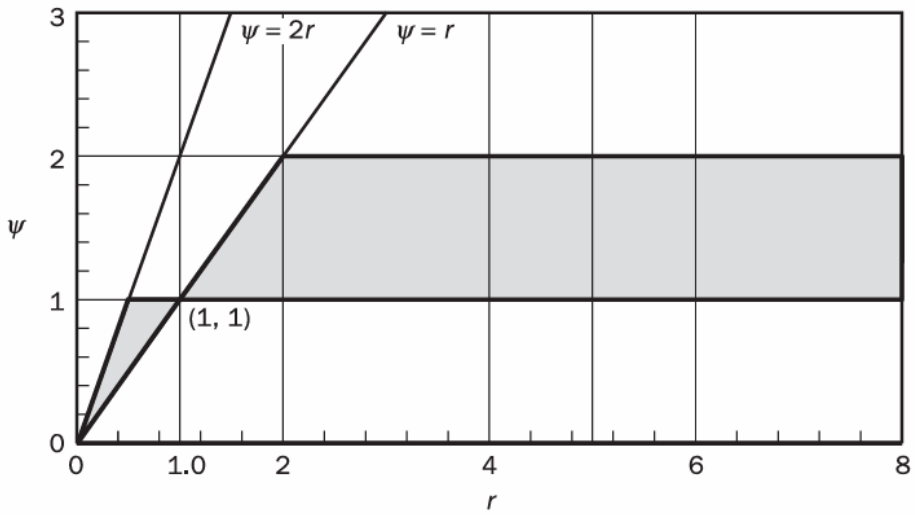

Figure B.3: Bounds for second-order accurate flux limiter function (Versteeg & Malalasekera, 2007)

$$\Psi(r) = \frac{r + |r|}{1 + r} \tag{B.11}$$

$$\Psi(r) = \frac{r + r^2}{1 + r^2} \tag{B.12}$$

$$\Psi(r) = \begin{cases} \min(r, 1), & \text{if } r > 0 \\ 0, & \text{if } r \leq 0 \end{cases} \tag{B.13}$$

At each node i, the model uses the concentrations at nodes $i - 1$ and $i - 2$. At the near boundary, these nodes do not exist. To compensate, mirror nodes are created, for which the concentration is linearly interpolated from the concentration at the near boundary and the concentration at the first node, as shown in Figure B.4 (Versteeg & Malalasekera, 2007). At the far boundary, the same strategy is used to determine the concentration at node $i + 1$, but due to the Neumann boundary condition, the mirror node has the same value as the final node.

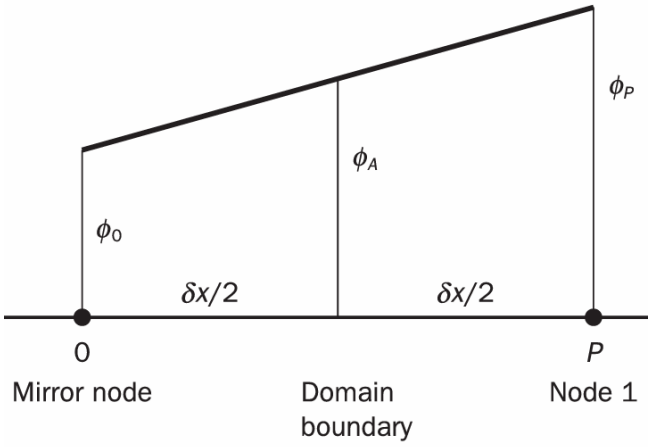

Figure B.4: Mirror nodes (Versteeg & Malalasekera, 2007)

Under this implicit time stepping formulation, the concentration at a given node i at timestep $n+1$ cannot be directly calculated using the concentrations at timestep n. Instead, the concentration at all nodes must be determined simultaneously as a system of equations. The concentrations in the mobile and immobile zones are determined simultaneously. In Equations B.14 through B.19, each coefficient is assigned to a variable to make the matrix formulation easier to read.

$$\left[\frac{\phi_g^m}{\Delta t} + \frac{2D\phi_g^m}{\Delta x^2} + \frac{v_g}{\Delta x} - \frac{v_g}{2\Delta x}\Psi(r_{e,i}) - \frac{v_g}{2\Delta x}\Psi(r_{w,i})\right] = \alpha(r_{e,i}, r_{w,i}) \tag{B.14}$$

$$\left[-\frac{D\phi_g^m}{\Delta x^2} + \frac{v_g}{2\Delta x}\Psi(r_{e,i})\right] = \beta(r_{e,i}) \tag{B.15}$$

$$\left[-\frac{D\phi_g^m}{\Delta x^2} + \frac{v_g}{\Delta x} + \frac{v_g}{2\Delta x}\Psi(r_{w,i})\right] = \delta(r_{w,i}) \tag{B.16}$$

$$\left[\left(1-\phi_g^m\right)\frac{R_f}{\Delta t}\right] = \lambda \tag{B.17}$$

$$\left[\frac{\phi_g^m}{\Delta t}\right] = \kappa \tag{B.18}$$

$$\left[\left(1-\phi_g^m\right)\frac{R_f}{\Delta t}\right] = \epsilon \tag{B.19}$$

The matrix form of the equations is then formulated according to Equation B.20, where **A** through **F** are N x N matrices and **J** is a vector of length N. The values of these matrices are given by Equations B.21 through B.27. The near boundary condition is introduced via the first row of the matrix equation, where the mirror points are included in the vector **J**. The Neumann condition at the far boundary is introduced by the last row of the equation, where the final entry in matrix **A** accounts for the fact that the concentration at the mirror node is equal to that at the final node.

$$\begin{bmatrix}\mathbf{A} & \mathbf{B}\\ \mathbf{C} & \mathbf{D}\end{bmatrix}\begin{bmatrix}c_g^{\bar{m}}\\ c_g^{im}\end{bmatrix}^{n+1} = \begin{bmatrix}\mathbf{E} & \mathbf{B}\\ \mathbf{0} & \mathbf{F}\end{bmatrix}\begin{bmatrix}c_g^{\bar{m}}\\ c_g^{im}\end{bmatrix}^{n} + [\mathbf{J}] \tag{B.20}$$

$$\mathbf{A} = \begin{bmatrix}
\alpha(r_{e,i}, r_{w,i}) & \beta(r_{e,i}) & 0 & 0 & 0 & \dots & 0\\
\delta(r_{w,i}) & \alpha(r_{e,i}, r_{w,i}) & \beta(r_{e,i}) & 0 & 0 & \dots & 0\\
0 & \delta(r_{w,i}) & \alpha(r_{e,i}, r_{w,i}) & \beta(r_{e,i}) & 0 & \dots & 0\\
0 & 0 & \delta(r_{w,i}) & \alpha(r_{e,i}, r_{w,i}) & 0 & \dots & 0\\
\vdots & \vdots & \vdots & \vdots & \vdots & \ddots & \\
0 & 0 & 0 & 0 & 0 & & \alpha(r_{e,i}, r_{w,i}) + \beta(r_{e,i})
\end{bmatrix} \tag{B.21}$$

$$\mathbf{B} = \begin{bmatrix} \lambda & 0 & 0 & \dots \\ 0 & \lambda & 0 & \dots \\ 0 & 0 & \lambda & \dots \\ \vdots & \vdots & \vdots & \ddots \end{bmatrix} \tag{B.22}$$

$$\mathbf{C} = \begin{bmatrix} -\gamma/\theta_g & 0 & 0 & \dots \\ 0 & -\gamma/\theta_g & 0 & \dots \\ 0 & 0 & -\gamma/\theta_g & \dots \\ \vdots & \vdots & \vdots & \ddots \end{bmatrix} \tag{B.23}$$

$$\mathbf{D} = \begin{bmatrix} \epsilon + \gamma/\theta_g & 0 & 0 & \dots \\ 0 & \epsilon + \gamma/\theta_g & 0 & \dots \\ 0 & 0 & \epsilon + \gamma/\theta_g & \dots \\ \vdots & \vdots & \vdots & \ddots \end{bmatrix} \tag{B.24}$$

$$\mathbf{E} = \begin{bmatrix} \kappa & 0 & 0 & \dots \\ 0 & \kappa & 0 & \dots \\ 0 & 0 & \kappa & \dots \\ \vdots & \vdots & \vdots & \ddots \end{bmatrix} \tag{B.25}$$

$$\mathbf{F} = \begin{bmatrix} \epsilon & 0 & 0 & \dots \\ 0 & \epsilon & 0 & \dots \\ 0 & 0 & \epsilon & \dots \\ \vdots & \vdots & \vdots & \ddots \end{bmatrix} \tag{B.26}$$

$$\mathbf{J} = \begin{bmatrix} -\delta(r_{w,0}) c_{g,mirror}^{m,n+1} \\ 0 \\ 0 \\ \vdots \end{bmatrix} \tag{B.27}$$

It is very important to note that α, β and δ all include $\Psi(r)$ and are thus different for each row. This means that the system of equations is nonlinear and must be solved iteratively. The exceptions to this rule are when $\Psi(r)$ is set to one to recover a central differencing scheme (which is not TVD) and when $\Psi(r)$ is set to zero to recover an upwind differencing scheme (which is only first-order accurate). In either case, the system of equations can be solved at each timestep n to calculate the concentrations in both the mobile and immobile zones at timestep $n+1$. This is then repeated until the entire interval of interest has been simulated.

However, during the period of this thesis, it proved very difficult to efficiently formulate a method of iteratively solving the nonlinear system of equations. Thus, $\Psi(r)$ was set to one to recover the central differencing scheme. **This non-TVD approach was used for all simulations discussed in this work.** The numerical model is presented as derived, which includes the TVD flux limiters, as this still accurately represents the system as applied.

Throughout all simulations, a grid spacing of 0.05 m and a time step of 0.1 h were used. These values were chosen because they were found to result in stable simulations for all relevant values of the model variables without being so small that the simulation took too long to complete. This was determined through a trial and error process.

Inverse Model

The model described above can be used to predict the breakthrough curve for a given set of parameters v_g, D, ϕ_g^m, γ, and F_{dil}. (Recall that F_{dil} is a factor which accounts for dilution of the simulated stream tube when it is sampled by the monitoring well.) However, the goal is to predict these parameters from a measured breakthrough curve. To do so, an inverse model was developed using a coordinate descent (CD) method.

The inverse model is based upon an algorithm which attempts to minimize the objective function shown in Equation B.28, where M is the number of data points in the measured breakthrough curve and w is a penalty

function. The penalty function is necessary because the algorithm does not inherently include constraints for the values of the variables. When all variables are within their prescribed bounds, the penalty function is set to one. If any values are outside of their bounds, the penalty function is set to 10,000 so as to eliminate that solution from being considered optimal. The bounds require that all variables must be positive. Additionally, ϕ_g^m must be between zero and one. $\mathbf{x}$ is the solution vector made up of v_g, D, ϕ_g^m, γ, and F_{dil}. When referenced individually, the elements of $\mathbf{x}$ are called $\mathbf{x_k}$.

$$G(\mathbf{x}) = \sum_{j=0}^{M} (c_{model}(\mathbf{x}, t_j) - c_{meas,j})^2 \cdot w(\mathbf{x}) \tag{B.28}$$

$$\mathbf{x} = \begin{bmatrix} v_g \\ D \\ \phi_g^m \\ \gamma \\ F_{dil} \end{bmatrix} \tag{B.29}$$

The algorithm begins from an initial guess $\mathbf{x}_0$ for the model parameters, which is obtained by attempting to match the forward model to the measured data using trial and error. The objective function is then evaluated at the initial guess to provide a baseline from which to improve. Each element in the solution is then subjected to the following sub-algorithm:

1. Generate ten new guesses for this element ($\mathbf{x_k}$) of the solution based on Equation B.30, where ϵ is the step size.
2. For each guess in $\mathbf{x}_k^{new}$, generate $\mathbf{x}^{guess}$ by replacing $\mathbf{x}_k$ with $\mathbf{x}_k^{guess}$ and evaluate the objective function $F(\mathbf{x}^{guess})$.
3. If any of the guesses results in a reduction of the objective function, replace $\mathbf{x}_k$ with $\mathbf{x}_k^{guess}$. Store this value of $F(\mathbf{x})$ to compare future guesses with.

$$\mathbf{x}_k^{guess} = \mathbf{x}_k + \mathbf{x}_k \cdot \epsilon \begin{bmatrix} 0.2 \\ 0.4 \\ 0.6 \\ 0.8 \\ 1 \\ -0.2 \\ -0.4 \\ -0.6 \\ -0.8 \\ -1 \end{bmatrix} \tag{B.30}$$

This sub-algorithm is repeated for each element of $\mathbf{x}$ to complete one iteration of the CD algorithm. If an iteration of the CD algorithm proceeds without a single reduction in the objective function, the step size ϵ is divided by two (its starting value is 2). The inverse model proceeds until it has converged, i.e. the value of the objective function has not improved by a factor of more than δ in the previous 50 iterations, where δ is the acceptable error. δ was set to 10^{-3}. Under these conditions, the model generally converged in around 1000 iterations of the CD algorithm. When the algorithm got caught in a trough, up to several thousand more iterations were required.

Appendix C: Uncertainty Quantification

For each calculated parameter, it was desired to estimate the uncertainty of the result. Since the calculations were highly nonlinear, it was not possible to apply simple rules of uncertainty propagation. Uncertainty was therefore evaluated numerically for both PFT and PGTT results.

Gas Permeability

Under the Baehr and Joss method, gas permeability is calculated using steady-state flow rate and well pressure. However, there is always variability in these values and in some tests there are significant fluctuations due to factors like water in the extraction well. These uncertainties are then carried forward into the calculated gas permeability.

To account for each of these uncertainties, pressure and flow are each fitted to a gamma distribution using the `scipy.stats` package for Python. A gamma distribution was chosen over a normal distribution because this method allows only positive values of the sample variable. This is preferable for this application because, even when there is very high variability in the pressure or flow, it is certain that they will not change sign. Additionally, a gamma distribution allows for asymmetric probability distributions, which was sometimes the case for this data. Example distributions are shown in Figures C.1 and C.2.

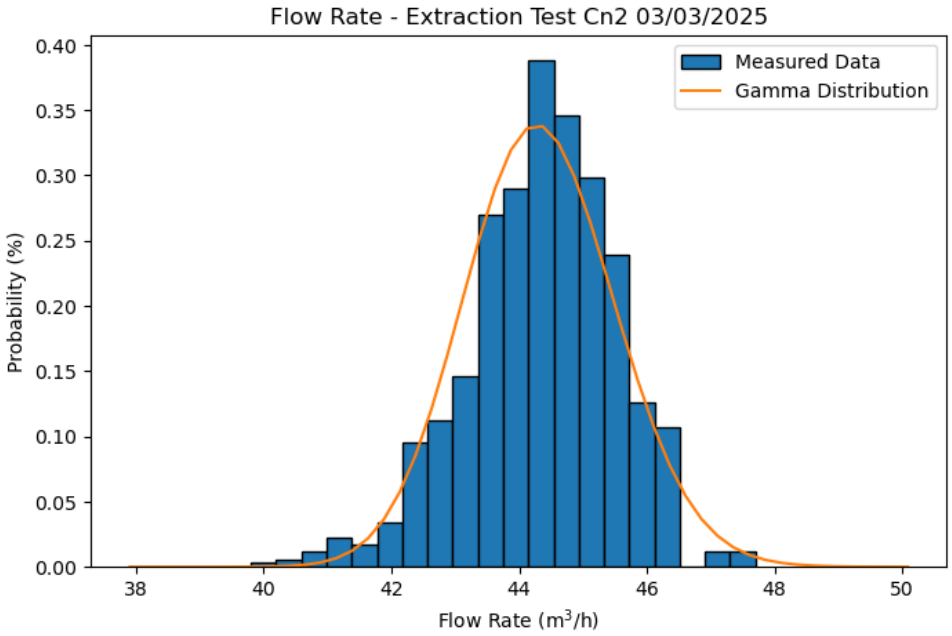

Figure C.1: Gamma flow distribution

It should be noted that when the Kolmogorov-Smirnov test was used to test whether the data fit a gamma distribution, the resulting p-value was not always greater than 0.05. This should normally mean that the data cannot be said to follow the gamma distribution. However, the gamma distribution almost always gave a better p-value than a normal, lognormal, truncated normal, or uniform distribution. The poor fit in these cases was attributed to an insufficient number of data points since the steady-state portion of the test was often only ten minutes long. In the interest of treating all tests the same, a gamma distribution was used for all tests.

Using the fitted distributions, the 95% confidence intervals could be determined for steady-state pressure and flow. The Baehr and Joss calculations were then repeated using these values to find the 95% confidence interval for gas permeability. This was repeated for each well pair in each test.

When using the Hantush method, the same sources of uncertainty apply, but additional uncertainty is also introduced by the loglinear fit of pressure against time. The uncertainty on each measurement of pressure causes an uncertainty in the slope, which is then used in the calculations of gas permeability. The standard deviation of the linear fit parameters was estimated using Equations C.1 and C.2 (Eberly College of Science -

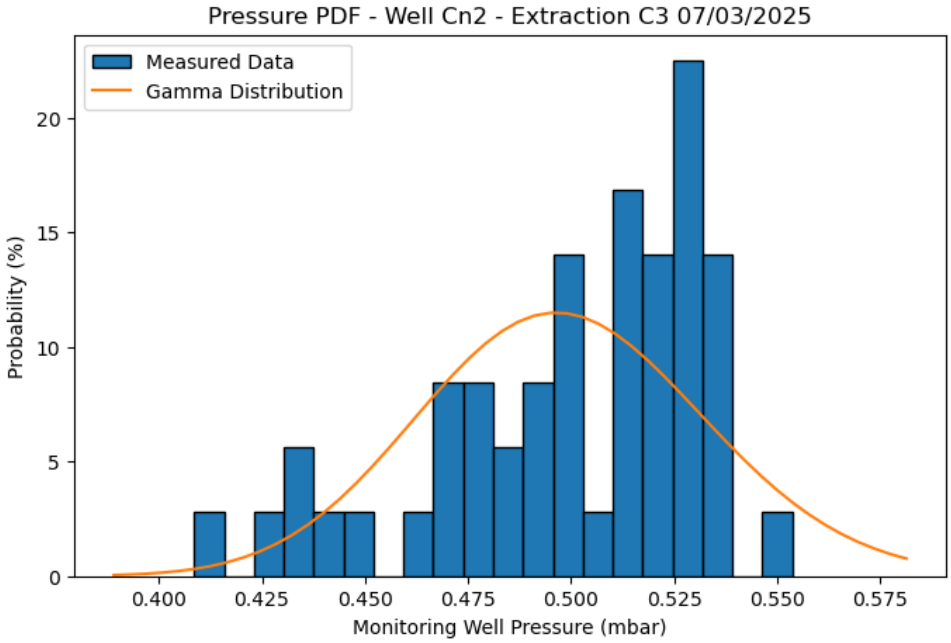

Figure C.2: Gamma pressure distribution

Department of Statistics, 2024). Here, α is the intercept of the loglinear fit and β is the slope. Additionally, n is the number of points included in the fit and σ is the standard deviation of the difference between the measured pressures and the loglinear fit. In this manner, tests with a better quality of fit have a lower uncertainty in the fit parameters. Using these standard deviations, the 95% confidence intervals for the loglinear fits were constructed based on a normal distribution.

$$\sigma_\alpha^2 = \frac{\sigma^2}{n} \tag{C.1}$$

$$\sigma_\beta^2 = \frac{\sigma^2}{\sum_{i=1}^{n}(x_i - \bar{x})^2} \tag{C.2}$$

The confidence intervals for the Hantush gas permeability were then calculated based on the confidence intervals of the pressure, flow, and linear fit parameters. The gas permeability calculations were repeated for each combination of minimum/maximum flow, pressure, and slope. The resulting minimum and maximum values were then taken to be the 95% confidence interval for the Hantush gas permeability.

Retardation Factor and Saturation

The calculations for the retardation factor R_f and saturation S_w are based on the LumaSense measurements and a loglinear fit of concentration against time. In this case, however, the logarithm is applied to the concentration values instead of time, so the same equations discussed above cannot be applied.

First, the uncertainty deriving from the LumaSense measurements is evaluated. Based on the lab testing described in Section 2.7, it was found that, when measuring a constant concentration of propane, the LumaSense has a standard deviation of around 11 ppm regardless of the measured concentration. Based on this standard deviation, a normal error distribution was created.

At each point in the breakthrough curve, a random amount of error was added using the error distribution. The calculations for R_f and S_w were then repeated. This process was repeated 100 times, starting each time from the measured LumaSense breakthrough curve. After this was complete, the standard deviation of R_f and S_w were calculated. This was taken to be the portion of the uncertainty deriving from the error in the measurement.

The loglinear extrapolation of the concentration was performed using the `optimize.curvefit` function of Python's `scipy` library, which is based on nonlinear least squares. The function also takes the standard deviation of the measured values as an argument and outputs the standard deviations of the fit parameters. In the

same manner as for the gas permeability, the 95% confidence interval for each parameter was determined and the calculations were repeated with each combination to find the uncertainty in R_f and S_w.

The uncertainty stemming from the loglinear extrapolation was then added to the uncertainty from the error in the LumaSense measurements to obtain the overall uncertainty.

Dual Domain Model

For the dual domain model, the only source of uncertainty is the error in the LumaSense measurements. The uncertainty in the results were therefore determined similarly to the uncertainty in R_f and S_w. After the model converged to find ϕ_g^m, D, v_g, γ and F_{dil}, error was added to the breakthrough curve using the same error distribution. The model was then restarted and allowed to converge to a new set of parameters. This process was repeated 10 times, with the standard deviation of the model parameters being determined from the variability of the results. Fewer repetitions were used in this case because the inverse model was very time-consuming to run.

Appendix D: Gas Permeability Maps

The spatial maps of gas permeability are all provided below. In addition to these maps, there were five tests which did not result in any gas permeability connections. These are listed in Table D.1 below. It is worth noting that not all possible wells were monitored during these tests, so it possible that these wells do still have pressure connections.

Table D.1: Pressure Field Tests without measured connections

Date	Injection/Extraction Well	Test Type	Monitoring Wells
03/03/2025	D2	Extraction	C1, C2, C3, Cn1, Cn2, D1, D3
03/03/2025	D3	Extraction	C1, C2, C3, Cn1, Cn2, D1, D2
18/03/2025	B2	Extraction	An1, An2, B3, Bn1, Bn2, Bn3, C1, C2, Cn1, Cn2
18/03/2025	B3	Extraction	An1, An2, B2, Bn1, Bn2, Bn3, C1, C2, Cn1, Cn2
18/03/2025	B3	Injection	An1, An2, B2, Bn1, Bn2, Bn3, C1, C2, Cn1, Cn2

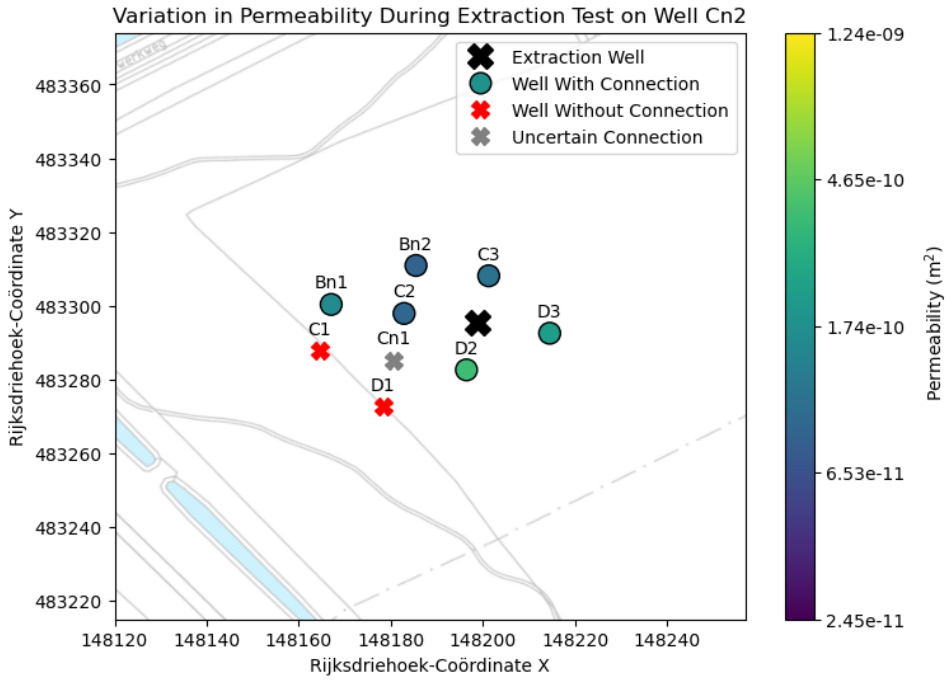

Figure D.1: 2025-03-03 - Extraction on Cn2

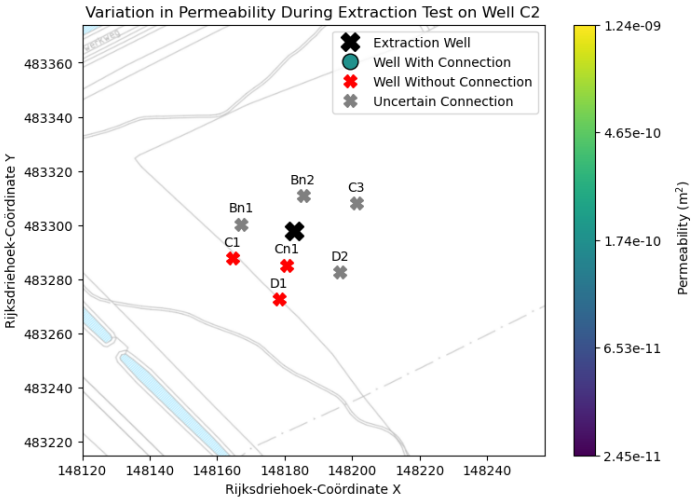

Figure D.2: 2025-03-03 - Extraction on C2

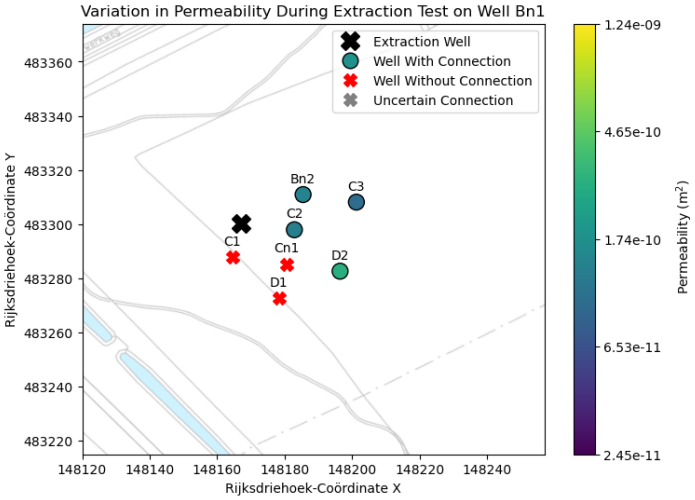

Figure D.3: 2025-03-03 - Extraction on Bn1

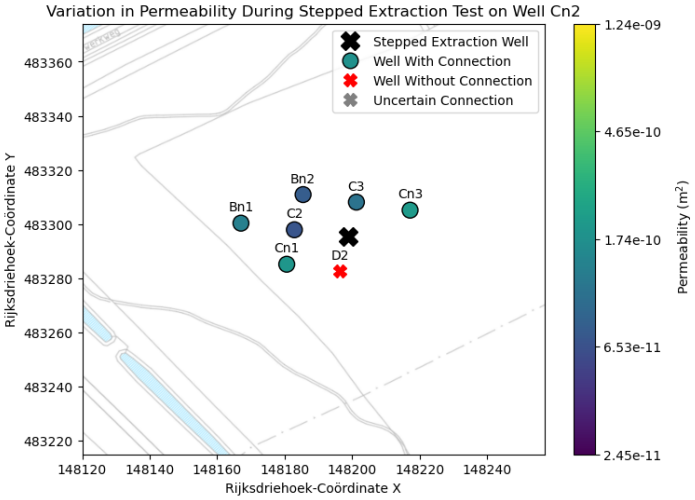

Figure D.4: 2025-03-07 - Stepped Extraction on Cn2 - Step 1

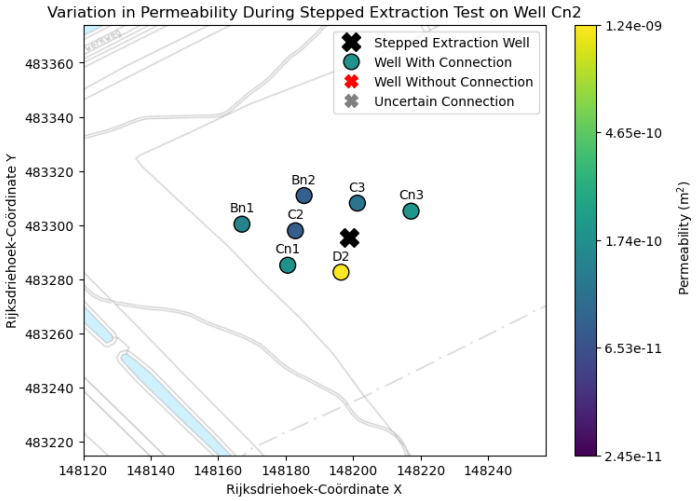

Figure D.5: 2025-03-07 - Stepped Extraction on Cn2 - Step 2

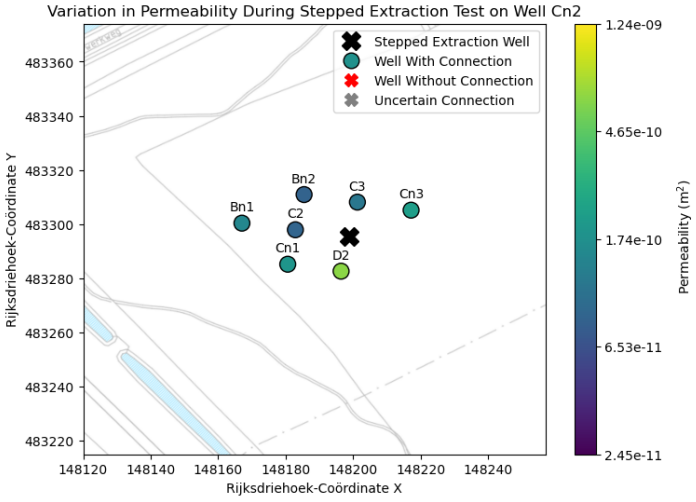

Figure D.6: 2025-03-07 - Stepped Extraction on Cn2 - Step 3

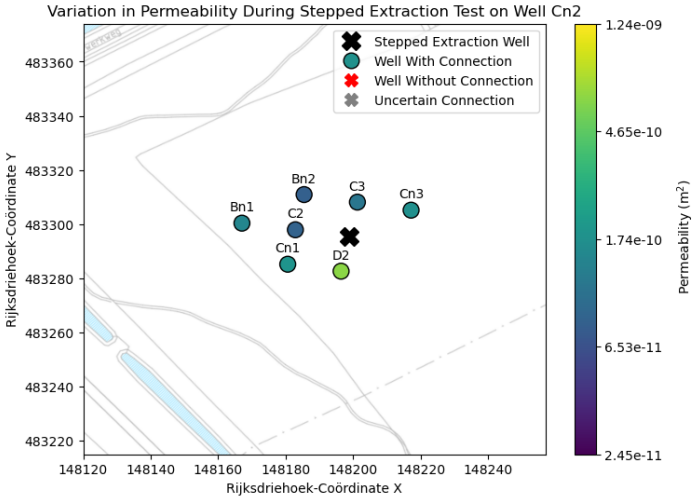

Figure D.7: 2025-03-07 - Stepped Extraction on Cn2 - Step 4

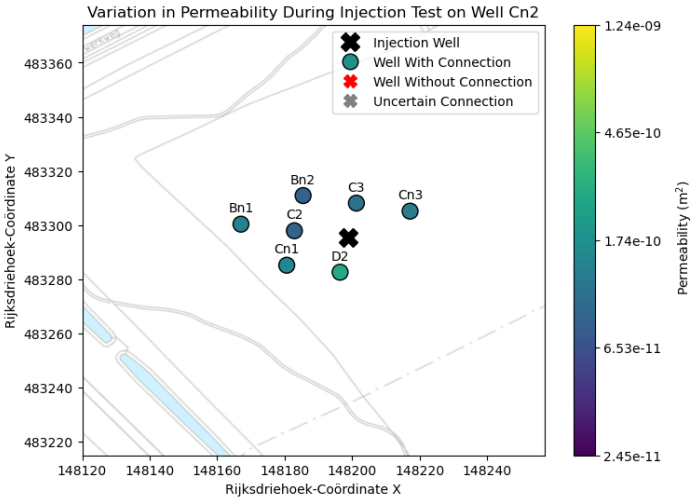

Figure D.8: 2025-03-07 - Injection on Cn2

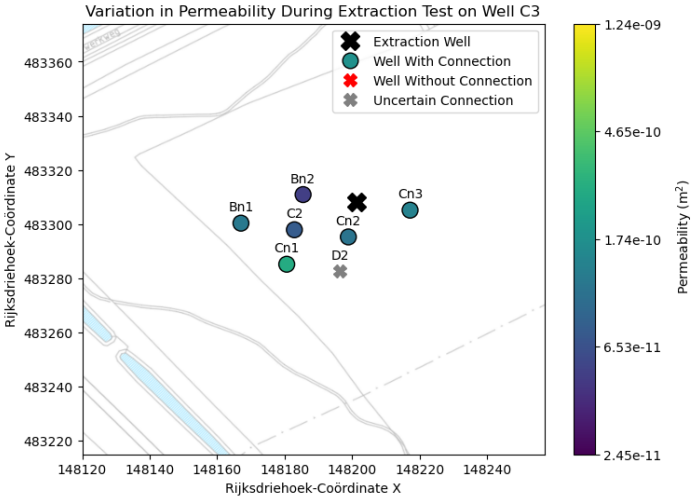

Figure D.9: 2025-03-07 - Extraction on C3

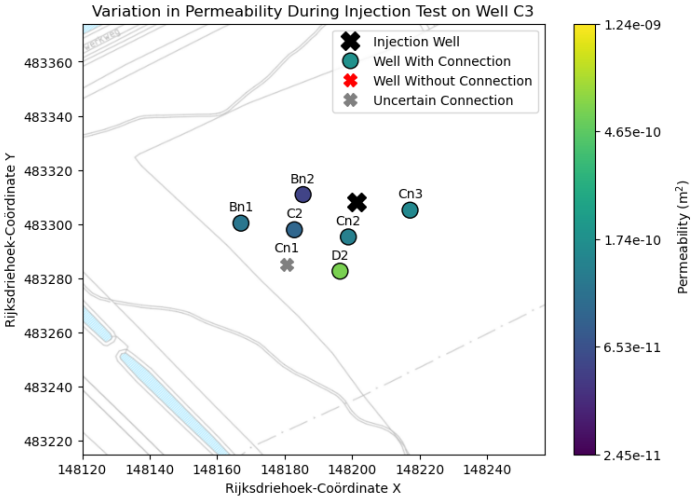

Figure D.10: 2025-03-07 - Injection on C3

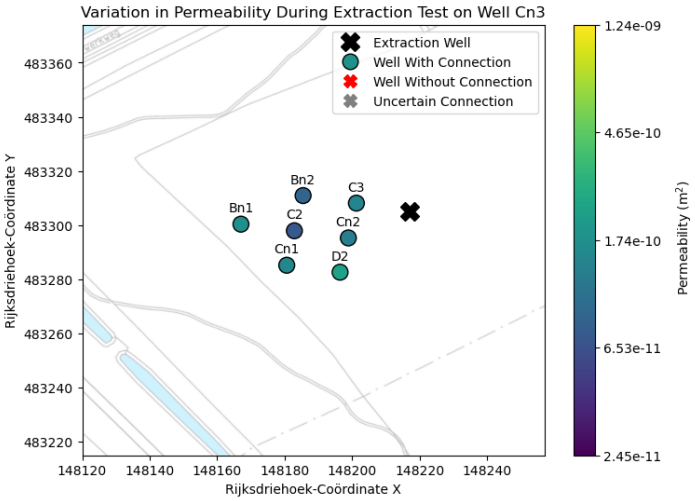

Figure D.11: 2025-03-07 - Extraction on Cn3

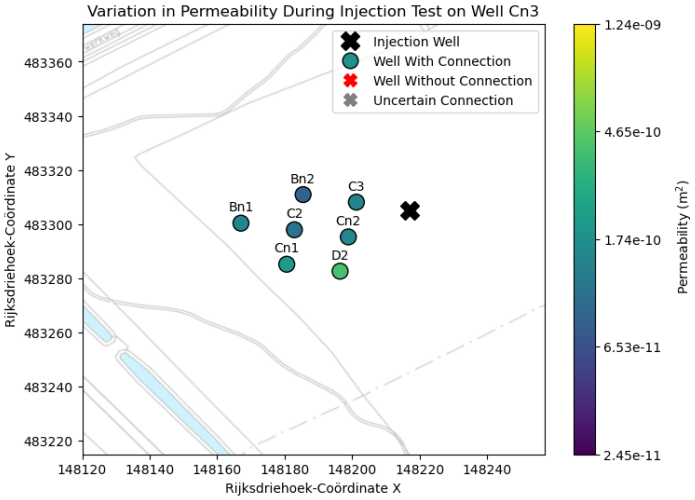

Figure D.12: 2025-03-07 - Injection on Cn3

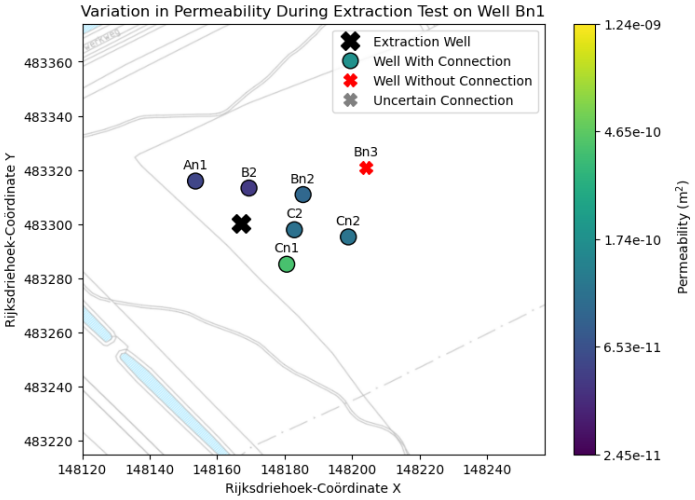

Figure D.13: 2025-03-18 - Extraction on Bn1

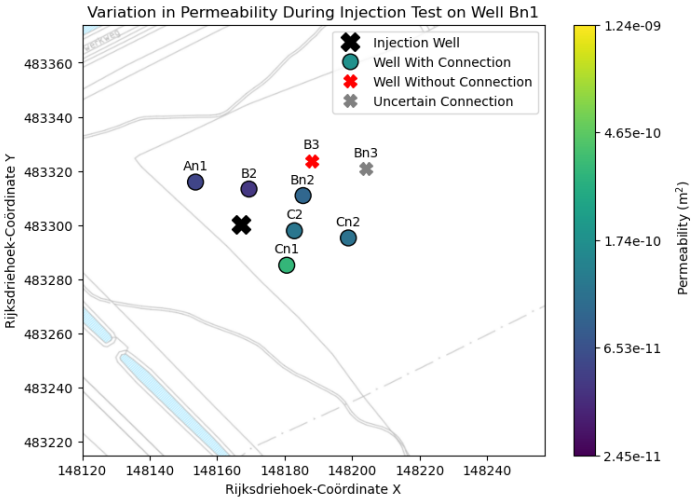

Figure D.14: 2025-03-18 - Injection on Bn1

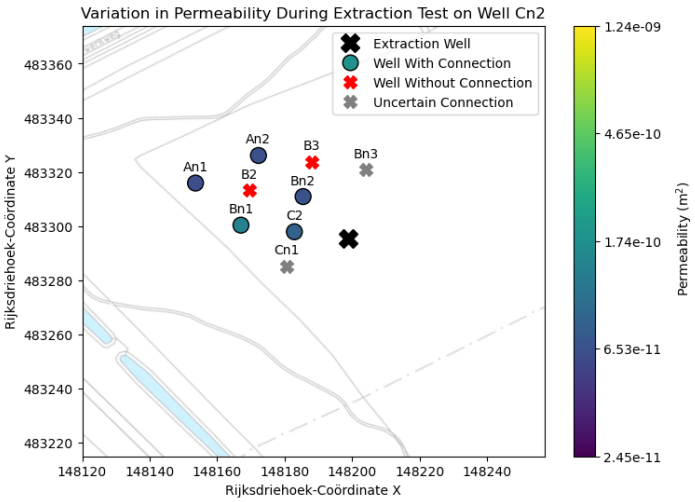

Figure D.15: 2025-03-18 - Extraction on Cn2

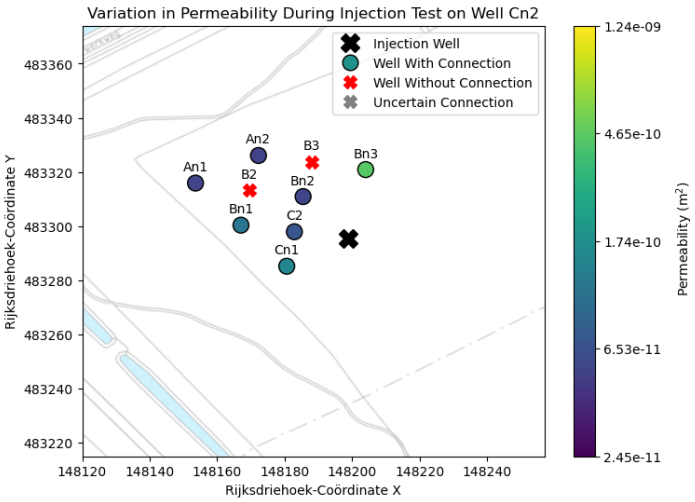

Figure D.16: 2025-03-18 - Injection on Cn2

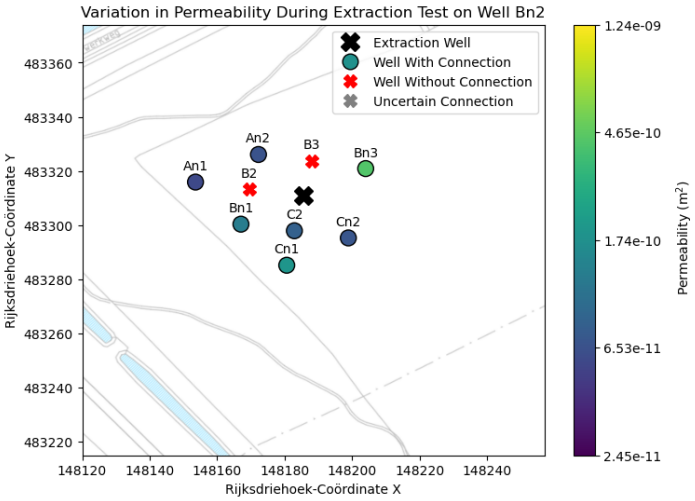

Figure D.17: 2025-03-18 - Extraction on Bn2

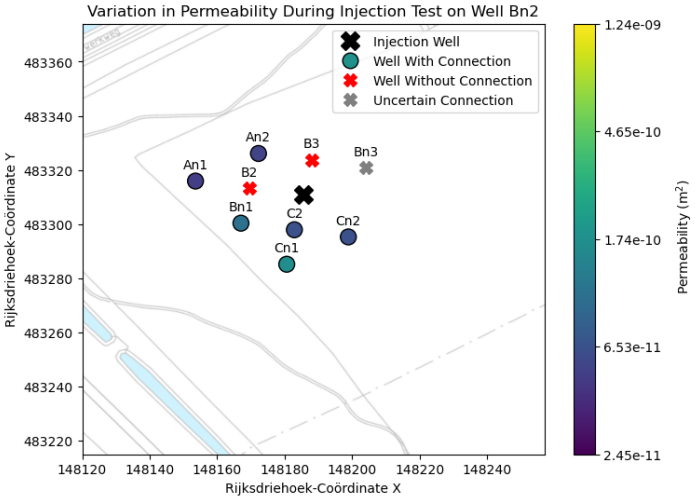

Figure D.18: 2025-03-18 - Injection on Bn1

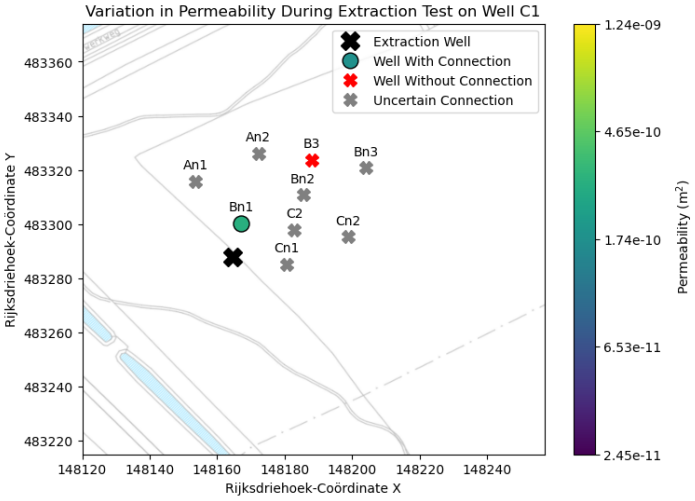

Figure D.19: 2025-03-18 - Extraction on C1

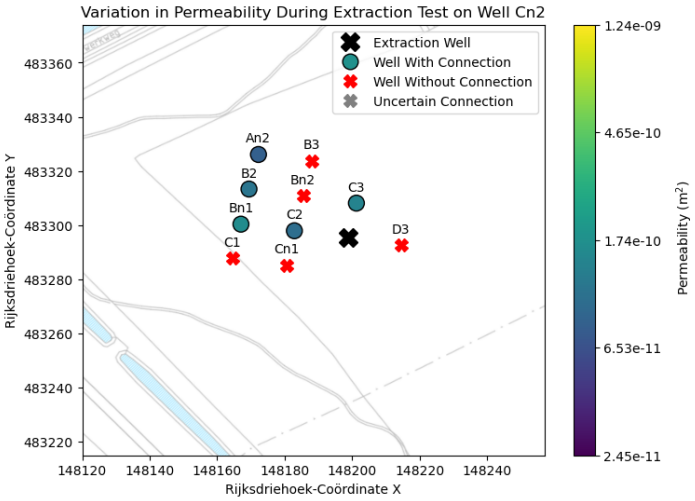

Figure D.20: 2025-04-25 - Extraction on Cn2

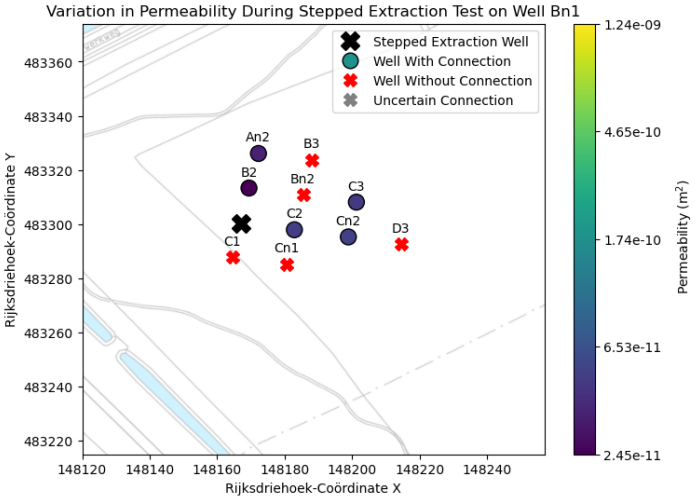

Figure D.21: 2025-04-25 - Stepped Extraction on Bn1 - Step 1

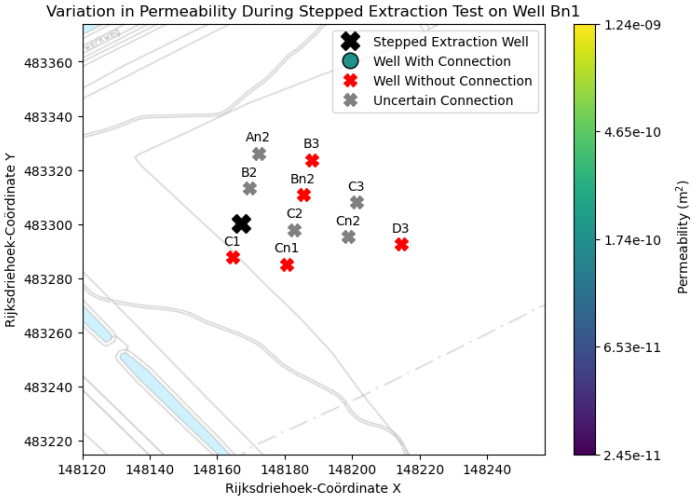

Figure D.22: 2025-04-25 - Stepped Extraction on Bn1 - Step 2

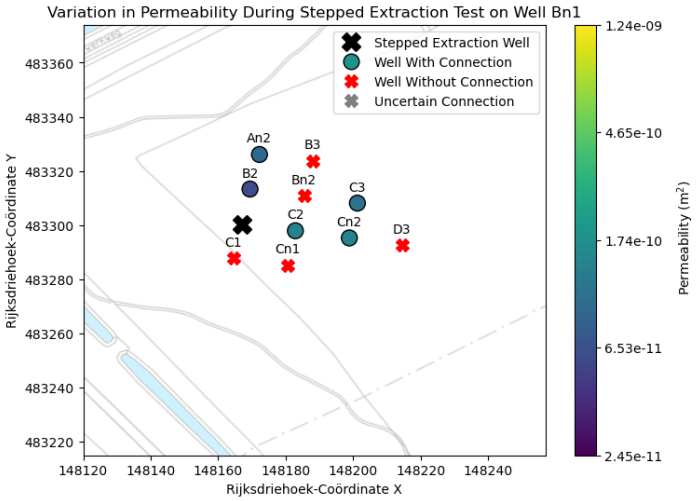

Figure D.23: 2025-04-25 - Stepped Extraction on Bn1 - Step 3

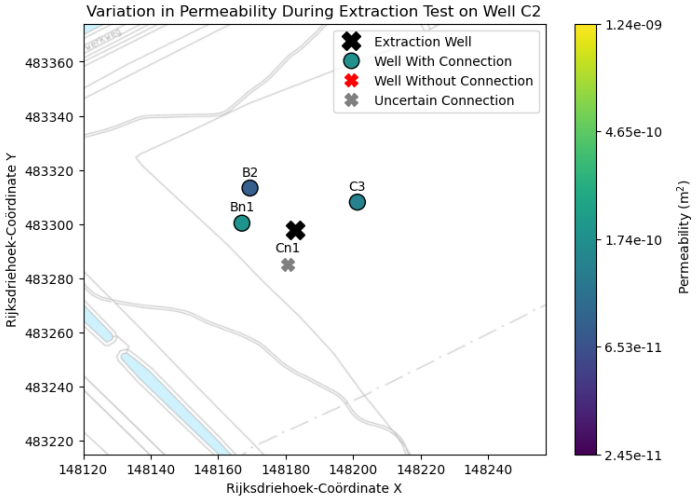

Figure D.24: 2025-04-30 - Extraction on C2

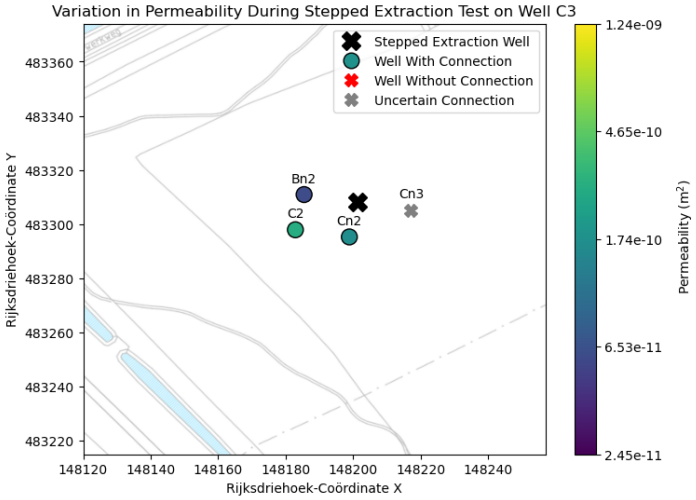

Figure D.25: 2025-06-11 - Stepped Extraction on C3 - Step 1

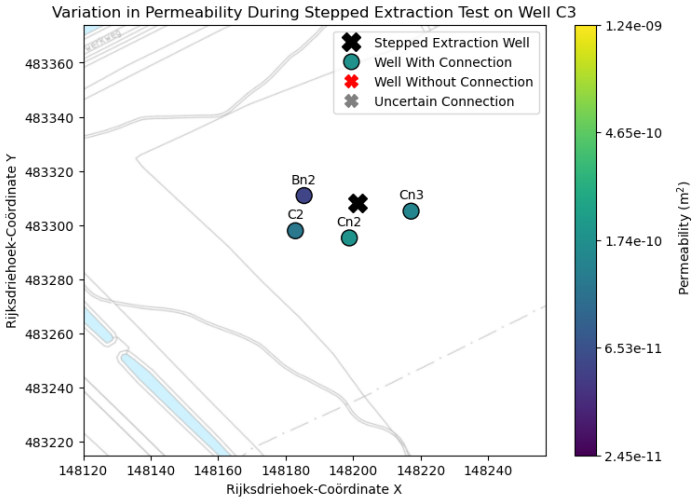

Figure D.26: 2025-06-11 - Stepped Extraction on C3 - Step 2

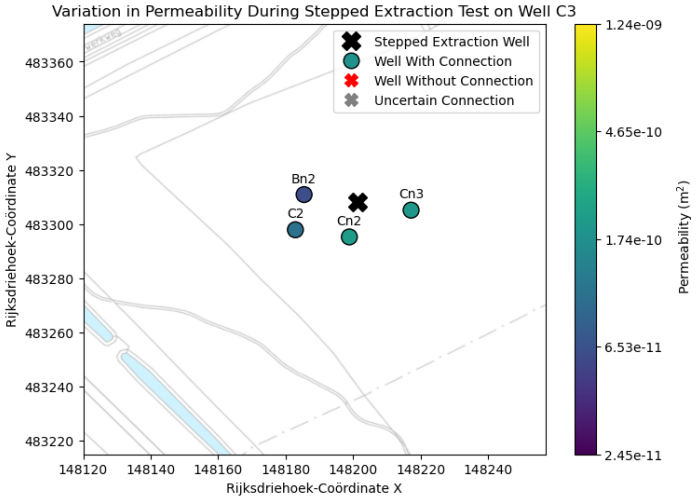

Figure D.27: 2025-06-11 - Stepped Extraction on C3 - Step 3

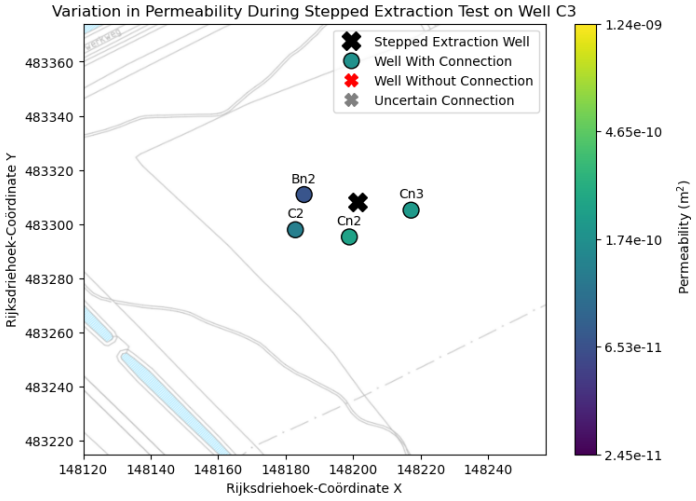

Figure D.28: 2025-06-11 - Stepped Extraction on C3 - Step 4

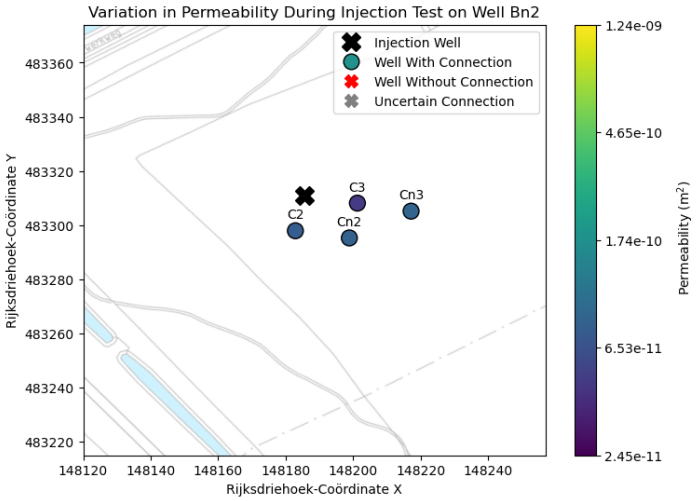

Figure D.29: 2025-06-11 - Injection on Bn2

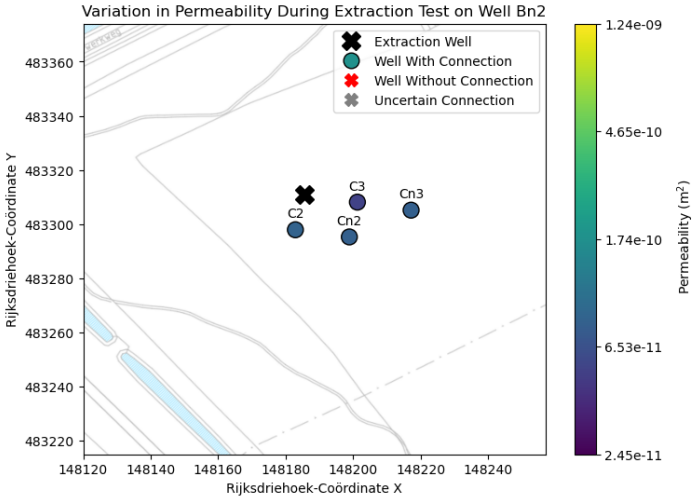

Figure D.30: 2025-06-11 - Extraction on Bn2

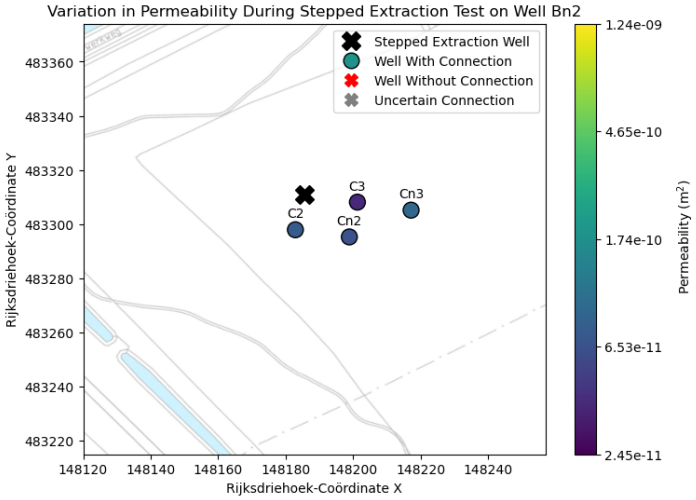

Figure D.31: 2025-06-11 - Stepped Extraction on Bn2 - Step 1

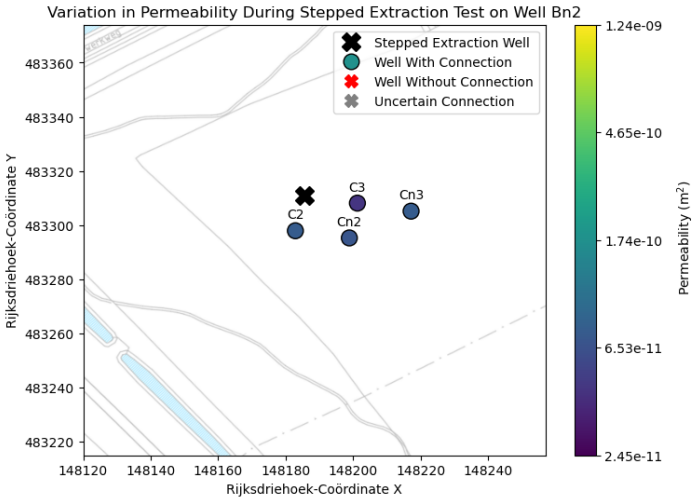

Figure D.32: 2025-06-11 - Stepped Extraction on Bn2 - Step 2

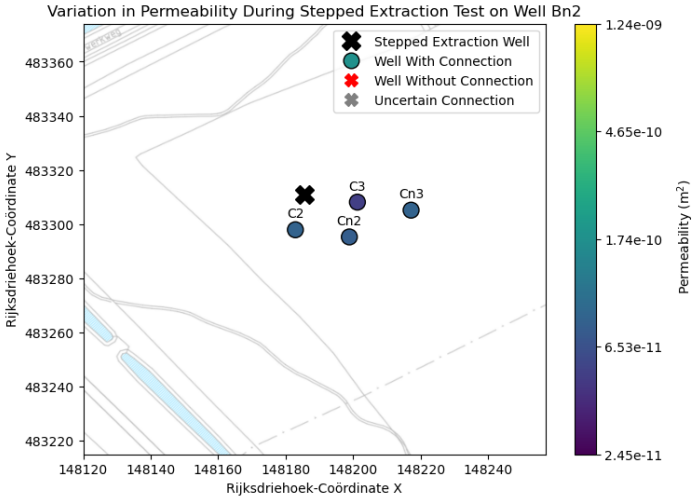

Figure D.33: 2025-06-11 - Stepped Extraction on Bn2 - Step 3

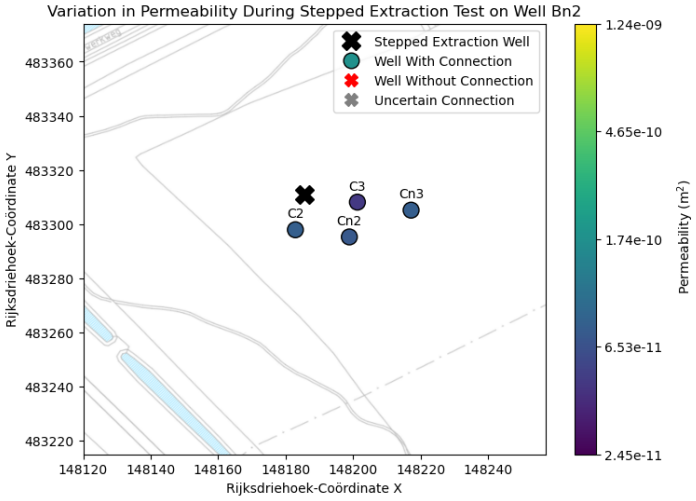

Figure D.34: 2025-06-11 - Stepped Extraction on Bn2 - Step 4

Appendix E: Additional Dual Porosity Correlations

This appendix provides additional plots of parameters which were checked for correlation, but where none was found. Figure E.1 shows additional correlations with saturation, as originally discussed in connection with Figure 58. Figure E.2 shows additional correlations with LFG composition, as originally discussed in connection with Figure 61. Figure E.3 shows additional correlations with LFG composition, as originally discussed in connection with Figure 62. Figure E.4 shows additional correlations with LFG composition, as originally discussed in connection with Figure 63. The unbounded values of γ are not included as the upper bound is not representative of any actual process.

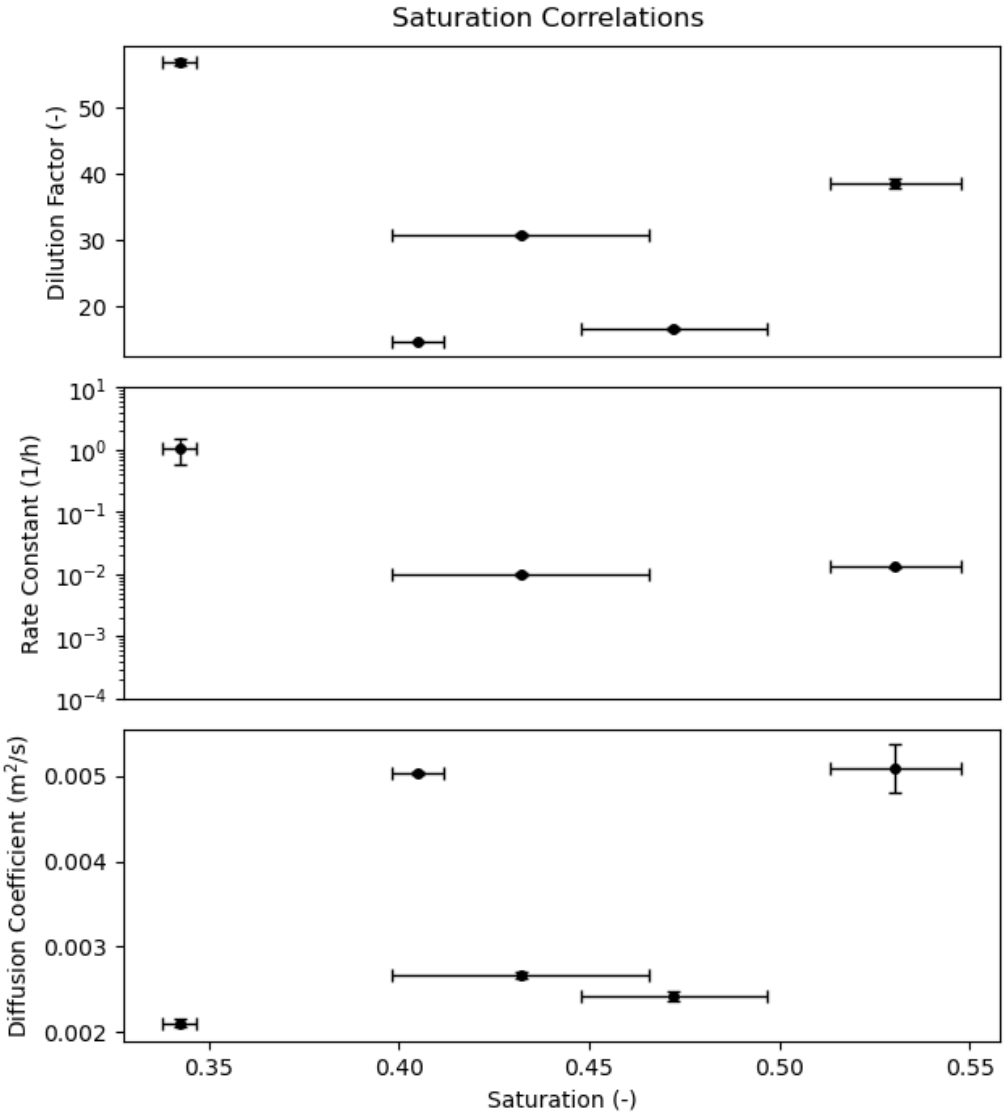

Figure E.1: Additional correlations with saturation

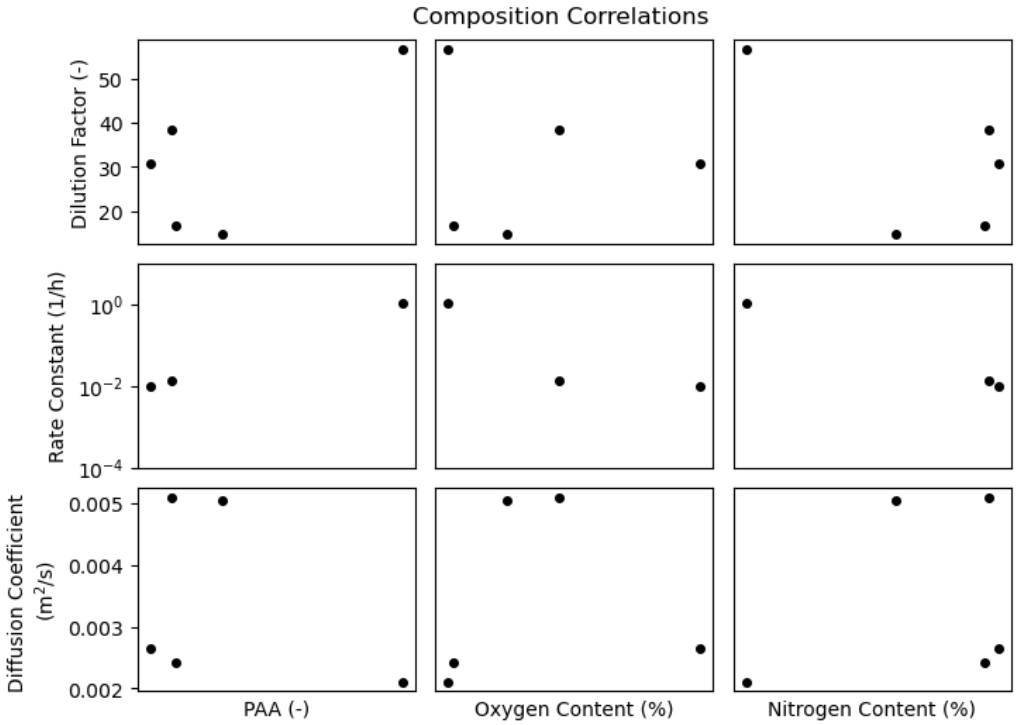

Figure E.2: Additional correlations with LFG composition

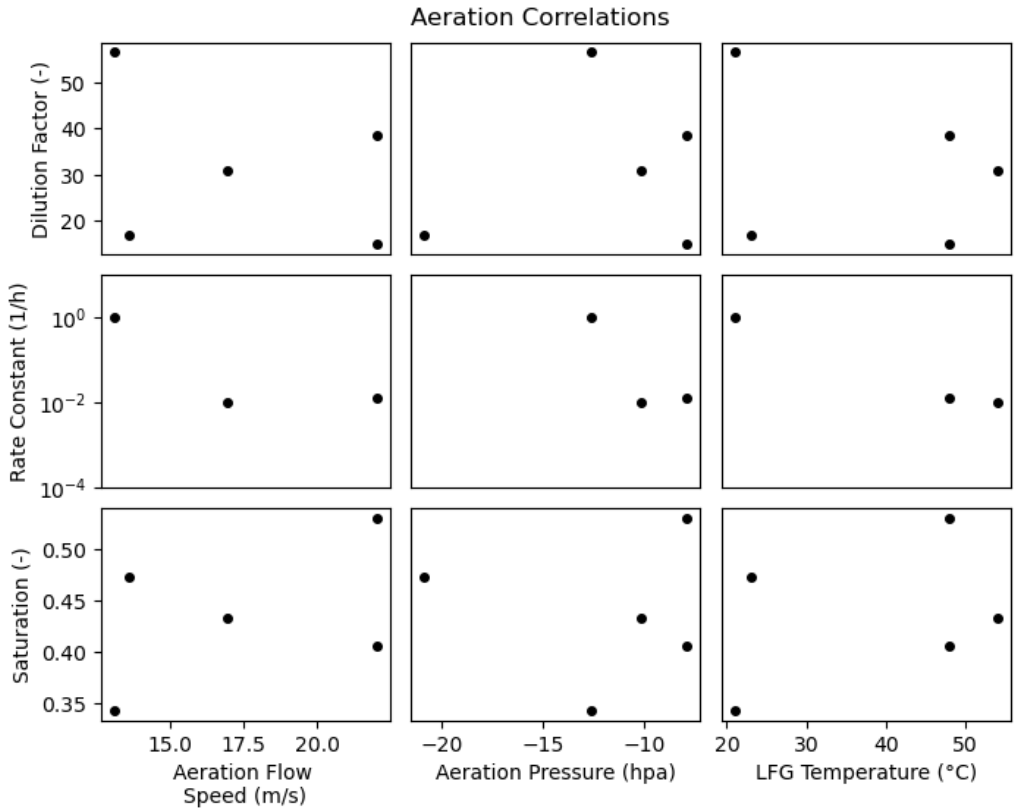

Figure E.3: Additional correlations with aeration performance

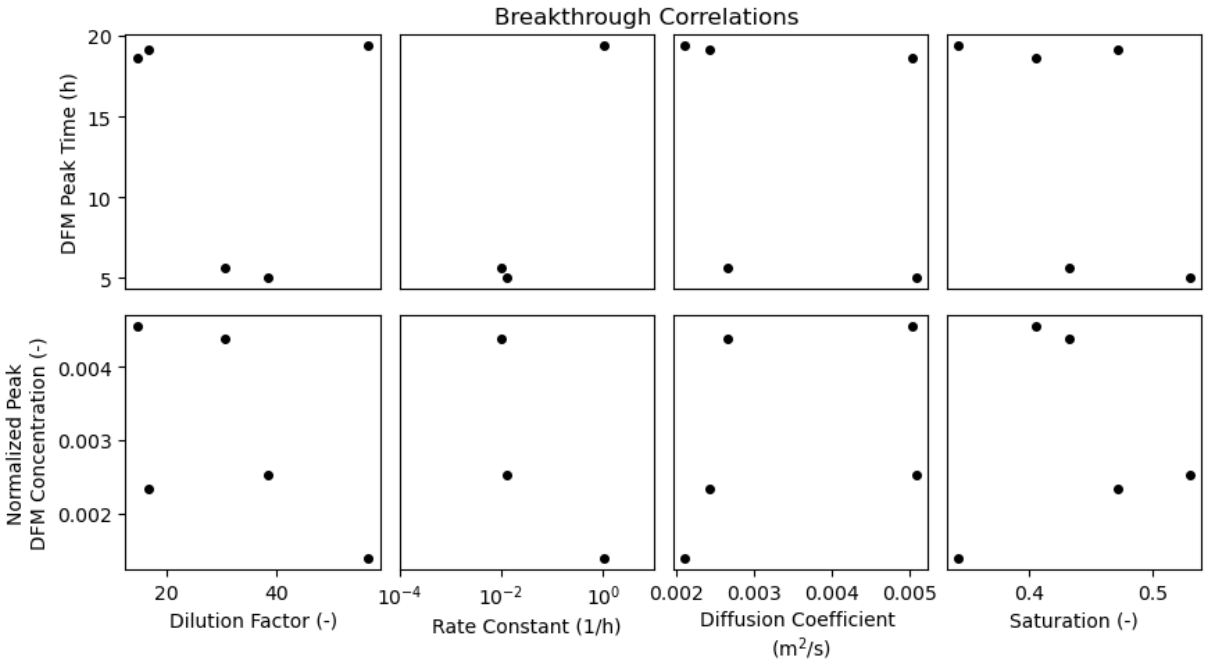

Figure E.4: Additional correlations with BTC parameters